UNIVERSITÀ DI PARMA

UNIVERSITA' DEGLI STUDI DI PARMA

DOTTORATO DI RICERCA IN SCIENZE DEL FARMACO, DELLE BIOMOLECOLE E DEI PRODOTTI PER LA SALUTE

CICLO XXXII

DEVELOPMENT OF THREE-DIMENSIONAL PRINTED SCAFFOLD PROTOTYPES AS DRESSINGS AND IMPLANTS INTENDED FOR THE TREATMENT OF SKIN TISSUE REGENERATIVE-RELATED PATHOLOGIES

PhD Coordinator:
Chiar.mo Prof. MARCO MOR

PhD Supervisor:
Chiar.ma Prof. LISA ELVIRI

PhD Candidate:
CARLO BERGONZI

Anni 2016/2019

Summary

Abstract

Abstract

Tissue engineering is a more and more maturing field of medicine, needing increasingly automated manufacturing processes for the creation of tissue repair solutions.
Herein this thesis, design and development of biocompatible materials as well as 3D printing (3DP) technology were focused and deepened in particular for the realization of hydrogel-based advanced medication prototypes, mostly dedicated to the skin regeneration but also suitable for dentistry purposes rather than for further applications.
In brief, overall pre and post-3D printing process parameters were investigated, in terms of correct material processing through the developed instrumentation, as well as chemico-physical features characterizing the hydrogels. Biocompatibility, cell proliferation enhancement were also probed by inoculating human fibroblasts and/or keratinocytes and measuring their viability, distribution and morphology.
In vivo experimental on diabetic ulcerated rats was assessed to prove their validity as wound dressing prototypes in comparison to a commercial patch, selected as model, and spontaneous healing.
Further, alternative antimicrobial compounds to antibiotics were included in hydrogel constructs, studied in this case like controlled drug delivery systems for the treatment of infected wounds.

Development and functionalization of polymer hydrogels can boost tissue regeneration, in this work, film materials for dentistry were doped with fibronectin and its engineered binding aptamer for bone reconstruction or epithelial repair. A Further functionalization, by collagen coating, was instead adjusted for 3D printed chitosan scaffolds; several characterizations and assays were performed in order to explore their potentiality for the purpose targeted.
Moreover, an analytical approach based on mass spectrometry, defined as hydrogen/deuterium exchange (HDX-MS), was tuned to better evaluate proper material functionalization with fibronectin.

Sterilization of developed prototype materials is not trivial for potentially marketable hydrogels, gamma irradiation was assessed and preliminary studied as promising suitable procedure.
The 3DP overall process was retained innovative in terms of obtainable hydrogel forms, furthermore, their general technical features seemed to be prone to favor cell growth through the 3D polymer structures. *In vivo* trials even more efficiently demonstrated their effectiveness as medications for ameliorating tissue regeneration, proved in particular by histological staining and

microscopical analysis conducted. *In vitro* antimicrobial activity of silver sulfadiazine-loaded scaffolds was fully achieved on *P. aeruginosa* and *S. aureus*, very common wound bed infecting pathogens.

The functionalization of these hydrogel materials for dentistry aims resulted particularly effective in terms of *in vitro* osteoblast and epithelial cells growth enhancement as well as for those cultured on 3D printed chitosan-collagen scaffolds. Moreover, the HDX-MS analysis confirmed fibronectin could selectively recognize the aptamer, indicating an efficient docking of the complex on the biomaterial.

Mass spectrometry was used also for the determination of collagen composition of decellularized rat thyroid matrixes, revealing which matrix preparation protocol was more appropriate for scaffold re-colonization.

Gamma rays sterilization procedure seems in a preliminary way to be feasible, but further technical investigations are required.

A step forward in the research on biocompatible materials intended for several purposes particularly focusing on wound dressings as well as their processing through additive manufacturing has been made, giving a small but hopefully significant contribute for the prototyping of hydrogels-based three-dimensional scaffolds.

As additional application, resourcefulness of 3DP was exploited also for the production of biocompatible wastewaters filtering system models for detoxification from amoxicillin as pollutant pharmaceutical. TiO_2 was included in form of powder in the material *ad hoc* developed for the purpose as drug photocatalytic agent. Characterizations and utilization tests were conducted in order to assay the feasibility of the idea. The formulation and 3D development of models of wastewaters filters surprised for its effectiveness and re-usability, further tests on other drugs are running to finely ameliorate the promising system.

Preface

Skin tissue engineering represents a continuous chase in biomedicine to the conclusive solution for chronic wounds at early-medium stage, not interested by severe conditions such as cellulitis or osteomyelitis. The latter constitutes a major issue in house-care and clinical settings of developed countries, affecting deeply both patient's quality of life and private/public expenditures.

A review of the accessible literature concerning the etiologic causes, pathogenesis, treatment, research and other relevant aspects was conducted and described in the section 1; followed by the aim of the work, particularly focused on skin, in section 2.

The majority of the activity was based on the development, adjustment and exploitation of a 3D printing process for the production of prototypes of medications intended mainly for direct application on the damaged skin or for other soft tissues repair.

Considering that the cornerstone of scaffold development was individuated in the 3D printing process, section 3 technically presents the features of the instrumentation as well as the main procedures and their significance for the resulting hydrogels.

Printing exploration focused on the control of the process parameters, with the aim of revealing whether it was suitable as novel hydrogel processing technique. Control of porosity, micro-architecture and material freezing were achieved after proper optimization of the formulation in terms of polymer concentration, excipients addition and blends viscosities as well as for the overall process.

Section 4 (chapter 1) in particular reports studies of temperature at deposition during 3D printing with a cryocooled sensor thermal camera, employed in order to deeply study the process.

Hydrogel chitosan scaffolds represented the first products born by this method; their design, production and characterization were accomplished, next, *in vitro* experiments served to demonstrate their biocompatibility as cell-growth supporting items rather than three-dimensionality progress against homologous material processed by solution casting.

The second work published gave an important contribute to the automated 3D printing procedure implementation; the complex issue concerning gelation reaction, as resumed in the title "Study of 3D-printed chitosan scaffold features after different post-printing gelation processes" (section 5), was originally examined screening a vast series of gelling agents, evaluating them for the time of complete gelation needed, together with 3D structure maintenance, selecting those that responded to determined requirements explained in the paper. Post printing gelation process can finely modulate product hydrogel parameters such as porosity, mechanical properties, capacity to swell,

retain or regain water and most of all, how human fibroblast cells, the predominant type involved in the process of skin regeneration, respond to these differences.

This aspect was further object of research (section 6); one among the prototypes developed, considered the promising the results attained that far, was employed in three-dimensional human cells culture with fibroblasts and keratinocytes over 35 days, to better simulate wound healing cell fauna and timing.

The encouraging results testified by the analysis described, suggested it would have been worth to test the objects on an animal model, since *in vitro* ones are not representative enough of the pathological condition aimed to ameliorate. Hyperglycemic diabetes condition was induced in rats on which dorsal circular excision were made; the further application of 3D printed chitosan scaffolds demonstrated their validity as contingent wound dressings, even supported by analogue contemporaneous comparison with both commercials patches and spontaneous healing.

Chronic infections at the wound bed are recurrent in patients suffering from chronic ulcers. Systemic administration of antibiotics can be substituted or coupled to the use of active medications having antimicrobial activity, preferably with controlled release patterns of the active compound. Moreover, the use of alternative antimicrobics can help in the fight against the development and spread of antibiotic resistant bacteria strains. Section 7 (chapter 4) tells about the proposal of 3D printed hydrogel-combined medications loaded with silver sulfadiazine, having demonstrated antimicrobial activity and different drug release patterns and quantities, in order to develop a prototype of tunable platform for infected ulcerated skin tissue treatment.

The materials employed till this point of the research suggested thinking about the design and subsequent creation of scaffolds intended for other soft tissues. Their proper functionalization can be exploited for tailoring the item for a determined tissue type; protein adsorption to the surface of a biomaterial can help cell-protein recognition and stimulation of the repair process, small molecules such as aptamers can further be engineered to conformationally favor protein biological activity, probably by binding the material surface and the protein at the extremities.

Cell morphology can, moreover, be highly influenced by the formation of such cell-protein connections, executing or not their physiological duties.

Indeed, section 8 (chapter 5) is dedicated to the preparation of the material as first step, including functionalization with fibronectin, that constitutes for the majority the provisory cytoskeleton protein synthesized when functional ECM is lacking, and its engineered binding aptamer. Cell morphology evaluation and activation of the integrin-mediated pathway were evaluated as well as quantification of protein adsorption.

The confirmation of the hypothesis that the aptamer favored fibronectin functional functionalization of the chitosan surface was exposed in a second publication treating the topic in section 9, entitled "Surface modification of chitosan films with a fibronectin fragment-DNA aptamer complex to enhance osteoblastic cell activity: A mass spectrometry approach probing evidence on protein behavior", in facts, as previously hypothesized, the aptamer was able to bind to residues of chitosan and selectively fibronectin; this interaction in solution or on chitosan films was demonstrated by Amide Hydrogen/Deuterium Mass Spectrometry Exchange (HDX-MS). The biological activity of aptamer-bound fibronectin compared to the "normally" adsorbed one (functionalization without the aptamer) is explained by *ad hoc* experiments inoculating osteoblastic cells.

Other approaches of functionalization of developed biocompatible materials are described in section 10 (chapter 7), where collagen is applied on chitosan 3D printed scaffolds already investigated. The aim is the regeneration of epithelial tissue, studies conducted for dentistry research tissue regenerative purposes; several *in vitro* and analytical work was executed in order to evaluate from a biological and analytical point of view the effectiveness of the system in supporting epithelial cell proliferation through the three-dimensional weft of the scaffold.

The HDX-MS technique used to study biomaterial-aptamer-fibronectin interaction can be employed in several fields, of course including pharmaceutical technology and drug development. Biocompatible polymers are constantly studied as controlled drug delivery systems by non-covalently interacting with therapeutic proteins. In section 11 (chapter 8), HDX-MS was employed to localize insulin dynamics induced by interactions with three natural polysaccharides, chitosan, sodium alginate and chondroitin sulfate.

Returning to tissue engineering, decellularizing organs to extract their three dimensional composition is a more and more utilized practice for both a scaffolding approach and study of the processes involved to obtain it, in order to evaluate which technique of cell removal is better applicable. A mass spectrometry original method in section 12 (chapter 9) was tested after development and then validated for the screening of different protocols adopted to retain the native 3D architecture of the ECM, quantitatively characterizing the obtained stromal matrixes.

An automated system implies that the procedure for prototyping is fully covered by a robust scalable model. "Sterilization" for *in vitro* and *in vivo* experimental told until section 7 (included), has been always performed by aseptic procedure of disinfection by immersion in 70 % ethanol, an effective practice at laboratory level but not adequate for industrial manufacturing settings. Gamma rays sterilization of chitosan 3D scaffolds suitability was preliminary tested in terms of

chemico-physical characteristics and effectiveness of sterilization in section 14 (chapter 11). Further investigations are currently running, like biological cell response evaluation and molecular weight distribution analytics, although early results let think about a suitable technology for the purpose.

Finally, the big versatility of the 3D system widely described in chapter 1, 2, 3, 4, 7 led to development of an item dedicated to environmental sustainability, communicated through a publication on the Journal Water Research and exposed in section 13 (chapter 10).

Antibiotics water pollution can trigger positively the development of resistant bacteria strains. Cleaning waters from these active compounds is challenging, amoxicillin, for instance, is secreted at the 80 % in its unaltered form from mammalian's body. Titanium dioxide has been quite recently discovered having catalytic activity versus some among such compounds under UV irradiation, but the issue of immobilizing it into a proper biocompatible water filtering system remains evident. The need of non-toxic filtering materials supporting the photocatalysis of antibiotics rather than other pharmaceuticals is imminent; chitosan is known for its biocompatibility and non-toxicity, its gels are biodegradable and the expertise of manipulating it through 3D printing matured, as well as preparing inks for three-dimensional printing, suggested to develop chitosan hydrogel supports including TiO_2, having a high surface area to volume ratio and thus providing numerous catalytic sites thanks to homogeneous dispersion in the formulation phase.

1 Introduction

1.1 Tissue engineering for chronic skin wounds

1.1.1 Brief history of Tissue Engineering

The term "Tissue Engineering" refers to the science involving and joining from a technical and theoretical point of view disciplines related to life sciences, applying them in the field of medicine with the aim of restoring unhealthy tissues.

The first reliable proof of restoring attempts is represented in the painting dated 1438-1440 by Fra Angelico, "*The Healing of Justinian*", depicting the Saints Damian and Cosmos trying to transplant a lower limb onto an injured soldier and symbolizing the conception of substituting or cure damaged body parts[1] (image 1).

Image 1. Fra Angelico - "*The Healing of Justinian*" by Saint Cosmas and Saint Damian

Development and evolution of medicine led to the rise of studies concerning manipulation of living tissues as well as their integration with other materials. In the early 70's of the past century, W.T. Green, an orthopedic surgeon, seeded chondrocytes onto spicules of bone and implanted them in nude mice with the final aim of obtaining regenerated cartilage. Mice died afterwards, probably due to infection, but he captured the interest of the scientific community, since he

correctly hypothesized that it was possible to make tissues grow *in vitro* with the employment of *ad hoc* configured innovative biocompatible materials. Further similar lines of experiments were conducted at the Massachusetts Institute of Technology (M.I.T.) in the early 80's, when Drs. Burke and Yannas engineered a collagen matrix to support the growth of dermal fibroblasts to create a skin substitute, or when Dr. Howard Green transferred sheets of keratinocytes onto burn patients.

The emblem of the birth of tissue engineering is considered the meeting between Dr. Joseph Vacanti of the Children's Hospital and Dr. Robert Langer of M.I.T., in mid 80', in which they decided to start designing appropriate scaffolds for cell delivery, instead of trying to achieve regeneration seeding cells onto naturally occurring materials, that did not present tunable chemico-physical properties.

From the early 90', the first centers dedicated to tissue engineering research were founded, in order to deepen different aspects of the new-born discipline, focusing mainly on cardiology studies, use of stem cells and liver regeneration. At the end of 90's, tissue engineering organizations were springing-up almost in every developed country all over the world.

1.1.2 The skin

Skin is an impressive organ, both for its structure and functionalities and it accounts for about 15% of the total adult body weight. It has the duty to prevent dehydration and maintain water balance in the body, rather than avoiding loss of solutes. It protects from bacterial infections, it is involved in thermoregulation, it produces a vitamin D precursor, it protects us from damage by ultraviolet light and it detects information from the environment. The skin is not just a physical protection against microorganisms, in facts, it is not a complete waterproof barrier and this is the reason why it's possible to administer drugs having the right physico-chemical properties through the skin pores by topical application[2].

1.1.2.1 Skin anatomy in brief

The skin consists mainly of two layers: the epidermis and the dermis, the first one consists of the outer layer, the second is deeper and adjacent to the subcutaneous tissue.

All of these layers have precise structures and functions and their activities are crucial for human health. Epidermis is only a few cells thick and it can be subdivided into five identifiable layers:

the *stratum corneum*, *stratum lucidum*, *stratum granulosum*, *stratum spinosum*, and *stratum basale* (Figure 1)[3].

The *stratum corneum* (SC) consists of stratified thin layers of dead, keratinized cells that are constantly being shed, its main function is the ability of withstand mechanical forces[3] (Figure 1).

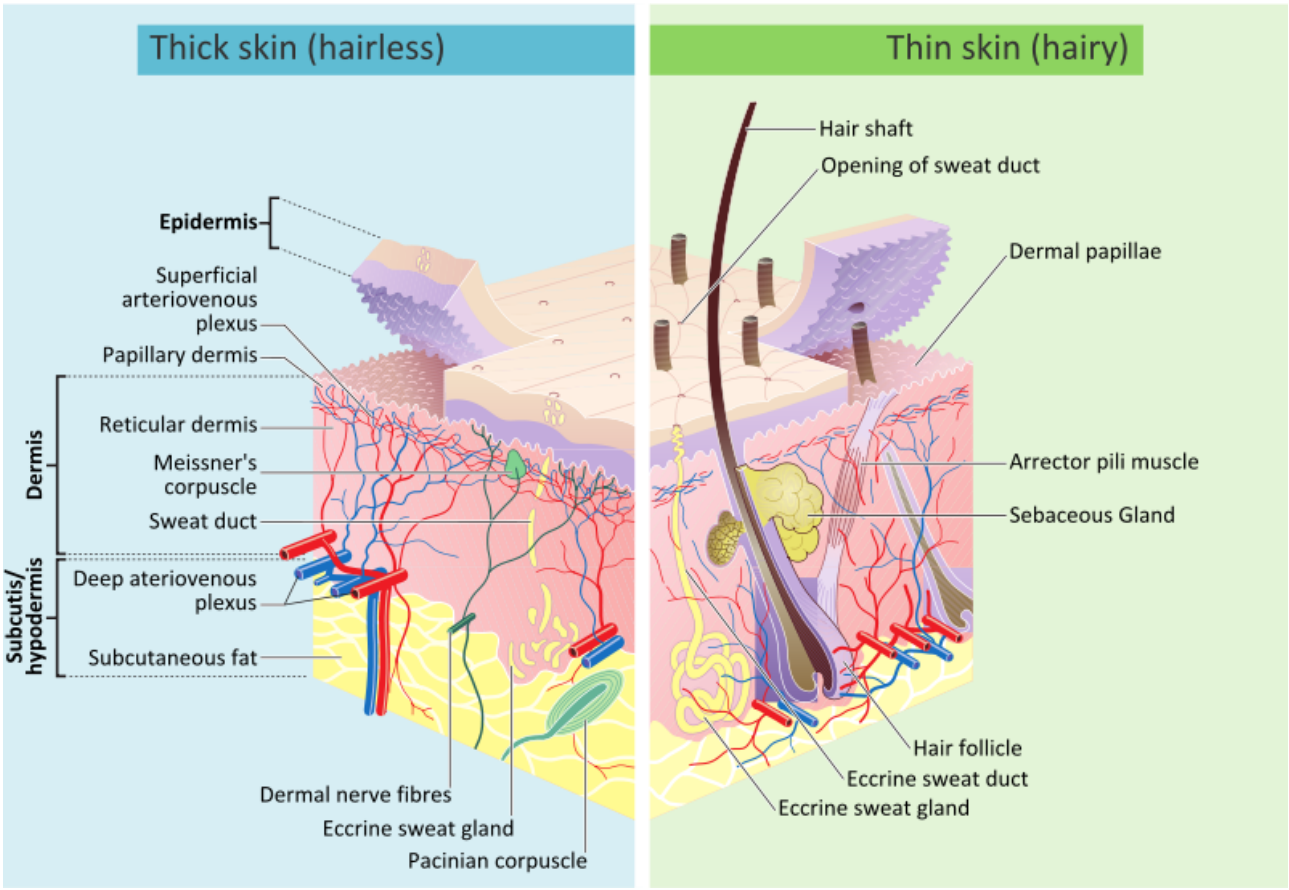

Figure 1. Cross section representation of skin[3].

The SC forms a continuous sheet of protein-enriched cells (corneocytes) connected by corneo-desmosomes and embedded in an intercellular matrix enriched in non-polar lipids and organized as lamellar lipid layers. Moreover, it presents an acid mantle to the external environment, helping to protect the body and reduce the growth of pathogenic microbes.

The *stratum lucidum* consists of 2-3 layers of cells, present in thicker skin found in the palms and soles, it is a thin clear layer consisting of eleidin which is a transformation product of keratohyalin[4].

The cells of the *stratum granulosum* or granular layer appear flattened or diamond shaped, and contain keratohyalin granules. Skin macrophages in this layer are responsible for immune reactions, such as inflammation. The *stratum spinosum* or prickle layer contains several layers of

cells and owes its name to a network of intracellular bridges or spines that extend between the cells. Cells from this transitional layer begin the process of keratinization into the flattened, tough cells of the outer layers.

The *stratum basale* or basal layer consists of a single layer of columnar cells, including keratinocytes and melanocytes responsible for skin pigmentation. The basal layer generates the cells found in the outer layers of the epidermis.

Although there are five layers in the epidermis, it is relatively thin and contains no blood vessels of its own. The basal layer continuously generates new cells that migrate upward, lose their nucleus, and transform via a process known as keratinization, to eventually become part of the horny layer. The entire epidermis is replaced with new cells from the basal layer every four to six weeks. A major problem in wound healing is that loss of the basal layer over a wound cuts off the direct supply of new epithelial cells, and healing then requires epithelial cells to migrate from the wound edges to cover the deficit. Such migration is seriously impeded or delayed by the presence of scab tissue or a dry wound surface.

Below the epidermis lie the two layers of the dermis that contains mainly collagen and elastin fibers, hair follicles, sebaceous glands, blood and lymph vessels, nervous sensory receptors and cells from the immune system.

The papillary dermis is closest to the epidermis and is rich in blood vessels, collagen, and reticular fibers, which allow nourishment of the basal layer of the epidermis and provide high tensile strength. Looking like a mountain range under a microscope, the papillary dermis consists of thousands of hills and valleys that form an intimate connection to the epidermis called the dermal-epidermal junction. This junction firmly anchors the dermis to the epidermis and provides the skin with significant ability to stretch.

Flattening of the dermal-epidermal junction, as occurs with aging, significantly reduces the ability of skin to stretch before tearing.

The reticular dermis, the second layer of the dermis, is a thick layer of collagen fiber bundles in an extra-cellular matrix of ground substances, such as proteoglycans and hyaluronic acid. The reticular dermis contains dermal appendages, blood vessels, and nerves and anchors the dermis to subcutaneous tissue.

Appendages in the dermis can be classified as cornified or glandular. Cornified appendages generate nails and hair, while glandular appendages produce oils essential for the components of sweat and hydration and lubrication of the skin. Dermal appendages, such as hair follicles or sweat glands, are lined with epidermal cells. In the event that the epidermis is destroyed or injured, the lining of the appendages can generate islands of new epidermis that can grow and unite to

regenerate a fully functional epidermal layer over the wound. If the wound is deep enough to destroy the dermal appendages, new epidermal cells must migrate from the wound edges, and the healed wound will lack its complement of appendages. Thus, full-thickness wounds cannot heal by regeneration and will heal instead by scar formation where the wound is covered by skin lacking in several functional capabilities.

Located beneath the dermis, the hypodermis or subcutaneous layer serves as a location for the formation and storage of fat. It contains adipose tissue and connective tissue, and it supports nerve fibers and major blood and lymph vessels. Deeper sweat glands and hair follicles can extend into this layer. The subcutaneous layer permits mobility of the skin over underlying tissue, insulates against cold, provides a reserve of calories, and protects underlying fascia, muscle, and bony structures from injury. It varies in thickness, with thinner areas overlaying bony prominences. Full-thickness wounds, such as venous leg ulcers and Stage III pressure sores, may extend into subcutaneous tissue.

1.2 Skin tissue regenerative-related pathologies

Age, disease and trauma can often give a strong contribute to chronic pathological conditions, usually requiring treatments helping in tissue regeneration enhancement or even organ transplantation[5]. Tissue engineering proposes cures not relying on transplants, a general promising remark that could potentially solve or at least lighten the problem of organ availability and rejections[6-8].

Currently, transplantation of whole organs finds a limit consisting in limited donor supply as well as immune responses issues[9].

In particular, pathologies discussed in this thesis as well as the respective proposed treatments are mainly related to defects of, or insults to the extracellular matrix (ECM) in tissues, especially concerning skin.

ECM is an organ-specific highly hydrated three-dimensional network of proteins, glycoproteins and proteoglycans, non-cellular components interconnecting all tissues and organs. It plays a crucial role providing physical scaffolding for cells and it regulates many biochemical and biomechanical cues required for tissue morphogenesis, homeostatis and other key cellular events such adhesion, migration, proliferation, differentiation and survival[10].

ECM macromolecules are strictly organized and this organization determines the bioactivity of the tissue, thus, even minor alterations of their composition and integrity can lead to altered

physicochemical properties of the tissues and cellular phenotype giving rise to several pathologies[11].

1.2.1 Diabetic Foot Ulcers (DFU)

Diabetic Foot Ulcers can develop in diabetic fellows especially in elder age due to traumas or mechanical insults associated to peripheral neuropathy.

Diabetes-related peripheral neuropathy (DPN) is a diabetes-related complication characterized by damage of nerves caused by high glycemic conditions, which reduces the ability to feel pressure or pain and leads to the tendency from the patient to ignore pressure points and avoid pressure relief strategies.

Accidental and/or repeated strikes in peripheric area of the body, such as legs for example, can injure the tissues irreparably, since in these pathological conditions repair mechanisms can results altered and compromised[12].

The healing process is an innate mechanism of tissue repair that is defective under certain pathological conditions, in which the ECM of the dermal layer, critical mediator of cutaneous wound healing, is not properly repaired.

Normally, skin regeneration consists of four overlapping and simultaneous steps, that in sequential order are represented by:

- Blood clotting, characterized by events such as vascular constriction and formation of a clot by platelets. Apart from physically avoiding blood leakage, it serves as support for migratory cells adhesion. Moreover, blood clot releases cytokines and growth factors (GF), boosting in this phase the rate of cellular division.
- Inflammation, during which vessels dilatate and exudate levels raise, phenomena like erithema, heat and functional disturbance occur.
- Proliferative phase is characterized by the formation of a granulation tissue in which angiogenesis takes place to form new vessels and fibroblasts synthesize ECM proteins. A provisional matrix, consisting of fibronectin, tenascin, and Type III Collagen is secreted and assembled by fibroblasts and it works as scaffold for cell migration and proliferation.
- Re-modelling phase consists in the rearrangement of the dermal tissue, possible thanks to the replacement of non-functional fibroblasts by functional ones[13-15].

  During the last phase, Type I Collagen replaces fibronectin, becoming the main ECM constituent and resulting in a more mature ECM[16].

In diabetic individuals these processes can be significantly altered both in terms of molecules production and secretion rather than proliferation capacity, since blood vessels at peripheral levels can be highly damaged. This implies that decreased arterial perfusion of the extremities, usually diagnosed by angiography (considered the gold standard technique for its identification)[17], leads to a reduced nutrients supply, crucial for cells proliferation and functionality in the restoring course of action.

For instance, it has been recently investigated the influence of hypoxic conditions on DFU's healing capacity, in particular, it was hypothesized and demonstrated that angiogenesis is decreased as well as marrow-derived endothelial progenitor cell (EPC) recruitment. Moreover, fibroblast and keratinocyte proliferation and migration is limited in these oxygen-poor conditions[18].

Diabetic ulcers that develop after injury are characterized by increasingly hypoxic wounded area as a result of vascular disruption and increased oxygen consumption due to inflammatory responses[19]. Hypoxia-inducible factor-1 (HIF-1) is a transcription factor stabilized and activated in hypoxic conditions in healthy individuals, designated to regulate oxygen homeostasis, angiogenesis, erythropoiesis, proliferation, migration and cell survival[20]. HIF-1 governs multiple cellular processes that contribute to healing, for instance, the enhancement of EPC motility and recruitment to wound site and furthermore, it improves bactericidal capacity of immune cells such as myeloid ones by increasing the production of defense factors (granule proteases, nitric oxide, antimicrobial peptides)[21]. A deficiency in the functionality of this transcription factor, as in diabetic individuals, is always translated in a delayed or missed repair and thus it gives a significant contribute to the insurgence of chronic sores.

Bacterial infection is usually the consequence of skin ulceration, but meanwhile is considered the cause of deterioration.

Infection can be superficial and local, it can interest soft tissue and it can spread (insurgence of cellulitis and osteomyelitis). Soft tissue infections are quite evident when the limb is perfused, since the inflammation is obvious. When the limbs are ischemic infection can be characterized by large amounts of exudates, inner localized pain and in more-complicated cases by digital gangrene in the foot. Early local antibiotic treatments have to be considered when such infections are diagnosed. Infections typically imply the involvement of many bacterial species, both $gram^+$ and $gram^-$, aerobic and anaerobic, in particular *Staphilococcus aureus* is the most common pathogen in most serious situations[22].

In general, etiologic factors are multiple and a deeper understanding of the mechanisms involved, that are so far not totally clear, would help in terms of identifying efficient therapeutic approaches.

1.2.1.1 DFU epidemiology

Diabetic foot ulcers have a strong impact from a social point of view, since quality of life of diseased patients is deeply impaired, often leading to prolonged hospitalization and serious disabilities in everyday life.

Incidence of DFU's has increased due to worldwide increased prevalence of diabetes mellitus and to the prolonged life expectancy of patients.

One of the major complications of DFU's is amputation of lower limbs; it is in facts estimated that a foot is amputated due to diabetes every 30 seconds[23].

An extensive epidemiological study was conducted in 2017 by Zhang P. *et al.*, 800,000 global participants from 67 studies were surveyed and the results indicate that the average prevalence of DFU's was about 6.3% worldwide.

The following table shows the prevalence of DFU's in each country analyzed.

Country	No. of studies	Prevalence	95%CI	I^2
Belgium	1	16.6	10.7–22.4	NA
Canada	1	14.8	9.4–20.1	NA
USA	3	13	8.3–17.7	98
Trinidad	1	12.2	10.8–13.6	NA
India	2	11.6	6.4–16.8	90.8
Norway	1	10.4	8.8–11.9	NA
Cameroon	3	9.9	6.3–13.5	86.6
Italy	1	9.7	7.8–11.6	NA
Thailand	2	8.8	1.7–15.9	95
Iran	2	8.1	0.1–16.1	94.9
Denmark	1	7.8	5.6–10.1	NA
Pakistan	4	7.4	0.5–14.3	99
Tanzania	2	7.3	2.1–12.6	83.4
Pacific island countries	1	6.8	4.5–9.0	NA
UK	4	6.3	4.6–8.0	79.8
Egypt	2	6.2	4.1–8.2	49.8
Bahrain	1	5.9	4.7–7.1	NA
South Africa	2	5.8	3.8–7.9	0
France	1	5.6	2.4–8.7	NA
Greece	1	4.8	3.3–6.2	NA
Jordan	2	4.2	3.4–5.1	0
China	10	4.1	3.1–5.2	97.4
Uganda	1	4	1.6–6.4	NA
Ireland	1	3.9	2.3–5.5	NA
Turkey	1	3.1	1.9–4.3	NA
Spain	5	3	1.9–4.4	97
Germany	2	2.8	2.4–3.3	0
Saudi Arabia	1	2.3	2.2–2.4	NA
Japan	1	2	1.4–2.6	NA
Netherland	2	1.8	1.0–2.6	0
Korea	2	1.7	0.6–2.9	85.1
Poland	1	1.7	1.1–2.3	NA
Australia	2	1.5	0.7–2.4	58.1

NA: not available.

Table 1. Prevalence of diabetic foot ulcer in each country[24].

Belgium scored the highest value in terms of prevalence (16.6 %), followed by countries from North America (13 %) while Oceania showed instead the lowest one (3 %). Since the very high prevalence in North America and Belgium was unclear, national smoking surveys were also consulted, demonstrating that smoke habit was more common among citizens of these countries. In facts, smoking was identified as a strong risk factor for diabetic foot ulcers, since daily hypoxia causes vascular and neuropathic disorders in the lower body extremities of diabetic patients[25-26]. Thus, the relatively large proportion of smokers in these countries could explain the high prevalence of diabetic foot ulcers.

Other risk factors, for instance, are represented by elder age, diabetic duration, Body Mass Index (BMI) distribution, hypertension and obesity; the latter seems to be a controversial etiologic factor, since there are prospective studies showing that BMI has no significant correlation with diabetic foot ulcer[27-28], while there are others suggesting that patients with a BMI <25 kg/m^2 and BMI >45 kg/m^2 were correlated with higher risk of developing ulcerations[29].

The lifetime risk of developing ulcers for any diabetic is up to 15 %[30], amputation often recurs when the sore is strongly disabling. The amputation rate depends on many critical factors such as prevalence, complication of the wounds and it is also driven by surgeon *modus operandi*. In some cases early amputation means low healthcare standards, while in some others can represent the fastest way to ensure a relative independence to the patient. Conversely, lower rates of amputation can be attributed to better care but also reflect an excessive conservative approach, frequently resulting for the patient in protracted incapacity, suffering and death with ulcers unhealed.

By the way, incidence of major amputations ranges from 0.05 to 0.5 % for diabetic patients[31-33] but the variability of these range is pretty high due to racial differences, unequal access to care and differing opinion on best practices, also depending on the country healthcare systems.

1.2.1.2 Global burden of diabetic foot disease

Foot lesions related to diabetes, apart from causing pain, suffering and morbidity, represent a huge burden from an economical point of view. All the procedures involved in the management of these sores include interventions to prevent foot ulcers, treatment strategies to healing and costs attributable to administration and care necessary for disability after surgical interventions.

In US, healthcare expenditures concerning ulcerations and amputations reached 10.9 billion in 2001[34-35]. The same type of estimates applied to UK showed that diabetes-related foot complications consisted in 252 million £/year and that the total annual expenditure in 2001 for diabetes represented the 5 % of the total national health service[36].

In particular, the majority of costs occur in the inpatient setting, and include direct costs such as hospitalization itself, nursing, dressings change and other treatments but also indirect costs should be considered, as home treatments, equipment to help disabilities (especially for amputated individuals), home services and drugs. Prevention is a practice every diabetic should care about, since in the most of cases atherosclerosis and consequent circulatory problems can be limited by having a correct lifestyle for these pathologic conditions. Moreover, physicians should weigh the cost of the indicated therapy for patient, although in many cases it's difficult to determine if a determined treatment would be successful or not.

1.2.2 Decubitus wounds

The pathogenesis of bed sores, also called pressure sores, is quite similar to that of diabetic foot ulcers; blood supply impairment plays a significant role in the insurgence of these complication. Constant pressure on soft tissues and muscles, especially those close to bony prominences, initially causes poor blood irroration of the interested tissues. Coupling this dangerous prolonged condition with tissue malnutrition lead to capillary bed occlusion and local ischemia. Scarce blood flow causes the accumulation of toxic metabolites inside skin and muscle cells, that prematurely drives to cell death and subsequently to ulceration and necrosis of skin and underlying tissues[37]. Pressure ulcers are likely to occur under relatively low pressures over long periods of time rather than under short episodes of high pressure. A healthy adult can develop a pressure ulcer if pressure sufficient to close capillaries (25-32 mm Hg) is applied for sufficient time, such as when undergoing a lengthy surgical procedure. In the compromised or elderly patient, significantly lower pressures may lead to pressure ulcer formation.

Several pressure sore classification systems have been used since 1975:

- Stage I ulcers are indicated by damaged friable surface skin with considerable hidden cell death caused by continuous pressure damage usually from immobilization in a single position. Identification of signs of pain and early indications of visible damage is a significant event in that it alerts caregivers of the need for interventions to prevent more serious damage.
- Stage II ulcers present as partial thickness wounds, which may heal with early intervention by regeneration under advanced wound care techniques.
- Stage III ulcers are usually full-thickness pressure sores. These are often difficult to classify due to the presence of eschar that obscures visualization of the wound bed.
  The presence of eschar does indicate a full thickness wound but the eschar must be debrided before classification can be established.
- Early Stage III or Stage IV pressure ulcers may superficially resemble Stage I ulcers. A wound initially classified as Stage I may, therefore subsequently appear to progress to higher stages as the already damaged deeper tissues slough off or as auto-debridement occurs with moist wound healing therapy.
- Stage IV pressure ulcers are characterized by full thickness skin loss with extensive destruction, tissue necrosis, or damage to muscle, bone, or supporting structures (e.g.,

tendon, joint capsule). Undermining of healthy surrounding skin and sinus tracts may also be associated with Stage IV pressure ulcers[38].

1.2.3 Venous Leg Ulcers (VLU's)

Venous disease is defined as an alteration in the vein integrity, resulting in decreased venous return or thrombosis. Arterial blood is pumped from the heart into arteries (muscular, elastic vessels) which maintain the pressure required to drive the blood throughout the body[39].

The venous blood vessels receive blood at low pressure and lack muscular walls to push the blood back to the heart; this part of the circulatory system must rely on the force provided by skeletal muscles of the leg and foot to squeeze blood upward against the pull of gravity. Veins contain a number of one-way valves that ensure that venous blood moves toward the heart and does not pool in the lower leg. In patients with chronic venous insufficiency or venous hypertension, there is a failure of the valves to perform their function. The blood pools in the lower leg, venous pressure increases, and blood vessels stretch and dilate[40-41]. The smallest blood vessels become thin enough to leak intravascular fluid and cells into the tissues, producing edema of the lower leg. Edema increases the distance oxygen and nutrients must travel to support tissue metabolism, possibly leading to tissue death and the appearance of venous leg ulcers. Heredity, injury, and occupation can contribute to the inefficient function of venous valves. Occupations that require standing or sitting still for long periods, or frequent prolonged high altitude flights, have been linked to higher incidences of venous stasis complications[42].

The typical venous leg ulcer (VLU) is characterized by its location on the inside surface of the lower leg, diffuse wound border, full-thickness crater, and tendency to exude fluid. Pain associated with VLUs is worse when the leg is in the dependent position and relieved when the leg is elevated because elevation aids venous return. The lower limb will be edematous and often presents with a reddish-brown stain around the ulcerated area. The wound rarely contains necrotic tissue and may be bright red in appearance.

It is now widely recognized that the VLU is only a symptom of underlying venous hypertension or chronic venous insufficiency. Dressings and other treatments for the ulcer can only succeed if there is also some treatment directed to reduce or counteract the underlying condition[43].

The choice of wound dressing has been shown to be far less critical than compliance to compression therapy. Wound dressings may be simple wound contact layers designed to protect the wound bed from contamination or advanced dressings selected on the basis of the amount of exudation noted when changing bandages[44]. Conformability under the compression bandage,

control of fluid and moisture, removal of odor, and infection control, are important considerations for the primary layer dressing used for treatment of venous ulcers in the home care setting. Dressings that can remain in place for a whole week have a distinct advantage since they avoid the need for frequent attendance by a visiting nurse to change dressings.

1.3 Advanced therapies for wound management

Chronic wounds are harder to manage compared to acute ones. The biologic healing behavior once the dermal tissue is injured changes depending on the state of health; in general, in instances where the normal regenerative process is dysregulated, due to vascular diseases, diabetes and/or microbial infections, the possibility to develop chronic sores becomes quite high.

Normal procedure to manage wounds depends, as mentioned above, from the practitioner in charge of treating these complication, that usually opt for conventional protocols while just rarely go for the use of advanced devices, that are still considered secondary and complementary treatments[45].

In contrast, in some life-threatening situations, often represented by severe burns, advanced devices are employed as standard wound management modalities[46], that include in particular biological dressings or skin substitutes with the aim of replacing the skin with autologous, allogenic and xenogenic grafts.

Gene therapy as well as GF-based therapies are also included, by the way, in these thesis a particular focus and commentary on the use of dressings, grafts and scaffolds for tissue regeneration will be assessed.

The novel strategies that will be presented and discussed rely on the development of devices based on acellular matrices; these mime the composition of the ECM, which can also be enriched by GF's and drugs that can act on several different mechanisms such for instance reduction of inflammation to the wound site, scavenging of free radicals, often cause of ECM impairment, delivery of antimicrobial drugs capable of helping cure pathogenic infections rather than destroying the forming biofilms.

The combination between such types of medication and the standard treatments can lead to successful results or anyway increase their overall effectiveness; it's important to remark that advanced medications don't replace but rather complement conventional wound care management procedures, that must not be avoided.

Early diagnosis of wounds is crucial to plan an adequate treatment, all the patients with DFU's, VLU's, pressure sores or who suffer from peripheral neuropathy necessitate an accurate assessment of the physiologic impairments.

Bypasses and stents represent the first step when extremity ulcers develop, in order to repristinate impaired arterial inflow, moreover, their skin should be examined daily, since a break might represent a high risk of insurgence of a new ulcer.

First intervention in healing is debridement, namely the cleaning from necrotic and infected tissue and removal until 2-3 mm inside the wound margins, in order to reach healthy bleeding soft tissue.

Once the whole infection has been removed, antibiotic and antimicrobial therapies should be considered, since infection does not permit proper healing. This is also due to the frequent formation of biofilms, that protect bacteria against phagocytic cells and antibiotics, enhancing the production and accumulation of proteases and toxic oxygen radical species. These compounds are produced as defense against the microorganisms, anyway, their accumulation in these pathological condition causes severe damage to the healthy surrounding tissue, overall worsening the wound[46].

Moreover, the infection has often a polymicrobial nature and it's caused by both aerobic and anaerobic species, thus, early antibiotic treatment after accurate debridement is compulsory to address the infection[47]. Topical antibiotics in creams and ointments can be helpful, anyway, parenteral administration seems necessary to ensure effectiveness[48].

All patients should be periodically controlled in terms of measuring important wounds parameters, such as wound length, depth and width, that are necessary to establish whether the wound is healing or not.

These measurements permit also to plan how to prepare the wound-bed, that is usually intended as a well-vascularized granulation tissue without signs of local infection (drainage, cellulitis, and odor)[49].

The process of wound-bed preparation implies also keeping the wound environment moist, to promote epidermal cells migration to the granulation tissue and angiogenesis.

The advanced medicated dressings are of crucial importance at this point, it is appropriate to select the right type of medication, as a function of wound location, depth, amount of eschar and exudate, presence of infection, condition of the wound margins, adaptability and conformability of the dressing[50].

In the last decades several types of active medications capable of managing various kinds of chronic wounds were developed and commercialized; for instance, exudate absorbing patches, dressings characterized by sustained release of antimicrobial, anti-inflammatory drugs and

stimulating tissue regeneration, rather than providing a barrier against environmental contamination, bacteria, and some viruses[51]. Again, other dressings are "biologically active" and usually consists of biocompatible polymeric matrixes cultured with human fibroblasts and/or keratinocytes, capable, once applied *in situ*, of producing human collagen, glycosaminoglycans, fibronectin, growth factors and other proteins, boosting healing, preventing infection and creating a self-produced dermal matrix[52].

1.3.1 Biological dressings and skin substitutes

Biological dressings can be divided into three main categories, differing from one another in particular for the source of materials. Tissue engineered products are usually obtained by the manipulation of natural/naturally-derived or synthetic polymers in order to obtain a living skin substitute or an acellular scaffold as ECM tissue mimetics, that can provide a moist environment, serving as temporary coverages and even potentially being loaded with growth factors and/or other pharmaceuticals. By the way, so far the clinical use of such dressings is unfortunately still limited, despite their efficacy, they represent major constrains for manufacturers and customers since skin cells are living organisms grown on these matrices and it's obviously not trivial to fabricate, transport, storage and scale these products[45].

Cadaveric dermal tissue is often used as temporary dressing, especially for large burns, however its use is restricted since episodes of rejection and transmission of diseases were reported[53-54].

Animal-derived decellularized tissues are also used as skin biological grafts, in order to provide intact ECM's intended to be implanted into the damaged tissue; several products are commercially available (e.g. The OASIS® Wound Matrix, Smith & Nephew)[45] and it has been demonstrated that multifunctional ECM matrixes lead to significant healing improvement of chronic DFU's[55] and VLU's[56] compared to standard treatments. Other products based on mimicking extra cellular matrix have been employed for healing enhancement, for example Xelma® (Molnlycke Health Care, Göteborg, Sweden), that is a dressing obtained from the ECM protein amelogenin, extracted from porcine tooth enamel and included in a propylene-glycol alginate gel and intended to be applied weekly via a syringe after proper wound-bed preparation. Clinical studies showed granulation tissue formation was improved as well as cells migration thanks to the adhesion sites provided by the main constituent protein[57].

1.3.2 Biomimetic acellular matrices

In general, advanced wound dressings based both on naturally derived and synthetic polymers should provide fundamental structural and biological stimuli for proper healing; a great effort has been made in order to modulate physical and chemical properties of the firsts, that might be considered as "the gold standard" materials for wound healing, anyway, despite this, the intrinsic features of their precursors do limit their flexibility and thus their potential spectrum of applications[45].

On the contrary, properties of non-functionalized synthetic materials are more tunable but lack biological signals such as those for cell adhesion and activation sites[45].

An emerging approach for wound dressings development consists in the creation of 3D ECM-like microenvironments, usually in form of water-rich hydrogels (up to 95%), capable of serving as physical and biological support for cells involved in tissue regeneration[45]. Furthermore, polymeric materials employed can absorb exudates and at the same time maintain the wound moist; reducing inflammation and providing a more adequate environment for healing[58].

Functionalization of both synthetic and natural-derived materials can improve dermal regeneration, for example, the use of Hyaluronan, a glycosaminoglucan found with abundance in skin, or other biomolecules, like peptides, cell-binding motifs and GF's.

Another important feature of these dressings is biodegradability, achievable by functionalizing them with motifs facilitating passive hydrolysis, especially in the case of synthetic materials, or simply by using polymers that are subject of hydrolysis catalyzed by proteases secreted by cells involved in the regeneration.

The ideal rate of biodegradation of acellular matrices should match the time of healing, giving the cells the right time to populate three-dimensionally the "medication" and progressively re-create and organize a functional ECM physical surrounding.

Not by chance 3D acellular matrixes are also named scaffolds; in facts this term, in the field of tissue engineering, is globally used to indicate a physical structure capable of providing a three dimensional cell-accommodating environment, that can actively or passively present biological cues able to aid and promote tissue healing.

1.3.3 Scaffolds as dressings for cutaneous tissue regeneration

Poor integration with the host tissue is perhaps the most relevant drawback concerning skin substitutes that has been spotted during the last decades.

Tissue engineering approaches this issue by designing and developing skin substitutes as scaffolds that serve as ECM analogs, and thus that are supposed to execute part of its physiological functions.

These are represented by biological activities needed for a correct wound healing like adhesion, proliferation and differentiation, further to act like traditional wound dressing covers that physically protect it, limiting microbial contamination, mechanical traumas and shearing.

Basically, their overall design relies on the achievement of a proper surface chemistry and microstructure, in order to reproduce the most adequate environment to let the tissue re-grow correctly.

This gives the possibility to have available a physical frame capable of hosting the formation of vasculature, lymphatic system and nerve bundles[59], rather than providing mechanical properties such as tensile strength and elasticity[60].

Moreover, currently scaffolds are thought to be conceived as three-dimensional networks into which colonizing cells can communicate through paracrine and mechanical signals but also provide the support for cells to spatially secrete and organize cytoskeleton molecules.

Doubtless, both the materials used and their arrangement give a significant contribute in terms of cell behavior and capacity to repristinate a determined healing tissue; these are also defined by the production technique exploited for manufacture.

For this reason in the following paragraph materials employed nowadays are presented, both in terms of intrinsic/extrinsic properties and use in products research and development. Later on most promising techniques to manipulate them will be reviewed as well (section 4).

1.3.4 Materials currently used and scaffolds in wound healing, features and state of the art

Advanced medications, as said, rely on the use of biomaterials, that are studied in particular for regenerative medicine purposes.

A biomaterial is defined as a nondrug substance suitable for remaining in contact with body fluids and used to ameliorate, regenerate or fully replace any damaged tissue or organ[61].

Since these materials are employed in the field of tissue engineering targeting the development and the production of medical devices, several combined features are required.

The most important conception is that a material intended to be implanted or in contact with living tissue must be biologically safe.

It's well known that for all drug-based pharmaceuticals are mandatory to be evaluated in terms of safety and efficacy. The pre-clinical and clinical evaluation of drugs follows defined procedures to determine whether the product can be marketed and/or tested on patients.
Unlike drugs, biomaterials safety has been based for decades on the concept that a biomaterial should not harm. This leading idea brought to the establishment and standardization of internationally accepted procedures, in particular the ISO-10993[62].
In addition to satisfying the mechanical and biological requirements for the application, if a material is to be used as a biomedical device, it will have to have a specific set of properties. In particular is crucial to highlight biocompatibility, this term refers to the idea that a biomaterial is supposed to be non-toxic nor carcinogenic, rather than providing biological or mechanical inputs to cell healing-promoting activities.
A distinction between commercialized products and those at the laboratory stage will be done and ultimate state of the art will be presented as a function of the basic material used.

1.3.4.1 Collagen

Collagen is a protein-based major component of the dermis layer in the skin; for this reason, the first approaches of trying to reproduce the ECM implied its use as biomaterial[60].
Studies on the use of this biopolymer as biomaterial started since the early 80's, when the conception of scaffold was concretizing as well as their development attempted, although it's reported that its first use as biomaterial refers to 1881, when biodegradable strings termed "catgut," a collagen-rich material prepared from the small intestine of a sheep, were used for suture[63].
Collagen was also chosen because it is considered a highly versatile material, indeed, it has some particular properties that can be exploited in the development of tissue-engineered products like biocompatibility, biodegradability, non-toxicity and weak antigenicity[64].
This polymer is capable of being cross-linked into lattice-like gels[65], this quite stable physical form permits in facts to obtain resorbable burn/wound cover dressings, that are sometimes engineered to serve as drug delivery systems too.
The collagen molecule is composed by three polypeptide chains twined around one another; the main characteristic that affects a helix formation is a high content of glycine and other amino acid residues. The basic molecule contains mainly three amino-acids: glycine, proline and hydroxyproline and it has an approximate molecular weight of 300 kDa[66].

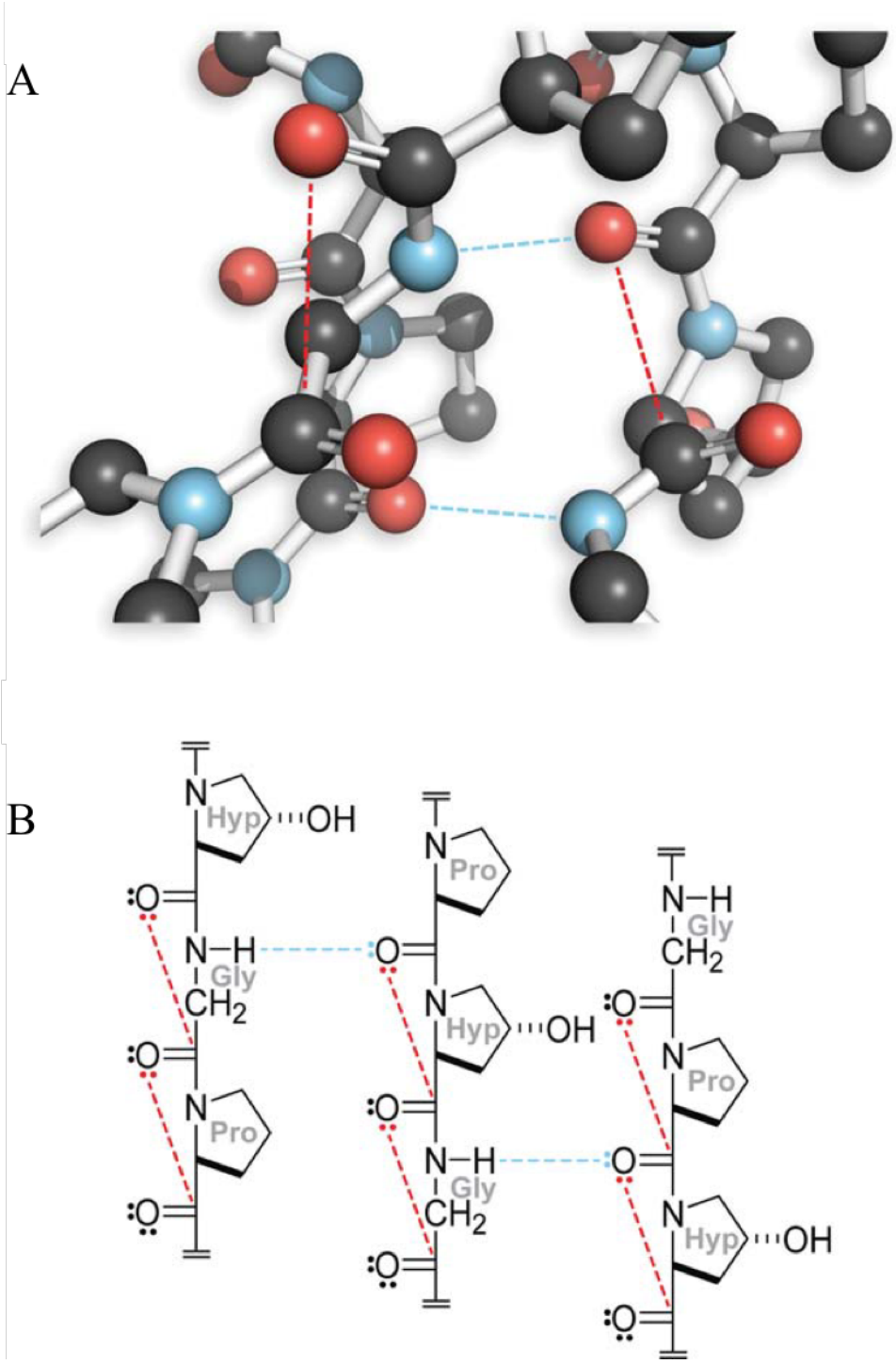

Figure 2. A. Cross section; B. Structure of triple-helical collagen[67]. Hydrogen bonds are indicated in blue-dashed lines.

Helices of collagen molecules form fibrils characterized by high tensile strength and elasticity, moreover, from a biological point of view, collagen also provides an adequate support for cell adhesion, growth and differentiation thanks to its biocompatibility rather than chemico-physical

intrinsic stimuli that it gives to the cells, in particular when combined in sponges with other materials such as elastin, fibronectin or other glycosaminoglycans[68].

Sponges are widely employed for the cure of wounds including pressure sores, venous, decubitus and diabetic ulcers, they can indeed absorb a large amount of exudates from infected wounds, simultaneously keeping its bed moist and preventing against further mechanical insults and microbial contaminations[68].

Several collagen-based products reached the market during the first ten years of the new millennium.

Some examples of widely used dressings dedicated to wound care are represented by:

- Apligraf™ (Organogenesis, Inc, USA): Bovine collagen gel seeded with neonatal foreskin fibroblasts and keratinocytes. It belongs to the category "biological dressings and skin substitutes", Organogenesis received the first Food and Drug Administration (FDA) approval of a living, allogeneic, cell-based product, Apligraf®, approved for the indication of treating venous leg ulcers. Two years later, Apligraf ®was FDA approved for treating DFU's, and in general it has been the first cell-based product for wound healing that received FDA approval.
- Biobrane™ (Smith & Nephew, UK): Outer epidermal analog made with an ultrathin silicone film; the inner dermal analog is instead made of 3D nylon filaments with type I collagen peptides. It is intended as a temporary wound dressing that can be removed when the wound is healed.
- Integra™ Dermal Regenerative Template & Meshed Dermal Regeneration (Integra LifeSciences) It's another dermal analog of bovine collagen and chondroitin-6-sulfate GAG; epidermal analog—complex Silicone layer is removed upon vascularization of dermis, and replaced by a thin layer of autograft.
- Oasis® Ultra Tri-Layer Matrix (Smith & Nephew). It is composed by three layers of bioresorbable ECM. It is minimally processed and it's sterilized through the use of a proprietary method that retains key collagen and non-collagen components.
- PuraPly (Organogenesis, Inc, USA) This product consists of layers of strong, purified and biocompatible natural collagen matrix. PuraPly is designed to provide broad antimicrobial coverage, protecting against a wide range of bacteria that colonize wounds and can progress to biofilm formation and infection.

  PuraPly is a freeze-dried, porcine-based, 100 % type 1 collagen matrix. The product has been approved for acute and chronic wound management across a variety of wound types,

including partial and full-thickness wounds, pressure ulcers, surgical wounds, trauma wounds, venous and diabetic ulcers.

- Woun'Dres® Collagen Hydrogel (Coloplast Corp.). It is conceived to rehydrate dry wounds and eschar, it promotes moist wound healing environment and autolytic debridement.
- Regenecare® HA (MPM Medical, Inc.) Hydrogel dressing containing collagen, aloe, lidocaine 2% and hyaluronic acid, indicated for management of pressure ulcers, leg ulcers, minor cuts and burns.

  Clinical *in vitro* trials mandated by the FDA showed cells are protected from oxidative damage, that is an exhausting action of reactive oxygen species (ROS) for the remodeling of ECM during last phases of healing. Moreover, cross-over studies proved that pain and itching are reduced without side effects.
- Grafix® (Osiris Therapeutics) Cryopreserved Placental Membrane Comprised of an ECM rich in collagen, growth factors, fibroblasts, mesenchymal stem cells (MSCs), and epithelial cells native to the tissue.
- Promogran™ Acelity, LP, Inc. (KCI, LifeCell, Systagenix). This is among the most used collagen dressings, the manufacturer is considered the leader of collagen matrixes market. It's made of 45 % oxidized regenerated cellulose and 55 % of purified collagen. Furthermore, it has been clinically proven to efficaciously heal wounds such as DFUs.
- Fibracol™ Plus (KCI, LifeCell, Systagenix) Collagen Wound Dressing with Alginate dressing is a soft, absorbent, conformable wound dressing made of 90 % collagen and 10 % calcium alginate.
- ColActive® Plus Ag, ColActive® Transfer (Covalon Technologies, Ltd.). This line of products are collagen based wound dressings. Those containing a combination of silver and chlorhexidine should guarantee for up to 7 days broad spectrum antimicrobial activity, meeting current FDA standards. Moreover, the medication is designed to stay transparent for that period of time, giving the practitioners the possibility to monitor wound condition, lowering potentially the frequency of removals.
- TheraSkin® (Soluble Solutions, LLC). It consists of a biologically active, cryopreserved real human skin allograft, composed of living cells, fibroblasts and keratinocytes, and a fully developed extra cellular matrix (ECM) in its epidermis and dermis layers. This product provides the chronic wound with growth factors, cytokines, and a collagen scaffold to jumpstart healing.

- CellerateRX® (Wound Management Technologies, Inc.). Another wound care product based on collagen (65 % in gel form), clinical validations showed it is effective on a broad spectrum of wounds, moreover, it doesn't need special handling such as for example refrigeration and it's active in all phases of wound healing.

It's possible to resume that, all these types of templates intended as medications for wound healing rely on the preparation of freeze-dried constructs, whose porosity is controlled by varying collagen content and freezing rate. These "sponges" can absorb large quantities of exudate, adhere smoothly to the wet wound bed keeping it moist and shielding against microbial infection.

At the laboratory stage, more and more collagen-based products are under development, with the aim of obtaining more and more efficient medications.
Up to now, indeed, there have been many advances in the field of wound healing, anyway, neither the already marketed products nor those still involved in experimental studies are conclusive and capable of fully replace natural living skin[71].
The approaches are various but, in general, as mentioned above, the majority of them is based on the conception that to heal wounds its main constituent is necessary[71].

1.3.4.1.1 Pure collagen scaffolds

Bowling *et al.* worked on the production of electrospun collagen scaffolds, finding out that collagen type I, II and III were able to assemble in collagen fibers accurately reproducing structural and biological features of natural collagen ECM. Indeed, electrospinning technique allowed to obtain the fibrillar pattern characteristic of native collagen. Freeze-drying was performed at the end of the production process, in order to obtain a dried sponge presenting high tensile strength. Moreover, microscopic evaluation *in vitro* revealed that the scaffolds were densely populated with the cells within 7 days (Figure 3). Cross sectional analysis indicated that electrospun collagen promoted extensive cellular infiltration into the fibrillar network. Smooth muscle cells were observed deep within the matrix and fully enmeshed within the fibrils of the electrospun collagen[72].

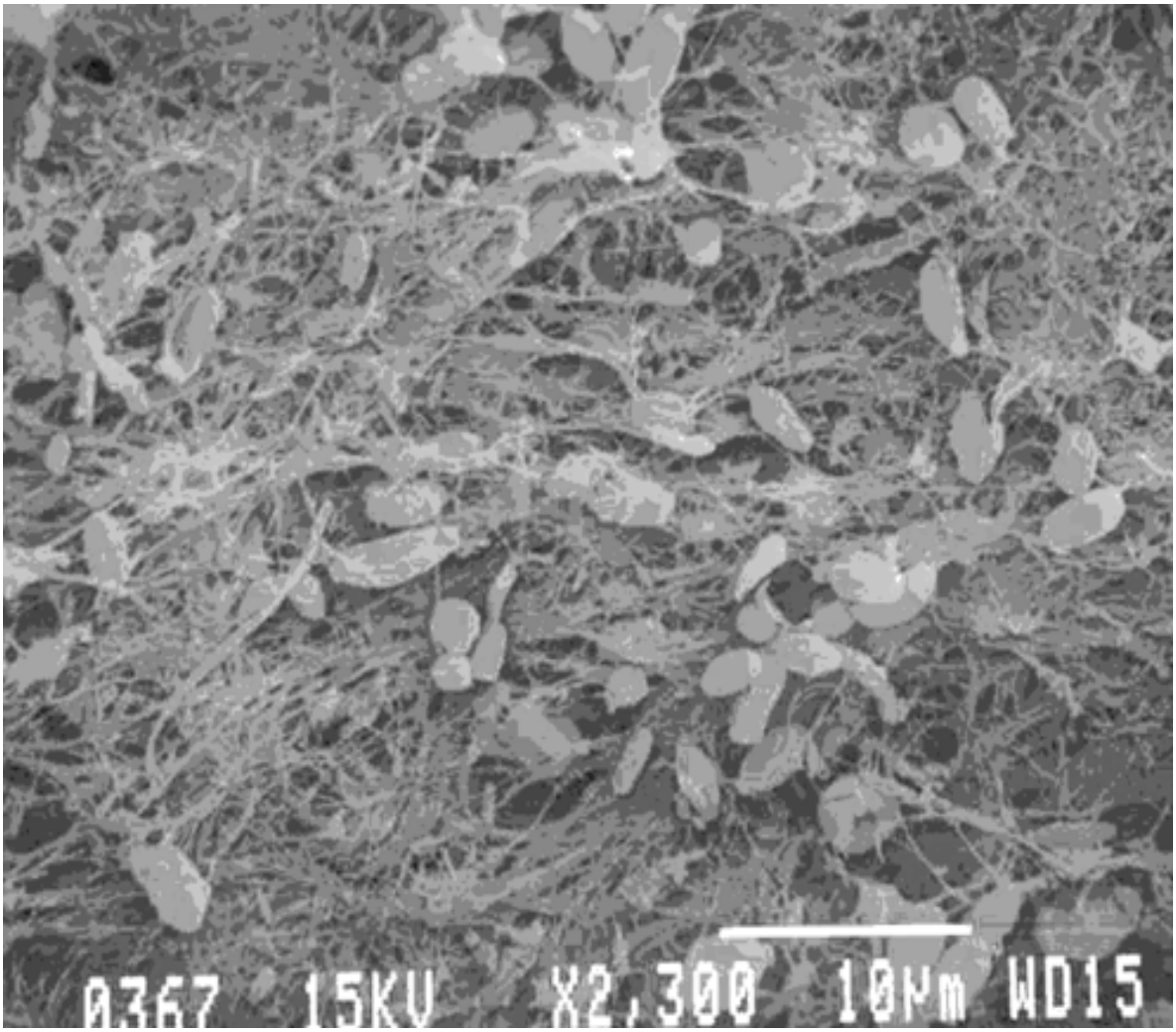

Figure 3. Smooth muscle cells seeded into the electrospun matrix within 7 days[72].

The development of a collagen sponge, characterized by fibrillar structure showed through microscopic analysis the potentiality of culturing human cells in this matrix. Moreover, it is not banal that cells interpenetrated the template within 7 days, populating the material and giving the proof of concept that the system could work in an *in vivo* condition. Anyway, some "defects" are also highlighted, in facts, this mono-component system, further to show poor mechanical properties, might stimulate some adverse reaction when implanted *in vivo*, since its cross-linking was glutaraldehyde-mediated and thus, possibly slightly toxic.

1.3.4.1.2 Collagen/Natural Polymer Blend Scaffold

Blending collagen with other substances can ameliorate certain aspects of these prototypes of dressings: toxicity can be lowered and mechanical properties enhanced, for instance, its

association with natural/naturally-deriver polymers such as chitosan, silk fibroin hyaluronic acid and alginates, can improve these parameters.

Martinèz *et al.* studied the conjunction of chitosan and collagen prepared at different rates and cross-linked through different methods.
All the production processes studied led to the attainment of highly porous scaffolds (96-99 %); pores tended to be round-shaped and their dimensional distribution ranged between 120-300 μm. Moreover, the formed pores are interconnected, theoretically giving nutrients, once the scaffold is applied, the possibility to reach cells even in the inner portion of the matrix.

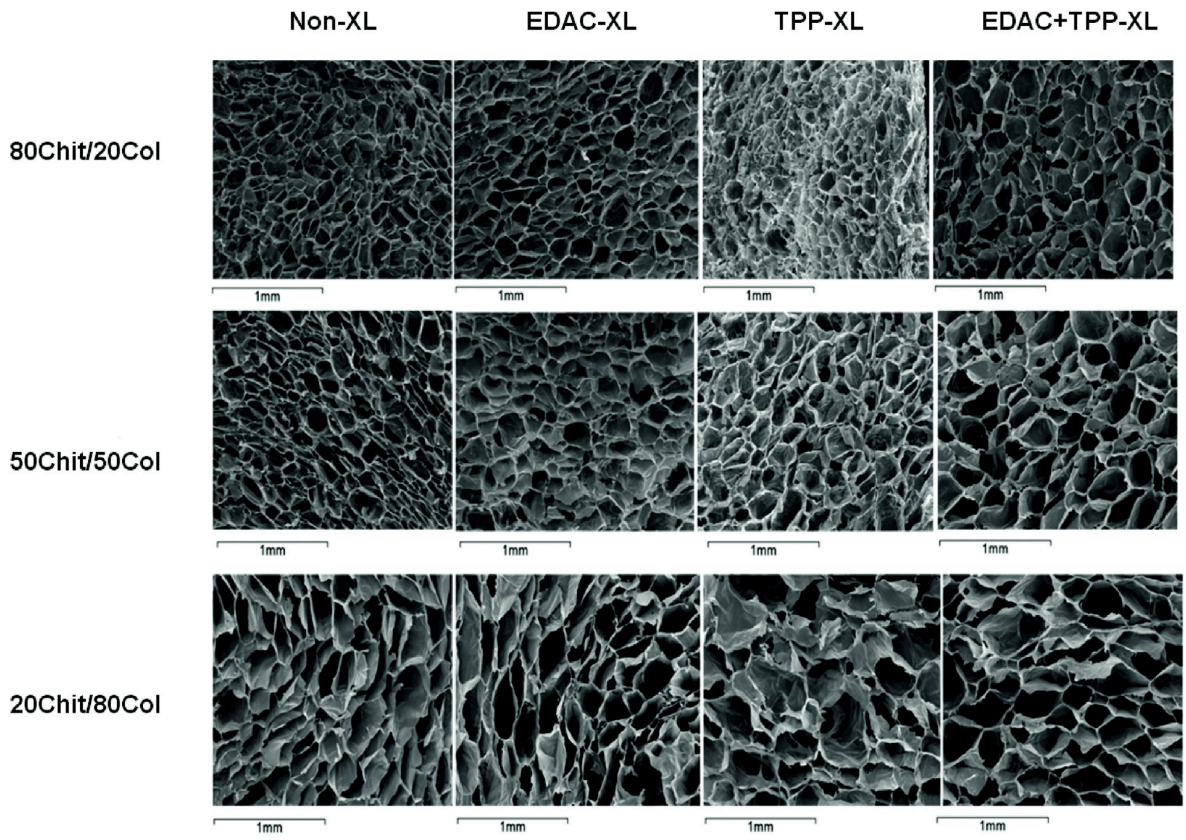

Figure 4. SEM images of porous collagen/chitosan scaffolds. The image is reported solely to highlight the meaning of the comments related to the scaffold structure reported above, the use with different cross-linking agents did not significantly affect pore morphology[73].

Cell culture viability assay conducted over 5 days showed that after 24 h of incubation cells continued growing up to the 4th day. Thus, the experiment revealed that all the scaffolds prepared resulted cyto-compatible and adequate to host cell proliferation.

Moreover, the development of scaffolds with proper mechanical properties is one of the major challenges in designing tissue constructs, in this work the variety of compressive properties of 3D matrices were achieved by changing component ratios in chitosan/collagen scaffolds and by variations in their crosslinking procedures. This represents a great chance in dressing development since this demonstrates the importance of developing strategies to modulate scaffold mechanics according to the biological requirements of a specific application[73].

1.3.4.1.3 Collagen combination with ECM components

Collagen was prepared in combination with fibronectin and GAG's (e.g. hyaluronate), being known as factors that are found during embryonic development and wound healing. These materials could be cross-linked further with glutaraldehyde and conjugated with polymers like poly (hydroxyethylmethacrylate) to produce hydrophilic matrices with increased mechanical strength.
These systems were tested *in vivo* on excised wounds on the back of guinea pigs, in order to assess their suitability as dressing materials.
They appeared to offer cells a template that allowed for spatial deposition of newly synthesized collagen fibers; furthermore, SEM analysis showed that these fibers were oriented, uncrimped and organized. These morphological aspects are peculiar of the remodeling phase of wound healing[74].

1.3.4.1.4 Collagen dermal equivalents

Xenografts, autografts and allografts have been used as skin substitutes for full-thickness wound defects in the past decades, however, antigenicity and limitation of donor sites caused non-satisfactory results in terms of skin recovery[75-79].
Ma *et al.* developed full-thickness collagen/chitosan skin substitute by preparing a blend of the two polymers, molding it and then freeze-drying. The produced wafers showed to be cytocompatible and promoted cell infiltration and proliferation. Cell cultures were performed using human fibroblasts, since compatibility with this cell type is crucial in order to demonstrate the potentiality of being intended as skin substitute.
Moreover, cultured fibroblasts were observed through optical microscopy after proper staining, the characteristic shuttle-like shape (cells tightly adhered to scaffold walls) was underlined as well as the proof that original good cytocompatibility of collagen was preserved.

In vivo trials were conducted on twelve healthy rabbits, scaffolds were then were embedded subcutaneously on the dorsal surface of the rabbit ear.

After 28 days from implantation, the scaffold had almost disappeared and the blood vessels could be observed (Figure 5). These results demonstrated that the collagen/chitosan scaffolds can effectively support and enhance the fibroblasts infiltration from the surrounding healing tissue. *In vivo* results have showed that the collagen/chitosan scaffolds had good biocompatibility and might likely be employed as skin tissue substitutes to be integrated within the tissue[80].

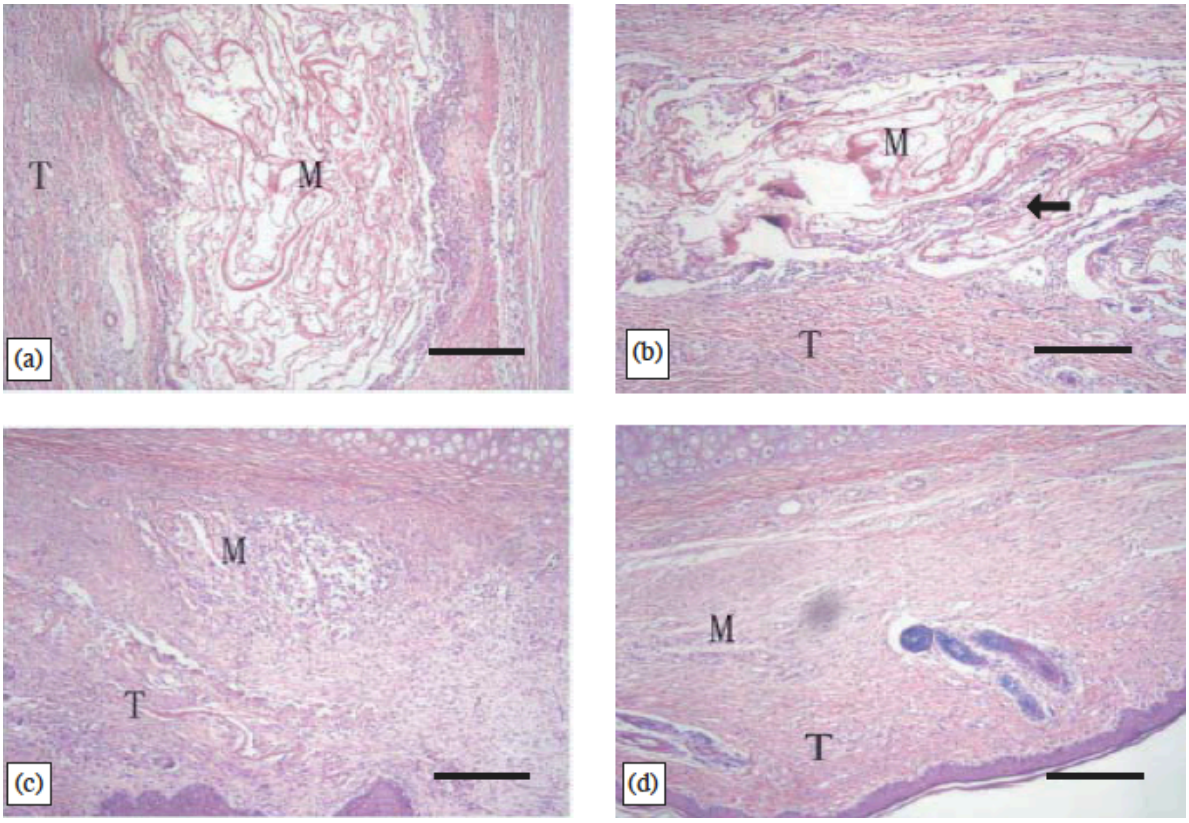

Figure 5. Histological staining of collagen/chitosan scaffolds after implantation in rabbit ear for different times, X 100

a. 3 days; b. 7 days; c. 14 days; d. 28 days. Scale bar: 200 μm

Key: M. Implanted collagen/chitosan scaffold. T. Subcutaneous tissue. Arrowhead. Infiltrated fibroblasts[80].

In general, collagen-based scaffolds, meant as scaffolds containing over 50 % of collagen, can be developed directly manipulating the raw biomaterial rather than mixing it in blends or further formulations.

Collagen matrixes showed over years of intensive academic and corporate research excellent biocompatibility and sufficient mechanical properties, gaining great achievements in tissue engineering in both settings.

These research findings led to the marketization of several products since 90's up to now, including various fields of regenerative medicine apart from skin, such as nerve, bone, cartilage, tendons/ligaments and vascular grafts[81].

State of the art for collagen-based medications is limited, since no conclusive dressings are nowadays available, thus, further research should be devoted to the design of scaffolds with ad-hoc structures and properties in relation to the tissue to be cured and its pathophysiological condition.

However, *in vitro* and *in vivo* experimentations demonstrate the suitability of these systems in attempting to obtain restored functional skin tissue, making the efforts accomplished so far a great advance in terms of developed products often very useful in order to ameliorate the overall quality of life of diseased patients.

1.3.4.2 Hyaluronic acid (HA)

As discussed previously, mimicking ECM structure and composition is the main target of scaffolding, for this reason hyaluronan couldn't be neglected, since it is one of the most important of its components.

It's a linear polysaccharide biologically involved in multiple mechanisms such as cell differentiation, migration, angiogenesis and inflammation responses[82].

In particular, it is a non-sulfated glycosaminoglycan composed of repeating disaccharides [β-1,4-D-glucuronic acid and β-1,3-N-acetyl-D-glucosamide] (Figure 6).

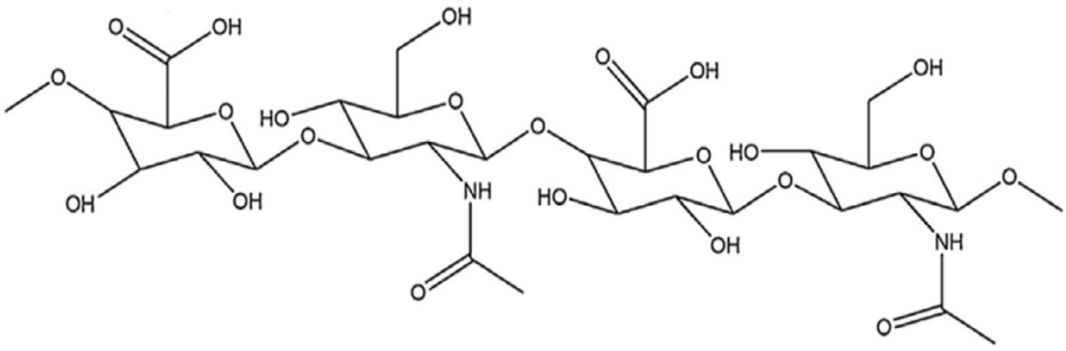

Figure 6. Molecular formula of hyaluronic acid disaccharide unit[82].

Its interest has increased in the field of scaffold material because of its ubiquitously distribution in vertebrate tissues, good biocompatibility and non-toxic degradation products[82].

HA is produced by cells on the membrane, and not in the Golgisome like all the rest of GAG's; mainly three types of HA are synthesized by isoenzymes, differing from one another in particular for their molecular weight, that can obviously address their biological activity.

At present is known that HA binds to the receptor cluster of differentiation 44 (CD 44), that plays a crucial role in providing agents for maintenance and anchoring the proteoglycan polymer to the cytoplasmic membrane and for tissue formation by mediating the ECM remodeling, intercellular interactions and cell-matrix communications[83].

Induction of these receptors is believed to be useful in promoting wound healing process and its application in the preparation of biomaterials might be successful.

Besides, properties that we have already mentioned such as biocompatibility, biodegradability and possibility to be manipulated are innate in this polymer. On the contrary, a fundamental requirement for a scaffold is to provide good adhesion sites to surrounding cells, HA, instead, tends to have week cell adhesive properties[82].

In terms of chemico-physical intrinsic features HA has been demonstrated to have similar water content as human tissue and thus contribute to the exchange of oxygen, nutrients and metabolic waste[84-85].

Further, carboxylic and hydroxyl groups can be exploited to produce hydrogels under mild conditions like chemical modification, crosslinking or photo-crosslinking[82].

The versatility coming from these properties explains the wide use of this polymer both alone and compounded with other materials; the latter in particular gave rise to the commercialization of some products that will be presented herein:

- Regenecare® (MPM Medical, Inc.). Already reported and discussed in the section 1.3.4.1 Hyaluronic acid is one of the main constituent of the formulation, its task is to act as moisturizing agent adhering to the wound bed, moreover, medium molecular weight HA reduces inflammation.
- Hyalomatrix® (Anika Therapeutics, Inc.) is a bi-layered, sterile and flexible scaffold for wound management and care. It is intended for treating a range of wounds, including pressure ulcers, diabetic foot ulcers, tunneled wounds, trauma wounds, and deep second-degree burns. The product is made of a wound contact layer made from a derivative of HA in fibrous form with an outer layer comprised of a semipermeable silicone membrane. The wound contact layer is biodegradable, and the silicone layer controls water vapor loss and provides protective coverage.

- Hyalogran® (Anika Therapeutics, Inc.). Biodegradable wound dressing, it is an absorbent dressing made of micro granules of Hyaff® (an ester of HA) and sodium alginate. It is appropriate for managing a variety of exuding wounds including leg ulcers, pressure sores, ischemic and diabetic wounds, particularly those which are covered with slough and necrotic tissue or areas that are difficult to dress.

1.3.4.3 Chitosan

It's a linear polysaccharide formed by D-glucosamine and N-acetyl-D-glucosamine. It can be obtained by the partial deacetylation of chitin, a natural polymer constituting the exoskeleton of crustaceans, insects, arthropods and fungi cell wall. It is the most abundant biopolymer present in nature after cellulose.

The process of deacetylation implies the removal of acetyl groups from the molecule and, depending on the reaction strength and duration differently deacetylated polymer can be obtained.

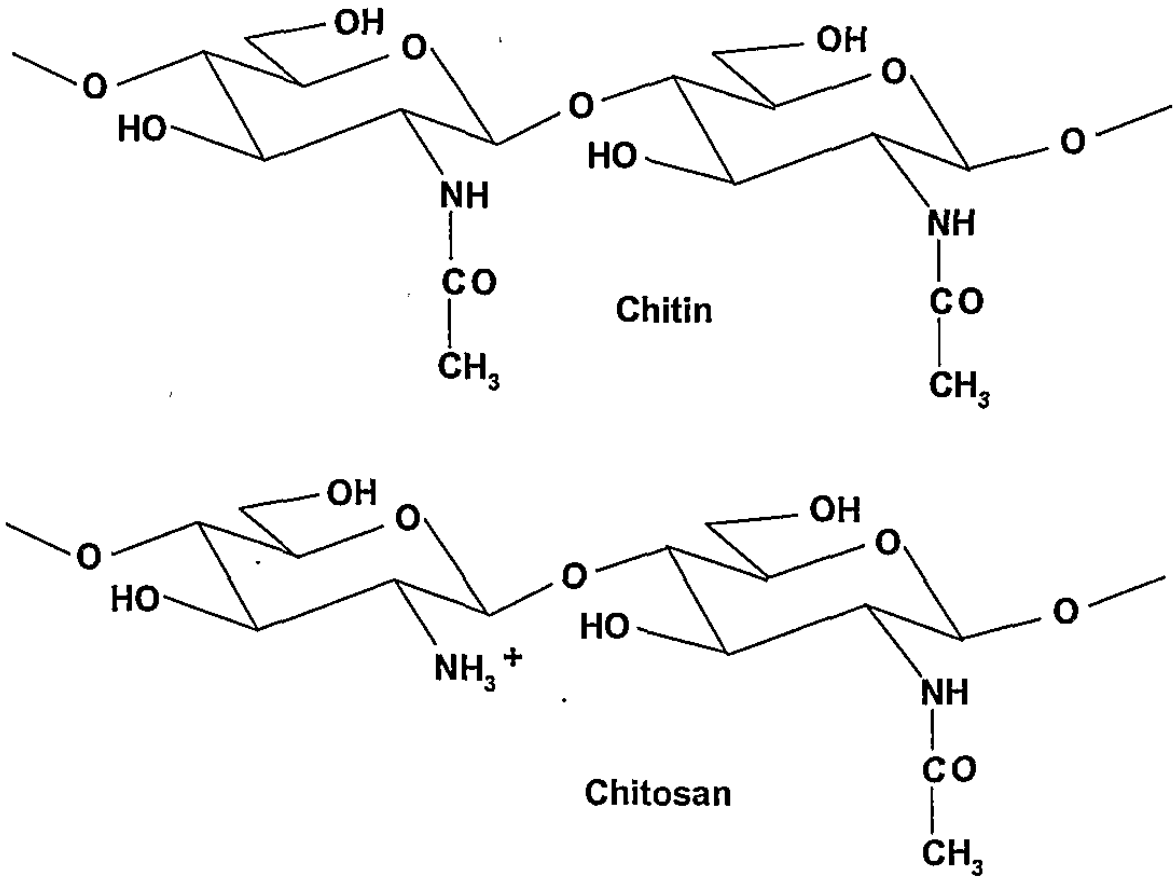

Figure 7. Chitin deacetylation reaction and chitosan formation[86].

Vegetal sources of chitosan are traditionally preferred to animal ones, the reason is the lower presence of allergens and pathogens and thus a higher compatibility in a subsequent adoption in biomedicine.

The degree of deacetylation (DD) varies between 60 and 99 % and its molecular weight can reach 1000 kDa. Its solubility is possible thanks to the presence of amine groups, that are protonated in aqueous acid solutions with a pH inferior to 6. Once protonated chitosan is considered the unique positively charged natural-derived polysaccharide, this permits the formation of electrolytic complexes with a huge number of anionic natural and synthetic species.

Its intrinsic properties are multiple and include antibacterial and antifungal activity, muco-adhesiveness, analgesic and hemostaticity.

It can be biodegraded in non-toxic residues, speed of biodegradation can be easily controllable, since strictly depending from the DD and molecular weight.

These chitosan-peculiar features make this polymer particularly interesting in the field of tissue engineering.

1.3.4.3.1 Chitosan properties

As mentioned in the last paragraph several structural chemico-physical properties can be exploited for biomedical applications:

- Muco-adhesiveness: being a cationic polysaccharide, the number of positive charges is proportional to the DD. Mucin, the major glycoprotein of the mucus, is composed by sialic acid residues, that are negatively charged.

  High molecular weight chitosan is highly mucoadhesive due to the capacity to establish ionic bridges with sialic acid residues[87].

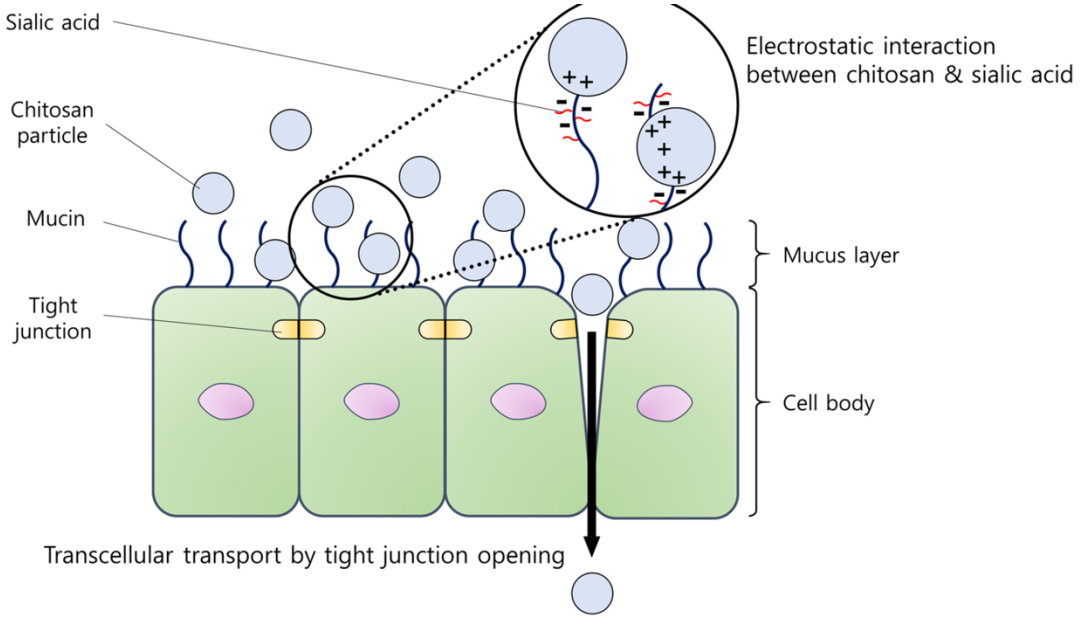

Figure 8. A diagrammatic presentation of the electrostatic interaction between chitosan particles and the mucus layer. Positively charged chitosan particles are prone to interact with the negatively charged sialic acid, resulting in enhanced adherence[87].

- Hemostaticity: This property can also be attributed to the presence of positive charges inasmuch membranes of red blood cells (RBC's) and platelets are negatively charged and can interact with protonated portions of the structure.

  The anionic nature on the surface of these cell types are due to the presence of negatively charged molecules such as phosphatidylcholine and phosphatidylethanolamine (platelets) and sialic acid residues (erythrocytes).

  The negative charges on platelets and RBC's cause electrostatic repulsion between them thus retarding the aggregation process which is crucial for the onset of hemostasis process. The application of chitosan favor the aggregation process by interacting electrostatically with the cell surfaces, promoting the formation of a blood clot[88].

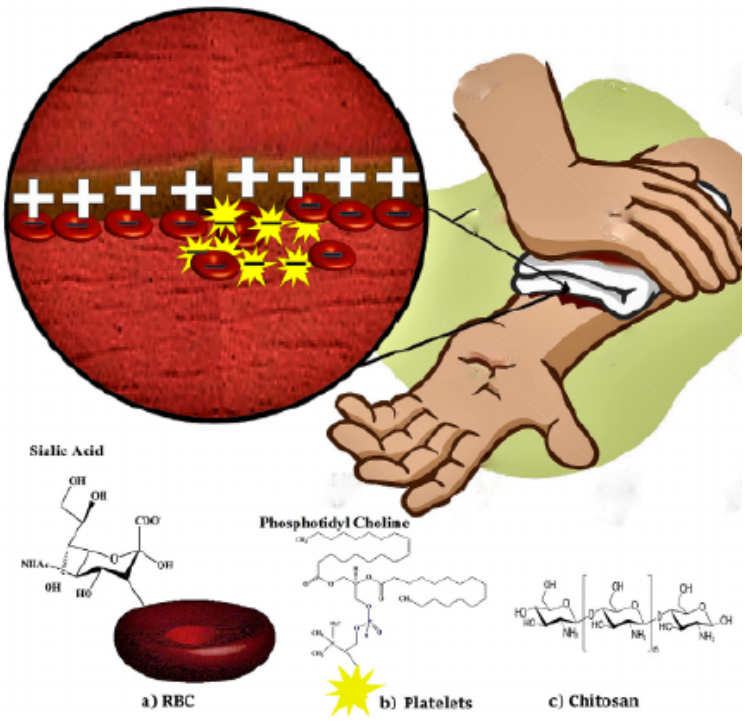

Figure 9. Hemostatic mechanism of chitosan based bandage: a) RBC's contain sialic acid; b) platelets contain phosphatidyl choline groups which are negatively charged and prevent aggregation necessary to start hemostasis process. Positively charged amine groups on chitosan bandages promote platelet aggregation due to electrostatic interactions with it[88].

Hemostaticity can result very useful in designing wound dressings, since as we have discussed above, the formation of a blood clot as soon as possible is crucial for the iniziation of the healing process.

- Biodegradability: It occurs *in vivo* through the lytic action of the constitutively expressed lysozyme[89], producing variable length non-toxic oligosaccharides that can be assimilated systemically and successively excreted.
- Anti-microbial activity: Positively charged chitosan molecules bind to negatively charged microbial cell membranes, which leads to the disruption of microbial membrane, and subsequently the leakage of proteinaceous and other intracellular constituents.
- Gelling capability: chitosan, once dissolved in water at pH < 6 can undergo gelation processes through several mechanisms, ionotropic, covalent crosslinking rather than by photocrosslinking (through proper modifications). In its "state" of gel it can be exploited for the production of hydrogels, thus being rich of water, that as we have seen so far means greater biocompatibility and possibility to help in maintaining moisture to the wound bed.

Moreover, gelation can be exploited to prepare physical hydrogel dressings with a defined three-dimensional structure and with "good" mechanical features, that in concrete mean higher manipulability and resistance to stress forces like traction and compression[90].

- Similarity with ECM is one of the most important chitosan characteristics; the micro-environment influences the building up of a tissue, starting from the early phases of wound healing hierarchically and structurally mimicking glycoproteins and thus exerting similar morphogenic functions[89].

1.3.4.3.2 Chitosan-based products for wound healing

- Kytocel (Aspen Medical): It is a highly absorbent dressing composed of natural, biodegradable acylated chitosan fibers using a carding/non-woven process. These fibers bond with wound exudate to form a clear gel that locks-in fluid (Figure 10), absorbs pathogens and is conformable to the wound bed.

  The absorbent properties of KytoCel enable it to bind and lock away commonly encountered wound pathogens such as *Escherichia coli*, *Staphylococcus aureus*, *Candida albicans* and meticillin-resistant *Staphylococcus aureus* (MRSA), thereby reducing wound bioburden and the risk of cross-contamination at dressing change[91].

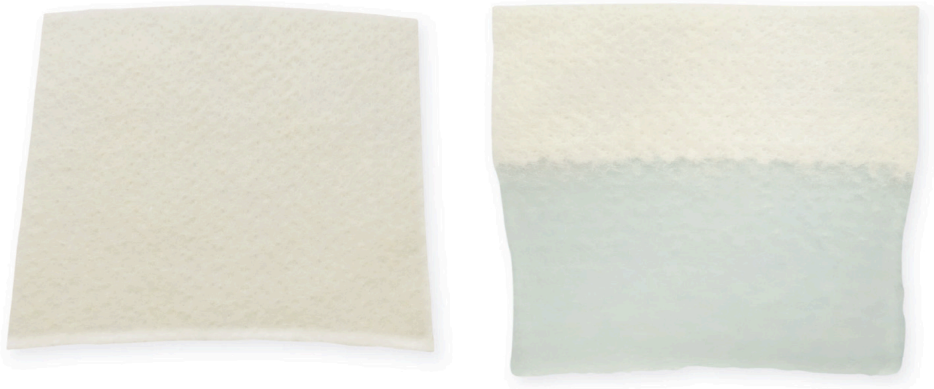

Figure 10. Flat dressing showing KytoCel's ability to absorb and retain wound fluid[91].

Due to its absorbent properties, KytoCel locks fluid within its core, reducing the lateral wicking action seen in other exudate management dressings. This means that KytoCel prevents the spread of wound exudate to the edges of the dressing, protecting the periwound skin from potential maceration. The dressing's high wet strength also offers clinicians the ability to remove the dressing in one-piece, as it remains intact even when

fully saturated, without leaving behind dressing fibers or residues. This makes dressing changes easier and promotes patient comfort and compliance.

- Chitoderm® is a sterile medication consisting of a transparent polyurethane support that is extremely thin (20 μm) capable of serving as an efficient protective barrier against external agents (mainly microorganisms).

  The support is conceived to maintain moisture in the wound bed, allowing at the same time cutaneous transpiration. The dressing core is constituted of a chitosan tampon that assists the natural processes of skin tissue repair, and it is specifically intended for chronic sores (DFU's, VLU's and pressure ulcers).

  The dressing has great absorbing capacities, resulting adequate for application to wounds with copious exudate.

1.3.4.3.3 Three dimensional chitosan-based scaffolds for wound healing

Chitosan dressings must own determined properties beyond material intrinsic ones; the research is focusing on the development of objects with right defined parameters, depending on the targeted applications.

For instance, from a technical point of view, macro/micro-porosity of the developed item, as well as pore interconnectivity, are crucial since cells can penetrate the inner structure of the scaffold being surrounded by *ad hoc* architectures and engineered materials that provide the proper mechano-biological cues to them. Interconnectivity is also of fundamental importance, in facts, nutrients must reach even the most interpenetrated cells; moreover, a certain macro/micro-porous structure should promote angiogenesis and tissue re-vascularization of the healing tissue[92].

Lim *et al.* developed prototypes of chitosan scaffolds with complex three-dimensional geometries, controlling the size, the geometry itself and pore connectivity. A novel technique, called cryogenic prototyping, permitted to fabricate scaffolds with controlled macro/micro structure, then, they've been evaluating cellular infiltration and neo-vascularization *in vitro* and *in vivo*.

Scaffolds were implanted subcutaneously in mice, neo-vascularization and cellular infiltration were observed after 28 days from the implantation, the results were attained with scaffolds characterized by micropores of ± 90 μm and macro-pores of ± 300 μm (diameter ∅); microscopic analysis after proper histological staining demonstrated that fine control of the architecture can be a viable solution towards the way of wound healing.

Furthermore, the rapid prototyping technique employed for scaffold production seemed to be promising specifically in building complex three dimensional structures[92].

Other works report the importance of designing and produce dressing with three-dimensionality at the micro-level.

Ye *et al.* prepared three-dimensional scaffolds starting from a 3 % w/v chitosan solution in 2 % acetic acid. Rapid prototyping was adopted as manufacturing technique, working by extruding the polymeric solution through a 200 μm inner diameter needle directly in a gelling isopropyl alcohol bath.

Infrapatellar Fat Pad-Derived Stem Cell (IPFP-ASC's) were seeded on the final product showing promisingly an adequate growth for potentially being applied for tissue engineering purposes[93].

1.3.4.4 Alginates

Alginate is a natural anionic polymer extracted from brown seaweed[94], it is composed of a varied ratio of guluronate and mannuronate (Figure 11), depending on the source it is obtained from. The disposition of these two molecules within the chains of the polymer determine its overall physical properties rather than molecular weight[95].

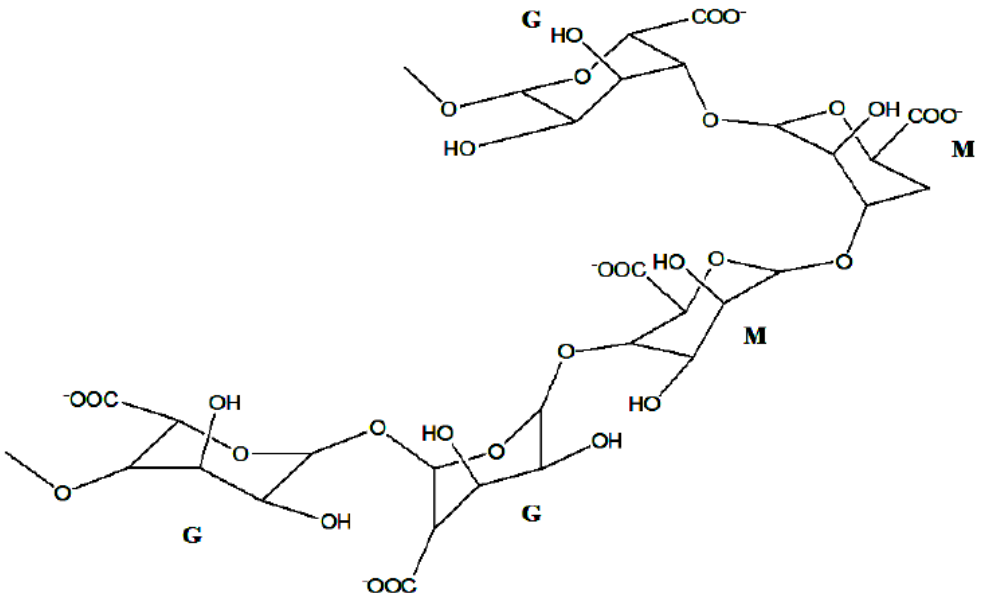

Figure 11. Structure example of alginate: -L-guluronic and -D-mannuronic alginate residues[95].

The formation of alginate-based gels can occur by co-operative binding of divalent cations, forming a diamond shape (or egg-box shape) macromolecule, or by using trivalent cations such as Al and Fe and causing the obtainment of stiff and compact gels compared to those gelled by divalent ions[96].

Alginate is a further polymer with favorable properties to be applied in the tissue engineering field, being biocompatible and non-toxic and particularly attractive in wound healing applications to date. As aforementioned, multiple techniques can be used to form alginate gels, in particular, those employed industrially are gelled by either ionic cross-linking of its solution with calcium, magnesium, barium, cadmium, cobalt, zinc, nickel, manganese and strontium, otherwise it can be freeze-dried in order to produce dressings that must be porous and fibrous.

In general, like the majority of wound dressings commercially available rather than those at previous stages, alginate dressings aim to provide a moist environment, absorbing exudates at the same time, as well as limiting bacterial infections, thereby supporting rapid re-epithelialization and formation of the granulation tissue[97].

Several products are based on alginate, in these paragraph the most used are described and some clinical evidences reported:

- Algicell™ is a dressing dedicated to DFU's, leg ulcers, pressure ulcers, donor sites, and traumatic and surgical wounds; it's composed of sodium alginate and it contains 1.4 % of silver as wide spectrum antimicrobial agent.

  It is designed to gel while keeping its physical integrity for intact removal and it does provide a high absorption capacity that also helps to reduce the risk of tissue maceration and allows for increased time between dressing changes.

  It's reported that under the supervision of a health care professional, Algicell® Ag Antimicrobial Alginate Dressing is an effective barrier to bacterial penetration in moderate to heavily exuding wounds[98].
- Algisite M™ is a calcium-alginate dressing which forms a soft gel that absorbs when it comes into contact with wound exudate. Algisite M™ helps utilize the proven benefits of moist wound management[99].
- Sorbsan Flat™/Sorbsan Silver are calcium alginate-based dressings known for its absorbency, conformability and hemostatic properties. When applied to the wound, Sorbsan forms an amorphous gel which can be irrigated away from the wound with normal physiological saline 0.9 % for pain free removal[100-101]. Sorbsan has been used for over 30 years, several positive clinic outcomes have been published.

Callaghan (2007) reports that the management of a woman with colonized circumferential bilateral venous leg ulcers with Sorbsan Silver. He concluded that the dressing fought the bacterial infection, achieving quick and effective control of exudate. It was not reported nor evaluated whether healing had taken place or not[102].

Odugbesan and Barnett (1987) reported the use of Sorbsan on a 68-year-old woman with diabetes with venous ulcers on both legs.

Although the bandage system that was in use was not mentioned in the report, healing coincided with the use of Sorbsan.

The authors concluded that they have used Sorbsan in other venous, neuropathic and ischemic ulcers with good success. Moreover, the handling features of Sorbsan were superior to the commonly used wound dressing, but the comparative dressing was not identified[103].

The vast use of alginate in the development of medical devices such as dressings explains its effectiveness and safety as biomaterial.

Due to their proved efficacy, more and more researches are focusing on the innovation of this class of medications, trying to finely modify their composition, functionalization, loading of drugs, control of chemico-physical cues.

Yu *et al.* developed wound dressings composed of alginate hydrogel and simvastatin-incorporated in hydroxyapatite microspheres. The results of *in vivo* studies showed that wound dressings enhanced the formation of new blood vessels as well as re-epithelialization of the cutaneous wounds.

In vitro simvastatin was proved to have an angiogenic effect on the differentiation of human umbilical vein endothelial cells, furthermore it was found out through molecular studies that the expression of hypoxia-inducible factor-1 and vascular endothelial growth factor were boosted, thus, being potentially effective in the management of full-thickness sores[104].

Üstündāg *et al.* evaluated the potential of electrospun nanofibrous mats as wound dressings *in vivo* on rabbits. The used material was composed of sodium alginate and poly(vinyl alcohol) at the concentration of 9 % and sodium alginate at 1 %, the substances were blended in the volume ratio of 2:1. The nanofibers were measured in terms of diameter, that resulted 100.35 ± 12.79 nm, that denote an ECM-like microstructure.

In vivo studies on rabbits revealed that the percentage wound contraction ability of the nanofiber after 15 days from the application reached 98 %, which was comparable to Suprasorb-A, a commercially available product based on nanofibers, that indeed scored a percentage of wound

contraction of 99 %, making this prototype promising as effective wound dressings to help tissue regeneration[105].

1.3.5 Advanced dressings overall considerations on their applicability

Resuming, alginate-based scaffolds, like those composed of other naturally derived/synthetic polymers alone or in association, do exist in different forms as reported, such as hydrogels, foams, semi-solid formulations, nanofibers, freeze-dried wafers[97].
Regardless of the pharmaceutical form used and its composition, the target remains the achievement of a rapid re-epithelialization, formation of granulation tissue and subsequent functional healing.
The myriad of products available and those under clinical evaluation or at the laboratory stage are investigated from different points of view. For instance, clinical research reveals itself fundamental to collect data that can be systematically analyzed to better understand correct application of the various forms; in facts, certain dressings are conceived for determined types of wounds and stages.
Addition of bioactive agents to the dressings is also a common approach leading the way to wound healing; antimicrobial agents, anti-inflammatory drugs rather than growth factors and other compounds are often employed in order to reduce infection, inflammation and stimulate skin restoration.
Dressings can be thus intended also as drug/biological factors delivery devices, that should be able to deliver the compounds at the desired rate rather than serving as their depots in the case of erodible or biodegradable systems[106].

1.3.5.1 Indication of application timing and modality per type of dressing

As reported in the previous paragraph each dressing can be more effective than another one depending on the type of wound to apply on.
Herein, general indications for each material used in dressing production among those discussed above is reported, as well as indications concerning dressings labeled for their activity.
(Data taken from http://www.woundsource.com)

- Broadly speaking, alginates are soft and conformable for the patient, easy to apply over irregular-shaped wounds and are usually indicated for sores with moderate to heavy

exudation, such as pressure ulcers, infected wounds and venous insufficiency ulcers. often needing a secondary dressing[107].

- Antimicrobial dressings are covers that alter the wound bed bioburden. The main obvious indication is related to the reduction of the risk of infection in partial- and full-thickness wounds. These dressings are available as sponges, impregnated gauzes, films, absorptive products, island dressings, nylon fabric, non-adherent barriers or a combination of materials. The ability to handle exudate depends on the characteristics and composition of the product[107].
- Collagen wound dressings are gels, pads, particles, pastes, powders, sheets or solutions derived from bovine, equine, porcine or avian sources. Some interact with wound exudate to form a gel. Indicated for partial- and full-thickness pressure ulcers, venous ulcers, surgical wounds, vascular ulcers, diabetic ulcers, second-degree burns, abrasions and traumatic wounds. Usually a secondary dressing is required[107].
- Composite dressings are wound covers that combine physically distinct components into a single product to provide multiple functions such as a bacterial barrier, absorption and adhesion. Usually, they are composed of multiple layers and incorporate a semi- or non-adherent pad that covers the wound. They may also include an adhesive border of non-woven fabric tape or transparent film. Composite dressings can function as either a primary or a secondary dressing on a wide variety of wounds and may be used with topical medications[107].
- Gelling fiber dressings are absorbent wound covers that help manage drainage and removal of dead, damaged and infected tissue from the wound. As wound fluid is absorbed into the dressing, a gel forms, which assists in maintaining a moist environment for optimal wound healing and the formation of granulation tissue. Gelling fiber dressings can retain and control exudate levels to reduce the risk of peri-wound maceration. Gelling fiber dressings can also conform to various wound shapes and be removed in one piece[107].
- Amorphous hydrogel dressings are formulations of water, polymers and other ingredients with no shape, designed to donate moisture to a dry wound and to maintain a moist healing environment. The high moisture content serves to rehydrate wound tissue. Indicated for partial- and full-thickness wounds, wounds with necrosis, minor burns and radiation tissue damage. Preserved products are multi-dose. Sterile, unpreserved products are single use. May require a secondary dressing cover[107].
- Hydrogel wound dressing sheets consist of three-dimensional networks of cross-linked hydrophilic polymers that are insoluble in water and interact with aqueous solutions by

swelling. They are highly conformable and permeable and can absorb varying amounts of drainage, depending on their composition. Non-adhesive against the wound for easy removal. Indicated for partial- and full-thickness wounds, wounds with necrosis, minor burns and radiation tissue damage. Available in various sizes, with and without adhesive borders[107].

1.4 Production techniques overview

Manufacturing processes have a great impact on the properties and subsequently on the effectiveness of a developing device. Apart from this, many other aspects should be considered, for instance, the scalability of the process depends from several parameters such as costs and object production rates. And again, a production operation should be safe for operators and for the users of the device.

These managerial criteria should match the more technical ones, in facts, the choice of the process, or simply its ideation in more premature phases, should take into account all these issues as well as the manipulability of the material that wants to be used.

Each technique results more or less adequate, presenting advantages and drawbacks, depending on the material and from the pharmaceutical form that is planned to develop; in particular, in this thesis mostly hydrogels will be explored.

Among the most studied in research settings, mainly three techniques emerge for its interesting ways of producing dressings: solvent casting, electrospinning and 3D printing.

A special focus will be addressed for 3D printing, since as we will see, it was the main designed and developed process of this work.

1.4.1 Solvent casting

Solvent casting technique is widely used in preparing polymeric scaffolds for tissue engineering, it mainly consists in molding polymer blends, often dissolved through the use or organic solvents. The preparation method is sometimes coupled with a further complementary technique, called particle leaching (PL), the latter implies the addition of insoluble salts in the polymer blend. The significance of PL is given by the possibility to wash away salt particles, once the blend has been poured into a mold and solvents are evaporated[108]. The removal of particles create a sort of three-dimensional porous network, that can be quite easily controlled in terms of pores interconnectivity

and size distribution by means of a proper selection of the polymer, of the porogens and their relative amounts[109].

Of course the technique is often modified in terms of parameters such as temperature during molding, compression or not after the molding phase, time of particle leaching in water or other solutions, etc[110].

Moreover, evaporation, or anyway elimination of solvents till drying can be achieved by various methods as well, such as vacuum drying, freeze-drying or drying in oven.

The advantages of this technology include material uniform thickness distribution, maximum optical purity and low haze. The optical orientation is virtually isotropic and the films have excellent flatness and dimensional stability[111]. Concerning the loading of Active Principle Ingredients (API's) it can also result favorable since thermosensitive drugs do not pass through high temperature processes.

Further, the technique doesn't require specific expensive equipment or instrumentation.

Despite these features, some drawbacks are worth to be mentioned; for instance, the use of organic solvents implies that once dried, solvent-cast films can contain trace amounts of residual solvents, which could present issues with compendial compliance and biocompatibility. Also, if any of the solvents used is flammable, like ethanol, special safety equipment and procedures must be employed to prevent fire and environmental hazards from vaporized solvents[112].

Solvent casting is one of the oldest technique for making films as scaffolds, by the way is reasonable to say that three dimensionality in terms of micromorphology can be achieve just indirectly and thus with scarce control. Furthermore, the geometry depends on the mold, due to this, no complex controlled architectures can be obtained, in contrast with less obsolete techniques.

On the contrary it remains effective in the production of thin films, that can be exploited for instance for the development of diagnostic or biocompatibility tools or for other applications concerning wound dressings, like those devices designed to remove biofilms from wound beds.

1.4.2 Electrospinning

Electrospinning is indicated as the fabrication process that uses an electric field to allow the spreading and deposition of polymer fibers on a given substrate. A polymeric solution passes through an electrified nozzle, lowering the surface tension of the solution and permitting the deposition of fibers ranging from micro meters to less than 100 nm[72].

The result is the creation of a fibrous matrix, where fibers are disposed in a random fashion or oriented along defined axis.
This latter feature partially permits to tune some mechanical properties of the matrix by designing determined fibers orientation[72]. On the contrary, spatial control of deposition represents one of the major challenges in electrospinning, that also has something in common with solvent casting method, since the majority if not the totality of the liquid preparations that feed the machine are prepared by dissolving polymers in organic solvents.
Certain electrospun materials, such as those described above, promote cell growth and the penetration of cells into the engineered matrix.
Three-dimensionality is then achievable, electrospinning is for sure considerable for microtissues development, anyway, no complex architectures can either be obtained, since the distribution of the material along *x*, *y*, and *z* axis is not directly controlled.
Many different relevant researches are focusing on the refinement of this preparation method, since it partially permits to control fiber size and orientation, obtaining ECM-like structures, characterized by a very high surface area to volume ratio, that can often result a favorable feature in terms of biological cell compatibility for the material and their possibility to adhere and proliferate through a proper physical support.
Organic solvents are always used to dissolve polymeric materials to form spinnable blends, anyway this aspect doesn't represent a big issue, due to the fact that during spinning procedure solvents evaporate, avoiding to affect materials biocompatibility. Contrarily, spinnability of materials also depends on initial polymer concentration, highly concentrated polymer solutions are indeed to much viscous and cannot be spun. This consists in a technique technical limit that can have implications in terms of obtainment of loose structure, that sometimes do not present enough adequate mechanical properties such as elasticity and toughness[113].
The structural, material, and biological properties of electrospun collagen, for example, suggest that this material may represent a nearly ideal tissue engineering scaffold[72]. As a matter of fact, electrospun matrixes result suitable for dressing fabrication, although full thickness skin substitutes as well as scaffolds patterned by complex structures such as those serving as implants for organ regeneration are still difficult to attain.

1.4.3 3D printing (additive manufacturing methods)

The conception of three-dimensional printing was introduced in the past century around 1980, formerly like method for prototypes development in the industrial manufacturing sector.

Afterwards, researchers started to think about the technique applicability to regenerative medicine and generally to medicinal purposes.

Despite the fact that the technology can be considered relatively new, its success in pharmaceutical field is noticeable and with ambitious future perspectives due to the continuous amelioration and refinement of the dedicated technologies.

The main spread idea of 3D printing associated to biomedicine relies on the development of biological constructs designed to promote cellular infiltration, proliferation and execution of functional activity till the restoration of the targeted tissue.

The typical approach consists in the deposition of material layer by layer till the formation of a three-dimensional network mimicking the physical acellular structure of the tissue[114].

The most diffused technique include some precisely defined steps; a three-dimensional model needs to be created, commonly by means of Computer-Aided-Design (CAD) software or by the use of electronic scanning methods such as computed tomography (CT) and magnetic resonance imaging (MRI)[115]. The polymer material used to build the object is then usually deposited through one or more extruders, that constitute the dispensing apparatus, on a thermo-regulated printing surface, mandatory support for the realization in three-dimensions.

3D printing is an additive manufacturing process, its main scope is the construction of precise 3D structures, that would not be achievable by means of further techniques. One of the greatest driving forces that led the scientific community to investigate deeply and to develop more and more advanced methods is the increasing need of tissues and organs to be transplanted, since donors do not cover even the 5 % of the requests[116-117]. Organ transplantation, replacement and repair are the future options for patients with tissue damages, for this reason scientists constantly search for effective methods to help save lives and improve the quality of life.

Three-dimensional scaffold fabrication boasts effective microstructural control both for the deposition method as well as printing resolution, that varies between 10 and 10000 μm; this makes the technique very flexible compared to other assembly methods such as molding (solvent casting)[118-119].

Mostly, a three-axis mechanical platform controls the movements of extruders printing the ink in the required algorithm and shape. Many advantages can be mentioned, such as process control, ease of utilization, cost-effectiveness, distribution (even cells) controllability, and perhaps the most important one, that is versatility. Several materials, in different physical forms and concentration can potentially be applied to the technique, adapting the instrumentation depending on the needs[120].

1.4.3.1 Extrusion-based printing

Extrusion printing will be particularly deepened, due to the fact that our research was deduced and partially took inspiration from this technique in terms of conception.

It is usually categorized into pressure, piston or screw-driven extrusion[109]; the first is based on extrusion of material by pressurizing air in a capillary or container that serves as reservoir. The second relies on extrusion by means of a piston compressing and pushing the material out whereas the last one implies that a rotational driving-force compresses the material out to initiate printing[114].

Some principal parameters should be considered in terms of printability of a material, like viscosity, ink physical phase prior and during printing, material and compounds stability over the process.

"Extrusion-based" means in general deposition of polymeric material in its liquid viscous phase, its advantages consists in the wide spectra of biomaterials employable, both synthetic or natural, that can give rise to semi-liquid or gel-like objects rather than solid ones.

Moreover, cell-loaded materials can be bio-printed, in facts the technique is often exploited for the production of polymeric scaffolds wherein cells are distributed in a controlled way[114].

Several works report the effectiveness of scaffolds produced by this technique in terms of printability, possibility to obtain gel three-dimensional scaffolds and cell proliferation adequacy. Rees *et al.* reported the employment of extrusion-based 3D printing for the production of oxidized cellulose scaffolds as potential wound dressings, showing that it did not support bacterial growth. Moreover, the nanocelluloses form 3D structures characterized by porous printed filaments that have the potential to carry and release antimicrobial components rather than supporting cell-growth[121].

Elviri *et al.* described the development of a new 3D printing technique, applied to the automation of a freeze-gelation method for the preparation of chitosan hydrogel scaffolds with controlled porosity. An in-house built 3D printing machine was set and the parameters adjusted in order to obtain scaffolds with defined chemico-physical features. Furthermore, *in vitro* cell culture studies were undertaken comparing 3D printed scaffolds with their homologous produced by solvent casting, evidencing an improvement in terms of biocompatibility and proliferation deriving from the production technique[122].

Although 3D printing of biomaterials has been developing extensively in recent years, the current technologies implemented in this field are mostly incapable of printing functional solid organs.

Anyway, researches have approached this issue by developing three-dimensional templates that could be used *in vivo* to support the development of functional organs or units[118].

1.4.3.1.1 Pressure (Piston)-Assisted Microsyringe (PAM)

PAM belongs to the "family" of extrusion-based printing techniques, it has been ideated specifically for the development of tissue-like scaffolds using hydrogels or anyway viscous polymer solutions, containing cells or not[123]. Since the technique derives from standard extruded printing, it has obviously the same principle, with the only difference that the material is extruded through a microsyringe. Tirella *et al.* describe their technique claiming its capability of realizing particularly well-defined microstructures (Figure 12).

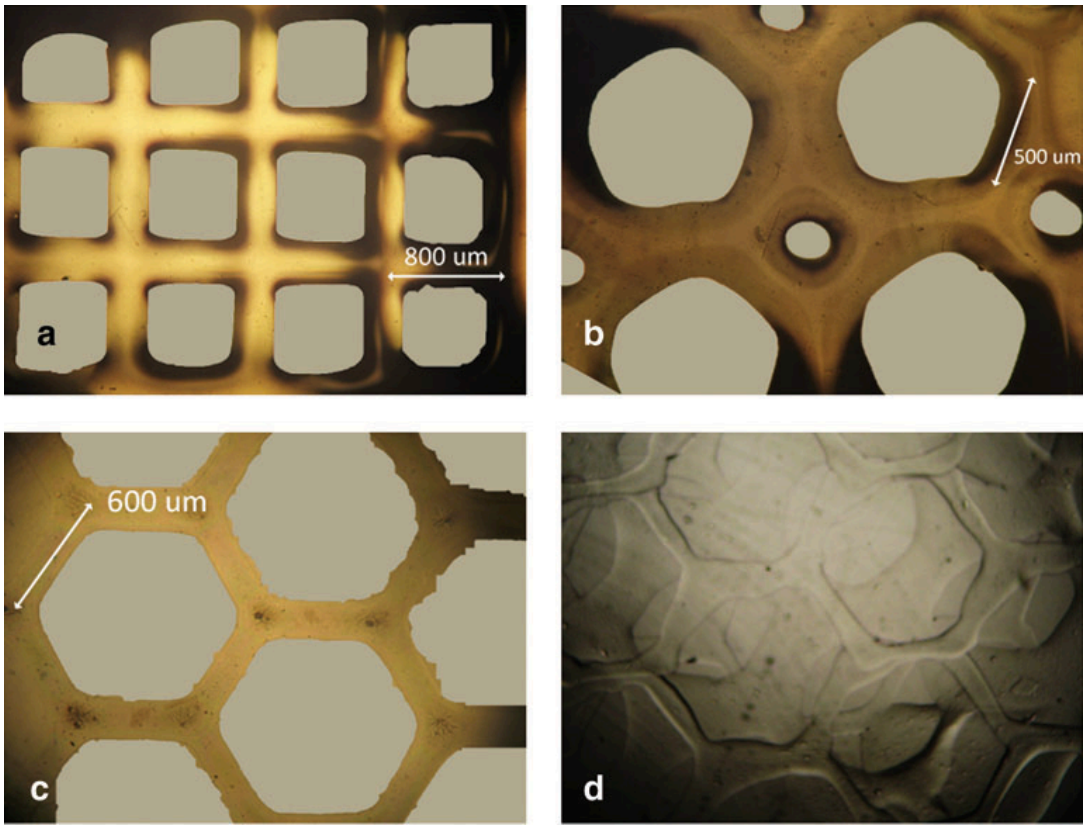

Figure 12. Hydrogel scaffolds realized with PAM system.
(a) square grid, (b) octagonal grid, (c) hexagonal grid, (d) three dimensional hexagonal grid scaffold[123].

Alginate was used as biocompatible gel and the optimum range of polymer concentrations was established for correct extrusion. On the basis of viscosity measurements, 4% and 6% (w/v in PBS) were chosen as suitable alginate concentrations. The results showed that well-defined

shapes and high spatial resolutions could be obtained with more viscous solutions, and that the lower the outflow, the higher the scaffold fidelity. *In vitro* investigations implied the use of a model consisting in liver hepatocellular carcinoma (HepG2) cells in the to-be-printed biomaterial. Their viability and metabolic activity in terms of albumin production was measured 48 h after printing; cells resulted lower in terms of viability, but higher concerning hepato-specific metabolic functions compared to controls, that were instead standardly 2D cultured on polystyrene. Porous three-dimensional microstructure seemed to be "appreciated" by HepG2 cells, making also hypothesize nutrients exchange was efficient. In contrast, a lower viability of 3D printed cells means cells are mechanically stressed during the process[123].

The concluding remark is that as for the other organs apart from skin that are often taken into account as models, the liver in this case, the technique has a great potential in terms of effectiveness in producing three-dimensional biocompatible templates, that might be of course applied for example for skin substitutes development.

1.4.3.2 Inkjet printing

Inkjet printing is based on the concept that a liquid or semi-liquid material is dropped or deposited through a continuous flow on a powder bed to bind particles together. The process is repeated until the final desired three-dimensional structure is obtained.

The first 3D-printed pharmaceutical form approved by Food and Drug Administration and commercialized (2016) was produced by this technique, its trade name is Spritam® (Aprecia Pharmaceuticals) and it's an oro-dispersible tablet for epilepsy attacks. The main advantage claimed compared to other tablets containing levetiracetam is the almost instantaneous disaggregation of the tablet once in contact with an aqueous medium (<10 sec.); this apparently trivial phenomenon is instead really important since Spritam is considered an emergency medicine and as such, the faster it acts the better it should be[124].

The application of the technique for tissue engineering purposes, in particular for soft tissue regeneration, results limited so far due to technical limits of the technique and poor suitability with the microstructural requirements.

As a matter of fact, the standard procedure implies a heat post-treatment to dry the object in order to let it maintain its shape and three-dimensionality and most of all to eliminate solvents used during the process being of advantage to avoid impurities and solvent residuals within the printed medicines[125]; moreover, the realizable structures are fragile in terms of mechanical properties, rendering it unsuitable for engineered tissue scaffolds. Compared to extrusion-based 3D printing

resolution is lower so as it is deposition accuracy. Contrarily, it results very versatile technique in other terms; the wide range of drugs employable can be loaded in great amounts and their release can be controlled in a tailored way by modifying composition parameters and employed materials. Poorly soluble compounds can be also easily included in the used formulation and regardless from the used drug individualized dose strength can be attained[126].

2 Aim of the work

The present work started at the beginning of 2015, since then, it had the main scope to develop and properly set an innovative 3D printing technique, successively called *"freeze-deposition 3D printing"*, for the development of a platform prototype of wound dressing.

The approach used implied during the first phase a deep technical engineering research and relative laboratory work, targeting optimum adjustment of parameters in order to obtain a solid, highly reproducible 3D printing process for the production of three dimensional porous hydrogel-based scaffolds. Optimization was preparatory for a further implementation of the versatile system, that was tuned in order to develop biocompatible hydrogel dressings capable of enhancing cell proliferation as well as maintaining tissue-specific functionality[122].

The achievements obtained were supported by studies on the influence of the entire pre and post-printing process[90], together with the employment of various polymer materials, on the micromorphology, chemico-physical characteristics and biological behavior *in vitro* with human and non-human cells rather than *in vivo* on diabetic rats[127].

Tissue regeneration, in general, represent the biggest objective of the work and for the whole soft tissue engineering field, for this reason the etiologic causes of ulcers and other tissues were taken into account for the design of different scaffolds as advanced medication prototypes at the laboratory scale. For instance, some were intended for treating wounds infections, other for general impeded or slow disorganized healing of wounds and epithelial tissue, in order to propose *ad hoc* devices for different chronic or acute relevant conditions.

Scaffolds platform created, as a matter of fact, suggested its material functionalization with active compounds for the regeneration of soft tissues[128-129].

Specific fields, such as wound healing and dentistry[128-129] were explored, as well as an environmental water sciences topic[130], giving rise to new objectives, since the technique, as well as the main materials used, revealed to be particularly resourceful.

3 Freeze-deposition 3D printing

The whole work conduced over the last 5 years relies on an additive manufacturing technology based on the deposition of a liquid or semi-liquid polymer material layer by layer till the complete construction of the desired object.
The logical concern rising regards the question: "how can liquid materials be accurately three-dimensionally printed?" By the way, several techniques have been developed over years, but up to now none of them meets determined requirements for the production of tissue-like scaffolds. The re-creation of a complex structure needs in facts high resolution machinery and a proper gelation/immobilization technique[89] to maintain three-dimensionality.

3.1 Material suitability

The overall 3D printing production process was standardized in terms of determination of sequential steps as well as their duration.
At room temperature (20-25°C), once the material has been prepared, it needs to be studied prior to trying printing; viscosity, as described in chapter 1[122] (section 4), is among the most relevant parameters, since an excessive viscous material would not be extruded respecting the set material flow while those under the described viscosity range would be extruded in an uncontrolled way, thus the three-dimensionality of the patterned object would not be respected.
Printable materials include polymeric solutions and many types of blends, usually suspensions of insoluble or poorly soluble materials/API's, that in this case necessitate a particulate below 30 μm.
Moreover, only Newtonian fluids can be used, since non-Newtonian ones would increase their viscosity as a function of the piston force applied.

3.2 Material loading

The material is loaded from the container in which it is stored by aspiration through a 5 mL sysringe, then a 26 G pre-cut needle is mounted on it and all the extruder apparatus fixed to the printer structure. Loading it is not trivial, it's important to degas completely the starting material as well as avoiding bubble formation during the procedure. Bubbles presence inside the syringe means scarce homogeneous extrusion and modification of pressure settings.

3.3 Material extrusion

Peltier's cells must be switched on in order to cool the printing surface temperature down till -15 °C, permitting a very rapid freezing of the polymer-based aqueous formulation (freezing speeds documented in section 4[122]). The instant freezing of the material, as the set working temperature, has been conceived, studied and applied in order to let the scaffold maintain both its macro and micro -structure, as reported in chapter 1, in facts, the faster the temperature decreases, the faster is ice crystals formation and the smaller is their dimension[131]. The microstructure remains thus unmodified till gelation, during which water is predominantly "entrapped" in the forming hydrogel network.

The adherence to the design parameters is fundamental in 3D manufacturing, since high reproducibility and printing fidelity represent major advantages of the technique, that would otherwise lose sense compared to others.

3.4 Fixation/sol-gel transition

Hydrogel products constitute a group of polymeric materials, the hydrophilic structure of which renders them capable of holding large amounts of water in their three-dimensional networks[132].

In this work mainly ionotropic procedures are exploited and deeply studied[90] with the aim of obtaining a very rapid complete and controlled sol-gel transition.

After deposition and freezing, the frozen object is always soaked in a gelling medium for short times (up to 1 hour), the latter determined by *ad hoc* experimentations in order to settle a procedure feasible for potential industrial transfer. Afterwards hydrogels undergo aqueous washing to get rid of any toxic residue (such as alkaline, hyper-osmotic, acid, and metal containing solutions) and to ensure that biocompatibility would not be compromised by this production phase.

3.5 Storage and sterilization/disinfection

Stability, interpreted as half-lives of compounds constituting the hydrogels, is crucial for their employment in *in vitro* and *in vivo* trials, for this reason, after proper washing procedure, scaffolds were systematically stored at 4 °C for a maximum time of one month.

Disinfection for cell cultures and animal testing was achieved by submerging stored hydrogels in 70 % v/v ethanol overnight, since this concentration is reported to be the more effective than

others on pathogenic microorganisms kill and thus considered a suitable mild technique for its use in laboratory settings.
(In order to maintain the same attitude of developing a potentially scalable process, gamma rays sterilization was performed* on hydrogel scaffolds and the major chemico-physical features as well as their total bacterial load were evaluated and compared with those disinfected through the aseptic procedure as well as those not-treated, as reported in the section 14).
*Gamma rays irradiation was carried out as courtesy of Gammatom s.r.l., Guanzate, (CO), Italy.

3.6 3D printing fidelity

Accurate extrusion and deposition is propaedeutical for the obtainment of highly defined three-dimensional items; in general, fused deposition modeling dedicated printers have a working resolution between 1/80 and 1/100 mm (corresponding to 12.5 – 10 μm) whereas the developed instrumentation achieves a nominal resolution of ~ 1/400 mm (2.5 μm).
This result was attained through the installation of endless screws driving the movements along *x*, *y* and *z* axis, avoiding the usual employment of rubber belts, that are cheaper and much easier to change when the service is needed but present the great drawback of a wider mechanical backlash.

References and Bibliography

1. Vacanti C. A., The history of tissue engineering. J. Cell. Mol. Med. Vol 10, No 3, 2006, pp. 569-576.
2. Proksch E., Brandner J. M. and Jensen J.M. The skin: an indispensable barrier. Experimental Dermatology Vol 17, 2008, pp. 1063–1072.
3. Madison K C. Barrier function of the skin: ‘‘la raison d’etre’’ of the epidermis. J Invest Dermatol Vol 121, 2003, pp. 231–242.
4. Hani Y., Mandy A., Sandeep S. Anatomy, Skin (Integument), Epidermis. StatPearls Publishing; 2019.
5. Mao A. S., Mooney D. J. Regenerative medicine: Current therapies and future directions. PNAS. Vol 112, No 47, 2015, pp. 14452-14459.
6. Jaklenec A., Stamp A., Deweerd E., Sherwin A., Langer R. Progress in the tissue engineering and stem cell industry “are we there yet?”. Tissue Eng Part B Rev Vol 18, No 3, 2012, pp. 155–166.
7. Bailey A. M., Mendicino M., Au P. An FDA perspective on preclinical development of cell-based regenerative medicine products. Nat Biotechnol Vol. 32, No 8, 2014, pp. 721–723.
8. Mendelson A., Frenette P. S. Hematopoietic stem cell niche maintenance during homeostasis and regeneration. Nat Med Vol 20, No 8, 2014, pp. 833–846.
9. Vacanti J. P., Otte J-B, Wertheim J. A. Introduction: Regenerative medicine and solid organ transplantation from a historical perspective. Regenerative Medicine Applications in Organ Transplantation, eds Orlando G., Lerut J., Soker S., Stratta R. J. (Elsevier, London), pp 1–15.
10. Frantz C., Stewart K. M., Weaver V. M. The extracellular matrix at a glance. J Cell Sci. Vol 123 No 24, 2010, pp. 4195–4200.
11. Inen H. J. R., Sainio A., Koulu M., Wight T. N., Penttinen R. Extracellular Matrix Molecules: Potential Targets in Pharmacotherapy. Pharmacol Rev Vol 61 No 2, 2009, pp. 198-223.
12. Calle-Pascual A. L., Redondo M. J., Ballesteros M., *et al*. Nontraumatic lower extremity amputations in diabetic and non-diabetic subjects in Madrid, Spain. Diabets Metab Vol 23, 1997, pp. 519–23.
13. Falanga V., *et al*. Topical use of human recombinant epidermal growth factor (h-EGF) in venous ulcers. J Dermatol Surg Oncol. Vol 18, 1992, pp. 604–606. [PubMed: 1624634]
14. Ehrenreich M., Ruszczak Z. Update on tissue-engineered biological dressings. Tissue Eng. Vol 12, 2006, pp. 2407–2424. [PubMed: 16995775]

15. Okiyama N., *et al*. Addition of the collagen binding domain of fibronectin potentiates the biochemical availability of hepatocyte growth factor for cutaneous wound healing. J Dermatol Sci. Vol 61, 2011, pp. 215–217. [PubMed: 21288695]
16. Maione A. G., Smith A., Kashpur O., Yanez V., Knight K., Mooney D. J., Veves A., Tomic-Canic M., Garlick J. A. Altered ECM Deposition by Diabetic Foot Ulcer-Derived Fibroblasts Implicates Fibronectin in Chronic Wound Repair. Wound Repair Regen. Vol. 24 No 4, 2016, pp. 630-643.
17. Palumbo P. J., Melton L. J. Peripheral Vascular Disease and Diabetes. Diabetes in America, 2nd edition. 1995, pp. 401.
18. Sergiu-Bogdan C., Xiaowei Z. Disturbed hypoxic responses as a pathogenic mechanism of diabetic foot ulcers. Diabetes Metab Res Rev. Vol 32 (Suppl. 1), pp 179–185.
19. Varghese M. C., Balin A. K., Carter D. M., Caldwell D. Local environment of chronic wounds under synthetic dressings. Arch Dermatol Vol 122 No 1, 1986, pp. 52–57.
20. Semenza G. L. Hypoxia-inducible factors in physiology and medicine. Cell Vol 148 No 3, 2012, pp. 399–408.
21. Peyssonnaux C., Boutin A. T., Zinkernagel A. S., Datta V., Nizet V., Johnson R. S. Critical role of HIF-1alpha in keratinocyte defense against bacterial infection. J Invest Dermatol Vol 128 No 8, 2008, pp. 1964–19.
22. Jeffcoate W. J., Harding K. G. Diabetic foot ulcers. The Lancet. Vol 361 No 9368, 2003, pp. 1545-1551.
23. Boulton A. J. M., Vileikyte L., Ragnarson-Tennvall G., Apelqvist J. The global burden of diabetic foot disease. Lancet. Vol 366, 2005, pp. 1719–24.
24. Pengzi Z., Jing L., Yali J., Sunyinyan T., Dalong Z. & Yan B. Global epidemiology of diabetic foot ulceration: a systematic review and meta-analysis. Annals of Medicine, Vol 49 No 2, 2017, pp. 106-116.
25. Jensen J. A., Goodson W. H., Hopf H. W., Hunt T. K. Cigarette smoking decreases tissue oxygen. Arch Surg. Vol 126, 1991, pp. 1131–4.
26. Obaid H., Eljedi A. Risk factors for the development of diabetic foot ulcers in Gaza Strip: a case–control study. Int J Diabetes Res. 2015;4:1–6.
27. Merza Z., Tesfaye S. The risk factors for diabetic foot ulceration. Foot. Vol 13, 2003, pp. 125–9.
28. Boyko E. J., Ahroni J. H., Stensel V., Forsberg R. C., Davignon D. R., Smith D. G. A prospective study of risk factors for diabetic foot ulcer. The Seattle Diabetic Foot Study. Diabetes Care. Vol 22, 1999, pp. 1036–42.

29. Sohn M. W., Budiman-Mak E., Lee T. A., Oh E., Stuck R. M. Significant J-shaped association between body mass index (BMI) and diabetic foot ulcers. Diabetes Metab Res Rev. Vol 27, 2011, pp. 402–9.
30. Reiber G. E., Lipsky B. A., Gibbons G. W. The burden of diabetic foot ulcers. Am J Surg Vol 176, 1998, pp. 5S–10S.
31. Van Houtum WH, Lavery LA, Harkless LB. The impact of diabetesrelated lower-extremity amputations in The Netherlands. J Diabetes Comp Vol 10, 1996, pp. 325–30.
32. Witsø E, Rønningen H. Lower limb amputations: registration of all lower limb amputations performed at the University Hospital of Trondheim, Norway, 1994–1997. Prosthet Orthop Int Vol 25, 2001, pp. 181–85.
33. Calle-Pascual AL, Redondo MJ, Ballesteros M, *et al*. Nontraumatic lower extremity amputations in diabetic and non-diabetic subjects in Madrid, Spain. Diabets Metab Vol 23, 1997, 519–23.
34. Shearer A., Scuffham P., Gordois A., Oglesby A. Predicted costs and outcomes from reduced vibration detection in people with diabetes in the US. Diabetes Care Vol 26, 2003, pp. 2305–10.
35. Gordois A., Scuffham P., Shearer A., Oglesby A., Tobian J. A. The health care costs of diabetic peripheral neuropathy in the US. Diabetes Care Vol 26, 2003, pp. 1790–95.
36. Gordois A., Scuffham P., Shearer A., Oglesby A. The healthcare costs of diabetic peripheral neuropathy in the UK. Diabet Foot Vol 6, 2003, pp. 62–73.
37. Shea JD. Pressure sores: classification and management. Clin Orthop Rel Res. Vol 112, 1975, pp. 89–100.
38. Black J., Baharestani M. M., Cuddigan J., Dorner B., Edsberg L., Langemo D., Posthauer M. E., Ratliff C., Taler G. and The National Pressure Ulcer Advisory Panel (NPUAP). National Pressure Ulcer Advisory Panel's Updated Pressure Ulcer Staging System
39. Collins L., Seraj S. Diagnosis and Treatment of Venous Ulcers. American Family Physician Vol 81 No 8, 2010, pp. 989-996.
40. De Araujo T., Valencia I., Federman D. G., Kirsner R. S. Managing the patient with venous ulcers. Ann Intern Med. Vol 138 No 4, 2003, pp. 326-334.
41. Etufugh C. N., Phillips T. J. Venous ulcers. Clin Dermatol. Vol 25 No 1, 2007, pp. 121-130.
42. Luciana P., Fernandes A. , Lastória S. Venous ulcer: epidemiology, physiopathology, diagnosis and treatment. International Journal of Dermatology Vol 44, 2005, pp. 449-456.

43. Sandeman D., Shearman C. P. Clinical aspects of lower limb ulceration. In: Mani R., Falanga V., Shearman C. P., Sandeman D., eds. Chronic Wound Healing, 1st edn. London: W. B. Saunders, 1999; pp. 4-25.
44. Zimmet S. Venous leg ulcers: modern evaluation and management. Dermatol Surg Vol 25, 1999, pp. 236–241.
45. Rizzi S. C., Upton Z., Bott K., Dargaville T. M. Recent advances in dermal wound healing: biomedical device approaches. Exp. Rev. Med. Devices Vol 7 No.1, 2010, pp.143-154.
46. Hutmacher D. W., Ng K. W., Khor H. L. Biodegradable Systems in Tissue Engineering and Regenerative Medicine. Skin tissue engineering part 1. Routledge, NY, USA, 2004, pp. 509-528.
47. Bowering C. K. Diabetic foot ulcers: pathophysiology, assessment, and therapy. Can Fam Physician Vol 47, 20011007–1016.
48. Adler A. I., Boyko E. J., Ahroni J. H., Smith D. G. Lower-extremity amputation in diabetes: the independent effects of peripheral vascular disease, sensory neuropathy, and foot ulcers. Diabetes Care Vol 22, 1999, pp. 1029–1035.
49. Brem H., Balledux J., Sukkarieh T., Carson P., Falanga V. Healing of venous ulcers of long duration with a bilayered living skin substitute: results from a general surgery and dermatology department. Dermatol Surg Vol 27, 2001, pp. 915–919.
50. Millington J. T., Norris T. W. Effective treatment strategies for diabetic foot wounds. J Fam Pract Vol 49 (suppl), 2000, pp. S40–S48.
51. Boulton A. J., Meneses P., Ennis W. J. Diabetic foot ulcers: a framework for prevention and care. Wound Repair Regen Vol 7, 1999, pp. 7–16.
52. Brem H., Sheehan P., Boulton A. J. M. Protocol for treatment of diabetic foot ulcers. The American Journal of Surgery. Vol 187 (Suppl to May 2004), pp. 1S–10S.
53. Jones I., Currie L., Martin R. A guide to biological skin substitutes. Br. J. Plast. Surg. Vol 55 No 3, 2002, pp. 185-193.
54. Greenleaf G., Hansbrough J. F. Current trends in the use of allograft skin for patients with burns and reflections on the future of skin banking in the United States. J. Burn Care Rehabil. Vol 55 No 5, 1994, pp. 428-431.
55. Mostow E. N., Haraway G. D., Dalsing M., Hodde J. P., King D. Effectiveness of an extracellular matrix graft (OASIS Wound Matrix) in the treatment f chronic leg ulcers: a randomized clinical trial. J. Vasc. Surg. Vol 41 No 5, 2005, pp. 827-843.

56. Niezgoda J. A., Van Gils C. C., Frikberg R. G., Hodde J. P. Randomized clinical trial comparing OASIS Wound Matrix to Regranex Gel for diabetic ulcers. Adv. Skin Wound Care Vol 18 No 5 Pt 1, 2005, pp. 258-266.
57. Huldt-Nystrom T., Meuleneire F., Acton C. Xelma®, an advanced wound treatment for venous ulcers: a European perspective. Wounds UK Vol 4 No 1, 2008, pp. 106-110.
58. Winter G. D. formation of the scab and the rate of epithelization of superficial wounds in the skin of the young domestic pig. Nature Vol 193, 1962, pp. 293-294.
59. Pomahac B., Svensjo T., Yao F., Brown H., Eriksson E. Tissue engineering of skin. Crit Rev Oral Biol Med, Vol 9, 1998, pp. 333–344.
60. Zhong S. P., Zhang Y. Z., Lim C. T. Tissue scaffolds for skin wound healing and dermal reconstruction. Nanomed Nanobiotechnol Vol 2, 2010, pp. 510–525.
61. Nicolai J. P. A., Rakhorst G., Introduction: Biomaterials in Modern Medicine, 2008, http://www.worldscibooks .com/etextbooks/6562/6562.chap01.pdf.
62. International Standards Organization, biological evaluation of medical devices, part 1 evaluation and testing, ISO 10993: 2003.
63. Gibson T. Br J Surg Vol 77, 1990, pp. 824–825.
64. Maeda M., Tani S., Sano A. Fujioka K. Natural Polymers: Industry Techniques and Applications. J Control Release Vol 62, 1999, pp. 313–324.
65. Patino M. G., Neiders M. E., Andreana S., Noble B., Cohen R. E. Collagen as an implantable material in medicine and dentistry. J Oral Implantol. Vol 28, 2002, pp. 220–5.
66. Khan R., Khan M. H. Use of collagen as a biomaterial: An update. J Indian Soc Periodontol. Vol 17 No 4, 2013, pp. 539–542.
67. Shoulders M. D., Raines R. T. Collagen Structure and Stability. Annual Review of Biochemistry Vol 78, 2009, pp. 929-958.
68. Doillon C. J., Silver F. H. Collagen based wound dressing effects of Hyaluronic acid and fibronectin on wound healing. Biomaterials. Vol 7, 1986, pp. 3–8.
69. Wong S. F., Lloyd D. K., Vasko C., Mummaneni M., Osann K. A Pilot Cross-Over study to evaluate the use of Regenecare® topical gel in patients with cutaneous toxicity caused by epidermal growth factor receptor (HER1/EGFR) inhibitors. Presented at 9th National Conference on Cancer Nursing Research 126, Oncology Nursing Forum Vol 34 No 1, 2007, pp. 216-217.
70. Kozloff M., Gowland P. A., Vlamakis J., Koch J., Ratko G., Gravitt L., Palmer D. Evaluation of Regenecare Topical Gel in the Treatment of Skin Rash Associated with Cetuximab

(Erbitux), Tarceva® and Other EGFR Inhibitors-Treated Cancer Patients. CCRP, Ingalls Memorial Hospital, Cancer Research Center. Harvey Ill., 2007.

71. Ruszczak Z. Effect of collagen matrices on dermal wound healing. Advanced Drug Delivery Reviews Vol 55, 2003, pp. 1595– 1611.
72. Matthews J. A., Wnek G. E., Simpson D. G., Bowlin G. L. Electrospinning of Collagen Nanofibers. Biomacromolecules Vol 3 No 2, 2002, pp. 232-238.
73. Martínez A., Blanco M. D., Davidenko N., Cameron R. E. Tailoring chitosan/collagen scaffolds for tissue engineering: Effect of composition and different crosslinking agents on scaffold properties. Carbohydrate Polymers Vol 132, 2015, pp. 606–619.
74. Doillon C. J., Silve F. H. Collagen-based wound dressing: Effects of hyaluronic acid and fibronectin on wound healing. Biomaterials Vol 7, 1986, pp. 3-8.
75. Boyce S. T. Design principles of composition and performance of cultured skin substitutes. Burns Vol. 27, 2001, pp. 523–33.
76. Schul III J. T., Tompkins R. G., Burks J. F. Artificial skin. Annu Rev Med Vol 51, 2000, pp. 231–44.
77. Yannas IV. Regeneration templates. In: Bronzino J. D., editor. The biomedical engineering handbook. Boca Raton, FL: CRC Press; 1995. pp. 1619.
78. Yanas IV, Burke J. F. Design of an artificial skin I. Basic design principles. J Biomed Mater Res Vol 14 No 4, 1980, pp. 65–81.
79. Bell E., Ehrlich H. P., Battle D. J., Nakatsuji T. Living tissue formed *in vitro* and accepted as skin-equivalent tissue of full thickness. Science Vol 211, 1981, pp. 1052–4.
80. Ma L., Gao C., Mao Z., Zhou J., Shen J., Hu X., Han C. Collagen/chitosan porous scaffolds with improved biostability for skin tissue engineering. Biomaterials Vol 24, 2003, pp. 4833–4841.
81. Dong C., Lv Y. Application of Collagen Scaffold in Tissue Engineering: Recent Advances and New Perspectives. Polymers Vol 8, 2016, pp.42.
82. Zhu Z., Yin-Min W., Jun Y., Xu-Song L. Hyaluronic acid: a versatile biomaterial in tissue engineering. Plast Aesthet Res Vol 4, 2017, pp. 219-27.
83. Knudson C. B. Hyaluronan and CD44: strategic players for cell-matrix interactions during chondrogenesis and matrix assembly. Birth Defects Res Part C Embryo Today Vol 69, 2003, pp. 174-96.
84. Li L. Recent advances of biomaterials in biotherapy. Regen Biomater Vol 3, 2016, pp. 99-105.

85. Hunt N. C., Grover L. M. Cell encapsulation using biopolymer gels for regenerative medicine. Biotechnol Lett Vol 32, 2010, pp. 733-42.
86. Dupuis G., Lehoux G. J. A simplified method to retrieve chitosan from acidic solutions thereof. Publication of CN1938335A.
87. Hong S. C., Yoo S. Y., Kim H., Lee J. Chitosan-Based Multifunctional Platforms for Local Delivery of Therapeutics. Mar. Drugs Vol 15 No 3, 2017, pp. 60.
88. Khan M., Mujahid M. A Review on Recent Advances in Chitosan based Composite for Hemostatic Dressings. International Journal of Biological Macromolecules Vol 124, 2019, pp. 138–147.
89. Muzzarelli R., Baldassare B., Conti F., Ferrara P., Biagini G. Biological activity of chitosan: ultrastructural study. Biomaterials Vol 9, 1988, pp. 247.
90. Bergonzi C., Di Natale A., Zimetti F., Marchi C., Bianchera A., Bernini F., Silvestri M., Bettini R., Elviri L. Study of 3D-printed chitosan scaffold features after different post-printing gelation processes. Sci Rep. Vol 23 No 9 (1), 2019, pp. 362.
91. Stephen-Haynes J., Gibson E., Greenwood M. Chitosan: a natural solution for wound healing. JCN Vol 28, No 1, 2014, pp. 48-52.
92. Lim T. C., Chian K. S., Leong K. F. Cryogenic prototyping of chitosan scaffolds with controlled micro and macro architecture and their effect on *in vivo* neo-vascularization and cellular infiltration. Journal of Biomedical Materials Research A, Vol 94 a, issue 4, 2010, pp. 1303-1311.
93. Ye K., Felimban R. Chondrogenesis of Infrapatellar Fat Pad Derived Adipose Stem Cells in 3D Printed Chitosan Scaffold. Plos one Vol 9 No 7, 2014, e102638.
94. Lee K.Y., Mooney D. J. Alginate: Properties and biomedical applications. Prog. Polym. Sci. Vol 37, 2012, pp. 106–126.
95. Ching S. H., Bansal N., Bhandari B. Alginate gel particles—A review of production techniques and physical properties. Crit. Rev. Food Sci. Nutr. Vol 57, 2017, pp. 1133–1152.
96. Yang, C. H., Wang M. X., Haider H., Yang J. H., Sun J. Y., Chen Y. M., Zhou J., Suo Z. Strengthening alginate/polyacrylamide hydrogels using various multivalent cations. ACS Appl. Mat. Interf. Vol 5, 2013, pp. 10418–10422.
97. Aderibigbe B. A., Buyana B. Alginate in Wound Dressings. Pharmaceutics Vol 10, 2018, pp. 42.
98. ALGICELL®Ag Antimicrobial Alginate Dressing. Available online: http://www.woundsource.com/product/algicell-ag-antimicrobial-alginate-dressing (accessed on 13 December 2017).

99. AlgiSite M™. Available online: http://www.smith-nephew.com/professional/products/advanced-woundmanagement/algisite-m/ (accessed on 13 December 2017).
100. Morris C. Celebrating 25 years of Sorbsan and its contribution to advanced wound management. Wounds UK, 2008, Vol 4, No 4, 2008.
101. Allymamod A. Use of Calcium Alginate vs Hydrofibre dressing in City and Hackney Community Health Service. Poster presented EWMA 2011.
102. Callaghan R. (2007) A case study of a nursing home resident with infected venous ulcers. Poster presentation at Wounds UK, Harrogate.
103. Odugbesan O., Barnett A. H. Use of a Seaweed-based dressing in management of leg ulcers in diabetics: a case report. Pract Diabetes Vol 4 No 1, 1987, pp. 46–7.
104. Yu W., Jiang Y. Y., Sun T. W., Qi C., Zhao H., Chen F., Shi Z., Zhu Y. J., Chen D., He Y. Design of a novel wound dressing consisting of alginate hydrogel and simvastatin-incorporated mesoporous hydroxyapatite microspheres for cutaneous wound healing. RSC Adv. Vol 6, 2016, pp. 104375–104387.
105. Üstündāg G. C., Özbek S., Karaca E., Çavu¸sōglu I. *In vivo* evaluation of electrospun poly (vinyl alcohol)/sodium alginate nanofibrous mat as wound dressing. Tekstil ve Konfeksiyon Vol 20, 2010, pp. 290–298.
106. Saghazadeh S., Rinoldi C, Schot M., Kashaf S. S., Sharifi F., Jalilian E., Nuutila K., Giatsidis G., Mostafalu P., Derakhshandeh H., Yue K., Swieszkowski W., Memic A., Tamayol A., Khademhosseini A. Drug delivery systems and materials for wound healing applications. Advanced Drug Delivery Reviews Vol 127, 2018, pp. 138–166.
107. http://www.woundsource.com
108. Sola A., Bertacchini J., D'Avella D., Anselmi L., Maraldi T., Marmiroli S., Messori M. Development of solvent-casting particulate leaching (SCPL) polymer scaffolds asimproved three-dimensional supports to mimic the bone marrow niche. Materials Science & Engineering C Vol 96, 2019, pp. 153-165.
109. Cannillo V., Chiellini F., Fabbri P., Sola A., Production of Bioglass® 45S5 – polycaprolactone composite scaffolds via salt-leaching. Compos. Struct. Vol 92, 2010, pp. 1823–1832.
110. Mikos A. G., Temenoff J. S. Formation of highly porous biodegradable scaffolds for tissue engineering. EJB Electronic Journal of Biotechnology Vol 3 No 2, 2000.

111. Siemann U. Solvent cast technology – a versatile tool for thin film production. Scattering Methods and the Properties of Polymer Materials; Part of the Progress in Colloid and Polymer Science book series (PROGCOLLOID) Vol 130, 2005, pp 1-14.

112. Particle Sciences - Technical Brief Vol 3, 2010

113. Bhattarai N., Edmondson D., Veiseh O., Matsen F. A., Zhang M. Electrospun chitosan-based nanofibers and their cellular compatibility. Biomaterials Vol 26, 2005, 6176–6184.

114. Derakhshanfar S., Mbeleck R., Xu K., Zhang X., Zhong W., Xing M. 3D bioprinting for biomedical devices and tissue engineering: A review of recent trends and advances. Bioactive Materials Vol 3, 2018, pp. 144-156.

115. Szczerba R. J. No Donor Required: 5 Body Parts You Can Make With 3-D Printers. Forbes, June 17, 2015.

116. Derakhshanfar S., Mbeleck R., Xu K., Zhang X., Zhong W., Xing M. 3D bioprinting for biomedical devices and tissue engineering: A review of recent trends and advances. Bioactive Materials Vol 3, 2018, pp. 144-156.

117. (https://optn.transplant.hrsa.gov)

118. Daly A. C., Cunniffe G. M., Sathy B. N., Jeon O., Alsberg E., Kelly D. J. 3D bioprinting of developmentally inspired templates for whole bone organ engineering, Adv. Healthcare Mater. Vol 5 No 18, 2016, pp. 2353-2362.

119. Kesti M., Eberhardt C., Pagliccia G., Kenkel D., Grande D., Boss A., Zenobi-Wong M. Bioprinting complex cartilaginous structures with clinically compliant biomaterials, Adv. Funct. Mater. Vol 25 No 48, 2015, pp. 7406-7417.

120. Wu Z., Su1 X., Xu Y., Kong B., Sun W., Mi S. Bioprinting three-dimensional cell-laden tissue constructs with controllable degradation. Scientific Reports Vol 6 No 24474, 2016.

121. Rees A., Powell L. C., Chinga-Carrasco G., Gethin D. T., Syverud K., Hill K. E., Thomas D. W. 3D Bioprinting of Carboxymethylated-Periodate Oxidized Nanocellulose Constructs for Wound Dressing Applications. BioMed Research International Vol 2015, Article ID 925757, 7 pages.

122. Elviri L., Foresti R., Bergonzi C., Zimetti F., Marchi C., Bianchera A., Bernini F., Silvestri M., Bettini R. Highly defined 3D printed chitosan scaffolds featuring improved cell growth. Biomed. Mater. Vol 12 No 045009, 2017.

123. Tirella A., Vozzi F., Vozzi G., Ahluwalia A. PAM2 (Piston Assisted Microsyringe): A New Rapid Prototyping Technique for Biofabrication of Cell Incorporated Scaffolds. Tissue Engineering: Part C Vol 17 No 2, 2011, pp. 229-237.

124. Konta A. A., García-Piña M., Serrano D. R. Personalised 3D Printed Medicines: Which Techniques and Polymers Are More Successful? Bioengineering Vol 4 No 4, 2017, pp. 79.

125. Jonathan G., Karim A. 3D printing in pharmaceutics: A new tool for designing customized drug delivery systems. Int. J. Pharm. Vol 499, 2016, pp. 376–394.

126. Prasad L. K., Smyth H. 3D Printing technologies for drug delivery: a review. Drug Development and Industrial Pharmacy Vol 42 No 7, 2017, pp. 1019–1031.

127. Intini C., Elviri L., Cabral J., Mros S., Bergonzi C., Bianchera A., Flammini L., Govoni P., Barocelli E., Bettini R., McConnell M. 3D-printed chitosan-based scaffolds: An *in vitro* study of human skin cell growth and an *in-vivo* wound healing evaluation in experimental diabetes in rats. Carbohydr Polym. Vol 1 No 199, 2018, pp. 593-602.

128. Saccani M., Parisi L., Bergonzi C., Bianchera A., Galli C., Macaluso G. M., Bettini R., Elviri L. Surface modification of chitosan films with a fibronectin fragment-DNA aptamer complex to enhance osteoblastic cell activity: A mass spectrometry approach probing evidence on protein behavior. Rapid Commun Mass Spectrom. Vol 33 No 4, 2019, pp. 336-342.

129. Parisi L., Toffoli A., Bianchi M. G., Bergonzi C., Bianchera A., Bettini R., Elviri L., Macaluso G. M. Functional Fibronectin Adsorption on Aptamer-Doped Chitosan Modulates Cell Morphology by Integrin-Mediated Pathway. Materials (Basel). Vol 12 No 5, 2019.

130. Bergamonti L., Bergonzi C., Graiff C., Lottici P. P., Bettini R., Elviri L. 3D printed chitosan scaffolds: A new TiO_2 support for the photocatalytic degradation of amoxicillin in water. Water Res. Vol 15, 2019, pp. 163.

131. Marcellini M., Noirjean C., Dedovets D., Maria J., Deville S. Time-Lapse, *in Situ* Imaging of Ice Crystal Growth Using Confocal Microscopy. ACS Omega Vol 1, 2016, pp. 1019−1026.

132. Ahmed E. M. Hydrogel: Preparation, characterization, and applications: A review. Journal of Advanced Research Vol 6, 2015, pp. 105–121.

4 Chapter 1: “Highly defined 3D printed chitosan scaffolds featuring improved cell growth”

Elviri L.[1], Foresti R.[2], Bergonzi C[1]., Zimetti F.[1], Marchi C.[1], Bianchera A.[3], Bernini F.[1], Silvestri[2,4] M., Bettini R.[1]

[1] Food and Drug Department, University of Parma, Parco Area delle Scienze 27/A, I-43124, Parma, Italy
[2] Department of Engineering and Architecture, University of Parma, Parco Area delle Scienze 181/A, Università degli Studi di Parma, I-43124, Parma, Italy
[3] Interdepartmental Centre Biopharmanet-Tec, University of Parma, Parco Area delle Scienze 27/A, I-43124, Parma, Italy
[4] Department of Innovative Technologies, University of Applied Sciences and Arts of Southern Switzerland (SUPSI), CH-6928, Manno, Switzerland

Published on 12 July 2017, Biomedical Materials Vol 12

The article “Highly defined 3D printed chitosan scaffolds featuring improved cell growth” published in Biomedical Materials (BMM) has been selected to be part of the journal's Highlights of 2017 collection.

IF 3.44

Personal contribution

CB performed the experimental work related to materials preparation, analytical characterization, 3D development and contributed to the preparation of the manuscript.

Abstract

The augmented demand for medical devices devoted to tissue regeneration and possessing a controlled micro-architecture means there is a need for industrial scale-up in the production of hydrogels. A new 3D printing technique was applied to the automation of a freeze-gelation method for the preparation of chitosan scaffolds with controlled porosity. For this aim, a dedicated 3D printer was built in-house: a preliminary effort has been necessary to explore the printing parameter space to optimize the printing results in terms of geometry, tolerances and mechanical properties of the product. Analysed parameters included viscosity of the starting chitosan solution, which was measured with a Brookfield viscometer, and temperature of deposition, which was determined by filming the process with a cryocooled sensor thermal camera. Optimized parameters were applied to the production of scaffolds from solutions of chitosan alone or with the addition of raffinose as a viscosity modifier. Resulting hydrogels were characterized in terms of morphology and porosity. *In vitro* cell culture studies comparing 3D printed scaffolds with their homologous produced by solution casting evidenced an improvement in biocompatibility deriving from the production technique as well as from the solid state modification of chitosan stemming from the addition of the viscosity modifier.

Keywords: 3D printing, chitosan scaffolds, improved biocompatibility

4.1 Introduction

The general aging of the population and the increase in the prevalence of chronic diseases, injuries and traumas lead to an augmented demand for drugs and biological substitutes that could restore, maintain or improve tissue function[1]. The main target of tissue engineering is the identification and application of adequate materials for the design and production of supportive structures, generally defined as scaffolds, that possess desirable properties for promoting cell adhesion, proliferation and differentiation[2]. The performances of such scaffolds depend both on the characteristics of their components and on their structural architecture[3]. Polymers, natural or synthetic, offer a bunch of choices to tissue engineers: the ideal material is biocompatible, biodegradable and does not elicit a foreign body reaction[4]. Moreover, it is endowed with mechanical properties and physical characteristics suitable for mimicking the tissue to be repaired[4]. Among natural polymers, those that can give rise to hydrogels possess the most interesting features, thanks to their resemblance to extracellular matrix and, in general, for their better cytocompatibility[5]. Chitosan (CH) is a β-(1–4)-linked D-glucosamine and N-acetyl-D-glucosamine natural polysaccharide derived from the alkaline N-deacetylation of chitin[6]. It possesses a good combination of biocompatibility and biodegradability, it is non-toxic, not expensive, and it can be moulded into different shapes, thus making it suitable for many applications[7].

Scaffolds produced with chitosan in association with other components have found different applications in tissue engineering, but the use of chitosan alone is mainly devoted to skin, nerves and soft tissue regeneration[8-10]. One of the main fields of application of chitosan is wound healing[11-12], thanks to the combination of chitosan advantages such as hemostasis, stimulation of fibroblast synthesis of collagen, cell support and local drug delivery[13]. The structural similarity of chitosan with glycosaminoglycans also renders it a good candidate for chondrogenesis and bone cell colonization[14] but, without the addition of other components some limitations exist due to the low mechanical resistance of the material by itself. The enhancement of mechanical properties of chitosan can be achieved by modifying the production technique, as described by Zakhem *et al*[15] who prepared a tubular structure for the replacement of intestine that could withstand burst pressures of 715 mmHg and allowed growth and alignment of smooth muscle cells. Anyway further technical modifications are needed: this prompted us to look for new production methods for the development of chitosan scaffolds.

In a previous work[16] the use of sugar and salt enriched chitosan solutions for the preparation of hydrogels, which showed improved cytocompatibility and hydrophilicity was described. The

production method allowed a good control of pore size and distribution at the microscopic level[17], but a macroscopic control, in terms of geometry and architecture, was still elusive. The architecture of the scaffolds is of critical importance for the success of cell colonization[18], so, with the purpose of obtaining highly reproducible hydrogels in view of their possible application and industrial scale-up we applied a 3D printing technique to the production of chitosan hydrogels by automating the previously reported freeze-gelation technique[17]. The use of automation for the production of 3D chitosan scaffolds was already described by Ang *et al*[19], who reported the preparation of chitosan–hydroxyapatite scaffolds using a robotic system that dispensed the polymeric solution into a NaOH coagulation bath. The technique suffered the formation of precipitated lumps in the nozzle and was for this reason refined by Geng *et al*[20]. These authors introduced a dual-nozzle system for the sequential dispensing of chitosan and NaOH solution during the fabrication process of superimposed layers. This eliminated the need of a coagulation bath and allowed better uniformity, strength and an overall better quality of the scaffolds in terms of reproducibility. Almeida *et al*[21] more recently applied this method to the preparation of chitosan and PLA scaffolds to be evaluated in the presence of human macrophages. Anyway, all these techniques are based on the direct coagulation of chitosan solution upon deposition and give rise to closed chitosan filaments: no details are reported about the internal microporosity of those scaffolds. Some application of 3D printed chitosan scaffolds were reported by Ye *et al* for chondrogenesis: the association of chondrogenic culture conditions and the 3D printed support allowed the formation of a cartilaginous 'cap' by adipose stem cells isolated from human infrapatellar fat pad[22] Hsu *et al* prepared chitosan 3D printed scaffolds treated with air plasma that were tested with MC3T3-E1 cells[23]. Air plasma treatement improved hydrophilicity and this resulted in increased cell adhesion and bone mineral deposition.

In the present work the fabrication of a scaffold with a customized shape has been implemented as a variant of a family of additive manufacturing processes that in the literature are proposed by different names but which are, at least regarding the part of 3D printing, very similar to each other and possibly differ for the subsequent procedures of gelation or lyophilisation: low temperature manufacturing (LTM)[24], liquid frozen deposition manufacturing[25], cryogenic prototyping [26] and rapid freeze prototyping [27]. In contrast with the work proposed by Lim *et al*[28], in which chitosan scaffolds are prepared by deposition of the solution in a cryogenic chamber followed by lyophilisation, we propose to avoid this latter expensive and time-consuming step by directly transferring frozen chitosan structures into a coagulation bath. This is the direct transposition and automation of the freeze-gelation method described by Elviri *et al*[17] and associates the advantages deriving from the modification of the composition of chitosan solution with the technical

advantages of 3D printing. A deep investigation of the automation system as well as of the parameters that determine a satisfactory deposition was carried out. These include, among others, the role of the viscosity of the starting chitosan solution and the effect of temperature on the success of deposition and scaffold appearance.
The produced 3D printed hydrogels were characterized in terms of morphology and porosity while their suitability as scaffold supporting *in vitro* cell growth was investigated in comparison with their homologous produced by the previously described casting technique[16].

4.2 Materials and methods

4.2.1 Materials

Chitosan ChitoClear™ (CAS 9012-76-4, degree of deacetylation 95%; molecular weight by gel permeation chromatography 150–200 kDa; allergen free, water insoluble, soluble in acid media) was from PRIMEX Ehf (Siglufjordur, Iceland).
Acetic acid 99.8% v/v, dimethyl sulfoxide (DMSO) and potassium hydroxide were from J T Baker (Deventer, Netherlands).
Water was purified (0.055 uS cm^{-1}, TOC 1 ppb) with Purelab pulse + Flex ultra-pure water (Elga Veolia, Milan, Italy).
MTT (3-(4,5-dimethylthiazol-2-yl)-2,5-diphenyl tetrazolium bromide) reagent was purchased from Sigma-Aldrich (St. Louis, MO, USA), dissolved in water and stocked at concentration of 5mgml−1; final concentration used was 1$mgml^{-1}$; calcein-AM was obtained from Invitrogen Molecular Probe (Invitrogen Co., Carlsbad, CA, USA) (1$mgml^{-1}$ in DMSO) and used at a final concentration of 10 μM.

4.2.2 3D printer

A LTM system was designed and implemented at laboratory scale through the insertion of bespoke modules in the structure of a commercial fuse deposition manufacturing (FDM) 3D printer, whose architecture is based on three Cartesian axes, two of which enliven the printing plate in *x* and *y* direction on the horizontal plane, while the *z*-axis determines the progressive lifting of the extrusion nozzle. Such an approach follows the idea, demonstrated in [29], that the motion axis of an inexpensive FDM printer can provide enough accuracy and repeatability to manufacture highly defined scaffolds. Similarities between the two systems are limited to the

components for generating motion: the printing process based on freezing a polymer solution is entirely different from the FDM one and required a complete makeover of the other machine subsystems. Figure 1 shows the two main physical changes implemented: (1) by developing a new deposition system that uses a syringe pump; (2) by replacing the hot plate with a cooling system. In a first version, the latter was simply made up using liquid nitrogen contained in a Dewar flask positioned below the printing plate. Then, to improve the process knowledge and its control, the printing process was repeatedly filmed with a cryo-cooled sensor thermal camera FLIR SC7000 (Flir Systems Inc., Wilsonville, OR, USA), with a detector having a resolution of 640 ×512 pixels, and with a temperature sensitivity of 0.02 °C at 30°C and an accuracy of ±1 °C. The analysis was carried out by using the software tool Altair version 5.91.010 (Flir Systems Inc.), which allows selecting a spot at the point to be analysed and to automatically draw the temperature versus time plot. Figure 2 shows a sample of the acquired images and a diagram of the temperature field on varying the distance from the freezing surface. On the basis of the obtained result, a more repeatable and accurate freezing plate was designed and built by combining several Peltier cells and liquid/air exchangers. On the whole, the system allows avoiding the use of disposable fluids and requires neither a compressor nor potentially contaminating fluids, and it is therefore appropriate for the application requirements of simplicity, safety and reduced cost. Moreover, the adopted method did not present the disadvantages typical of other solid freeform fabrication systems (use of toxic organic adhesives, high process temperatures, difficulty in the removal of dusts). The design of scaffold shapes could be directly described by the geometric primitives of the axis control, without need of translating them through general purpose programmes for the transformation of the 3D CAD model in a mesh to be subjected to slicing: this introduces a significant advantage compared to systems available on the market in terms of exact correspondence between model and printed object, especially in case of artifacts with complex inner shape. The third major change activity has therefore covered the software programme for the management of the printing process, whose parameters are indicated in table 1, which presents also a comparison with the process parameters found in[29].

Chitosan concentration % (w/v)	PLA scaffold printing[a]	Proposed chitosan-based printing process
Deposition velocity	2 mm s^{-1}	3 mm s^{-1}
Nozzle tip size	350 µm	260 µm
Diameter of filament	175 µm	250 µm (nominal)
Extrusion temperature	180 °C	−2÷2 °C
Number of layers	variable	5÷45

Table 1. Printing process parameters. [a] as reported in [29]

The meaning of this comparison is mainly to provide a reference to evaluate the proposed prototype machine in relation to the typical specifications of one of the most well-established and widespread technology which constitutes an easily available, reproducible benchmark. Other prototypes[24-28] are not illustrated with sufficient details to make possible a meaningful confrontation of their feature values.

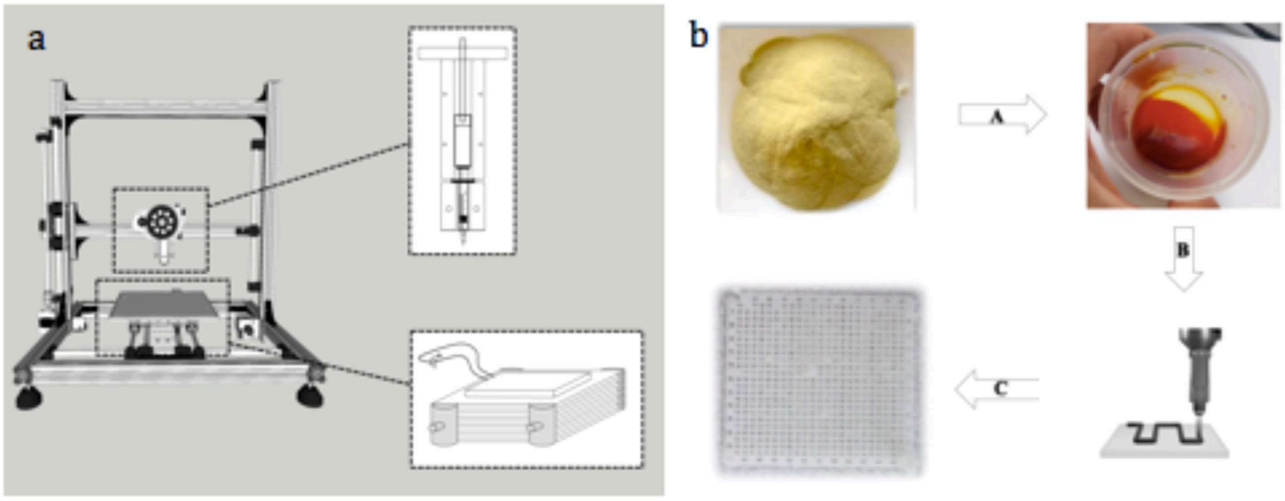

Figure 1. (a) A commercial FDM 3D printer has been customised by developing a new deposition system that uses a syringe pump and by replacing the hot plate with a cooling system combining air–liquid exchangers and Peltier plates. (b) Schematic illustration showing 3D chitosan scaffold fabrication: (A) dissolution of chitosan powder in acetic aqueous solution for 16–18 h; (B) deposition of chitosan solution on a substrate to develop the 3D chitosan scaffold by extrusion-based 3D printing method and (C) increase of material rigid of 3D chitosan scaffold after 1 h in gelling solution.

4.2.3 Scaffold preparation

Solutions of chitosan (6%w/v) and chitosan-modified (6% w/v) with raffinose suitable for 3D printer were prepared in 2% acetic acid. D-(+)raffinose pentahydrate (290mM) was added to the second solution as a viscosity modifier agent in order to obtain more hydrophilic hydrogels relative to that obtained from the pure chitosan solution[16]. Viscosity measurements of the solutions was performed at 60 and 100 rpm, with a rotational viscometer (Smart Series, Fungilab, Barcelona, Spain) equipped with a spindle # 7.

After printing, the frozen scaffold was immediately immersed in aqueous KOH (8% w/v) for 10 min in order to let it gel.

The chitosan solutions (6%w/v) were used also for the preparation of reference scaffolds following the casting procedure reported by Bettini *et al*[16]. Briefly, chitosan solutions were poured into rubber rings previously stuck on glass slides: these were transferred to a −60 °C refrigerator and, after 24 h, gelled in KOH (8%v/v) solution overnight.

4.2.4 Environmental scanning electron microscopy (ESEM) analysis

An ESEM Quanta 250 FEG™ (FEI, Hillsboro, OR, USA), equipped with EDS (energy ispersive spectrometer) for x-ray microanalysis (Bruker Nano GmbH, Berlin, Germany) was used to evaluate the macrostructure of the fully hydrated scaffolds. EDS was equipped with a QUANTAX XFlash® 6 30 Detector with ≤126 eVFWHM energy resolution at Mn Kα. Scaffolds were carefully deposited on a filter paper to remove the surface aqueous layer before analysis. Then, the samples were placed on conductive carbon (Agar Scientific) and measured at 89–114x magnification, through an accelerating voltage (EHT) of the electron beam of 10.00 kV. The photographs obtained were analysed with a software for image analysis (ESPRIT 1.9 software, Bruker Nano GmbH). ESEM images were taken on the central portions of the surfaces of the scaffolds and on the cross-sections. For each image the diameter of the pores and the filaments were measured.

4.2.5 Scanning electron microscopy (SEM) and x-ray diffraction (XRD) analysis

Chitosan scaffolds were lyophilized for 24 h with an Alpha 2–4 LCS Plus lyophylizer (Martin Christ, Osterode am Harz, Germany). Images of the dried scaffold were taken with a scanning electron microscope (Sigma HD, Carl Zeiss, Jena, Germany), at 300x magnification and EHT

1.00 kV and analysed by ImageJ software (NIH, Bethesda, MD,USA) for determining macro- and micro-structures.

XRD patterns on powder were recorded on a MiniFlex diffractometer (Rigaku, Japan) using Cu Kα radiation (λ = 1.5418 Å) generated with 30 kV. The sample of chitosan powder, chitosan scaffold with and without raffinose was transferred into the sample holder until it was completely full and then pressed with a glass slide in order to obtain a flat and homogeneous surface. The goniometer was set at a scanning rate of 1.5 min^{-1} (step size = 0.05) over the 2θ range 5°–50°. Each measurement was carried out at least in triplicate.

4.2.6 Evaluation of mechanical strength and water loss

A tractional dynamometer (Acquati, Italy) has been used to evaluate the mechanical strength of the 3D printed scaffolds, calculated as Young's elastic modulus (E). Scaffold sizes were 20 layers×5 cm×1.5 cm. The traction tests were performed by setting the following parameters: pre-fixed distance between clips ± 25 mm, traction speed 25mm min^{-1}, 5 DaN top head. To calculate water loss, scaffolds were deposited on filter paper to remove excess surface water and weighted with an analytical balance, then put in a vacuum oven at 30 °C for 3 h. The weight of the scaffold was regularly checked and registered until no further change occurred.

4.2.7 Cell culturing on scaffolds

Four types of scaffolds were tested: 3D printed and produced by casting, both with or without raffinose in starting solution composition. Fibroblasts coded as C84 were isolated and expanded, as previously described[19] starting from an underarm explant from a healthy, normolipaemic 45-years old female, and used at passage 14[20]. Cells were harvested from the flasks at the confluent state by incubation with trypsin solution for 2min at 37 °C. Cells were then re-suspended with 10% serum-supplemented Dulbecco's modified eagle medium, DMEM (Lonza, Verviers, Belgium), counted and plated at density of 105 cells/well onto the scaffolds, previously sterilized with ethanol 70% v/v for 18 h, washed three times with sterile phosphate buffer solution (PBS, from Lonza) and placed in 48 well-plates. 20 μl of cell suspension was initially seeded on scaffolds to facilitate adhesion for about 1 h; successively the growth medium was added in order to completely cover their surfaces. The medium was changed every three days and evaluations of cell viability and microscopy analyses were performed after 7, 14, 21 and 28 days.

4.2.8 Cell viability

Cell viability was evaluated by measuring the activity of the mitochondrial enzyme succinate dehydrogenase with the MTT test as previously performed in this type of studies[30]. The MTT assay is a colorimetric assay based on the metabolic activity of the mitochondrial enzyme succinate dehydrogenase that is able to reduce the MTT (3-(4,5-dimethylthiazol-2-yl)-2,5-diphenyl tetrazolium bromide) to insoluble formazan.

Briefly, at each indicated time point, scaffolds were transferred into a clear 48-wells plate and washed with PBS. 200 µl of MTT ($1 mg ml^{-1}$) in DMEM with 5% foetal calf serum, FCS (Sigma-Aldrich), were then added to each well and incubated for two hours at 37 °C under a continuous flow of 5% CO_2 in the dark. The resulting formazan crystals were dissolved in 200 µl DMSO under shaking for 10 min and absorbance was finally measured on an aliquot of 150 µl at wavelength of 550 nm. Absorbance obtained from the correspondent empty scaffolds was subtracted from each measurement. Cell number onto each scaffold was estimated by interpolation from a standard viability curve obtained with cells seeded at increasing density (from 1×10^3 to 50×10^3 cells/well).

4.2.9 Microscopic analysis

Empty and cell-seeded scaffolds were incubated with calcein-AM, a probe that becomes fluorescent and is retained inside cells in response to the activity of intracellular esterases. Such treatment was performed in growth medium at 37 °C and 5% CO_2 for 30 min. Excess calcein was then removed by washing twice with PBS and images were then captured using a Nikon Eclipse TE300 inverted fluorescence microscope. At least two images were analysed per scaffold at each time point, using empty scaffolds as controls.

4.2.10 Proliferation efficiency

Fibroblasts were seeded on scaffolds or on regular well-plates for 14 days and subsequently detached with trypsin. Cells were then re-plated at similar density (5×10^3 cells/well) in 48 well-plates. After 4 days of culturing, cell viability was evaluated on cell monolayers with the MTT assay as described above. Cells detached from a regular well-plate, re-seeded and cultured for the same period of time were taken as control.

4.2.11 Statistical analysis

Statistical analysis was performed with Graph Pad-Prism software version 5.0. Data obtained with the four scaffolds types were compared with one-way analysis of variance and the Dunnett's multiple comparison test. Significance was defined as $p<0.05$.

4.3 Results

4.3.1 Preparation and characterization of chitosan-based scaffolds

The first phase of the work was focused on the development of a 3D printing process suitable for obtaining chitosan hydrogels with precise and controlled structure. For this purpose, a LTM system was designed and implemented at laboratory scale.

A chitosan and a raffinose-containing chitosan solution were tested to produce scaffolds of different thickness, depending on the number of layers set (from 5 to 20), with a mesh structure having nominal opening of 400 μm.

To develop the 3D printing system a thorough study of the design space of the parameters within which the scaffold printing procedure could be satisfactory achieved. This implied the investigation of the chitosan solution concentration and viscosity, extrusion flow and pressure as well as the measurement of the temperature distribution in the work volume during the printing process. This resulted in the selection of a set of parameters that consistently allowed printing scaffolds with the most favourable structural, dimensional and mechanical (filament coherence and strength) characteristics.

The homogeneity and viscosity of the chitosan solution played a fundamental role on the printability and final structural quality of the 3D scaffold. Highly viscous solutions resulted in non-homogeneous material, whereas those with low viscosity in structures with high percentage of free water that induced a considerable swelling of the material during the freezing process. This effect caused not only a significant reduction of the mechanical strength of the material, but also a steric hindrance during the printing process which reduced the resolution. By performing different printing test, the suitable viscosity of the chitosan solution was found between 5000 and 45 000 cP (table 2).

Chitosan concentration% (w/v)	Viscosity[a] (cP)	Printability (3D structure retention)
5.0	5400 (±30)	√
5.5	8500 (±50)	√
6.0	9000 (±50)	√
6.5	15 000 (±200)	√
7.0	36 000 (±230)	√
7.5	45 000 (±310)	√

Table 2. Chitosan solution concentration, viscosity and 3D printability. [a] Spindle n.7; 13 ml solution; sampling after 10 s at 60 rpm.

The temperature is another critical point of the printing process affecting the quality of the scaffold. A specific effort was necessary to explore the design space of this parameter to optimize the printing result in terms of geometry tolerances and mechanical properties of the product. For this purpose, measures with a thermal camera equipped with a cryo-cooled detector were taken on different points of the forming scaffold (figure 2(a)). The temperature of the CH at the extrusion point was measured and proved to increase in a non-linear manner with the number of layers (from −18 °C for the first layer to −8 °C at layer n.26), namely, as the nozzle of the extruder displaced from the cooling surface. Differently, a linear trend as a function of the number of layers was observed for the tail point of the extruded filament (figure 2(b)). The extruded chitosan solution immediately froze once in contact with the surface of the underlying layer allowing the proper manufacture of the scaffold. At temperature values close to 0 °C, the solution did not solidify in a well-defined mesh structure giving rise to a solid matrix with poor mechanical characteristics and the printing process was no longer reliable.

Thus, the temperatures allowing to obtain a controlled CH structure ranged between −10 °C and −5 °C for the point of extrusion and, between −13 °C and −9 °C for the middle and the tail point of the filament, which represented quite a broad design space indicative of a robust process.

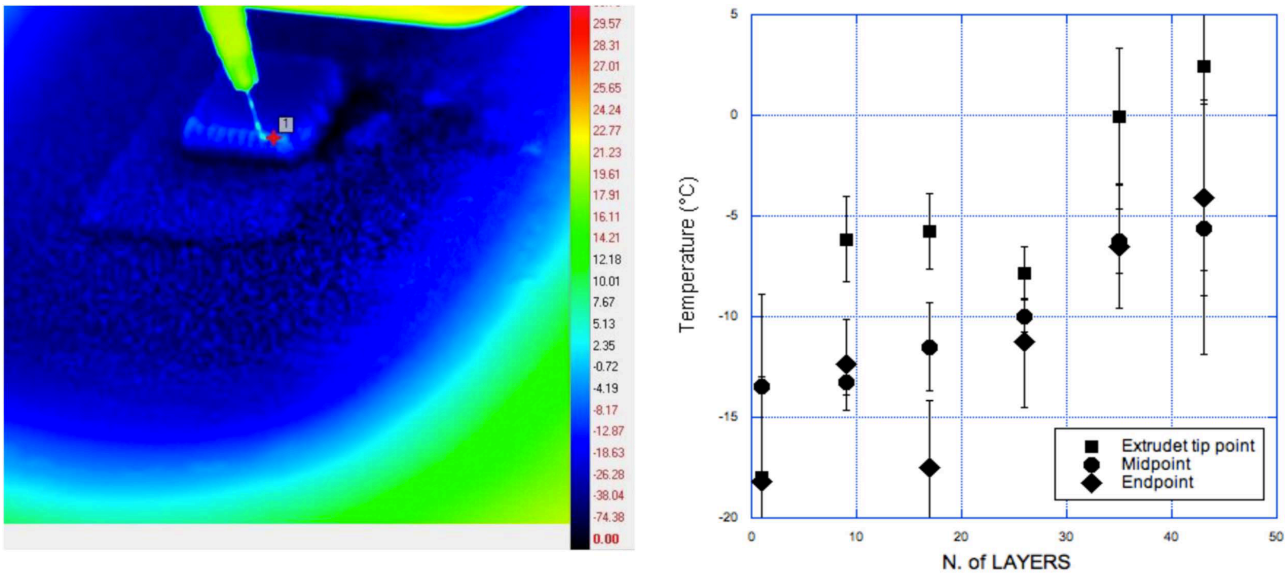

Figure 2. Acquisition of temperature values with a cryo-cooled sensor thermal camera FLIR SC7000 equipped with Altair software. The point temperature at the extruder tip, at the midpoint of the extruded filament and at the filament end point allowed the optimization of the 3D printer. The macro-structure and morphologies of the obtained chitosan scaffolds are shown in figures 3 and 4 for structure obtained staring from a raffinose-containing solution. ESEM analysis carried out on scaffolds in a fully hydrated state (figure 3(b)) allowed to verify the good agreement (mean change 8%; RSD 15%) between the experimental and theoretical structure designed with the CAD programme (figure 3(c)) in terms of filament and mesh size. Similar results were obtained for the scaffold prepared starting from the chitosan solution without raffinose.

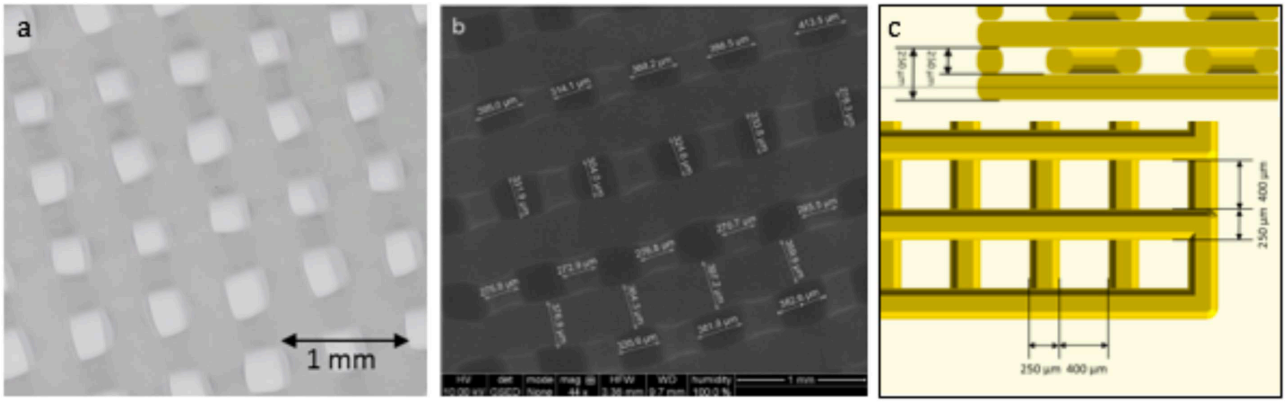

Figure 3. Appearance of a 3D printed chitosan scaffold (a); ESEM picture with mesh opening size (b); CAD design (c).

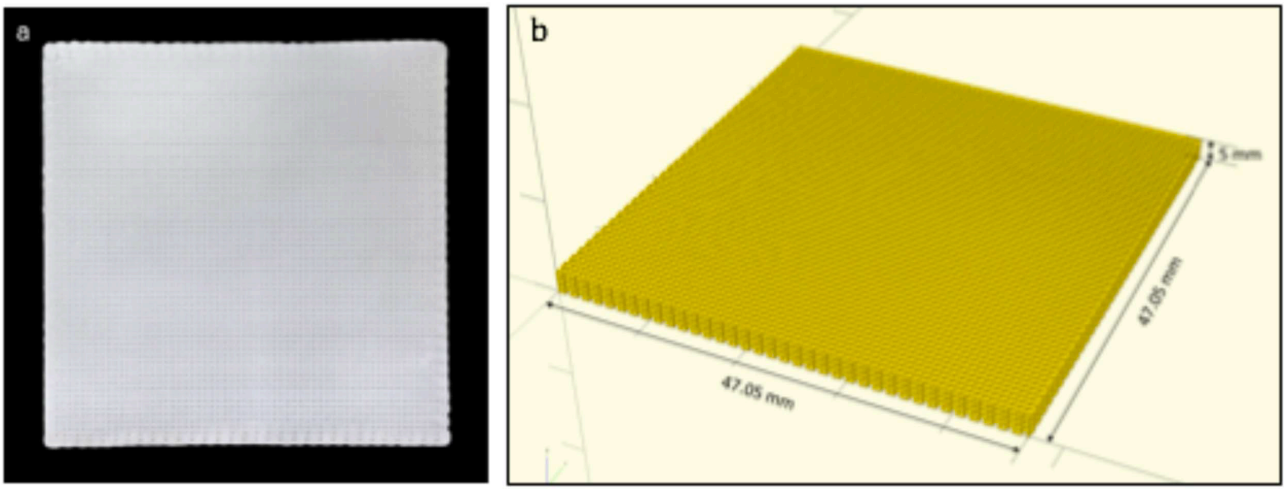

Figure 4. Macroscopic appearance of a 3D printed chitosan scaffold (a) and its CAD design (b).

The SEM images of the chitosan scaffold (figure 5(a)) and the chitosan scaffold obtained starting from a raffinose-containing solution (figure 5(b)) evidenced the presence of micropores on the surface of the filaments with a preferential orientation, that can be beneficial for cell adhesion and migration. This demonstrates that process automation does not interfere with the formation of the microstructure. The presence of raffinose in the starting solution did not influence filament size. As for morphology, SEM images of both chitosan scaffolds exhibited optimal surface homogeneity in terms of pore size and distribution with some differences between each other (Feret diameter: scaffold without raffinose 10 ± 20 μm; scaffold with raffinose 3.5 ± 3 μm). The cross-sectional micrographs revealed a regular interconnected and layered pore structure (Feret diameter: scaffold without raffinose 7 ± 14 μm; scaffold with raffinose 5 ± 4 μm) in the interior region (figure 5(c)).

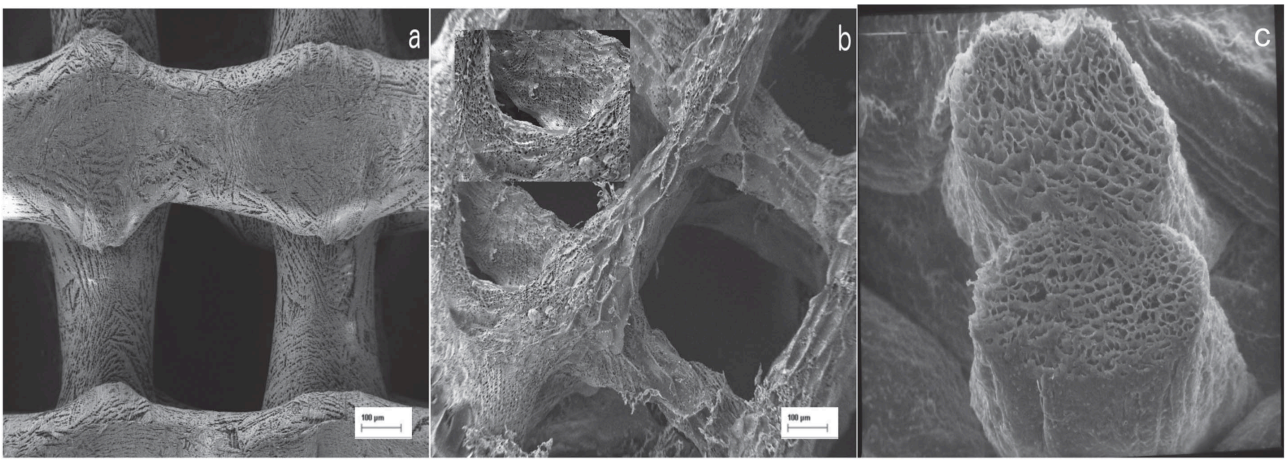

Figure 5. SEM images (200×magnification) of printed chitosan scaffolds (a), chitosan scaffolds prepared from a raffinose-containing solution (b) (inset 700×magnification) and (c) chitosan scaffolds prepared from a raffinose-containing solution cross-section.

The XRD patterns of the raw chitosan powder and the chitosan scaffolds with and without raffinose are shown in figure 6. The diffractograms of the three samples were very similar to each other, and no structural differences were observed between the scaffolds with and without raffinose.

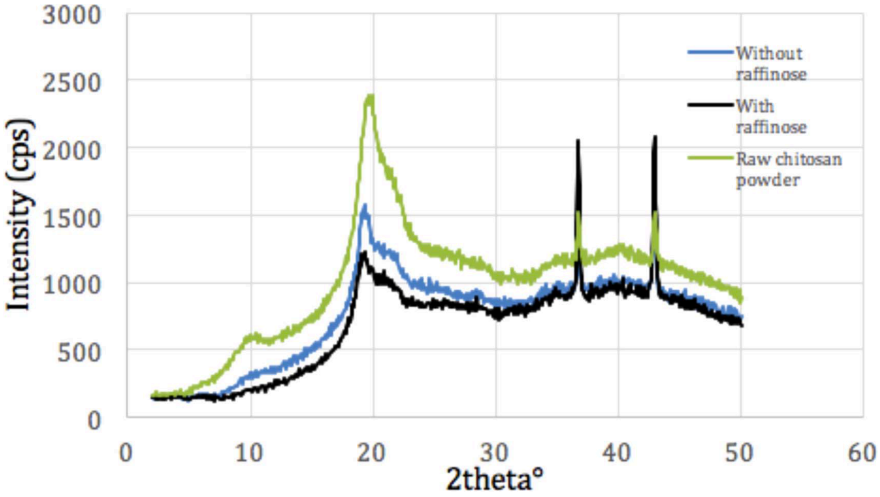

Figure 6. XRD of chitosan raw material (powder) and 3D printed scaffolds with and without raffinose.

In a further step the capabilities of the printed scaffold to retain water were tested. Dehydration in oven at 30 °C for 3 h untill constant weight afforded a homogeneous and significant loss of weight (from 67 ± 4% to 79 ± 3% for the scaffold prepared starting from chitosan solution and the raffinose-containing solution, respectively) irrespectively of the number of layers. This data confirms that the scaffold obtained from the chitosan solution containing also raffinose (initial water content 0.0487 g), were more hydrated that those obtained with the chitosan solution (initial water content 0.0332 g)[16].

4.3.2 Cell culture

As it has been well documented[12, 31-34], the scaffold regulates the cellular functions through its architecture. The percentage of porosity may, for example, affect the number of cells that can adhere to the scaffold. The diameter of the pores determines the surface area and the number of cells that can physically adhere to the surface influencing cellular infiltration into the pores, increasing cell colonization and growth within pores and along filaments. The 3D-printed scaffolds prepared from chitosan and chitosan enriched with raffinose solutions were thus

characterized for the interaction with cells and their capacity to allow cell growth. The results were compared with those obtained on chitosan scaffolds produced by pouring the solution on a cast according to Bettini *et al*[16]. For this purpose *in vitro* experiments with human fibroblasts were performed, as they represent a cell model frequently utilized for this kind of studies[23-24]. Figure 7 shows pictures of human fibroblasts proliferating on the tested scaffold 28 days after seeding. Cells seeded on scaffold obtained by casting were mainly round and isolated; this behavior was observed for both type of these scaffold, although a slightly higher number of cells seems proliferate onto the scaffold prepared from the raffinose-containing solution (figure 7(b)). As far as the 3D printed scaffold are concerned, those prepared from the pure chitosan (figure 7(c)) presented a more pronounced cell proliferations relative to the relevant scaffold prepared by casting (figure 7(a)); in this case the fibroblast were organized in clusters barely depicting the structure of the network of the scaffold. A significantly more pronounced cell proliferation was obtained on the 3D printed scaffold prepared from the raffinose-containing solution (figure 7(d)). Here the cell adhered and proliferated onto the filaments in a very regular manner practically covering the whole solid surface of the network.

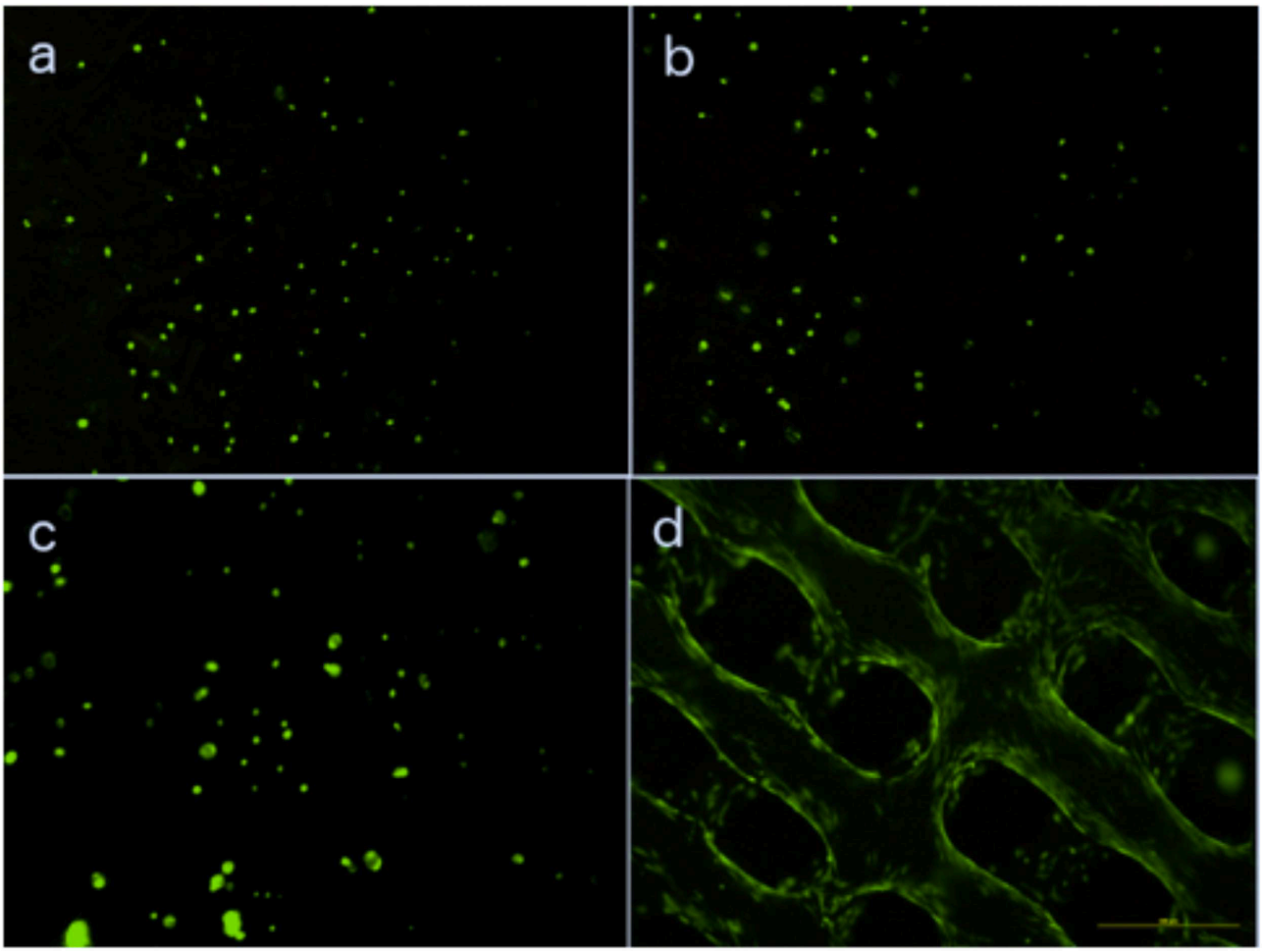

Figure 7. Image of calcein AM-stained fibroblasts grown for 28 days on chitosan scaffolds obtained from fluorescence microscopy at 40×magnification. Chitosan scaffolds (a) and chitosan scaffolds prepared from a raffinose-containing solution (b) prepared following the method proposed by Bettini *et al* (2008); 3Dprinted chitosan scaffold (c) and 3D printed scaffolds prepared from a raffinose containing solution (d).

These data were confirmed by SEM analysis as reported on figure 8.

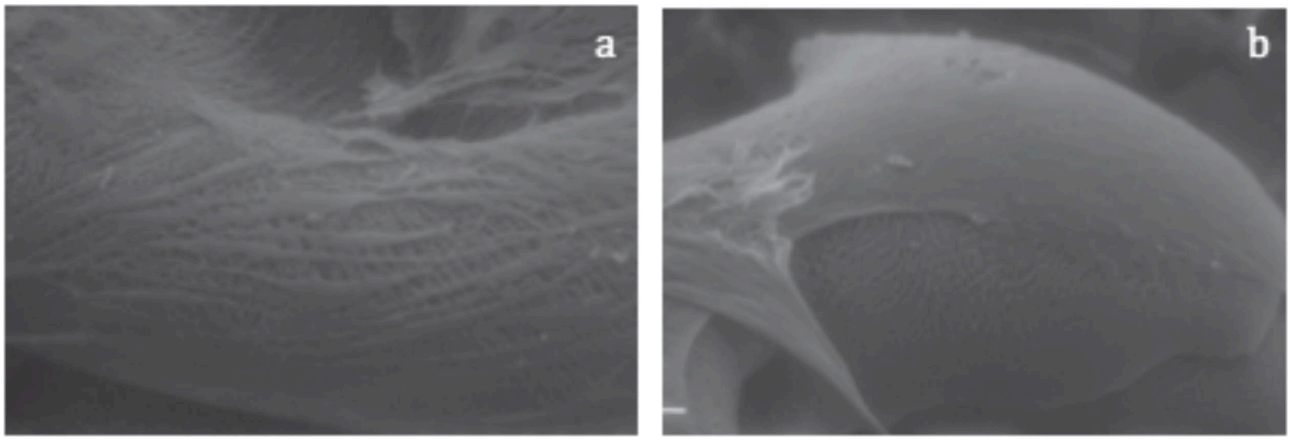

Figure 8. SEM images (500×magnification) of printed chitosan scaffolds (a), chitosan scaffolds prepared from a raffinose-containing solution (b) with fibroblasts grown for 28 days.

The proliferation curves over 28 days onto the four type of scaffold studied are presented in figure 9.

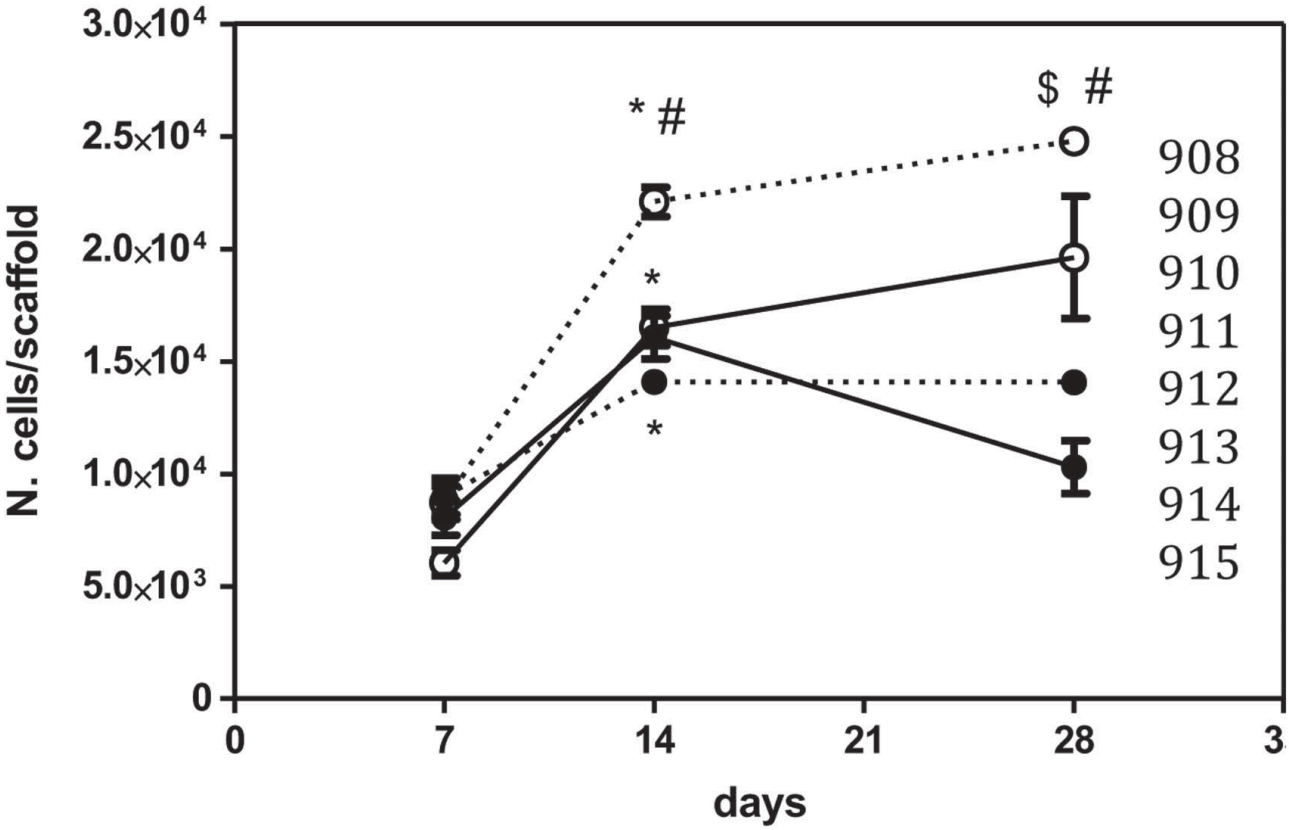

Figure 9. Proliferation curves, by MTT assay, of human fibroblasts grown on chitosan scaffolds (black circles) and chitosan scaffolds prepared from a raffinose-containing solution (empty circles). Scaffolds prepared according to Bettini *et al* (2008) solid line; 3D printed chitosan scaffold, dotted line. The bars represent the standard error of the mean (n=at least 3). Comparison among days of culture on the same scaffold: *p<0.01 versus day 7; p<0.05 versus day 14. Comparison among different scaffold at each time point: #p<0.05 versus all.

Cells seeded on both casted and 3D printed chitosan scaffolds displayed a significant and similar increase in number from day 7 to 14 (+2 fold and +1.5 fold for casted and 3D printed scaffolds, respectively; $p < 0.01$ versus day 7); at day 28, fibroblasts onto 3D printed scaffold prepared from pure chitosan solution did not further proliferate, as the cell number was similar to that of day 14. Similarly, cells onto chitosan casted scaffolds decreased to values similar to day 7 ($1.03 \pm 0.21 \times 10^4$ compared to $0.80 \pm 0.13 \times 10^4$; p = ns), indicating a lowering in their metabolic activity, likely ascribable to cell death. On the other hand, both scaffold types prepared starting from the raffinose-containing solution afforded a time-dependent cell growth from 7 to 28 days, which was more pronounced and less variable for 3D printed scaffolds. Comparing fibroblasts number at each time point of observation, it can be appreciated that, at 7 days of culture, cell number was roughly similar on all scaffolds, while after 14 days a significant higher number of cells was

detected on 3D printed chitosan scaffold prepared from the raffinose-containing solution (on average + 1.43 fold increase compared to others; $p < 0.01$); such difference was still appreciable after 28 days from plating (on average + 1.6 fold increase compared to others; $p<0.05$). These first results suggested that the combination of chitosan and raffinose in the solution used for the scaffold production, afforded the material that better interacted with cells, favouring a constant cell growth overtime. This confirms the findings of Bettini *et al*[16]; these authors identified the augmented hydrophilicity deriving from the viscosity modifying agent (i.e. raffinose) addition as the reason for the improvement in cell adhesion. These data are also in agreement with the more recent work of Romanova *et al*[35] who suggest that the electrostatic interaction of positively charged deacetylated amino groups of pure chitosan with the cell surface could induce specific reorganization of integrin β1 on the cell membrane that negatively affect both cell adhesion and proliferation: water, that is more retained on the surface of scaffolds prepared with raffinose-containing solution, acts as a shield on those charges, thus, favouring cell adhesion. The reticulated structure also offers a greater surface of contact with respect to scaffolds obtained by casting, which contributes to explain the significant improvement in cell growth observed on 3D printed scaffolds. Finally, the proliferation efficiency of fibroblasts allowed to grow onto scaffolds for 14 days and subsequently detached and re-seeded on regular well plates was measured. As control, an equal number of cells detached from a regular well plate and undergoing the same culture conditions was considered. As seen in figure 10, only cells detached from 3D printed chitosan scaffold prepared from the raffinose-containing solution reached a number of cells similar to that of the control ($3.85 \pm 0.04 \times 10^4$ compared to $4.12 \pm 0.5 \times 10^4$; p = ns), while on all other scaffolds cell number was significantly lower.

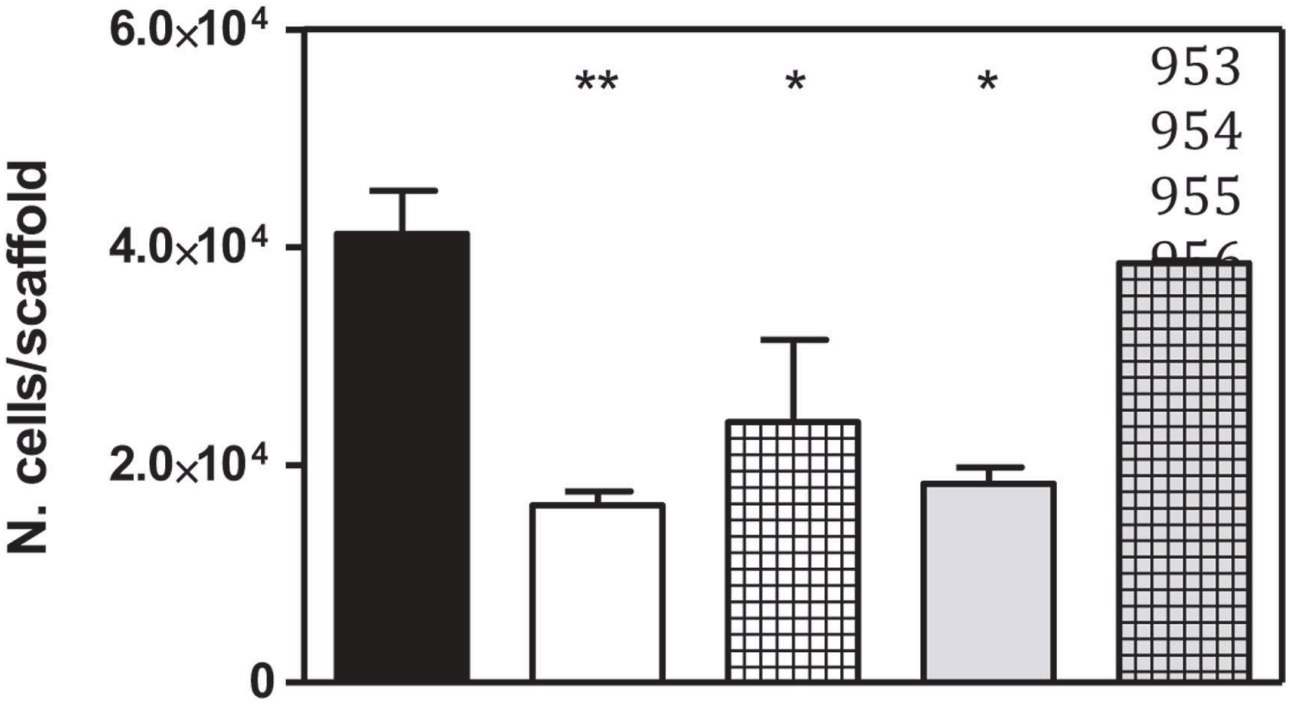

Figure 10. Proliferation (by MTT assay) efficiency of fibroblasts on the different scaffolds. Mean ± SEM (n=at least 3). Black bar, control; solid bars scaffolds prepared according to Bettini *et al* (2008), reticulated bars, 3D printed scaffold; white bars, chitosan scaffold, grey bars, chitosan scaffold prepared from a raffinose containing solution. *p<0.05; **p<0.01; p versus 3D chitosan-raffinose scaffold.

These data indicate that the 3D printed scaffold obtained from the raffinose-containing solution were a support for cell growth that afforded a cell functionality similar to that of a standard culture plate.

4.4 Conclusions

In this paper a new and low cost method for the automated production of chitosan scaffolds is described. The manufacture relies on a dedicated 3D printing system that directly transposes a freeze-gelation method allowing to overcome the drawbacks associated with the production by casting [17]. In other words, the proposed method affords highly reproducible structures both at the macro and micron level, however avoiding the expensive and time consuming lyophilisation step [28]. In fact the technique allows an elevated control of the geometry of the scaffold, that accurately corresponds to CAD design. Furthermore, the system for the 3D printing developed is simple, safe and cheap and avoids the use of organic solvent, the need of high process temperature or the difficulty in the removal of dust that is typical of analogous techniques of additive

manufacturing. The structural architecture of scaffold has a dramatic effect on cell adhesion and proliferation. A simple reticulated geometry with 400 μm opening affords a remarkable human fibroblasts adhesion and proliferation. The composition of the starting chitosan solution, in particular with the addition of raffinose, and the 3D structure conferred by 3D printing synergistically contribute to a significant improvement in cell adhesion and growth. This can have positive and consistent repercussion on tissue engineering application of these scaffolds in particular for soft tissue repair.

4.5 Acknowledgments

The authors wish to thank Professor Sebastiano Calandra from the Department of Biomedical, Metabolic and Neural Sciences, University of Modena and Reggio Emilia and Dr Claudio Rabacchi from the Department of Life Sciences, University of Modena and Reggio Emilia for providing the human fibroblasts.

4.6 Disclosures

Lisa Elviri, Ruben Foresti, Carlo Bergonzi, Annalisa Bianchera, Marco Silvestri and Ruggero Bettini are founders and shareholders of M3datek Srl, a company that develops 3D printed medical devices for wound healing. Nevertheless, they have not received any financial incentive for performing this study.

4.7 ORCID

Lisa Elviri https://orcid.org/0000-0002-5988- 618X
Ruben Foresti https://orcid.org/0000-0002- 1060-978X

4.8 References

[1] Langer R 2000 Biomaterials in drug delivery and tissue engineering: one laboratory's experience Acc. Chem.Res. 33 94–101
[2] Chan B P and Leong K W 2008 Scaffolding in tissue engineering: general approaches and tissue-specific considerations Eur. Spine J. 17 467–79

[3] Dhandayuthapani B, Yoshida Y, Maekawa T and Kumar D S 2011 Polymeric scaffolds in tissue engineering application: a review Int. J. Polym. Sci. 2011 290602
[4] O'Brien F J 2011 Biomaterials and scaffolds for tissue engineering Mater. Today 14 88–95
[5] Van Vlierberghe S, Dubruel P and Schacht E 2011 Biopolymer-based hydrogels as scaffolds for tissue engineering applications: a review Biomacromolecules 12 1387–408
[6] Kumar M N, Muzzarelli R A, Muzzarelli C, Sashiwa Hand Domb A J 2004 Chitosan chemistry and pharmaceutical perspectives Chem. Rev. 104 6017–84
[7] Bianchera A, Salomi E, Pezzanera M, Ruwet E, Bettini R and Elviri L 2014 Chitosan hydrogels for chondroitin sulphate controlled release: an analytical characterization J. Anal. Meth. Chem. 2014 808703
[8] Rodriguez-Vazquez M *et al* 2015 Chitosan and its potential use as a scaffold for tissue engineering in regenerative medicine BioMed Res. Int. 2015 821279
[9] Ji C, Annabi N, Khademhosseini A and Dehgani F 2011 Fabrication of porous chitosan scaffolds for soft tissue engineering using dense gas CO_2 Acta Biomater. 7 1653–64
[10] Dash M, Chiellini F, Ottenbrite R M and Chiellini E 2011 Chitosan—a versatile semi-synthetic polymer in biomedical applications Prog. Polym. Sci. 36 981–1014
[11] Elviri L, Bianchera A, Bergonzi Cand Bettini R 2016 Controlled local drug delivery strategies from chitosan hydrogels for wound healing Expert Opin. Drug Deliv. 14 897–908
[12] Ahmed S and Ikram S 2016 Chitosan based scaffolds and their applications in wound healing Achiev. Life Sci. 10 27–37
[13] Kim I *et al* 2008 Chitosan and its derivatives for tissue engineering applications Biotechnol. Adv. 26 1–21
[14] Dash M *et al* 2015 Enzymatically biomineralized chitosan scaffolds for tissue-engineering applications J. Tissue Eng. Reg. Med. 11 1500–13
[15] Zakhem E and Bitar K N 2015 Development of chitosan scaffolds with enhanced mechanical properties for intestinal tissue engineering applications J. Funct. Biomater. 6 999–1011
[16] Bettini R, Romani A A, Morganti M M and Borghetti A F 2008 Physicochemical and cell adhesion properties of chitosan films prepared from sugar and phosphate-containing solutions Eur. J. Pharm. Biopharm. 68 74–81
[17] Elviri L, Asadzadeh M, Cucinelli R, Bianchera A and Bettini R 2014 Macroporous chitosan hydrogels: effect of sulfur on the loading and release behaviour of amino-acid based compounds Carbohydrate Polym. 132 50–8
[18] O'Brien F J, Harley B A, Yannas IV and Gibson L J 2005 The effect of pore size on cell adhesion in collagen-GAG scaffolds Biomaterials 26 433–41

[19] Ang T H, Sultana F S, Hutmacher D W, Wong Y S, Fuh J Y H, Mo X M, Loh H T, Burdet E and Teoh S H 2002 Fabrication of 3D chitosan- hydroxyapatite scaffolds using a robotic dispensing system Mater. Sci. Eng. C20 35–42

[20] Geng L, Feng W, Hutmacher D W, Wong Y S, Han Tong Loh H Tand Fuh J Y H 2005 Direct writing of chitosan scaffolds using a robotic system Rapid Prototyping J. 11 90–7

[21] Almeida C R, Serra T, Oliveira M I, Planell J A, Barbosa M A and Navarro M 2014 Impact of 3D printed PLA and chitosan-based scaffolds on human monocyte/macrophage responses: unraveling the effect of 3D structures on inflammation Acta Biomater. 10 613–22

[22] Ye K *et al* 2014 Chondrogenesis of infrapatellar fat pad derived adipose stem cells in 3D printed chitosan scaffold PLoS One 9 e99410

[23] Hsu S, Lin C and T seng C 2010 Air plasma treated chitosan fibers-stacked scaffolds Biofabrication 4 0 15002

[24] Xiong Z, Yan Y, Wang S, Zhang R and Zhang C 2002 Fabrication of porous scaffolds for bone tissue engineering via low-temperature deposition Scr. Mater. 46 771–6

[25] Yen H, Hsu S, Tseng C, Huang J and Tsai C 2009 Fabrication of precision scaffolds using liquid-frozen deposition manufacturing for cartilage tissue engineering Tissue Eng. A 15 965–75

[26] Bang C, Kah P, Leong F, Chiun T, Kerm L and Chian S 2008 Rapid freeze prototyping technique in bio-plotters for tissue scaffold fabrication Rapid Prototyping J. 14 246–53

[27] Liu D, Liu Y, Jing C, Wang Q, Li Q and Hu Q 2012 The technological parameter optimization of rapid freeze prototyping for 3D tissue scaffold fabrication Przeglad Elektr.R. 88 9b/2012

[28] Lim T C, Chian K S and Leong K F 2010 Cryogenic prototyping of chitosan scaffolds with controlled micro and macro architecture and their effect on *in vivo* neo-vascularization and cellular infiltration J. Biomed. Mater. Res. A 94 1303–11

[29] de Ciurana J, Serenó L and Vallès È 2013 Selecting process parameters in RepRap additive manufacturing system for PLA scaffolds manufacture Proc. CIRP 5 152–7

[30] Favari E, Zanotti I, Zimetti F, Ronda N, Bernini F and Rotblath G H 2004 Probucol inhibits ABCA1-mediated cellular lipid efflux Arterioscler. Thromb. Vasc. Biol. 24 2345–50

[31] Thangavel P, Ramachandran B and MuthuvijayanV 2016 Fabrication of chitosan/gallic acid 3D microporous scaffold for tissue engineering applications J. Biomed. Mater. Res. B 104 750–60

[32] Lawrence B and Madihally S V 2008 Cell colonization in degradable 3D porous matrices Cell Adhes. Migr. 2 9–16

[33] Mohd Hilmi A B, Halim A S, Hassan A, Lim C K, Noorsal K and Zainol I 2013 *In vitro* characterization of a chitosan skin regenerating template as a scaffold for cells cultivation Springer Plus 2 79

[34] Bian S, He M, Sui J, Cai H, Sun Y, Liang J, Fan Y and Zhang X 2016 The self-crosslinking smart hyaluronic acid hydrogels as injectable three-dimensional scaffolds for cells culture Colloids Surf. B 1 392–402

[35] Romanova O A *et al* 2015 Chitosan as a modifying component for human skin tissue engineering Bull. Exp. Biol. Med. 159 557–66

5 Chapter 2: "Study of 3D-printed chitosan scaffold features after different post-printing gelation processes"

Carlo Bergonzi[1], Antonina Di Natale[1], Francesca Zimetti[1], Cinzia Marchi[1], Annalisa Bianchera[2], Franco Bernini[1], Marco Silvestri[3,4], Ruggero Bettini[1] & Lisa Elviri[1]

[1]Food and Drug Department, University of Parma, Parco Area delle Scienze 27/A, 43124, Parma, Italy.
[2]Interdepartmental Centre Biopharmanet-Tec, University of Parma, Parco Area delle Scienze 27/A, 43124, Parma, Italy.
[3]Department of Engineering and Architecture, University of Parma, Parco Area delle Scienze 181/A, 43124, Parma, Italy.
[4]Department of Innovative Technologies, University of Applied Sciences and Arts of Southern Switzerland (SUPSI), CH-6928, Manno, Switzerland.

Published on 23 January 2019, Scientific Reports Vol 9:362

IF 4.525

Personal contribution

CB performed the experimental work related to gelation studies, analytical characterization, 3D development and contributed to the preparation of the manuscript.

Abstract

3D biomaterial manufacturing strategies show an extraordinary driving force for the development of innovative therapies in the tissue engineering field. Here, the behaviour of 3D printed chitosan (CH)-based scaffolds was explored as a function of the post-printing gelation process. To this purpose, gel forming properties of different media were tested on their capability to retain 3D structure, water content, mechanical resistance and surface/internal porosity. Three different gelation media (i.e. KOH 1.5 M, Na_2CO_3 1.5 M, ammonia vapours) were selected and the 3D CH scaffolds were tested in terms of biocompatibility toward fibroblast as skin associated human cell line.

5.1 Introduction

A serious impairment in skin tissue or in other organs can be mainly due to traumatic events or by pathological alterations that lead to low availability of nutrients. The extra-cellular matrix (ECM) plays a primary role in the regeneration process, since its function consists in coordinating cell proliferation, spatial orientation, differentiation and maturation. ECM provides characteristics of storage and delivery of growth factors and cytokines and it supplies structural integrity and scaffolding features[1] as well as a substratum for molecules such as glycosaminoglycans, hyaluronic acid and collagens, naturally secreted by recruited cells during initial phases of regeneration.

One of the purposes of tissue engineering is that of developing synthetic or naturally-derived biological substitutes(scaffolds) capable to help injured tissues to heal properly.

Chitosan has been widely studied for decades targeting several potential application fields as, for instance, the biopharmaceutical one, that has been of increasing interest throughout years for its remarkable and promising biological and biomechanical properties, mainly explained by its unique polycationic character[2,3]. Furthermore, chitosan exploitability for medical purposes is sustained by the proofs of its biocompatibility and nontoxicity[4] as well as FDA approval[5]. Most of applications and research studies on chitosan focus on its hydrogel state. Chitosan is soluble in acid aqueous media at pH 5–6 at 24 °C; sol-gel transition can occur by known gelation techniques such as ionotropic, cross linker-mediated, polyelectrolyte complexed or self-assembled[6]. Each one provides different characteristics to the gel material formed; cross linking is often performed with glutaraldehyde, commonly used in protein complexation, that causes the formation of rigid irreversible textile, resistant to very-low pH's and to traction mechanical stress. Anyway, aldehydes frequently result toxic for mammals and in particular for human tissues and it's also reported they can have a pollutant environmental impact[7], for these reasons their use for *in vitro* or *in vivo* application is usually avoided.

Polyelectrolyte complexes formation can be exploited for the introduction in the system of other polymers such as gelatin, alginate or hydroxyapatite. Ionotropic gelation is based on the principle that negatively charged ions electrostatically interact with the cationic groups of the polymer chains, enabling the formation of hydrogen bonds, necessary to form a "rigid" but flexible network. The most commonly used substances include citrates, phosphates, sulphates, TPP or other alkaline media. The size and nature of negative ions, their concentration, their contact time with the polymer and pH can systematically influence its swelling behaviour in conjunction with its rehydration capacity. Mechanical properties as well in terms of elastic modulus (Young's

modulus) and toughness can be influenced by the type of gelation; in general, the higher is the number of interactions formed, the stiffer is the hydrogel obtained.

Physical cross-linked chitosan hydrogels can be prepared, avoiding the employment of toxic solvents or catalysts, by putting into contact chitosan solution with a basic agent, in liquid or gaseous state. Since bases that are used are water soluble and can be washed away by simply rinsing with water, resulting gels have a far least hazardous profile when in contact with the human body and as a consequence they are more suitable and easy to manage for pharmaceuticals. The reaction of gelation without the use of organic solvents is traditionally performed with the help of strong bases such as KOH or NaOH[8] this from one side guarantees a fast and complete gelation but, on the other side this limits the control and the fine tuning of swelling behaviour, porosity and of main mechanical properties such as strength and elasticity[3].

Another issue associated with the use of strong bases as gelation agents is the potential chemical degradation of any active compound included in the formulation: actually it is very desirable to use hydrogels also as storage or delivery systems of molecules[9], such as growth factors or drugs, and this urges the need for milder conditions of gelation, in order to avoid the chemical degradation of those substances during the manufacture process. In an interesting work by Xu and coworkers[10], the gelation of chitosan gels under mild conditions was reported by using NaCl or phosphate buffer saline as gelling solutions. Authors described a process that required a very long time of gelation and resulted in gels that dissolved completely within 24 or 48 hours. In our opinion this time is not adequate in view of a possible application of the product as medical device, so a first aim of this work was to propose and compare different mild gelation conditions in order to obtain hydrogels in a shorter time, namely not over 2 hours, having a longer persistence in biological buffers as well as being suitable for cell culture. Scaffold duration also depends on their mechanical properties, which can be modulated by the type of gelation agent used. Knaul *et al.*[11] described the production of chitosan fibres by wet spinning and reported the improvement of their mechanical properties by immersing them in a NaOH solution buffered with KH_2PO_4 at pH 5.4: they explained this behaviour by the formation of a cross-linked network generated by the bridging effect of phosphate ions between chitosan molecules.

On the basis of these data, in this work chitosan scaffolds were prepared from formulations already developed and studied for tissue engineering purposes[8] in different cell culture systems[12,13]. With the perspective of a serial production, the manufacture of chitosan scaffolds was automated with the help of a dedicated 3D printer for freeze-deposition. The polymer is extruded on a cooled surface, causing its instantaneous freezing before undergoing the controlled

ionotropic gelation process. This offers the chance to design *in silico* the microarchitecture of scaffolds as well as to guarantee high repeatability. This results in a significant improvement in control of pore size both at macroscopic and microscopic level, by creating *ad hoc* geometries to favour cell adhesion and growth with respect to traditional casting techniques[14]. Cryogenic 3D printing for hydrogel modelling based on different approaches (i.e. use of liquid nitrogen, cooled surfaces, dry ice) was successfully used for different inks (polyvinyl alcohol, Phytagel, etc.) demonstrating its ability to create scaffold mimicking soft tissues[15–17].

When chitosan is used, the structure deposed by 3D printing and frozen is then subjected to gelation which can significantly affect the final characteristic of the scaffold: for this reason, in this paper, different alkaline agents, salt concentration and times of gelation were investigated in order to identify which seem to be more promising for an accurate control of the aforementioned chemo-physical features, which respond better to *in vitro* biocompatibility tests.

5.2 Results

In this paper we addressed the role of the gelation medium on the physical, mechanical and biological characteristics of chitosan scaffolds prepared by 3D deposition and freezing.

The sol-gel transition of chitosan solutions is determined by the contact with basic media[18]. Having this in mind, and with the target of screening gelation conditions suitable to retain reproducible and accurate 3D printed structure, we took into consideration a gas, ammonia vapours, and a series of aqueous solutions prepared from a strong base such as KOH, at decreasing concentrations, or weak bases such as carbonate or phosphate salts alone or in association. The neutralization process was visualized by the observation of colour changes in scaffolds printed from a chitosan solution to which blue bromothymol was added as a pH indicator (see Methods) solutions (Figure S1, Supplementary Material). Solutions that required more than one minute to fix the structure were excluded, since this time was considered not compatible with the time of melting of 3D frozen scaffolds. In general, solutions with a pH inferior to 11 were not able to fix and maintain the structure of scaffolds (Table 1).

The addition of NaCl, ranging from 0.05 to 0.5 M, did not accelerate the time of gelation or rather resulted in a consistent increase in time of gelation with loss of 3D structure (data not shown): this is reasonably due to the acceleration of melting of the structure due to freezing-point depression.

Further experiments were performed on gelation media that guaranteed maintenance of 3D structure and neutralization: in particular a further selection was executed on the basis of

neutralization time. These tests lead to the selection of three gelation media, namely KOH 1.5 M, Na_2CO_3 1.5 M and ammonia gas, which showed a complete neutralization of solutions by 2 minutes. To confirm this observation, and to verify the real completeness of gelation, test on weight and water content were performed after different time of exposition to gelation media. Surface water was removed as described in Methods section, then W0 was recorded (Fig. 1). At first time point, the weight of scaffolds immersed in Na_2CO_3 was almost twice the weight of the other two types of scaffolds (Na_2CO_3 0.3412 g ± 0.0122 vs KOH 0.1742 g ± 0.0054 g; ammonia vapours 0.1688 g ± 0.0083 g). While the weight of scaffolds prepared with KOH or ammonia gas did not vary significantly at all time points (mean weight in KOH 0.1768 g ± 0.0131 g; in ammonia vapours 0.1720 g ± 0.0185 g; paired t test, $p < 0.05$), the weight of scaffolds prepared with Na_2CO_3 decreased with time and did not stabilize until 24 hours (Fig. 1). Even if for Na_2CO_3 group a longer time could give a more consistent gelation, the time of 1 h was chosen as optimal time for all conditions tested, also considering a possible translation of the method in a production environment.

Gelation Media	Concentration	pH	Maintenance of 3D structure	Neutralization time (sec)
KOH	1.5M 1M 0.5M 0.1M	14 14 13.70 13.13	✓ ✓ ✓ ×	30 50 60 300
Na_2CO_3	1.5M 1M	11.94 11.74	✓ ✓	40 50
Na_2CO_3+$NaHCO_3$	0.5M 0.5M	9.72	×	90
Na_2CO_3+$NaHCO_3$	0.01M 0.09M	9.22	×	n.d.*
Na_2CO_3+$NaHCO_3$	0.05M 0.05M	10.05	×	240
Na_2HPO_4 K_2HPO_4	0.1M 0.005M	8.08	×	n.d.*
Na_2HPO_4+Citric acid	0.1M 0.05M	7.6	×	n.d.*
Ammonia vapour from 28% aqueous solution		13	✓	18

Table 1. The effects of chitosan gelation media, solution concentration, pH on the maintenance of 3D printed structure (gelation process carried out at room temperature). *n.d. = not detectable.

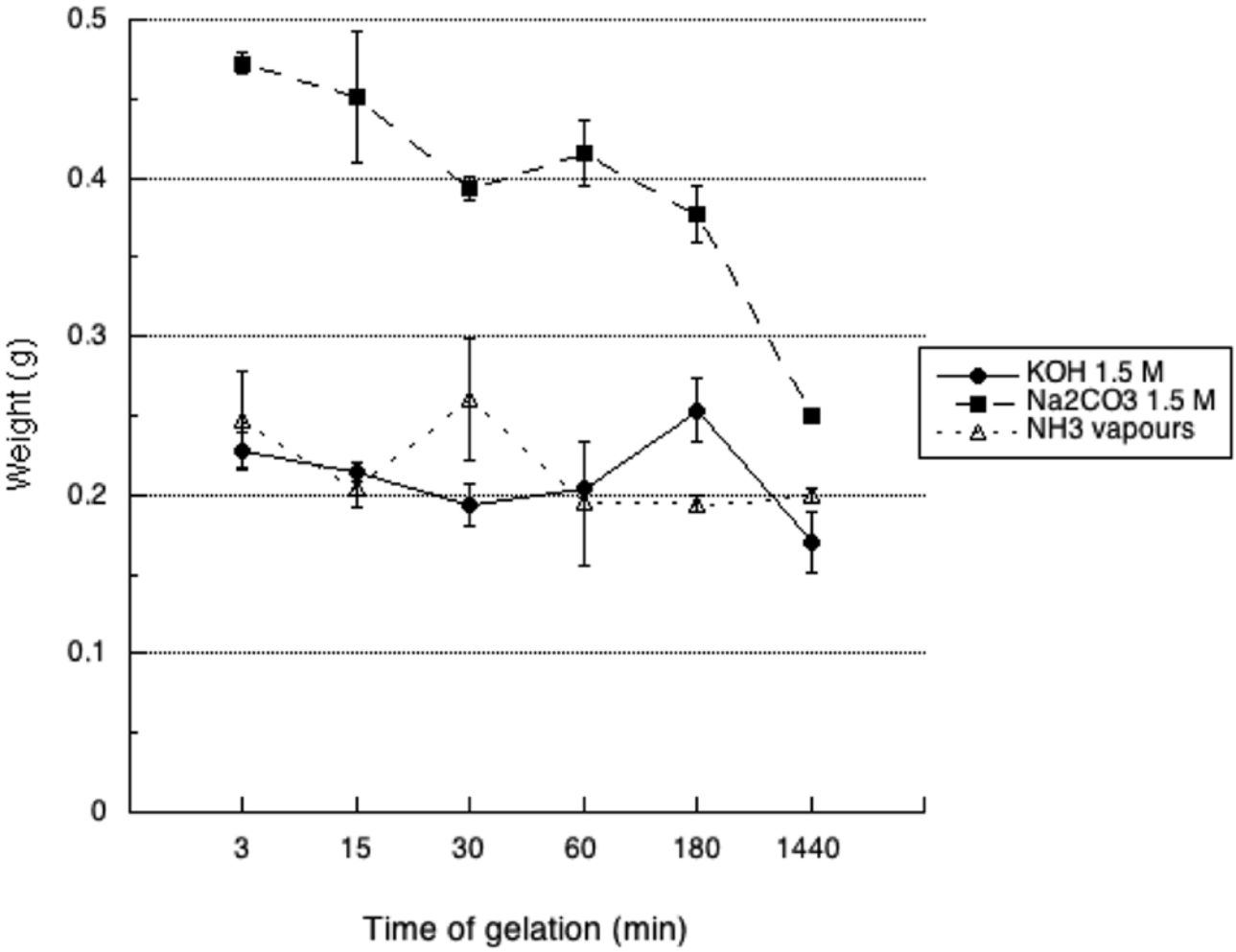

Figure 1. Measured wet weight (W0) of 3D printed CH-based scaffold gelled with KOH (1.5M), Na_2CO_3 (1.5M), NH_3(g) (from 28% ammonia solution) as a function of time.

Resolution of the structure is dependent on the 3D printing procedure and was reported on a previous work published by Elviri *et al.*[14]. Starting from the CAD design, the theoretical pore size was 200 μm while nominal filament diameter was 250 μm. After 1 h gelation, at the maximum swollen state, the filament size was measured (n = 9) depending on gelation media. Actually, for KOH mean filament size was 273 ± 28 μm, for Na_2CO_3 mean filament size was 293 ± 28 μm, whereas for NH_3 vapours mean filament size was 259 ± 29 μm.

After one hour of gelation and 20 seconds of water removal by vacuum on filter paper the weight of scaffolds was significantly different depending on the method of gelation. In particular, gelation in Na_2CO_3 gave the highest weight, followed by KOH then ammonia vapours. After lyophilisation all types of scaffolds reached a constant weight ($p < 0.05$) after one hour of drying but the rate of water loss was different on the basis of the gelation media (Fig. 2). Scaffolds prepared in KOH showed the steeper rate of drying, followed by those prepared in Na_2CO_3.

Scaffolds prepared in ammonia vapours showed an interesting two-phases loss of water reaching a plateau after 10′ of drying, when the amount of left water was about 55%, followed by a second dehydration phase that lead to complete drying.

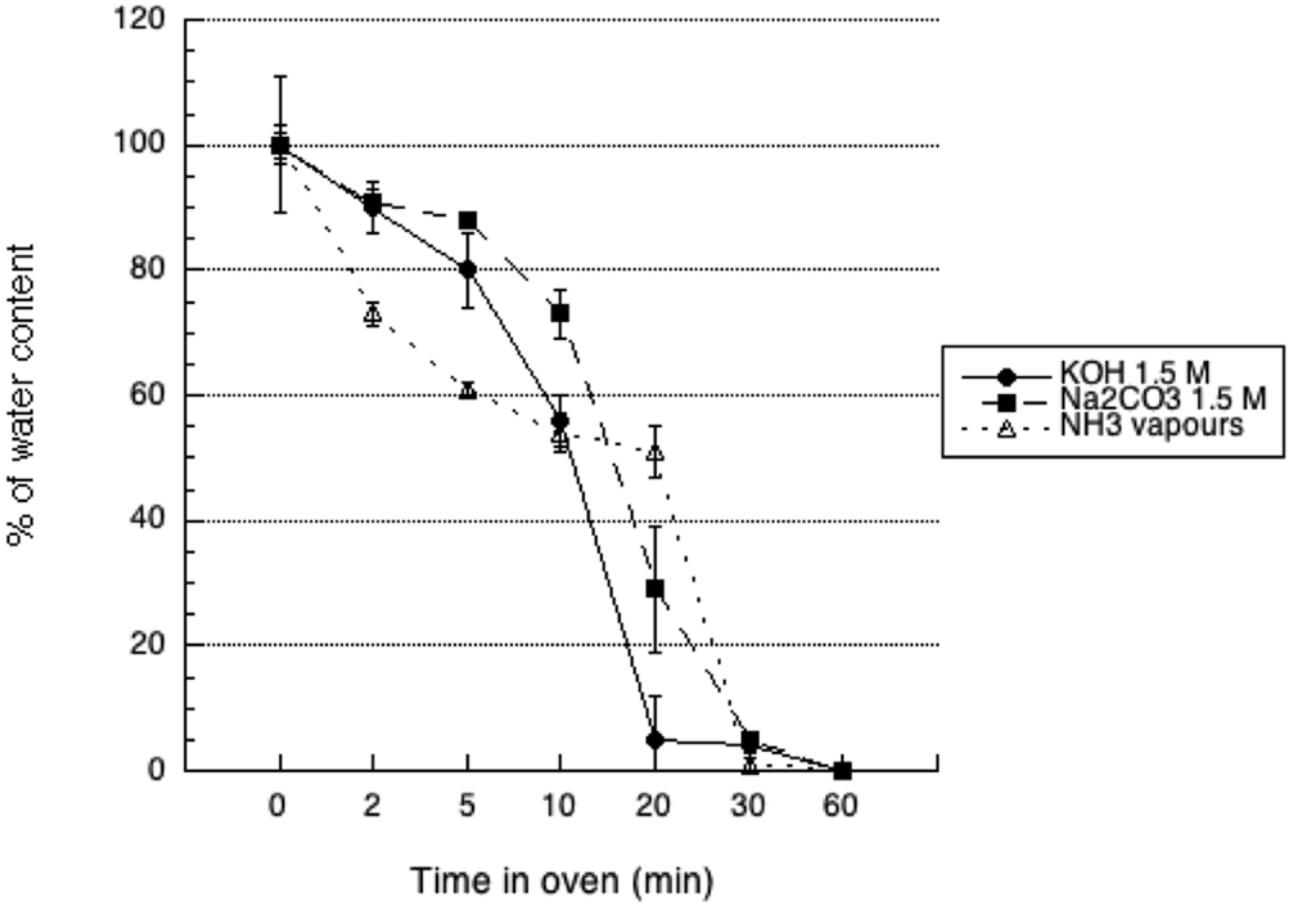

Figure 2. De-hydration profile of 3D CH-based scaffolds gelled with KOH (1.5M), Na_2CO_3 (1.5M), NH_3(g) (from 28% ammonia solution) as a function of time. Scaffolds were exposed to vacuum oven at 40 °C until complete loss of water.

The complete dehydration of scaffolds resulted in their deformation: the original morphology was lost and was not recovered even after immersion in water for more than 24 hours. Very similar volumetric decrease was observed (n = 9) for the three gelation media: 45.7% for KOH, 43.0% for Na_2CO_3 and 41.7% for NH_3 (RSD < 2%).

In order to test to which extent the drying could be pushed to get the complete recovery of original shape and water content, on the basis of the drying experiment described above, we selectively dried scaffolds to 80%, 60%, 45% and 30% of their starting weight. Those scaffolds were immersed in ultrapure water and their weight was checked at regular intervals up to 24 hours (Fig. 3). Scaffolds exposed to KOH failed in recovering their initial weight, whatever the starting dehydration state. This was probably due to the fact that in KOH gelation occurred suddenly,

leading to a rapid fixation of chitosan hydrogel in the shape given by 3D printing, preventing the set up of new interactions between chitosan chains and water. The ability to recover water was more and more hampered as the drying was pushed further: actually, while scaffolds dried at 80 or 60% of starting weight returned to the 95% of their starting weight after 24 hours, scaffolds dried at 45 or 30% of starting weight did not go beyond the 70% of weight recovery in 24 hours. On the other hand, scaffolds prepared in Na_2CO_3 recovered their starting weight in about 3 hours, provided that hydration state was not below 60%. On the contrary, scaffolds dehydrated to 45 or 30% did not go beyond the 68% of weight recovery after 24 hours of immersion. Also scaffolds prepared in ammonia vapours regained their starting weight in 3 hours if the starting hydration state was at 80 or 60%. Water recovery was at 93% for scaffolds starting from a 45% water content, while scaffolds dehydrated to 30% only reached a 55% of weight recovery.

DSC analysis showed that scaffold gelled in Na_2CO_3 showed the highest free water value of 96.78 ± 2.47%, followed by those gelled by exposure to NH_3 vapours reaching a value of 94.44 ± 2.42% whereas gelation by immersion in the KOH solution exhibited the lowest value of 88.57 ± 4.23%. Interestingly, it seems there is a correlation between the pH of the gelling conditions (Na_2CO_3 pH 12; NH_3 vapours pH 13; KOH pH 14) and the amounts of bulk water in the samples, suggesting that the stiffer is the network at the molecular level, due to a stronger ionotropic gelation, the more water is bound to the polymer.

Young's modulus was calculated from the linear portion of the stress-strain curve (Figure S2 Supplementary Material) and resulted respectively for KOH 105 kPa ± 18 kPa (% strain at rupture 34,6% ± 2,4%), for Na_2CO_3 94 kPa ± 19 kPa (% strain at rupture 43,9% ± 9,2%) and for ammonia vapours 128 kPa ± 21 kPa (% strain at rupture 52,3% ± 5,3%). For all the scaffolds, the stress-strain curve presented only a linear shape, with the elongation directly proportional to the applied stress. The scaffolds behaved elastically when subjected to stresses, and the application of an additional stress did not lead to further alterations of the hydrogel's mechanical properties (Figure S2 Supplementary Material).

No statistical difference existed between hydrogels prepared in KOH or Na_2CO_3, while scaffolds prepared in ammonia vapours showed a significantly higher elastic modulus with respect to both other media.

In an effort to explain the reason of such a different stiffness, we analysed internal morphology of scaffolds by SEM. Pictures of surfaces and transversal sections of hydrogel filaments were taken and pore size and distribution were measured, the appearance of surface is quite different on the basis of gelation media (Figure S3, Supplementary Material). Hydrogels prepared in KOH show a rough surface with pores having a mean size distribution ranging from 2 to 9 μm. Scaffolds

prepared in Na_2CO_3 have a mean pore size diameter distribution of 1–7 μm. Hydrogels prepared in ammonia vapours show pores that span in a wider range, from 0.5 to 13 μm. No correspondence is observed with internal porosity, that is between 3 and 14 μm for scaffolds prepared in KOH, 5 and 39 μm for scaffolds prepared in Na_2CO_3 and between 2 and 42 for those prepared in ammonia vapours (Fig. 4). Differences in surface appearance reflect the differences in the mechanism of gelation and could explain as well the differences in the ability to reuptake water after dehydration.

The ATR FT-IR spectrum of raw chitosan was compared with spectra of hydrogels prepared with the selected gelation media (Figure S4, Supplementary Materials). The transmittance spectrum of hydrogels prepared with KOH showed a broad widening of the O-H stretching band[19], masking the stretching vibration of N-H. In hydrogels prepared with Na_2CO_3 or ammonia vapours, the band was slightly shifted to higher wavenumbers, and the stretching vibrations of O-H or N-H were undistinguishable as well.

In KOH hydrogels only, the stretching vibration of the C-H attributed to the pyranose ring was smoothened with respect to raw material (2877 cm^{-1}), and slightly moved to higher wavenumbers (2886 cm^{-1}), while no differences were observed between raw materials and hydrogels prepared with Na_2CO_3 or ammonia vapours (2879 cm^{-1} and 2874 cm^{-1}). On the other hand, the bending of the C=O bond was slightly shifted to higher wavenumbers in hydrogels prepared in Na_2CO_3 or ammonia vapours (1655 cm^{-1} and 1653 cm^{-1}) with respect to raw material (1638 cm^{-1}), while the peak was maintained at 1636 cm^{-1} in hydrogels prepared with KOH.

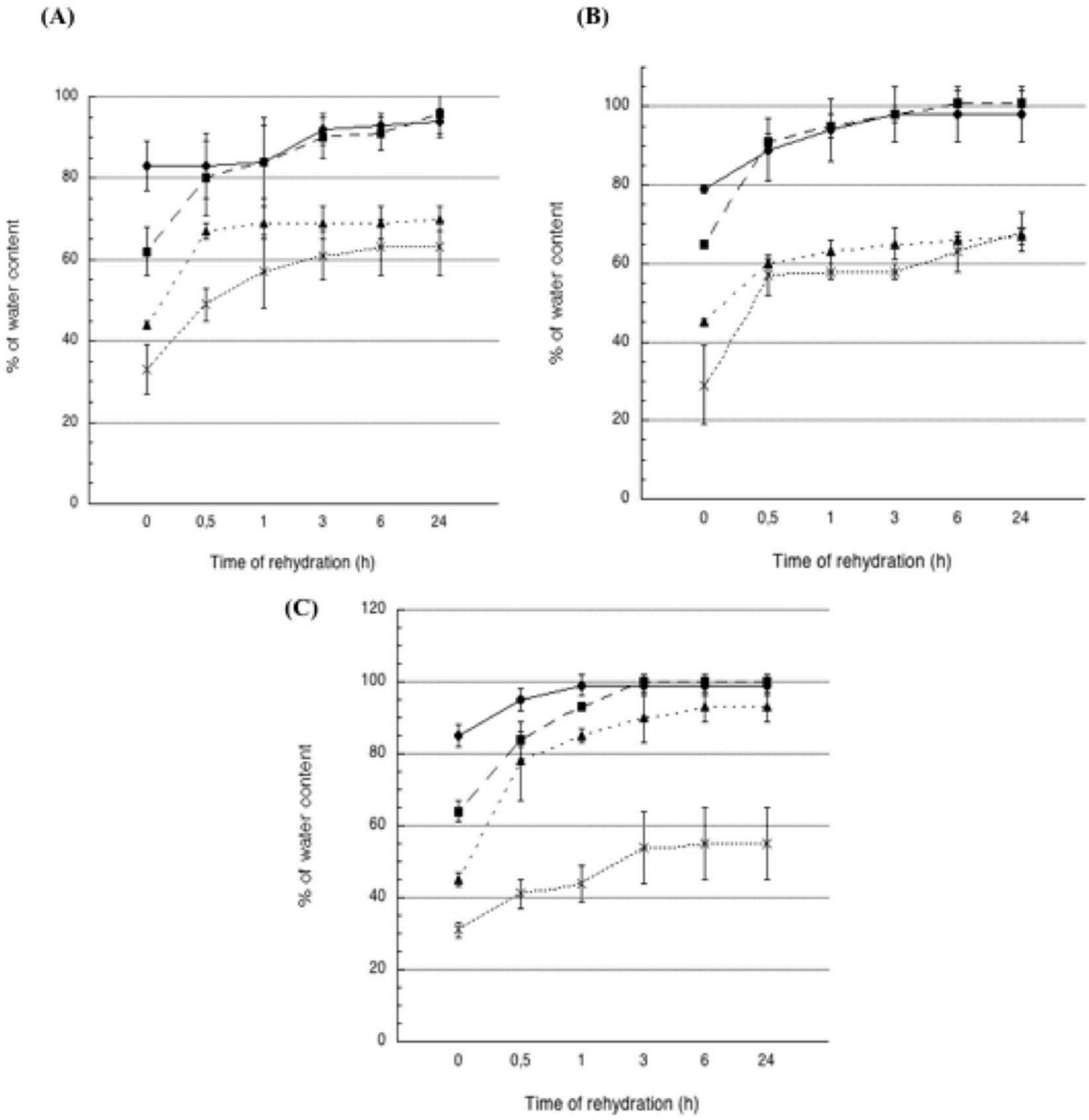

Figure 3. Re-hydration profile of 3D CH-based scaffolds previously de-hydrated at different percentages and left in water as a function of time. Scaffolds were gelled in (A) KOH (1.5M), (B) Na_2CO_3 (1.5M), (C) NH_3(g) (from 28% ammonia solution) and exposed to vacuum oven at 40 °C at different times to obtain the desired lost percentage of water, namely 30% (cross), 45% (solid triangle), 60% (solid square) or 85% (solid circle) of initial water weight.

In hydrogels prepared with KOH, the peak at 1570 cm^{-1} observed in raw material (probably attributable to N-H bending vibration in amide group[19]) was smoothened and almost disappeared, while it was preserved with almost the same intensity in the two other types of hydrogels prepared with Na_2CO_3 and ammonia vapours. In the fingerprint region, the symmetrical bending of C-H at about 1374 cm^{-1} was not affected by gelation. The region between 1160 cm^{-1} and 1025 cm^{-1}, derived from different stretching vibrations of C-O bond is the more affected one: with respect to

raw material, the transmittance in the KOH sample is increased, with a shift of the peak at 1074 cm^{-1} to 1080 cm^{-1} and a shift of the signal at 1026 cm^{-1} to 1035 cm^{-1} due to the stretching of C-O. In the Na_2CO_3 and ammonia vapour hydrogels, the transmittance of the 1074 cm^{-1} band increased with respect to raw material.

These data support the involvement of evidenced groups in the formation of hydrogen bonds that sustain the structure of hydrogels. The differences observed among the scaffolds could be attributed to the different distribution of water molecules occurring during the polysaccharide cross-linking process. In particular, scaffolds prepared with ammonia or Na_2CO_3 have very similar content of free water and presented almost overlapped ATIR spectra with respect to scaffolds prepared in KOH.

Human fibroblasts were cultivated on chitosan scaffolds prepared with KOH, Na_2CO_3 or ammonia vapours and their growth efficiency was compared. Living cells were checked during the whole experiment by periodically adding calcein AM to cultures and by observing them under fluorescent microscope. Images after 4 days confirmed that all scaffolds supported cell growth: cells that at the moment of seeding fell inside macropores created by scaffold design (see arrows in Fig. 5a) grew in clusters, while cells that initially adhered to plate migrated on the scaffold, covering it almost completely in 14 days. In Fig. 5f it is possible to appreciate that the direction of cell migration was driven by the orientation of filaments composing the grid of the hydrogel.

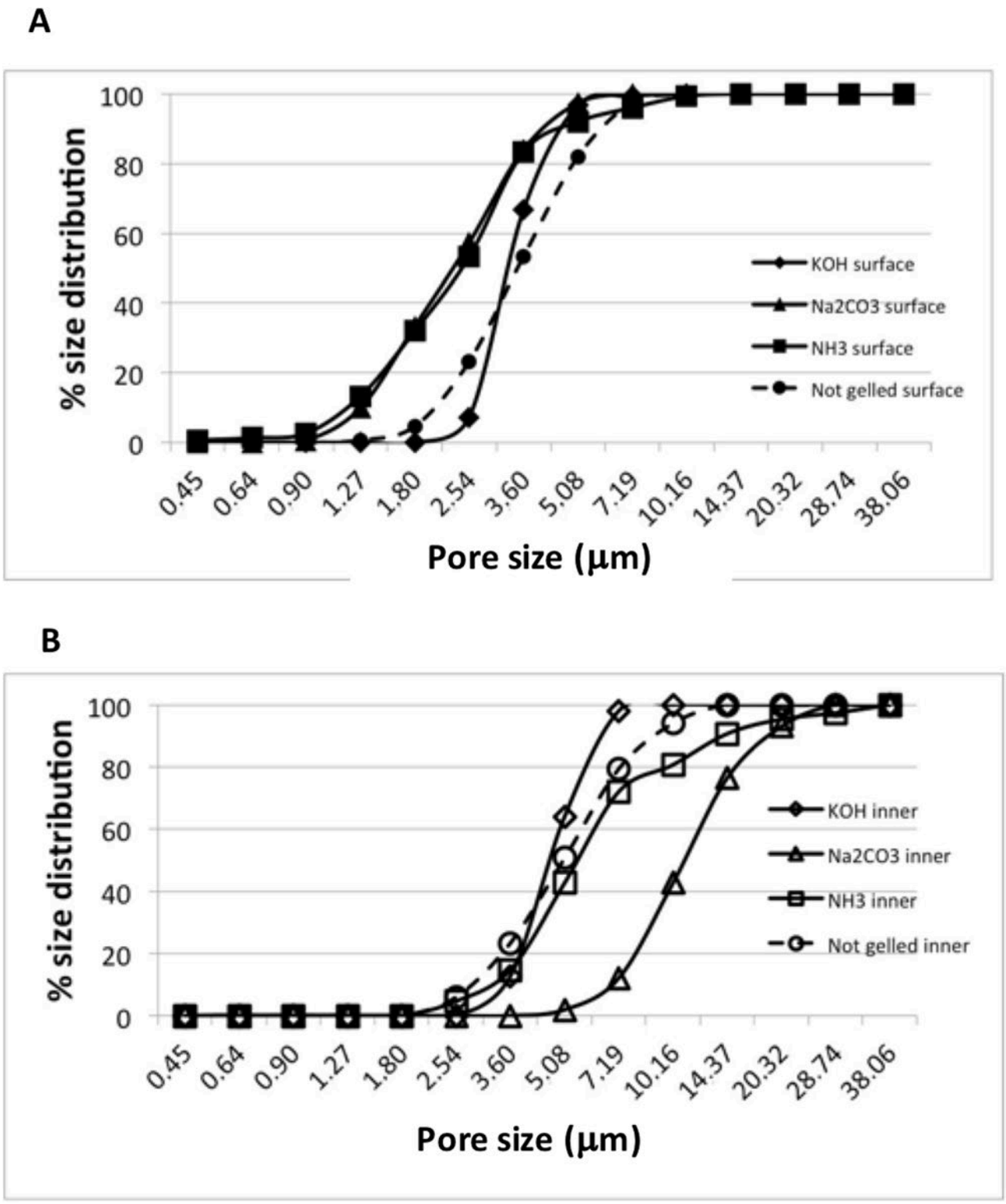

Figure 4. (A) Surface and (B) inner pore size distribution percentage measured by SEM of 3D printed CH-based scaffolds gelled with KOH (1.5M), Na_2CO_3 (1.5M), NH_3(g) (from 28% ammonia solution).

Cell proliferation onto scaffolds was monitored on the basis of the amount of DNA isolated at each time point over 21 days. Data in Table 2 and Fig. 6 show the growth trend of cells on

scaffolds. To assess cell viability an MTT assay was performed at all time point, confirming the growth trend observed by DNA extraction (Figure S5 supplementary Material). At 14 days of culture cell proliferation on scaffolds prepared on Na_2CO_3 is significantly less pronounced with respect to other types of scaffolds. After 21 days of culture, cells had almost completely covered scaffold surface: scaffolds prepared with ammonia vapours show a non-significant delay in cell colonization with respect to scaffolds prepared in KOH 1.5 M. On the whole, all kinds of scaffolds adequately support cell growth, favouring cell migration and proliferation.

5.3 Discussion

The utilization of chitosan as polysaccharide for manufacturing biomedical scaffolds is highly investigated. When using 3D printing technology the precise and accurate control of designed geometries is pivotal to fabricate the desired scaffolds and correlate the 3D macro- and micro-structure to cell responses. For these reasons, CH post processing gelation should be carefully investigated to understand its 3D behaviour. Obviously, the capability to retain the frozen 3D structure is directly correlated to the time of gelation, and different parameters are involved in this two-step network-structuring process: the pH, physical state, activity and the interaction capability of the basic medium. Independently from the resulting pH, not all solutions were adequate to keep the structure conferred by the 3D printing of the scaffolds (Table 1): in particular, solutions containing sodium bicarbonate arouse bubbling ($CO_2(g)$), which led to the deformation or collapse of the 3D structure (Figure S1A Supplementary Material).

KOH 1.5 M (pH 14) and 1 M (pH 14) solutions resulted in the same pH, but from our data, chitosan cross-linking resulted more efficient when the 1.5 M solution was used. This could be attributed to the higher concentration of OH^-, which are driven by diffusion gradient to penetrate into the scaffold in less time (Table 1) leading to a more rapid CH neutralization (~30 sec vs 50 sec): this leads to a faster formation of a stable network, better retaining the structure conferred by 3D deposition. Excellent homogeneous porous distribution both on the surface and inside the filaments was observed (Figure S3 Supplementary Material).

The use of sodium carbonate 1.5 M (pH 11.94) allowed for the rapid gelation (~40 sec) and retention of the 3D structure. As retention of the frozen structure is a compromise between a local exothermic acid-base reaction and the neutralization reaction, in this case a partial collapse of the internal CH network was observed (Figure S3B Supplementary Material) due to the slower formation and diffusion of OH^- ions through the filaments. As a consequence, a reduced homogeneity of the inner porosity of the filament was observed. The highest diffusive properties

of the ammonia gaseous medium (pH 13), together with the interaction properties of ammonia with chitosan have driven an extremely fast neutralization reaction (<20 sec). Excellent retention of the 3D structure and good homogeneity of the surface and inner porosity of the scaffold were observed.

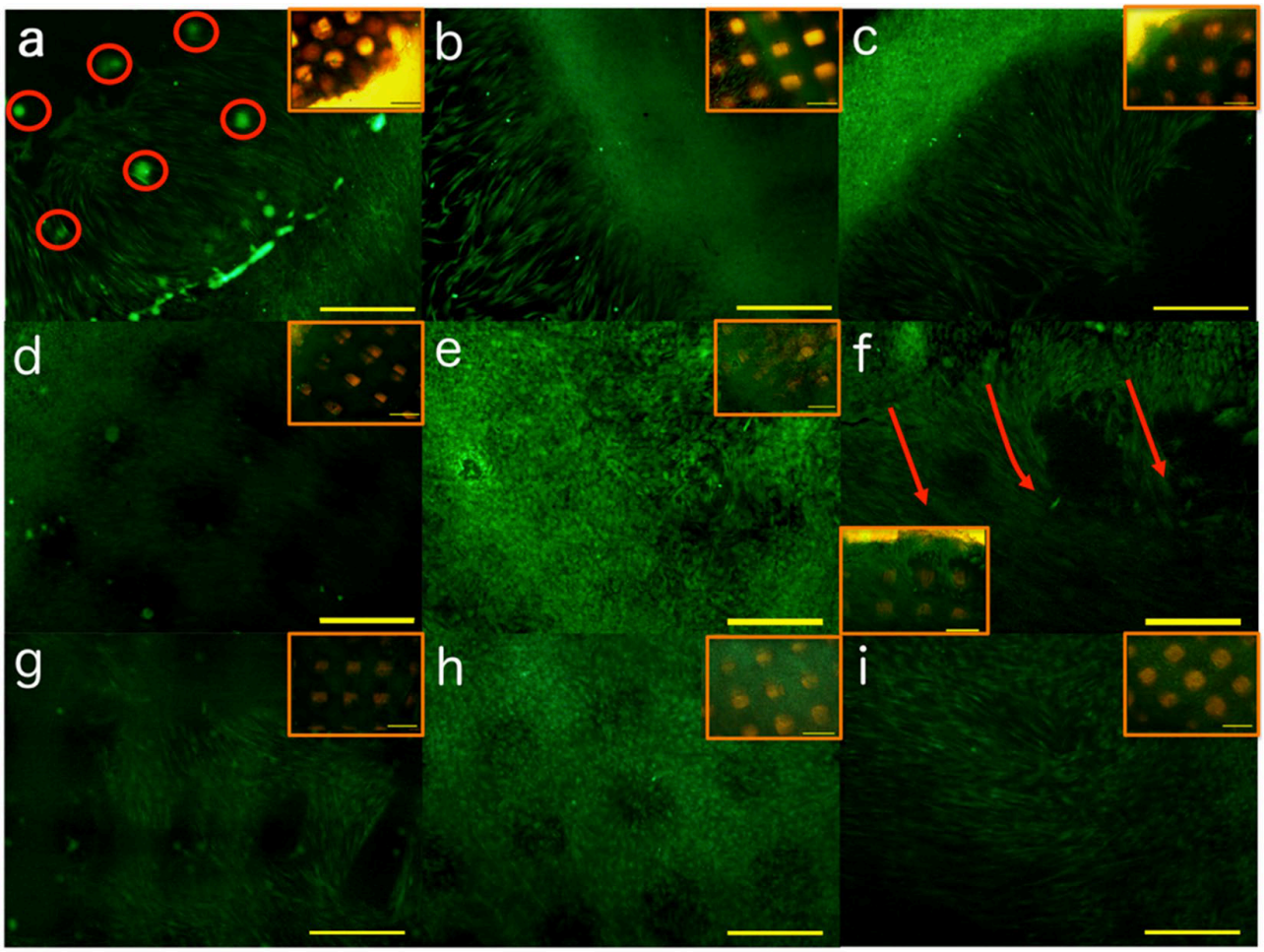

Figure 5. Fluorescence microscopy images of calcein AM-stained fibroblasts grown on hydrogels prepared in KOH 1.5M (a,d,g), Na_2CO_3 1.5M (b,e,h) or NH_3(g) (from 28% ammonia solution) (c,f,i). All images are at magnification 4 X O.M.; scale bars 500 µm). (a,b,c) cells grown for 4 days migrating from the plate onto chitosan scaffolds. Red circles indicate cells grown in clusters into macropores; (d,e,f) cells grown for 14 days. Red arrows indicate the direction of cell migration on the scaffold. (g,h,i) cells grown for 21 days. In this day differences in cell growth on different scaffolds are less appreciable from microscopic observation. Images in inserts show the picture of the same field taken by contrast phase microscopy, showing the position of scaffolds with the grid structure conferred by 3D-printing.

Gelation media	7 days	14 days	21 days
	Mean (µg) ± std.dev. (µg) per scaffold	Mean (µg) ± std.dev. (µg) per scaffold	Mean (µg) ± std.dev. (µg) per scaffold
KOH 1.5 M	0,51 ± 0,06	3,18 ± 0,12	4,40 ± 0,23
Na_2CO_3 1.5 M	0,77 ± 1,08	1,07 ± 0,21	3,46 ± 1,47
Ammonia vapours	0,64 ± 0,90	3,23 ± 0,70	3,16 ± 0,33

Table 2. Amount of DNA extracted per scaffold 7, 14 or 21 days after seeding on scaffolds prepared by different gelation media (mean ± standard deviation).

On the whole, the type of gelation influences water content as well as the ability to regain water after dehydration. Experiments dehydration and rehydration were performed with the purpose of evaluating the chance to propose a fully dehydrated scaffold for clinical application. As hypothesized, used gelation techniques gave rise to distinct stable polymeric networks, slightly affecting material affinity toward water in addition to their total content. Gelation reaction in Na_2CO_3 and ammonia vapours is milder, probably allowing a local re-adaptation of chitosan chains as long as the gelation medium penetrates into the scaffold, resulting in a higher affinity for water, as witnessed by the results obtained by DSC about the amount of free water (Na_2CO_3 > ammonia vapour > KOH). This is also consistent with the differences in structure evidenced in SEM images and with higher mechanical resistance recorded on scaffold produced with KOH as a gelation medium. This can be further supported by the fact that the overall contraction of the structure after dehydration was greater for scaffolds prepared with KOH, thus probably offering a smaller surface area for water to get into the scaffold in the rehydration phase.

Since the complete dehydration of scaffolds leads to an alteration of their characteristics, a partial dehydration (20–40% dehydratation) is considered anyway preferable to the fully hydrated scaffold in view of a clinical application: actually a partially dehydrated scaffold could act more efficiently when applied on a wound in absorbing exudates or fluids, positively contributing to stop bleeding.

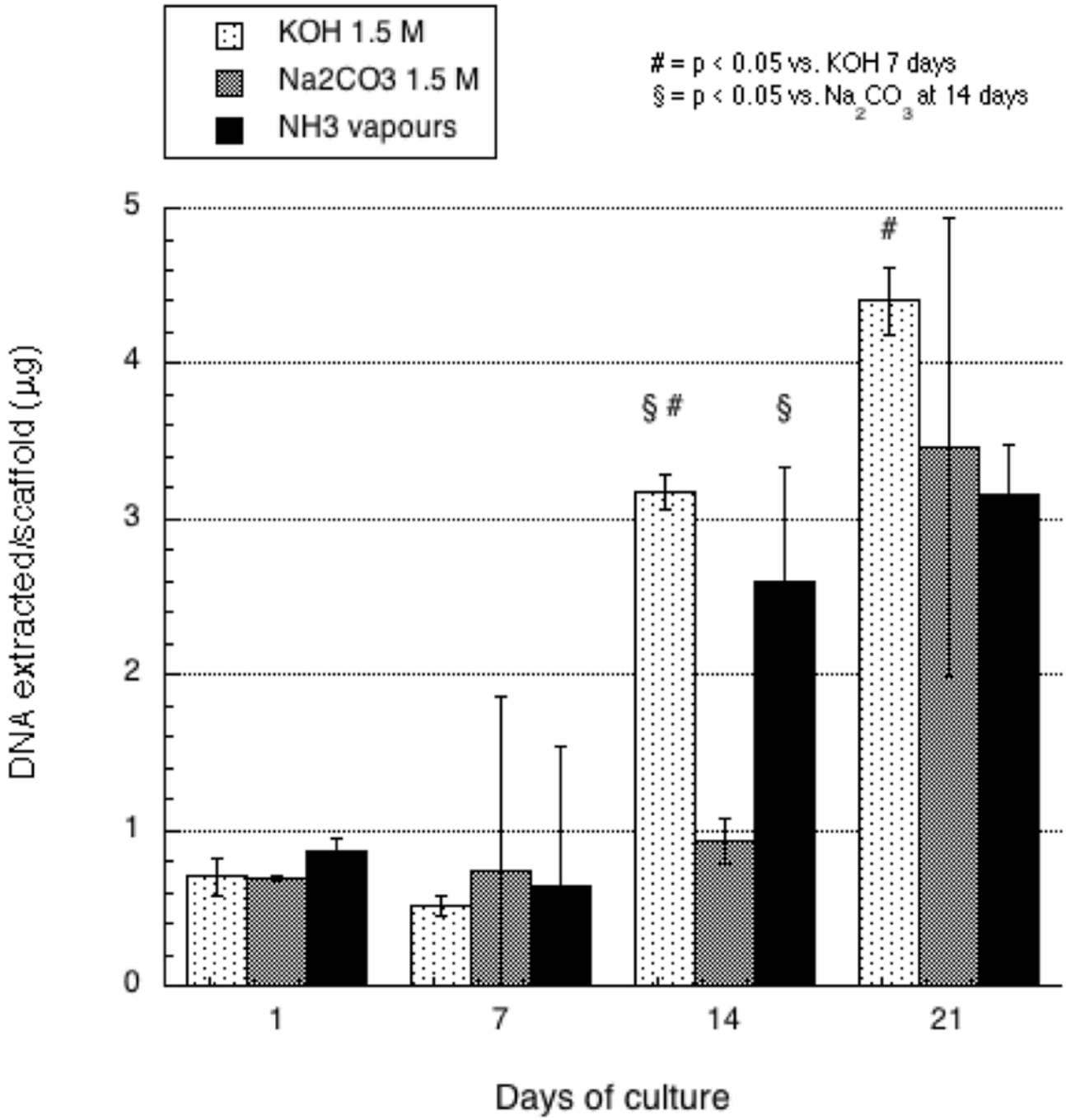

Figure 6. DNA assay of human fibroblasts grown on 3D printed chitosan scaffolds gelled with KOH (1.5M), Na_2CO_3 (1.5M), NH_3(g) (from 28% ammonia solution) performed at different time points. The bars represent the standard error of the mean (n= at least 3).

In regenerative medicine the quantification of free and bound water can be helpful to check the material similarity with respect to an autologue tissue. As mentioned, free water acts as solvent for proteins and several other compounds and, due to the fact that developed chitosan based scaffolds should mimic the native ECM, being able to control this parameter could help in maintaining the physiological turnover of compounds secreted by cells such as growth factors

and cytokines. Chitosan scaffolds hydrogelled by immersion in the 1.5 M KOH solution contained a higher amount of bound water that was significantly different from scaffolds prepared with other two gelation techniques considered (11.43 ± 4.23% in KOH of bound water vs ~4.4% average in carbonate or ammonia). Human body tissues contain more than 10% of bound water[20], and the differences in free and bound water here evidenced could be exploited for different applications of hydrogels, choosing the most appropriate one on the basis of the target area of the body and/or for the addition of active compounds.

In tissue repair the values of elastic moduli play a pivotal role. The results observed in this work demonstrated that the three selected gelation media allowed to obtain 3D structures with comparable elastic moduli having values comparable to those observed in skin, in particular in volar forearm region (Liang and Boppart[21]). This suggests that if applied as wound healing patch, this could be integrated into wound and adapt to it.

We have previously demonstrated[14] that chitosan-based 3D-printed scaffolds were characterized by a good interaction with cells and by an increased capacity to allow cell growth, compared to scaffolds obtained by pouring the solution on a cast[8]. In this work, we further find that all the three mild conditions tested for scaffold gelation ensure an efficient cell attachment and proliferation. The results obtained with the scaffolds gelled with Na_2CO_3 appear consistent with a previous work[22], while the approaches based on KOH and NH_3 were explored here for the first time. As clearly suggested by the fluorescence images, the complete covering of the scaffold surface observed after 14 days of cultures derives from both growth of cells directly plated onto the scaffolds and from migration from the well. This behaviour is consistent with previous data from our group on the ability of chitosan hydrogels, to support cell growth[8] and is probably a result of the entrapment and possible retain into the structure of chemotactic and growth factors deriving from serum. All the scaffolds were able to retain their structure for months when stored in water, saline solution, or in airtight environment after partial dehydration: in this case no statistically significant alteration of the structure occurred, up to six months ($p > 0.05$). When immersed in culture media all scaffolds retained their original dimensions up to 21 days, but the structure becomes softer and loses its consistency in about 7 days, preventing an estimation of residual mechanical resistance.

5.4 Conclusions

3D chitosan scaffolds with appropriate size, morphology, water content and mechanical properties can be prepared via a simple and reproducible 3D cryoprinting technology. Three

different gelation media having pH values greater than 12, i.e. KOH 1.5 M, Na_2CO_3 1.5 M and ammonia vapours resulted to be suitable to accurately retain the 3D printed structure starting from the CAD design (nominal filament diameter was 250 μm). At the maximum swollen state the structure accuracy was 101% for the scaffold gelled with the ammonia vapors, 109% for those in KOH and 117% for those in Na_2CO_3 (RSD < 10%). The physical properties and stability of these systems in biological media mostly depended on the gelation media and are a balance between chitosan network interactions and scaffold water content. The scaffold gelled in Na_2CO_3 resulted in highest free water content (96.78 ± 2.47%). The dehydration/rehydration experiments exhibited that scaffolds gelled in Na_2CO_3 and ammonia can be dehydrated up to 60% for storage, as they are able to reach the complete hydration condition after immersion in aqueous solution. The scaffolds prepared in KOH can be dehydrated up to 80% without losing they properties. No complete dehydration is allowed without irreversibly compromise the 3D structure. As for mechanical resistance scaffolds prepared with ammonia vapours showed a significantly higher elastic modulus with respect to both other media. All scaffolds were able to enhance and drive cell growth up to 21 days and this result has important therapeutic implications, since an efficient migration of cells into scaffolds is essential to guarantee the quality of tissues regeneration.

5.5 Methods

5.5.1 Materials

Chitosan ChitoClear™ TM4030, having a degree of deacetylation of 75% and a molecular weight of 50 kDa was obtained from Primex Ehf (Iceland) and used as received. Acetic acid and D-(+)-raffinose pentahydrate were obtained by Sigma-Aldrich, USA. All salts were from A.C.E.F. (Italy), while ammonia solution 28% was from VWR International (USA). All solutions were prepared using ultrapure water obtained with a Purelab Flex 1 system by ELGA Veolia.

5.5.2 Preparation of chitosan solution and 3D printing

Chitosan Chitoclear was dissolved in ultrapure water at 6% w/v concentration with the help of 2% v/v of acetic acid under stirring. As previously described by Bettini *et al.*[8], after complete dissolution of chitosan, D-(+)- raffinose pentahydrate was added at 290 mM final concentration as a viscosity agent and stirred until complete dissolution. (For the determination of neutralization process in different gelation media described below bromothymol blue was added as a pH

indicator). The resulting solution was loaded into a 10 ml syringe that was accommodated on a 3D printer built in-house[14]. Briefly, the machine is based on a three cartesian axes system that allows the movement on the horizontal plane of the printing plate and the vertical translation of the nozzle. Chitosan solution in the syringe is extruded by a pump acting on a syringe mounting a 26 G needle, deposed, layer by layer, on the printing plate at a velocity of 3 mm/s and instantaneously frozen to keep the structure of the scaffold conferred by the software. Scaffolds were shaped as a net of 1.6 cm × 1.6 cm in size, composed by the alternation of 10 or 20 orthogonal layers composed of parallel filaments being 200 μm distant from each other.

5.5.3 Gelation media

After freezing of the 3D printed scaffold, the structure was fixed by contact with a basic environment, in liquid or gaseous state. In order to obtain mild gelation conditions, different solutions were prepared in ultrapure water to obtain gelation of the scaffolds by immersion: the composition of the solution and the corresponding tested is reported in Table 1. As an alternative method for gelation, frozen scaffolds were transferred to a chamber saturated with ammonia vapor and exposed to the gas.

The effect of time of exposition to different gelation media was evaluated on the behavior of scaffolds in terms of water content, ability to recover water after dehydration: in particular gelation was evaluated after exposition to different media for 3, 15, 30, 60 minutes, 3 hours or 24 hours.

5.5.4 Evaluation of water content and water recovery after dehydration

Ten-layers scaffolds produced with selected methods of gelation were further analysed for water content and ability to absorb water after total or partial drying. After gelation, every scaffold was washed twice by immersion in ultrapure water for ten minutes; then surface water was removed by positioning each scaffold on a Buchner funnel covered by filter paper and by applying vacuum for 20 seconds. Time points checked were 3 min, 15 min, 30 min, 1 h, 3 h and 24 h. The wet weight of each scaffold was measured and registered as W0. The dehydration was performed by leaving each scaffold in vacuum oven (Gallenkam) at 40 °C and 200 mbar for 30 and 60 minutes and by recording the weight at each time point. All weights were compared to the dry weight (Wd) of scaffolds, which was obtained by lyophilization for 24 h in a Christ Alpha 2–4 LSC plus Freeze-Dryer. For each gelation medium and time point the experiment was repeated three times.

This first experiment gave us information about the time needed to obtain a specific degree of dehydration for each gelation medium. This was selected to obtain a residual 30%, 45%, 60% or 80% in weight of total water content. These partially dried scaffolds were immersed in ultrapure water to evaluate the ability to recover initial water content in 30 minutes, 1, 3 6 or 24 hours.

5.5.5 Differential scanning calorimetry analysis

Differential scanning calorimetry (DSC) has been chosen to evaluate the amount of bound water in chitosan-based scaffolds as a function of gelation with the conditions tested.
Once produced, scaffolds underwent the reaction in the three different gelation media (KOH 1.5 M, Na_2CO_3 1.5 M, ammonia vapors) for 1 hour and then were washed twice for 10 min in ultrapure water (UP) as in the standard procedure previously described. A Buchner filtration has been assessed for 20″ on filter paper to remove the excess of water present within macropores and a 4 mm diameter stamp has been used to obtain identical specimens.
DSC measurements were performed using an Indium calibrated (onset of melting Tm = 156.48 C, enthalpy of melting DHm = 28.60 J g1) DSC 821e instrument (Mettler Toledo, Switzerland) driven by STARe software (Mettler Toledo). DSC traces were recorded by placing accurately weighed quantities (6–12 mg) of frozen samples in a 40 μL aluminium pan which was sealed before the weightings to avoid water evaporation. Scans were performed between −7 and 35 °C at a scanning rate of 10 °C min^{-1} under a purging nitrogen atmosphere (100 mL min^{-1}). Each measurement was carried out at least in triplicate. Data relevant to the observed thermal events were reported as peak temperatures.
Total water amounts in the scaffolds have been determined by gravimetric analysis: 10 of each scaffold types (gelled by different alkaline media) at 100% of hydration have been weighted after 20″ of Buchner filtration and re-weighted after O.N. drying in a Thermocenter TC100 (Salvislab) oven at 40 °C. Total water content was thus calculated by means of the formula: (Wh-Wd); where “h” stands for “hydrated” and “d” for “dehydrated”.
Since only bulk water freezes and melts completely, it has been quantified integrating peaks of the endothermic thermal events of each scaffold, obtaining the amount of energy (Joules) required to melt free water in the sample.
In order to accurately calculate free water quantities in the samples a calibration has been priorly assessed analyzing with the same procedure known UP water quantities. This allowed to establish a mathematical correlation between a determined free water quantity and the required energy to melt it; a calibration curve with the function [y = −437.18x] has been drawn.

Melted water in the samples was then quantified and finally reported as percentage of free water compared to the total content initially calculated.

5.5.6 Mechanical resistance

The mechanical resistance of scaffolds obtained by different gelation media was compared on 20-layers scaffolds having size of 5 cm × 1.5 cm. Hydrogels at the maximum swollen state were tested. Thickness was determined as a mean of six measurements of the scaffold performed with a digital micrometer (Mitutoyo, Japan). Each scaffold was fixed on a tensile tester (AG M1 Acquati, Italy) loaded with a 5 daN cell. Force and time signals were digitalized by means of a PowerLab 400 board and recorded with Scope 3.5 software. Elongation at break (% strain) and Young's modulus were determined from the relevant stress-strain curves, taking into consideration the linear portion.

5.5.7 SEM analysis

Scaffolds obtained with different gelation media underwent critical point drying, then images were taken with a scanning electron microscope (Sigma HD, Carl Zeiss, Jena, Germany), at 300X magnification and EHT 1.00 kV. All images were analysed by ImageJ software (NIH, Bethesda USA) for the measurement of macro- and micro-structures, mean pore size and distribution.

5.5.8 ATR FT-IR spectroscopy

ATR FT-IR was used to observe any structural modification of scaffolds due to gelation. Spectra were taken by a Nicolet 5700 (Thermo Scientific, USA) in the range 400–4000 wavenumbers (cm^{-1}) with a resolution of 30 scan per second. Raw chitosan powder was analysed as a reference respect to 10 layers scaffolds produced by contact with KOH 1.5 M, Na_2CO_3 1.5 M or ammonia gas and dehydrated by lyophilisation.

5.5.9 Cell culture

Primary human skin fibroblasts coded as C84 were isolated with informed consent from an underarm explant from a healthy donor (female, 45-years old) and cultured, as previously described by Elviri *et al.*[14] before seeding them on scaffolds which underwent gelation in KOH,

Na_2CO_3 or ammonia vapours. After gelation, scaffolds were cut at a diameter of 6 mm, sterilized with ethanol 70% for 18 h, washed three times with sterile PBS, conditioned with complete medium for 30 minutes and then seeded in 48 well-plates. No scaffolds drying was performed before plating. Cells at passage 12 were harvested from the flasks at the confluent state by incubating it in trypsin solution for 2 min at 37 °C, then resuspended with DMEM supplemented with penicillin-streptomycin (100 U/mL), non essential amino acids, and serum (10%), counted and plated at density of 2×10^5 cells/well: 10 µl of cell suspension was initially seeded on scaffolds to facilitate adhesion for about 1 hour; successively, growth medium was added in order to completely cover their surfaces. The medium was changed every three days and evaluations of cell viability and microscopic analyses were performed after 7, 14 and 21 days.

5.5.10 Microscopic analysis

Empty and cell-seeded scaffolds, after washing 1x with PBS to remove dead cells, were incubated with calcein-AM, a probe that becomes fluorescent and is retained inside cells in response to the activity of intracellular esterases. Such treatment was performed in growth medium at 37 °C and 5% CO_2 for 30 minutes. Excess calcein was then removed by washing twice with PBS and images were captured using a Nikon eclipse TE300 inverted fluorescence microscope. At least two images were analysed per scaffold at each time point, using empty scaffolds as controls. Three scaffolds per group were analysed at each time point.

5.5.11 Cell viability and proliferation

Cell viability and proliferation onto scaffolds was evaluated by measuring the DNA content by adaptation of a method from Hoemann *et al.*[23]. Briefly, at each time point six scaffolds for each type were harvested, pooled into a 1,5 ml eppendorf washed with PBS, and 300 µl of a 3 mg/ml papain (Sigma-Aldrich, USA) solution were added. Digestion was performed overnight at 65 °C then the resulting suspension was centrifuged and 50 µl of supernatant were transferred in a 96-well dark plate (Costar) and mixed with 200 µl of Hoechst 33258 solution. Samples were measured with a Spark® Tecan fluorimeter with excitation wavelength of 360 nm and absorption wavelength of 460 nm. DNA content onto each scaffold was estimated by interpolation from a standard curve obtained with sperm salmon DNA (Sigma Aldrich, USA) at known concentration. Viability was also assessed with the MTT assay as previously described[14]. In both assays, the

absorbance obtained from correspondent empty scaffolds was subtracted from each measurement. Three scaffolds per group were analysed at each time point.

5.6 Statistical analysis

Statistical analysis was performed with Microsoft Excel and Graph Pad-Prism software version 5.0. Data obtained with the three scaffolds types were compared with One-way analysis of variance and the Dunnett's Multiple Comparison Test. Significance was defined as $p < 0.05$.

5.7 References

1. Xue, M. & Jackson, C. J. Extracellular Matrix Reorganization During Wound Healing and Its Impact on Abnormal Scarring. Advances in Wound Care 4(3), 119–136, https://doi.org/10.1089/wound.2013.0485 (2015).
2. Dhandayuthapani, B., Yoshida, Y., Maekawa, T., & Kumar, D. S. Polymeric Scaffolds in Tissue Engineering Application: A Review. International Journal of Polymer Science, 1–19, https://doi.org/10.1155/2011/290602 (2011).
3. Croisier, F. & Jérôme, C. Chitosan-based biomaterials for tissue engineering. European Polymer Journal 49(4), 780–792, https://doi. org/10.1016/j.eurpolymj.2012.12.009 (2013).
4. Rhoades, J. & Roller, S. Antimicrobial actions of degraded and native chitosan against spoilage organisms in laboratory media and foods. Applied and Environmental Microbiology, 66(1), 80–6. Retrieved from, http://www.ncbi.nlm.nih.gov/pubmed/10618206 (2000).
5. Ehf, P. (n.d.). GRAS Notice 000443: Shrimp-derived chitosan. Retrieved from, http://www.fda.gov/Food/FoodIngredientsPackaging/GenerallyRecognizedasSafeGRAS/GRASListings/default.htm.
6. Bellich, B., D'Agostino, I., Semeraro, S., Gamini, A. & Cesàro, A. "The Good, the Bad and the Ugly" of Chitosans. Mar.Drugs 14(5), 99–130 (2016).
7. Leung, H. W. Ecotoxicology of glutaraldehyde: review of environmental fate and effects studies. Ecotoxicol. Environ. Saf. 49, 26–39 (2001).
8. Bettini, R., Romani, A. A., Morganti, M. M. & Borghetti, A. F. Phyisicochemical and cell adhesion properties of chitosan films prepared from sugar and phosphate-containing solutions. Eur. Journ. Pharm. Biopharm. 68, 74–81 (2008).

9. Elviri, L., Bianchera, A., Bergonzi, C. & Bettini, R. Controlled local drug delivery strategies from chitosan hydrogels for wound healing. Expert Opinion on Drug Delivery 14(7), 897–908 (2016).
10. Xu, Y., Han, J. & Lin, H. Fabrication and characterization of a self-crosslinking chitosan hydrogel under mild conditions without the use of strong bases. Carbohydrate Polymers 156, 372–379 (2017).
11. Knaul, J. Z., Hudson, S. M. & Creber, K. A. M. Improved mechanical properties of chitosan fibers. Journal of Applied Polymer Science 72, 1721–1732 (1998).
12. Galli *et al.* Chitosan scaffold modi ed with D-(+) raffinose and enriched with thiol-modi ed gelatin for improved osteoblast adhesion. Biomedical Materials 11, 015004 (2016).
13. De Angelis, E. *et al.* The *in vitro* biocompatibility of D-(+) raffinose modified chitosan: Two-dimensional and three-dimensional systems for culturing of horse articular chondrocytes. Research in Veterinary Science 115, 310–37 (2017).
14. Elviri, L. *et al.* Highly defined 3D printed chitosan scaffolds featuring improved cell growth. Biomedical Materials 12(12), 045009 (2017).
15. Adamkiewicz, M. & Rubinsky, B. Cryogenic 3D printing for tissue engineering. Cryobiology 71, 518–521 (2015).
16. Wang, C., Zhou, Y. & Wang, M. *In Situ* Delivery of rhBMP-2 in Surface Porous Shape Memory Scaffolds Developed through Cryogenic 3D Plotting. Materials Letters, https://doi.org/10.1016/j.matlet.2016.11.039 (2016).
17. Tan, Z., Parisi, C., Di Silvio, L., Dini, D. & Forte, A. E. Cryogenic 3D printing of super soft hydrogels. Scientific Reports 7, 16293 (2017).
18. Montembault, A., Viton, C. & Domard, A. Physico-chemical studies of the gelation of chitosan in a hydroalcoholic medium. Biomaterials 26(8), 933–943 (2005).
19. Duarte, M. L., Ferreira, M. C., Marvao, M. R. & Rocha, J. An optimized method to determine the degree of acetylation of chitin and chitosan by FTIR spectroscopy. International Journa of Biological Macromolecules 31, 1–8 (2002).
20. Dubinskaya, V. A., Eng, L. S., Rebrow, L. B. & Bykov, V. A. Comparative Study of the State of Water in Various Human Tissues. Bulletin of Experimental Biology and Medicine 144, 3 (2007).
21. Liang, X. & Boppart, S. A. Biomechanical Properties of *In Vivo* Human Skin From Dynamic Optical Coherence Elastography. IEEE Trans Biomed Eng. April 57(4), 953–959 (2010).
22. Li, F., Liu, Y. & Xie, Q. A new injectable *in situ* forming hydroxyapatite and thermosensitive chitosan gel promoted by Na_2CO_3. Soft Matter 10, 2292–303 (2014).

23. Hoemann, C. D., Sun, J., Chrzanowski, V. & Buschmann, D. A multivalent assay to detect glycosaminoglycan, protein, collagen, RNA and DNA content in milligram samples of cartilage or hydrogel-based repair cartilage. Analytical Biochemistry 300, 1–10 (2002).

5.8 Author Contributions

L.E. designed and supervised the experimental design. C.B. and A.d.N. prepared the 3D printed scaffold and was responsible of their characterization. A.B., F.Z., C.M. were responsible of the *in-vitro* test. A.B. and L.E. prepared the manuscript. L.E., R.B., M.S. and F.B. edited the manuscript.

5.9 Additional Information

Supplementary information accompanies this paper at https://doi.org/10.1038/s41598-018-36613-8.

Competing Interests: Lisa Elviri, Carlo Bergonzi, Annalisa Bianchera, Marco Silvestri and Ruggero Bettini are founders and shareholders of M3datek Srl, a company that develops 3D printed medical devices for tissue repair. Nevertheless, they have not may gain or lose financially through publication.

5.10 Supplementary material

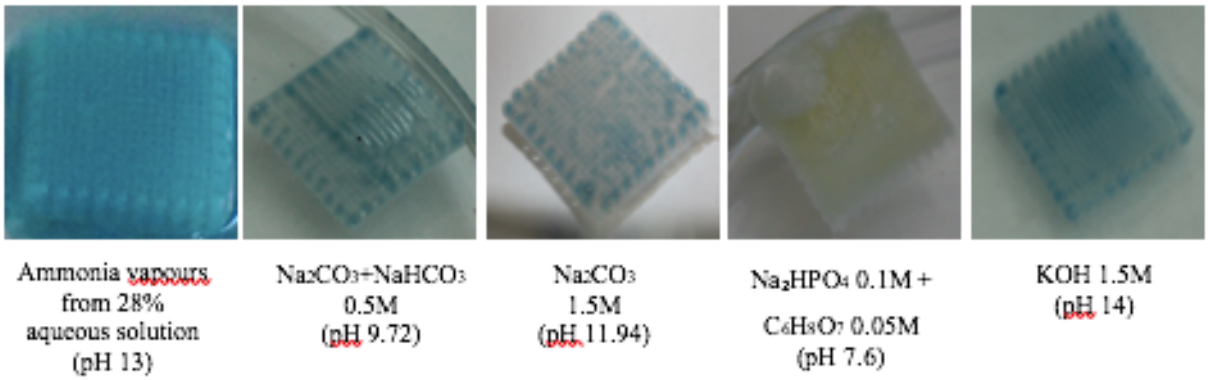

Figure S1. Neutralization process (after 1 min) and 3D retention structure observation by the colour changes in printed scaffolds from a chitosan solution to which blue bromothymol was added as a pH indicator.

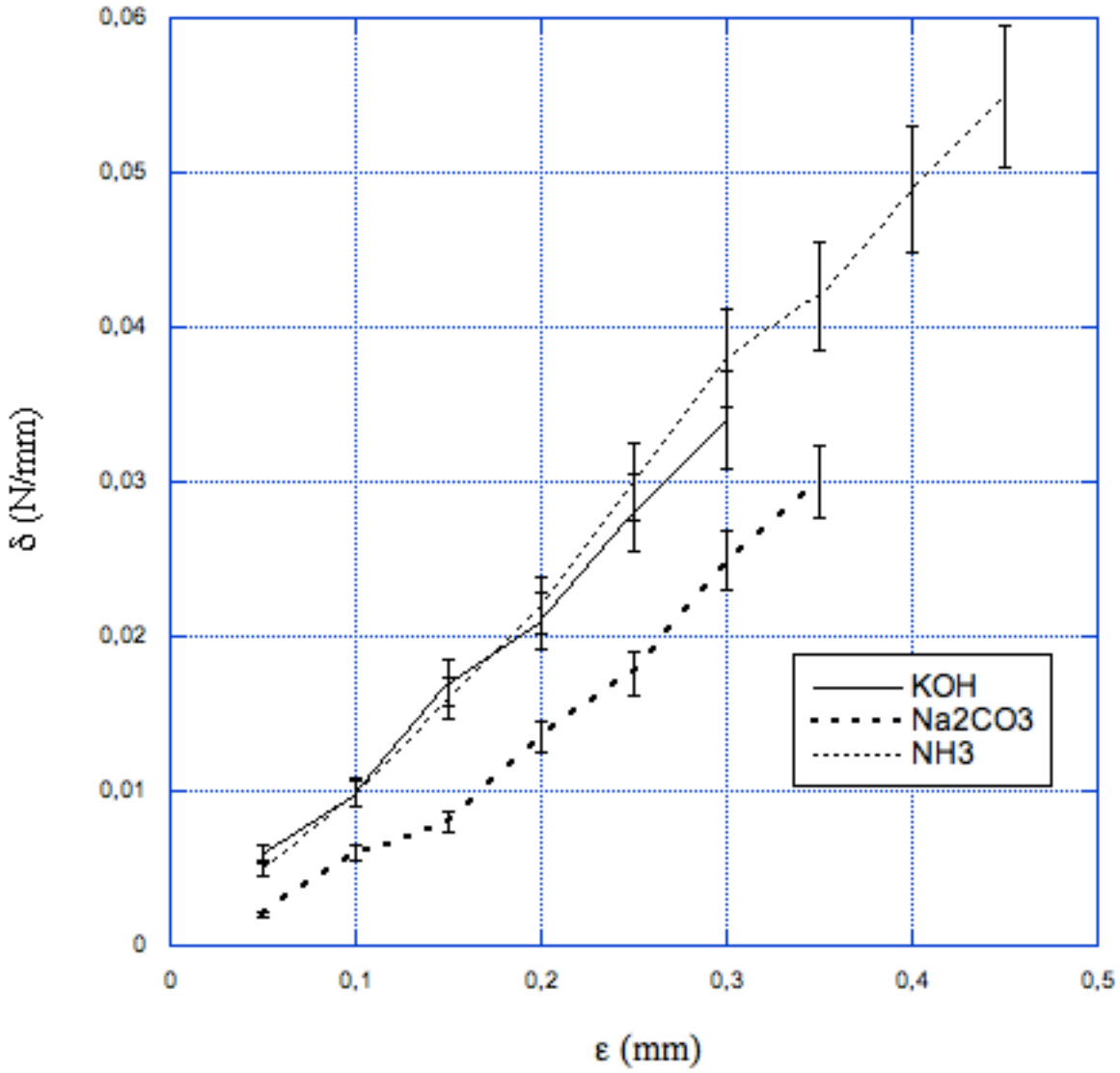

Figure S2. Stress-strain curve of the 3D printed chitosan scaffolds gelled in KOH 1.5M, Na_2CO_3 1.5M and ammonia vapours.

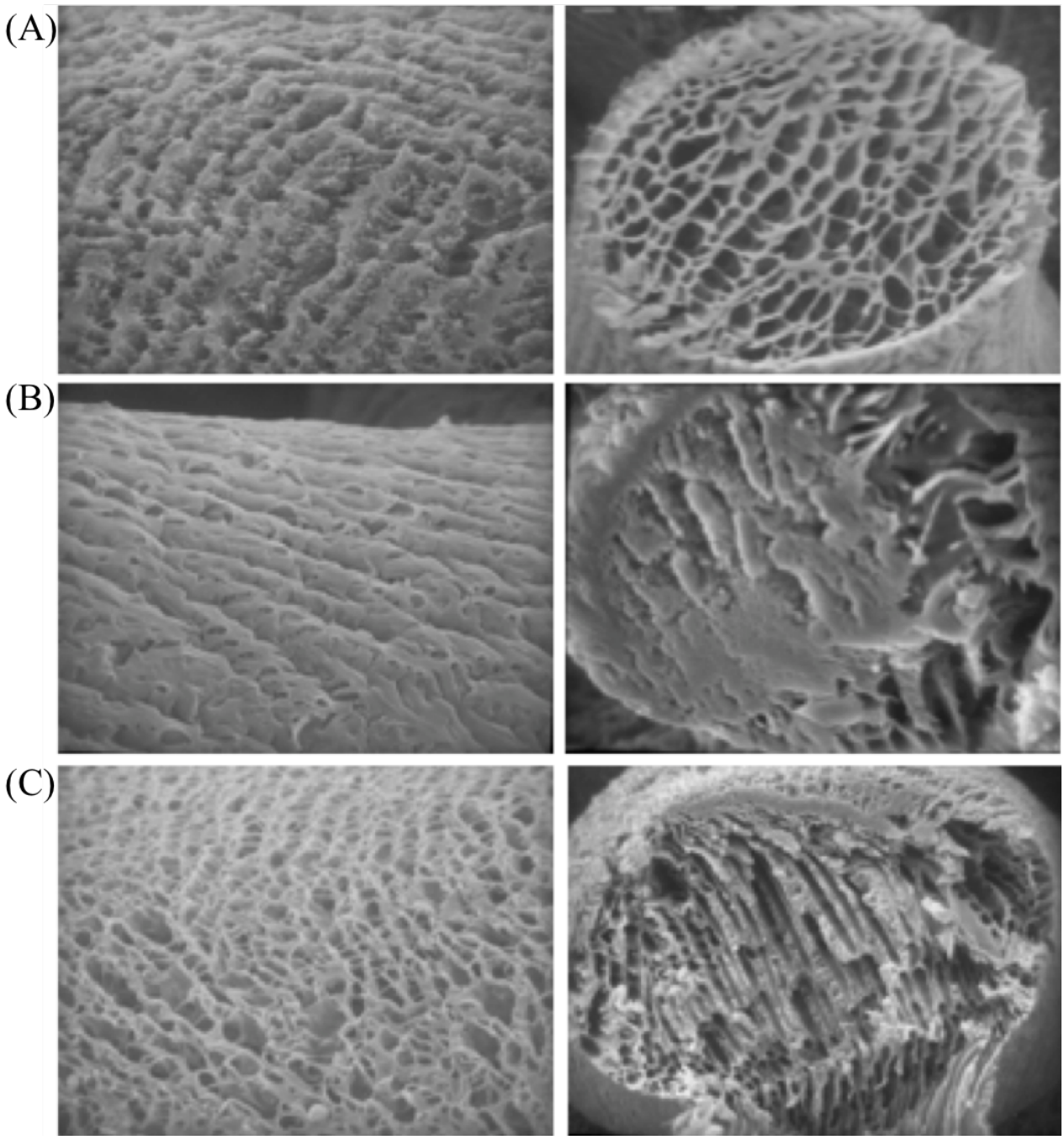

Figure S3. SEM images of printed chitosan scaffolds (filament surface and cross-section) processed in three different gelation media (A) KOH 1.5M; (B) Na_2CO_3 1.5M; (C) ammonia vapours. (500X magnification).

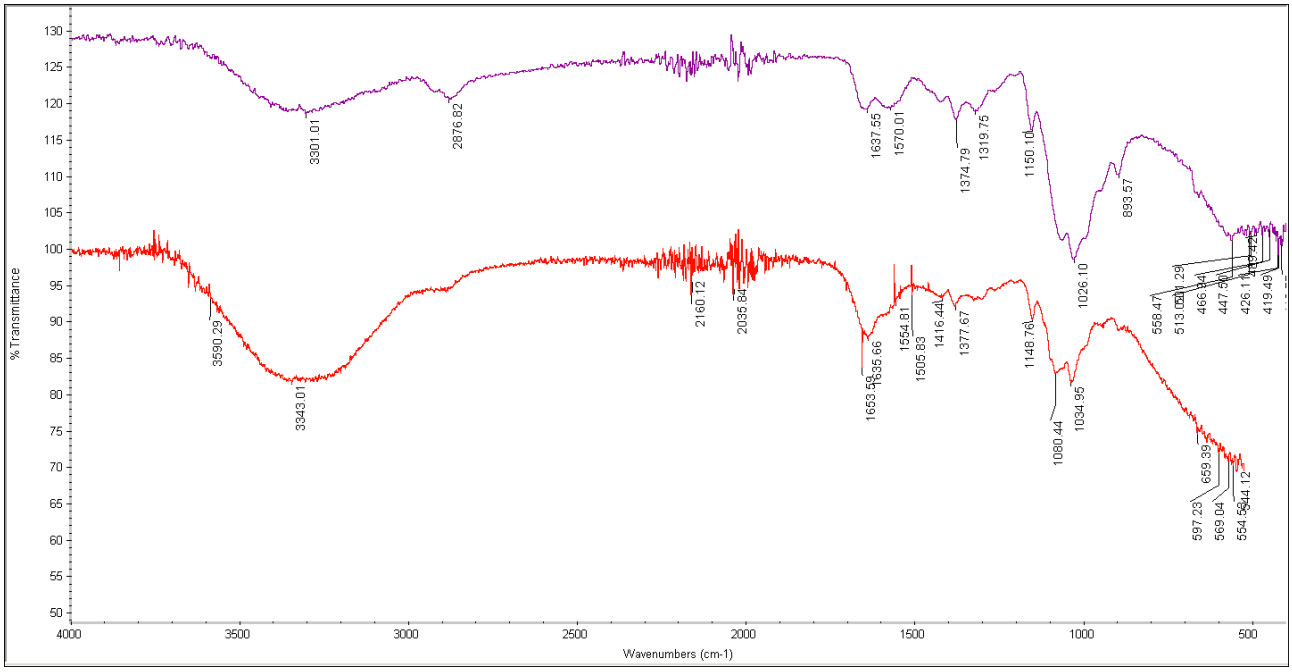
% Transmittance
Wavenumbers (cm-1)
3301.01
2876.82
1637.55
1570.01
1374.79
1319.75
1150.10
893.57
1026.10
3590.29
3343.01
2160.12
2035.84
1653.59
1635.66
1554.81
1505.83
1416.44
1377.67
1148.76
1080.44
1034.95
659.39
597.23
569.04
554.56
544.12

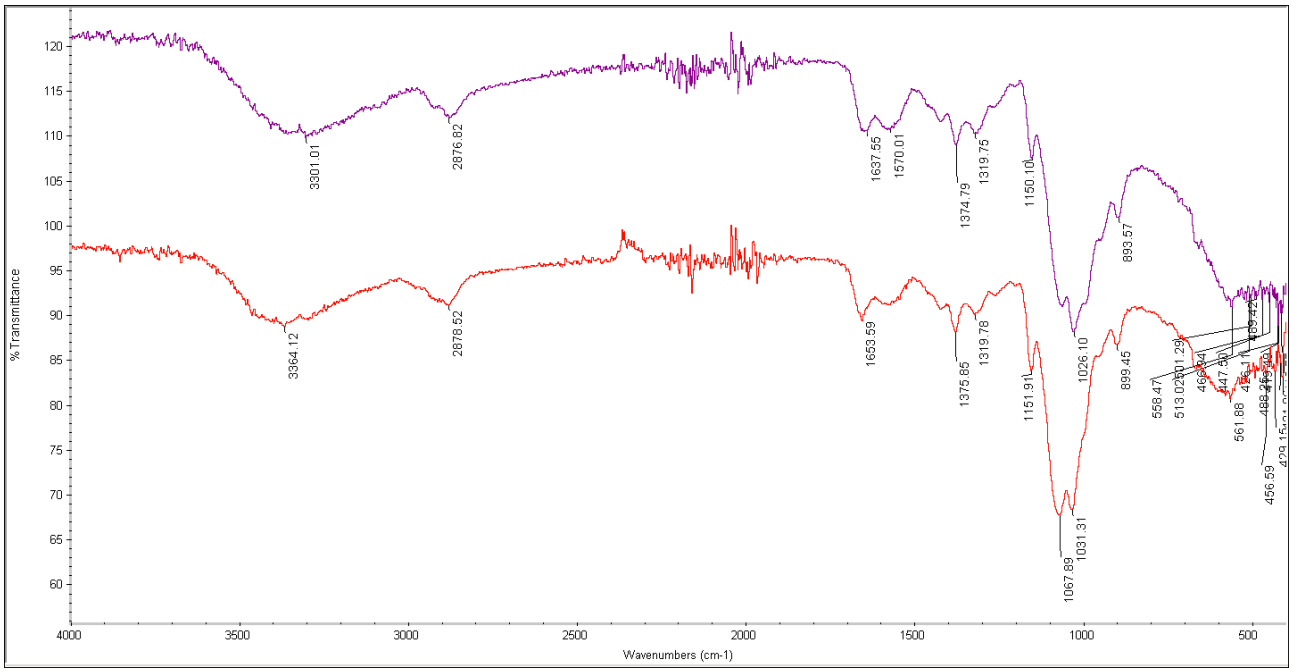
% Transmittance
Wavenumbers (cm-1)
3301.01
2876.82
1637.55
1570.01
1374.79
1319.75
1150.10
893.57
1026.10
3364.12
2878.62
1653.59
1375.85
1319.78
1151.91
1067.89
1031.31
899.45
558.47
561.88
456.59

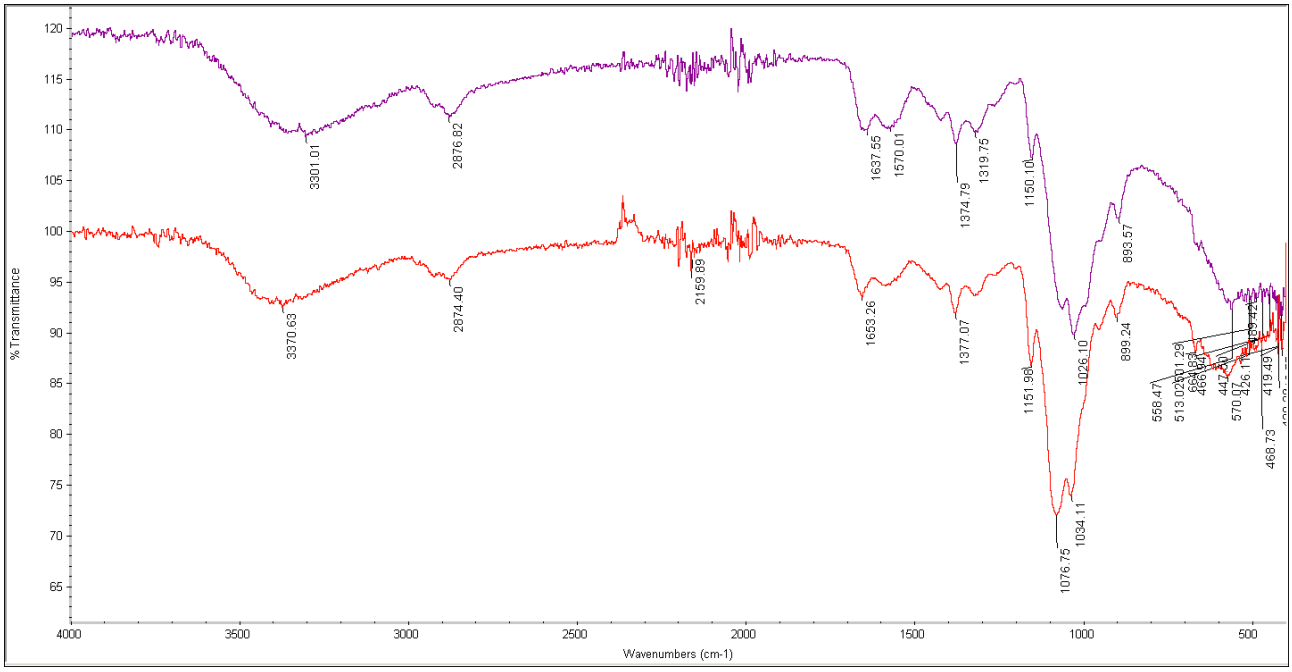

Figure S4. ATR FT-IR spectra of raw chitosan compared with spectra of hydrogels prepared with the selected gelation medium (gelation time 1 min).

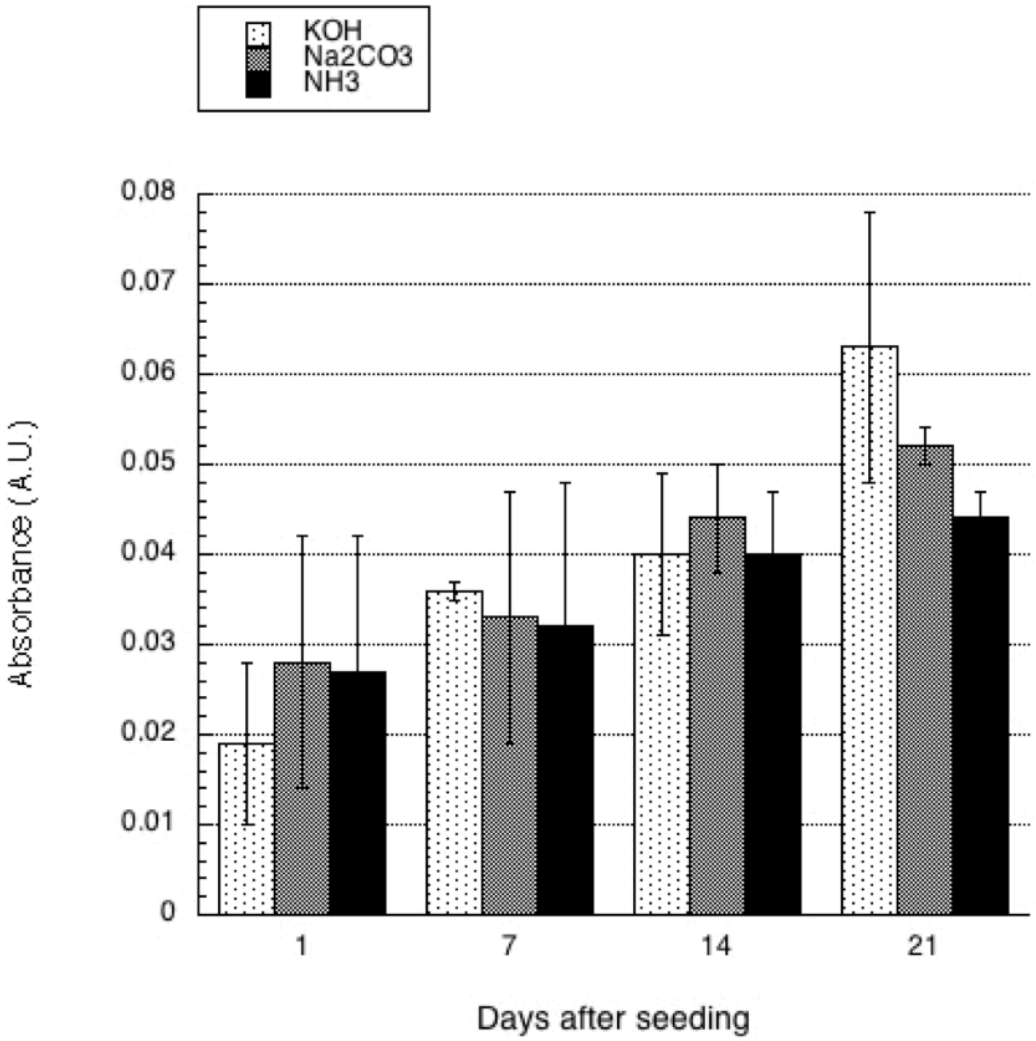

Figure S5. MTT assay of human fibroblasts grown on 3D printed scaffolds gelled with KOH (1.5M), Na_2CO_3 (1.5M), NH_3(g) (from 28% ammonia solution) performed at different time points. The bars represent the standard error of the mean (n= at least 3).

6 Chapter 3: "3D-printed chitosan-based scaffolds: An *in vitro* study of human skin cell growth and an *in-vivo* wound healing evaluation in experimental diabetes in rats"

Claudio Intini[a,c], Lisa Elviri[a,*], Jaydee Cabral[b], Sonya Mros[c], Carlo Bergonzi[a], Annalisa Bianchera[e], Lisa Flammini[a], Paolo Govoni[d], Elisabetta Barocelli[a], Ruggero Bettini[a], Michelle McConnell[c]

[a] Food and Drug Department, University of Parma, Parco Area delle Scienze 27/A, 43124, Parma, Italy
[b] Department of Chemistry, University of Otago, Dunedin 9054, New Zealand
[c] Department of Microbiology & Immunology, University of Otago, Dunedin 9054, New Zealand
[d] Department of Medicine and Surgery, University of Parma, 43124, Parma, Italy
[e] Biopharmanet TEC, University of Parma, Parco Area delle Scienze 27/A, 43124, Parma, Italy

Published on 18 July 2018, Carbohydrate Polymers Vol 199

IF 6.044

Personal contribution

CB performed the experimental work related to 3D development, analytical characterization, *in vivo* studies and contributed to the preparation of the manuscript.

Abstract

The fabrication of porous 3D printed chitosan (CH) scaffolds for skin tissue regeneration and their behavior in terms of biocompatibility, cytocompatibility and toxicity toward human fibroblasts (Nhdf) and keratinocytes (HaCaT), are presented and discussed. 3D cell cultures achieved after 20 and 35 days of incubation showed significant *in vitro* qualitative and quantitative cell growth as measured by neutral red staining and MTT assays and confirmed by scanning electron microphotographs. The best cell growth was obtained after 35 days on 3D scaffolds when the Nhdf and HaCaT cells, seeded together, filled the pores in the scaffolds. An early skin-like layer consisting of a mass of fibroblast and keratinocyte cells growing together was observed. The tests of 3D printed scaffolds in wound healing carried out on streptozotocin-induced diabetic rats demonstrate that 3D printed scaffolds improve the quality of the restored tissue with respect to both commercial patch and spontaneous healing.

Keywords: 3D printing, chitosan scaffold, chitosan biocompatibility, fibroblast and keratinocyte cells, skin tissue engineering, diabetic induced rats

6.1 Introduction

Tissue engineering is a promising field of regenerative medicine that relies on the interaction of three main elements: a supporting material, growth factors, and cells to develop a biological substitute for the replacement, restoration or regeneration of damaged tissues and organs (Khademhosseini, Vacanti, & Langer, 2009). The challenge of this matter is to mimic what happens in nature. Attempts are being made to engineer *in vitro* various tissues and organs. To date, the highest rates of success have been achieved in the areas of skin (Yannas, Lee, Orgill, Skrabut, & Murphy, 1989), bladder (Atala, Bauer, Soker, Yoo, & Retik, 2006), airway (Macchiarini, 2008), and bone (Schimming & Schmelzeisen, 2004; Warnke, 2004), where tissue-engineered constructs have been successfully used in patients (Bello, Falabella, & Eaglstein, 2001; Chen, Wu, & Chang, 2012; Zhang, Liu, Yang, Yao, & Tao, 2017).

Focusing attention on skin tissue engineering, the production of extra-cellular matrix (ECM) plays a pivotal role in the regeneration process, driving cell proliferation, differentiation and maturation. Furthermore, ECM provides characteristics of storage and delivery of growth factors and cytokines and it supplies structural integrity and scaffolding features as substratum for glycosaminoglycans, such as hyaluronic acid (HA), and collagens, naturally secreted by recruited cells during initial phases of regeneration (Xue & Jackson, 2015).

A relevant task of skin tissue engineering is thus focused towards the bio-fabrication and use of porous three-dimensional (3D) scaffolds (Khademhosseini *et al*., 2009) as appropriate environments for cell colonization and proliferation, thereby enabling the production of ECM and the reconstruction of complex tissues.

Among the different scaffold preparation processes (Ho *et al*., 2004; Ko, Oh, Kawazoe, Tateishi, & Chen, 2011; Weigel, Schinkel, & Lendlein, 2006), 3D printing and bioprinting are innovative technologies drawing tremendous attention from both academia and industry for their potential applications in various fields, including regenerative medicine and pharmaceutical drug delivery. Biomaterials, biomolecules and/or cells are patterned by 3D advanced additive manufacturing technologies to create scaffolds with arbitrary geometries and heterogeneous material properties, which can mimic the complexity of native tissues (Azhari, Toyserkani, & Villain, 2015; Patricio *et al*., 2014). Although 3D bioprinting presents revolutionary capabilities, the design and fabrication of 3D devices are critical. One of the key points is that scaffold constructs should address the needs for architecture design at the macro, micro, and nano level involved in structural cell-matrix interactions and nutrient transport (Karande, Ong, & Agrawal, 2004; Stevens & George, 2005). Current 3D printing techniques (i.e. extrusion printing, laser printing, droplet

printing) are feasible to make accurate and rapid fabrication of pre-designed structures with several natural (i.e. alginate, chitosan, collagen etc.) and synthetic polymers (polylactide, polyethylene glycol, etc.) with resolution ranging from 20 μm for laser techniques to 200–300 μm for the droplet and extrusion printing, respectively (Arslan-Yildiz *et al*., 2016).

In the present work, an innovative extrusion-based 3D printing technique has been used for the preparation of novel 3D chitosan scaffolds presenting controlled and reproducible macro- and microstructure to be applied in the regenerative skin tissue field (Bettini, Romani, Morganti, & Borghetti, 2008; Elviri *et al*., 2017). This manufacturing approach combines the freeze-gelation method described by Elviri, Asadzadeh, Cucinelli, Bianchera, and Bettini, (2014) alongside an advantageous modification of the chitosan solution with raffinose (Bettini *et al*., 2008) with the technical advantages of 3D printing. Chitosan (CH) is a natural polysaccharide derived from the alkaline N-deacetylation of chitin, the main structural component of the crustacean exoskeleton (Gasperini, Mano, & Reis, 2014). When the number of N-acetyl-glucosamine units is more than 50%, the biopolymer is referred to as chitin. Conversely, when the number of N-glucosamine units is higher, the term chitosan is used. Chitosan has the potential to be biocompatible, does not elicit adverse reactions in contact with human cells, is not allergenic and is widely available as a biowaste product of seafood processing industry (Galli *et al*., 2016; Patil, Ghormade, & Deshpande, 2000). It can be molded into a variety of shapes, can be degraded by ubiquitous enzymes in the human body, and oligomeric products from degradation can activate macrophages and stimulate synthesis of hyaluronic acid (Kumar, Muzzarelli, Muzzarelli, Sashiwa, & Domb, 2004; Peluso *et al*., 1994). Moreover, chitosan and chitin present haemostatic action, which can be exploited to enhance healing (Okamoto *et al*., 1992). For these reasons, chitosan is one of the most investigated biomaterials for tissue engineering and bio-fabrication. In the last decade, several chitosan-based biomedical applications including wound dressing (Mizuno *et al*., 2003; Straccia, Romano, Oliva, Santagata, & Laurienzo, 2014; Ueno *et al*., 1999), drug delivery (Ahn, Choi, & Cho, 2001, 2002), and space filling implants (Teng *et al*., 2002; Zhao *et al*., 2002) have been successfully achieved. Presently, many chitosan-based medical devices are in clinical trials predominantly associated with bone, cartilage and skin tissue regeneration (Borzacchiello *et al*., 2011; Mekhail & Tabrizian, 2014).

Although many chitosan scaffolds have been studied in different cell cultures, the interactions of 3D printed constructs and cell behaviors is still under investigation as this is an important feature to delve into before any *in-vivo* application.

In light of applications for chronic dermal wound treatments, in the present paper, the biocompatibility, cytocompatibility and toxicity of 3D printed chitosan scaffolds towards human

skin cell lines were investigated. In our previously published paper (Elviri *et al.*, 2017), the effect of a simple 3D printed architecture with 400 μm openings, with respect to scaffolds prepared by casting, was demonstrated to significantly improve human fibroblasts adhesion and proliferation. In this study, two different 3D scaffolds with 200 μm inter-filament opening were prepared (i.e. 3D printed scaffolds with or without the film of chitosan at the base) and individual and co-culture of fibroblast and keratinocyte cells were monitored for the first time in order to improve the understanding of the role of the third dimension on the accurate improvement of *in vitro* results. In addition, in order to obtain evidence about the 3D scaffolds properties to improve tissue regeneration, these 3D scaffolds were assessed *in vivo* in a context mimicking a clinical feature using a model of wound healing in streptozotocin-induced diabetic rats. Healing time, wound closure and histological data were provided and discussed.

6.2 Materials and methods

6.2.1 Materials

Chitosan ChitoClear® Fg90 TM4030 (CAS 9012-76-4, deacetylation degree 75%; molecular weight by gel permeation chromatography 50–60 kDa; allergen free, water insoluble, soluble in acid media) was from PRIMEX Ehf (Siglufjordur, Iceland). Acetic acid 99.8% v/v, dimethyl sulfoxide (DMSO) and potassium hydroxide were from J.T. Baker (Deventer, Netherland). Water was purified (0.055 uS/cm, TOC 1 ppb) with a Purelab pulse + Flex ultrapure water system (Elga Veolia, Milan, Italy). Neutral Red stain solution and MTT (3-(4,5-dimethylthiazol-2-yl)-2,5-diphenyl tetrazolium bromide) reagent were purchased from Sigma-Aldrich (St. Louis, MO, USA). MTT reagent was dissolved in water and stocked at concentration of 5 mg/mL; final concentration used was 1 mg/mL.

6.2.2 3D printer

A 3D home-made low temperature manufacturing system, built by combining Peltier cells and liquid/air exchangers, was used at the laboratory scale through the insertion of bespoke modules in the structure of a commercial Fuse Deposition Manufacturing (FDM) 3D printer. FDM architecture is based on three Cartesian axes, two of which enliven the printing plate in x and y direction on the horizontal plane, while the z-axis determines the progressive lifting of the extrusion nozzle. The design of scaffold shapes was directly described by the geometric primitives

of the axis control, without need of translating them through general purpose programs for the transformation of the 3D CAD model in a mesh to be subjected to slicing.

6.2.3 3D Chitosan scaffold fabrication

All 3D chitosan scaffolds were constructed from a chitosan solution (6% w/v) in acetic acid 2% (v/v) containing D-(+) raffinose pentahydrate at a final concentration of 290mM (Bettini *et al.*, 2008). Gentle heating was applied together with continuous stirring to help the dissolution of sugar. The resulted chitosan solution was treated in an ultrasonic bath for eliminating possible bubbles and clusters that could cause processing problems, such as nozzle clogging during 3D printing process. Thereafter, the solution was used to fill the 3D printer's cartridge, which was then assembled on the whole equipment. The 3D printer was constituted by a mechanical apparatus that could be moved along the three dimensions on axes x, y, z, an extrusion system, composed in turn, by a syringe (volume 5 mL) and a needle (26 gauge), that could be assembled and disassembled, and a mobile plate on which the solution was extruded and cooled at −14 °C with a series of Peltier cells. Several 3D chitosan scaffolds were printed following the extrusion-based 3D printing process. The 3D matrices were characterized from a projected area of 1 cm2, a thickness of the first layer of about 0.3mm and a thickness of the other layers of about 0.2mm for a total of 2.1 mm, and an opening of the network of 200 μm. Right after the 3D printing process, the scaffolds were gelled in potassium hydroxide KOH 8% (w/v) for 10 min and then stored in phosphate buffer saline PBS. This last passage was necessary to increase the material rigidity for filament shape retention. A further, 3D chitosan structure was produced which consisted of a compact chitosan film at the base to the previously realized scaffolds. The purpose of this film was to occlude the lower base of scaffold to improve the cell growth on it by keeping the cells inside. In detail, starting from the above-described chitosan solution, the film was casted and uniformly spread on the plate of the 3D printer using a roll film, before the printing process. After that, the 3D scaffold was printed above the film following the already mentioned procedures.

6.2.4 Mechanical resistance analysis

The mechanical resistance of scaffolds obtained was calculated on 20-layers scaffolds having size of 5 cm×1.5 cm. Thickness was determined as a mean of six measurements of the scaffold performed with a digital micrometer (Mitutoyo, Japan). Each scaffold was fixed on a tensile tester (AG M1 Acquati, Italy) loaded with a 5 Da N cell. Force and time signals were digitalized by

means of a PowerLab 400 board and recorded with Scope 3.5 software. Elongation at break and Young's modulus were determined from the relevant stress-strain curves.

6.2.5 Cell cultures

Normal dermal human fibroblast cells (Nhdf cells) and aneuploid immortal keratinocyte cells (HaCaT cells) obtained from American Type Culture Collection (ATCC®, Manassas, VA, USA) were used for *in vitro* tests.

Frozen stocks of these human cells at 1×106 cells/mL were initially put in 250 mL flasks, and sub-cultured in 750 mL flasks. Both cells were passaged in 750 mL flasks containing complete Dulbecco Modified Eagle Medium (DMEM, Gibco™, Thermo Fisher Scientific, Waltham, MA, USA) supplemented with 10% Fetal Bovine Serum (FBS, Gibco™, Thermo Fisher Scientific, Waltham, MA, USA) and 1% Penicillin and Streptomycin (PenStrep, Sigma-Aldrich, Saint Louis, MO, USA). Cells were incubated at 37 °C, 5% CO2, 95% relative humidity in a cell culture incubator and were sub-cultured at 70% confluence.

6.2.6 3D Cell cultures

Fibroblast (Nhdf) and keratinocyte (HaCaT) cells were seeded individually at a concentration of 1×10^5 cells/mL on 3D chitosan scaffolds with or without the film of chitosan at the base; scaffolds were previous sterilized for 24 h in 70% v/v ethanol. Each scaffold was inserted and seeded in a single well of a 12 or 24-well plate (Falcon® 12 or 24 Well Clear Flat Bottom TC-Treated Multiwell Cell Culture Plate, Corning®, New York, USA). Each plate's well was then filled with l or 2 mL of complete culture medium (DMEM, 10% FBS and 1% P/S) relative to whether the 12 or 24-well plate was used. The media was changed every 2 days in the first week of culture and every day in the remaining time of the experiment. When the cells were seeded together, Nhdf cells were added first on the scaffold in the specific well at 1×10^5 cells/mL concentration. Then, after one week, the culture medium was renewed and HaCaT cells at 2×10^5 cells/mL concentration were added. All 3D cell cultures were maintained in a 5% CO_2 incubator at 37 °C.

6.2.7 Neutral red assay

The Neutral Red assay (Babich & Borenfreund, 1990) was used to provide a qualitative estimation on the presence of viable cells on 3D chitosan scaffolds at defined time points. The medium was

removed from the 3D cell cultures to be washed with PBS. Thereafter, the 3D chitosan scaffolds were placed in a fresh plate in order to stain the cells growing on the scaffolds. The Neutral Red assay was performed by adding 150 µL of Neutral Red solution (0.5% w/v) for each well. The cultures were left in staining solution for 5 min at room temperature. They were washed two times carefully and gently with PBS for 5 min each and at the end, 150 µL of PBS were added to each culture/well before visualization. The results were observed under the transmitted light of an inverted microscope (Leica DM IL, Bio-Strategy Ltd., Albany, New Zealand). Each completed assay corresponded to one time point of analysis.

6.2.8 MTT assay

Fibroblast (Nhdf) and keratinocyte (HaCaT) cells, seeded together on 3D chitosan scaffolds with and without the film of chitosan at the base, were analyzed after 2, 13, 20 and 35 days by means of a MTT cell viability assay, as previously described (Favari *et al*., 2004). Using this method, the total number of cells that were situated on the scaffold and on the plastic at the bottom of the well were quantitated. In detail, at each time point, the medium was removed from the cultures, the 3D scaffolds were washed once with PBS and inserted in a fresh well plate to be analyzed. 1 mL of MTT reagent solution at concentration of 1 mg/mL dissolved in PBS was added to each well. The 12 or 24 well-plate was then covered with aluminum foil as MTT is light sensitive, and was incubated at 37 °C, 5% CO_2 for 1 h. MTT reagent was also added to the original wells where the 3D chitosan scaffolds came from in order to measure the cells grown on the bottom plastic surface of the well. Then, MTT solution was replaced by pipetting 1 mL of acidified isopropanol, prepared by adding hydrochloric acid (37% w/v) to isopropanol (1:1000 vol ratio) into each well. Finally, the plate was placed on a rotating platform for 10 min at 100 rotation per minute to ensure complete solubilization of the formed blue formazan crystals. The absorbance values were read at 570 nm using a Varioskan Flash Multimode Reader (Thermo Fisher Scientific, Waltham, MA, USA). Different dilutions of the samples, using acidified isopropanol solution, could be required depending on the viable cell numbers expected. Each completed assay corresponded to one time point of analysis. Moreover, this assay was also performed using two control groups, the 3D chitosan scaffolds only without cells, and cells only without scaffolds.

6.2.9 Scanning electron microscope (SEM) analysis

Fibroblast and keratinocyte cells were seeded alone and together on both types of 3D chitosan scaffolds. After 20 and 35 days, the cultures were fixed in 2.5% glutaraldehyde and in 0.1M cacodylate buffer for a total of 2 h. They were then washed 3 times with PBS, post-fixed in 1% osmium tetroxide, and in PBS for 1 h. Then the samples were dehydrated in 30%, 50%, 70%, 80%, 95%, 100% v/v (the latter for 3 times) ethanol for 10 min each step and the Critical Point Drying CPD (Bal-Tec AG, Balzers, Liechtenstein) was performed at 31 °C. Then, the 3D chitosan scaffolds were mounted on 12.5mm aluminum stubs using double sided carbon tape and carbon paste and coated with 10 nm of gold palladium for SEM viewing. 3D cell cultures were visualized with a scanning electron microscope (Zeiss Sigma VP, Carl Zeiss, Oberkocken, Germany), at several magnification values, EHT 1.00 kV and analyzed by Image J software (NIH, Bethesda USA).

6.3 *In vivo* wound healing studies

6.3.1 Induction of diabetes in rats

Research protocols were approved by the Italian Ministry of Health (D.Lgs 26/2014 ex D.Lgs.116/92) and the experiments were carried out in compliance with the Guide for the Care and Use of Laboratory Animals published by the US National Institutes of Health. Adult female Wistar rats, weighing 250–350 g, were used in this study. The animals were kept in environmentally controlled rooms (22° ± 2 °C, humidity 55 ± 10%, 12 h light and dark cycle). The animals were allowed to take normal rat feed (reference laboratory food pellets (4RF21, Mucedola Srl, Settimo Milanese, Italy)) and drinking water without restriction. After an overnight fast, all animals (n=25) received an intraperitoneal injection of streptozotocin (50 mg/kg; Sigma-Aldrich). Streptozotocin induces diabetes within 3 days by destroying the pancreatic β-cells; therefore 72 h after injection, blood glucose was measured in overnight fasting animals. STZ-treated rats with whole-blood glucose levels higher than 250 mg/dl were considered diabetic and used in the study. Fasting blood glucose was determined every 7 days throughout the experimental time to confirm the diabetic state, that leads to a delay in the time of wound healing with respect to physiological conditions. Rats were kept in cages individually, under feeding and drinking control: they were weighed daily and food and water consumption were measured.

6.3.2 Creation of skin wounds and treatment with 3D chitosan scaffolds

Three days before wounding, the dorsal interscapular area of each rat was depilated by a shaver and depilatory cream. On the day of wounding the rats were anaesthetized by intraperitoneal injection of 50 mg/kg ketamine and 5 mg/kg xylazine. The operative area of skin was cleaned with chlorhexidine. A punch biopsy instrument (diameter 8 mm) was used to create two full-thickness round wounds in the interscapular region of the upper back of each rat, and the skin flap was excised by using iris scissors. During the procedure particular attention has been placed to avoid incision of the muscle layer.

Rats were randomly divided into groups 1 (n=13) and 2 (n=12). In group 1, one wound was covered with the 3D chitosan scaffold whereas the other wound was covered by the commercial product as positive control (a wound dressing composed of carboxymethylcellulose with calcium alginate covered by a semi-permeable layer of polyurethane). In group 2, one wound was covered by the 3D chitosan scaffold and the other wound was bare as negative control. All the wounds of all the groups were additionally covered with a dry cotton gauze and adhesive film as secondary dressing.

All dressings were fixed with an elastic adhesive bandage. The rats were housed individually in large raised bottom mesh cages with free mobility. In the first week after the surgical procedure animals daily received paracetamol (100 mg/kg) in drinking water in order to alleviate discomfort and pain.

6.3.3 Wound closure evaluation

After 7, 10 or 14 days animals were sacrificed by CO_2 inhalation. The degree of wound healing was determined measuring the area of the wound with respect to a ruler by means of Image J software (https://imagej.nih.gov/ij/index.html) on photos of wounds taken at sacrifice. The percentage of wound contraction was calculated using the following formula (Karri *et al*., 2016):

$$\text{Wound contraction}(\%) = (\text{Initial wound area} - \text{wound area on the } n^{th} \text{ day}) / (\text{initial wound area}) \times 100$$

After animal sacrifice, samples were excised from the area of the wound and immediately fixed in PBS-buffered 4% paraformaldehyde at pH 7.4. Samples were then embedded in paraffin for sectioning using a microtome; 6 μm thick slices using a microtome were cut and stained with hematoxylin-eosin, with the addition of picro-sirius red F3BA to measure collagen fiber

distribution and hematoxylin. Images were taken using an optical microscope Nikon Eclipse 80i (Nikon Instruments, Calenzano, Italy), equipped with a camera Nikon Digital Sight DS-2Mv and connected to the control software, NIS Elements F (Nikon Instruments, Italy).

6.3.4 Statistical analysis

Results were expressed as mean ± standard deviation (SD). Student's t-test or one-way analysis of variance (ANOVA) was used for comparison of the experimental groups to a control group. A value of $p < 0.05$ was considered statistically significant.

6.4 Results and discussion

6.4.1 Preparation of 3D printed chitosan-based scaffolds and cell adhesion study

In order to properly evaluate, through qualitative and quantitative analysis, the formation of multi-layered, high-density cell populations in 3D scaffolds, a highly reproducible and defined 3D printing process should be used. The preparation and characterization of the 3D printed scaffolds employed in this study was described by Elviri *et al* (Elviri, Bianchera, Bergonzi, & Bettini, 2016). These scaffolds, referring to a grid with filament being 200 μm distant from each other, were characterized by an accurate geometry and good surface homogeneity in terms of pore size and distribution: on the surface of the filaments the pores (Feret diameter: 3.5 ± 3 μm) presented a preferential orientation, whereas regular interconnected and layered pore structure (Feret diameter: 5 ± 4 μm) within the filaments, were observed by SEM analysis (Elviri *et al*., 2017). Whereas the scaffold dehydration process causes a reduction in its size of about 45%, pore size ranges from 4 to 9 μm which could be beneficial for cell adhesion and migration.

As described in Materials & Methods section, mechanical resistance of scaffolds was measured with the help of a tensile tester. Young's modulus was calculated and resulted 105 kPa ± 18 kPa (n=6). As reported by Liang and Boppart (Liang & Boppart, 2010), these values of elastic moduli are comparable to those observed in skin, in particular in volar forearm region. This suggests that if applied as wound healing patch, this could be integrated into wound and adapt to it.

All further experiments herein described were carried out using 3D printed chitosan-scaffolds whose geometry was a grid of orthogonal filaments with an interfilamental distance of 200 μm, with and without a chitosan film at the bottom (Fig. 1A and B).

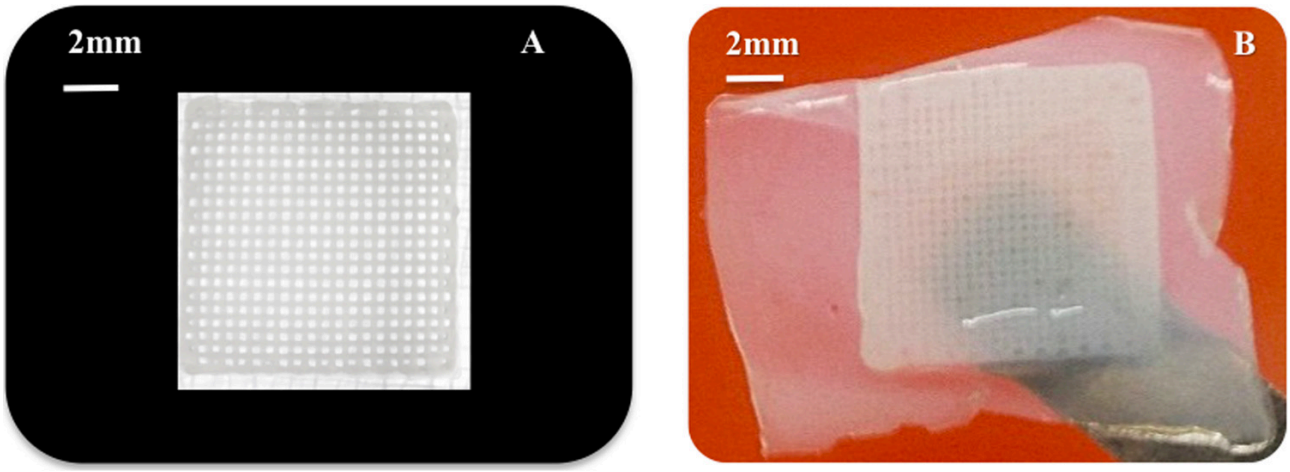

Fig. 1. Photographs of the 3D chitosan scaffold without (photograph A) and with (photograph B) a film of chitosan at the base.

Keratinocyte visualization by optic light or scanning electroscope microscopy on the 3D scaffolds from the bottom to the top was easier than that of fibroblasts, due to the geometry of these cells. Keratinocytes appeared as a ball with a rounded shape (Fig. 2A) possessing a diameter of approximately 20 µm, in agreement with the literature (Barrandon & Green, 1985). Fibroblasts, on the other hand, appeared elongated (about 50–100 µm length) and extremely thin, and for this reason were harder to visualize (Fig. 2B). Moreover, all neutral red and scanning electron microphotographs posted in this work were collected and scanned from the top to the bottom part of the 3D scaffold.

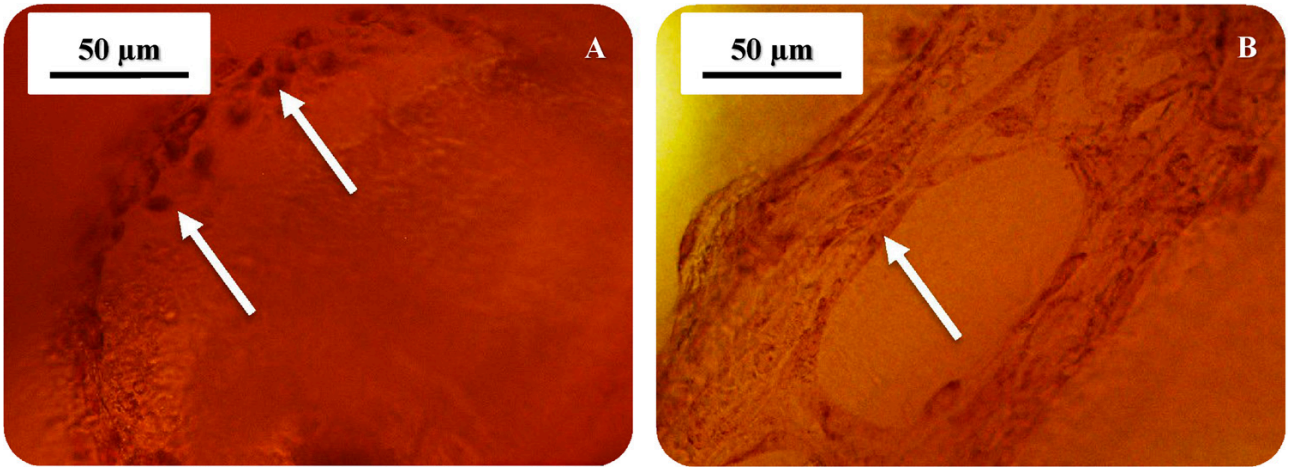

Fig. 2. Microphotographs showing the differences of cells' shape between keratinocytes taken from the same site (A) and fibroblasts (B) on 3D chitosan scaffolds upon Neutral Red staining.

By testing 3D chitosan scaffold without and with a film of chitosan at the scaffold bottom, it was possible to provide evidences of how fibroblast and keratinocyte cells were able to attach, live and grow after 20 days (Fig. 3).

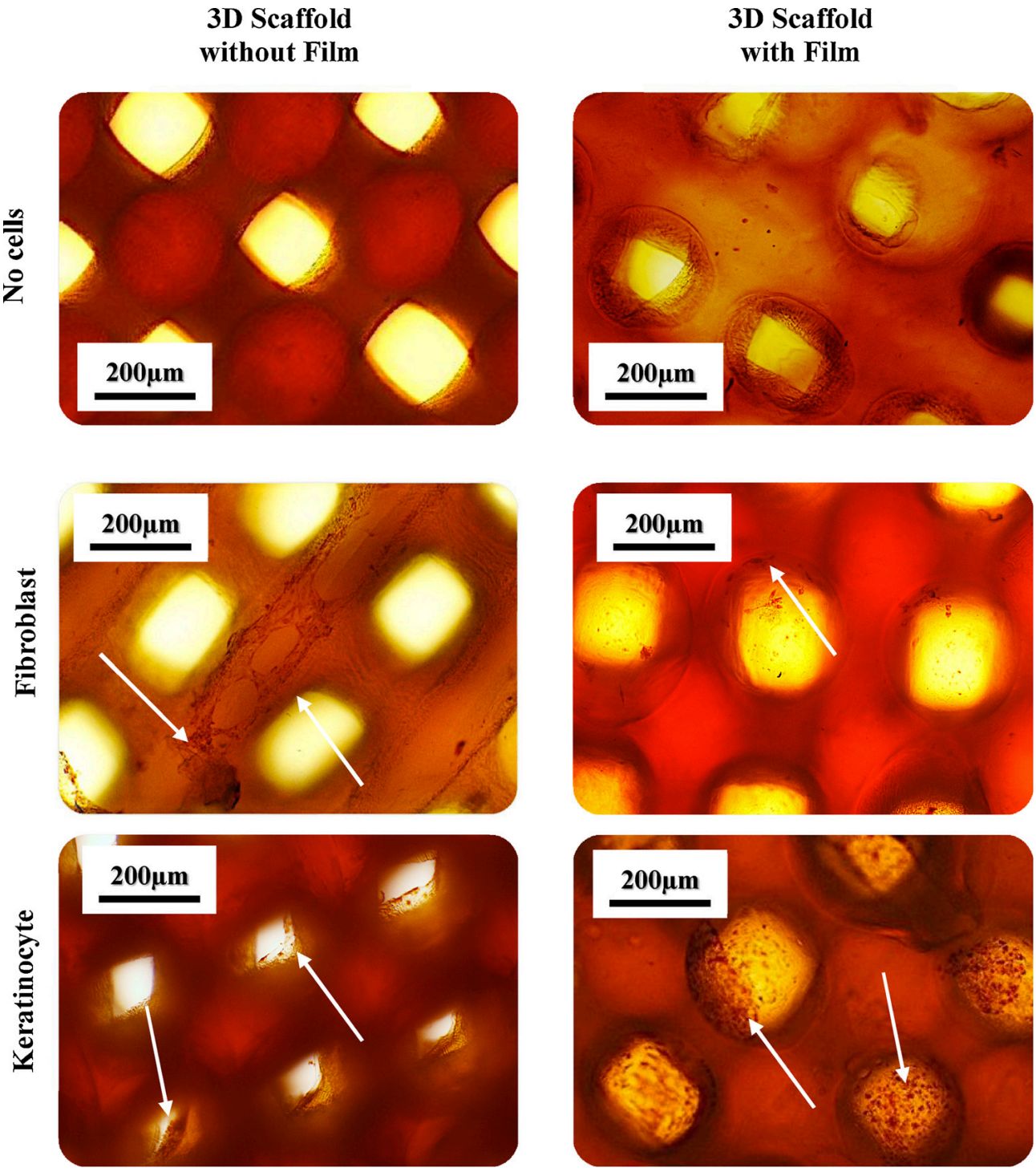

Fig. 3. Microphotographs of Nhdf and HaCaT cell growth 20 days after seeding on 3D chitosan scaffolds with and without the chitosan film at the base upon Neutral Red staining.

All parts of the scaffolds, on the filaments, inside the holes and on the planar substrate, seemed to be biocompatible with no toxicity observed towards the analyzed cells' phenotypes and appeared to be suitable to support colonization (Rnjak-Kovacina *et al*., 2011). These results indicated that the tested chitosan hydrogel was a suitable substrate for cell growth, in agreement with previous findings by Galli *et al*. (2016) and Bettini *et al*. (2008). Furthermore, Fig. 4(A–C) displays how the cells were able not only to grow on the structures, but also to fill the holes from the bottom to the top part of the scaffold trying to colonize the whole substrate. The best colonized scaffolds were observed with HaCaT cells seeded alone and analyzed after 20 days, as well as with Nhdf and HaCaT cells together after 35 days, in both cases on the 3D chitosan scaffolds with the film at the bottom (Fig. 4D and E).

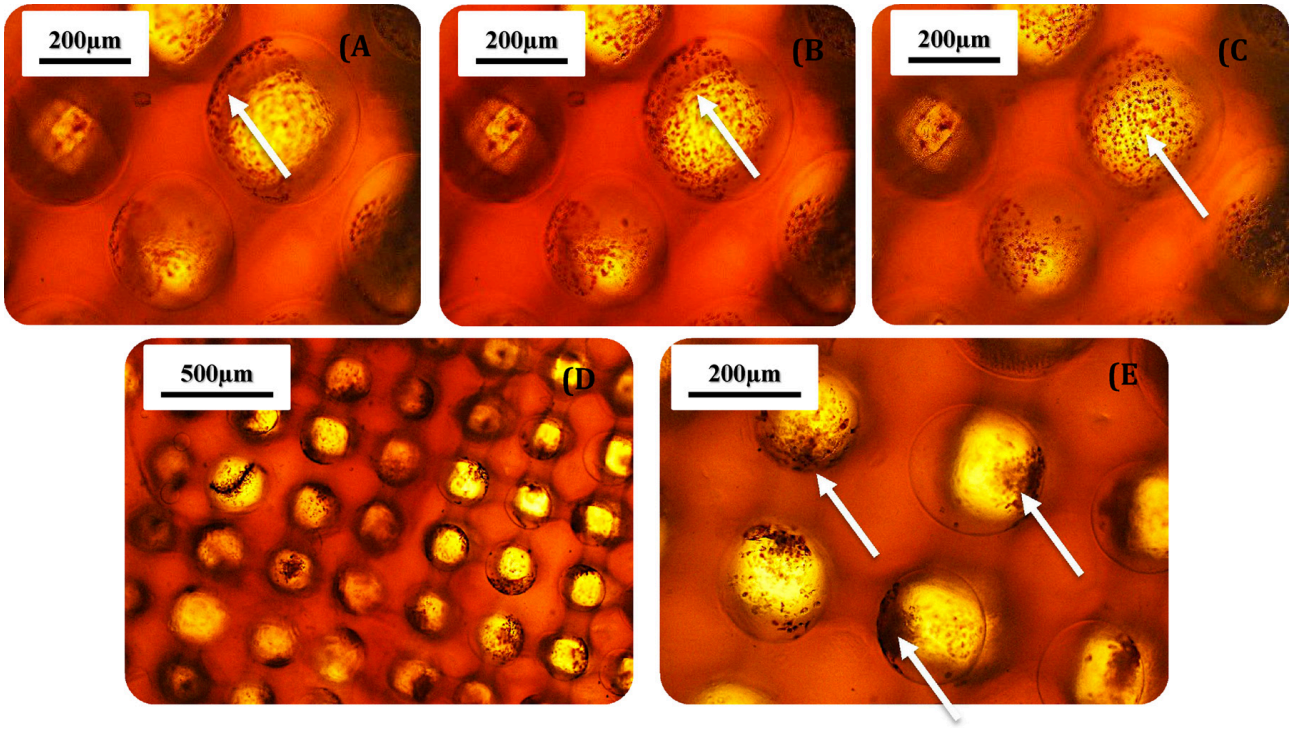

Fig. 4. (A-B-C) Microphotographs taken at three different focal points (from left to right > depth) of HaCaT cells seeded on 3D chitosan scaffolds with the film of chitosan at the base and processed after 20 days upon Neutral Red staining. (D–E) Microphotographs of Nhdf and HaCaT cell after 35 days seeding them together on 3D chitosan scaffolds with the film of chitosan at the base upon Neutral Red staining.

In Figs. 3 and 4, it was evident how the cells filled partially or completely the top part of the film and the walls of the holes. HaCaT and Nhdf cells seeded together exhibited the best situation likely because they can collaborate with each other releasing useful growth factors for improving growth and vitality (Barrandon & Green, 1985). Moreover, it was also clearly appreciable how

the presence of the film on the base of the 3D structure resulted in a significant improvement in keeping the cells inside the scaffold. A further evidence provided by this assay was that the fibroblast growth appeared visually slower than that of keratinocytes. This can be clearly seen in Fig. 3 depicting Nhdf and HaCaT cells, taken at the 20 day time point after individual seeding. This finding was taken into consideration for setting up the next experiment where a higher starting number of fibroblast with respect to keratinocyte cells was used.

6.4.2 Cell viability analysis

Cell viability was evaluated by measuring the activity of the mitochondrial enzyme succinate dehydrogenase by MTT test as previously described. Only the best experimental condition obtained by the Neutral Red analysis, namely, fibroblasts (Nhdf) and keratinocytes (HaCaT) seeded together on 3D chitosan scaffolds, was evaluated. The MTT assay confirmed the neutral red assay results showing how the chitosan substrate was not cytotoxic and that the cells were viable and able to grow and colonize 3D chitosan matrices. The graph in Fig. 5A displays a significant presence and a steady increase of metabolically active cells on 3D chitosan scaffolds analyzed between 2 and 35 days for both structures without (2–35 days +38%; $p < 0.001$) and with film (2–35 days +16%; $p < 0.001$) (3D chitosan scaffolds without film percentage increase: 2–13 days +18%; 13–20 days +13%; 20–35 days +3%) (3D chitosan scaffolds with film percentage increase: 2–13 days +1%; 13–20 days +5%; 20–35 days +9%). Furthermore, it is worthy highlighting that the amount of metabolically active cells on the scaffolds with film was significantly higher than without at every time point sampled. These data clearly suggest how cell colonization on 3D chitosan scaffold with a film at the bottom can significantly improve growth (percentage increase: 2 days +88%, $p < 0.01$; 13 days +62% $p < 0.0001$; 20 days +50% $p < 0.0001$; 35 days +58% $p < 0.0001$). 3D scaffolds with film kept higher number of cells on the structures but after 2 days a lower cell growth was measured in comparison with the structures without film. Instead, the graph in Fig. 5B shows the comparison of cell growth between 2D and 3D structures and demonstrates how cells exploit the advantages of more complex constructs. The total amount of metabolic active cells, adhered on the 3D scaffolds or located at the bottom of the well where they came from, was measured and represented on the graph. After 13 days in the 2D environment the cells reached the maximum confluence inhibiting cell growth, and remained almost constant during the later time points (13–20 days −2%; 20–35 days +2%). Contrariwise on the 3D substrate, the cell growth continued until 35 days for both experimental conditions assessed (3D chitosan scaffolds without film: 13–20 days +10%; 20–35 days +12%) (3D chitosan scaffold with

film: 13–20 days +19%; 20–35 days +27%) even though the amount of active cells after 13 and 20 days was lower than that measured on the 2D configuration (Fig. 5B). The rate of 3D growth is slower due to the 3D scaffold surface topography, which may reduce cell-to-cell signaling as cells are not interconnected in a single monolayer as they are in the 2D system.

Instead, after 35 days the total number of metabolically active cells in the 3D environments was comparable (3D scaffolds without film: 13 days -24% $p < 0.0001$; 20 days −15% $p < 0.01$; 35 days -7% $p < 0.05$) or higher (3D scaffolds with film: 13 days −28% $p < 0.0001$; 20 days -12% $p < 0.05$; 35 days +10% $p < 0.01$) with respect to the corresponding value to 2D at the same time point. These results demonstrated that in both conditions the 3D environment positively stimulated cell colonization and growth. Again, 3D chitosan scaffold with film seeded with both cells' phenotypes afforded the better results.

Furthermore, the graph in Fig. 5A, shows a slight increase in optical density values of the cultured scaffold relative to 3D scaffold without cells after 20 and 35 days (+1 fold and +3 fold to 3D chitosan scaffolds without and with film). This supports the previous hypothesis, as this increase could be ascribed to the absorbance of the oligosaccharides stemming from the chitosan degradation.

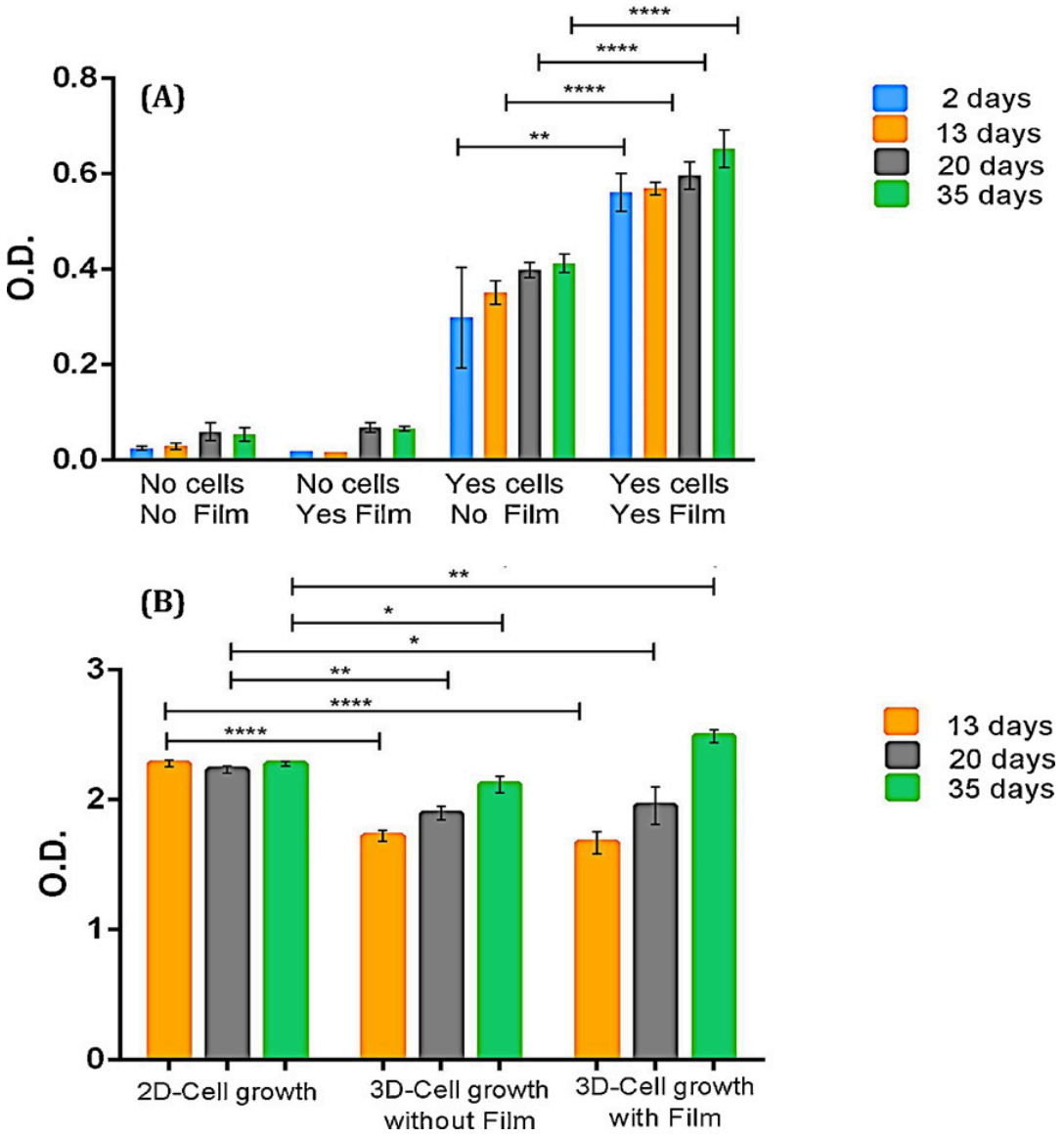

Fig. 5. (A) Optical Density measured in MTT assays on Nhdf and HaCaT cells seeded together on 3D chitosan scaffolds. O.D. values are an average of triplicate readings. ** $p < 0.01$; **** $p < 0.0001$.

1. No Cells No Film=Only 3D chitosan scaffold without film; 2. No Cells Yes Film=Only 3D chitosan scaffold with film; 3. Yes Cells No Film=Cells and 3D chitosan scaffolds without film; 4. Yes Cells Yes Film=Cells and 3D chitosan scaffolds with film. (B) Comparison between two-dimensional and three-dimensional cell growth. The O.D. values of the total number of cells in wells are represented on the y-axis, three different time points are shown on the x-axis. O.D. values are an average of triplicate readings. * $p < 0.05$; ** $p < 0.01$; **** $p < 0.0001$.

Three experimental conditions are reported: 1. 2D-Cell growth=Cells seeded in wells without 3D structures; 2. 3D-Cell growth without Film=Cells seeded in wells with 3D chitosan scaffolds

without film; 3. 3D-Cell growth with Film=Cells seeded in wells with 3D chitosan scaffolds with film.

6.4.3 SEM analysis

Scanning electron microphotographs confirmed the successful colonization of the 3D structures. Again, the best results appeared to be those obtained with Nhdf and HaCaT cells seeded together on 3D chitosan scaffold printed with the film at the bottom. Fig. 6, clearly shows the difference of colonization on the 3D structures in 20 and 35 days. In particular, after 20 days, only a few clusters of cells were spread on the surface areas of 3D scaffolds, whereas after 35 days the cells had filled the scaffolds and closed the gap between the previous clusters, reinforcing scaffold biocompatibility (Fig. 9B–C). In addition, SEM images captured from the bottom side of the structures without film, shows how the cells were able to build and develop an early skin-like layer, consisting of a mass of fibroblast and keratinocyte cells growing together. The lower surface of the scaffolds was completely covered by both cell phenotypes that in some cases were organized in several areas resembling a protruding cluster or filopodia.

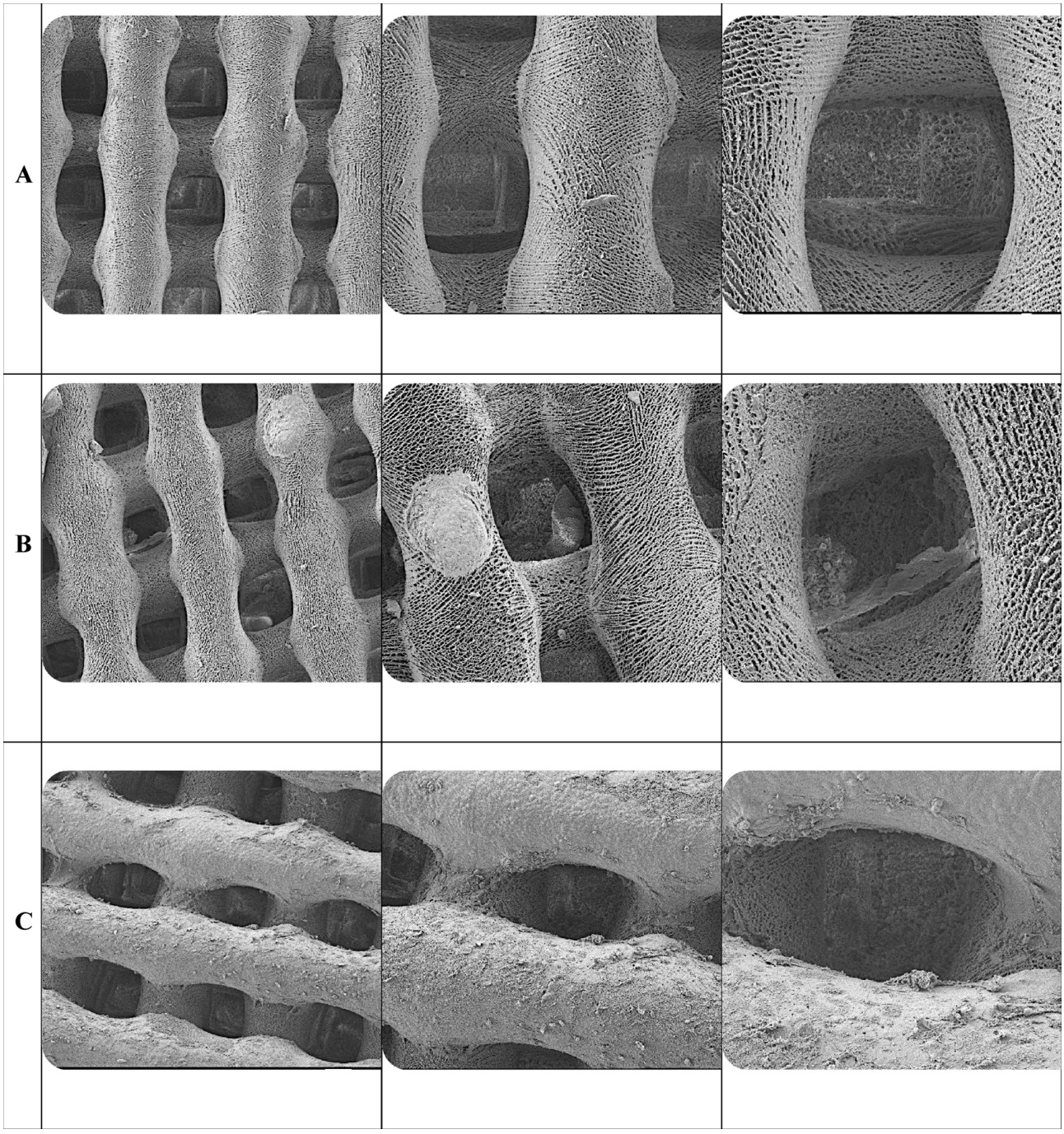

Fig. 6. Scanning electron microscope photographs of Nhdf and HaCaT cells seeded together on 3D chitosan scaffolds with a film of chitosan at the base at different magnification. Line A represents the control scaffold without cells, line B represents scaffolds with cells visualized after 20 days and line C shows scaffold with cells after 35 days.

6.4.4 *In vivo* test

STZ-treated rats having stable hyperglicaemia were selected for these experiments as a model of impaired wound healing. Images of wounds at day 7, 10 or 14 were taken and measured to

estimate wound contraction. As shown in Fig. 7A, starting from round excisions having an area of about 0,3 cm^2, seven days later, in animals treated with chitosan scaffolds or untreated ones, wounds appeared reduced of about 50% with respect to initial area (chitosan scaffold: 52 ± 21%); control group 46 ± 35%), while a more consistent, although not significant ($p > 0.05$) contraction in wounds treated with the commercial product was observed (reduction to about 20 ± 17%): in all cases an extremely high variability among animals was present. After 10 days, healing could be considered completed in animals treated with chitosan scaffolds or commercial product, while in control animals scabs were still present. After 14 days, all wounds were completely healed and only scars were visible. Representative images of wounds at different time points are collected in Fig. 7B. On the whole, visual inspection of wounds confirmed that treatment with chitosan scaffolds improved and accelerated wound healing with respect to untreated animals, but did not show significant differences with respect to the use of a commercial product: it is worth mentioning that in some cases, the use of the commercial product lead to infection in wounds, while no signs of infection were observed on any animal treated with chitosan scaffolds, probably thanks to its intrinsic antimicrobial activity (Goy, De Britto, & Assis, 2009).

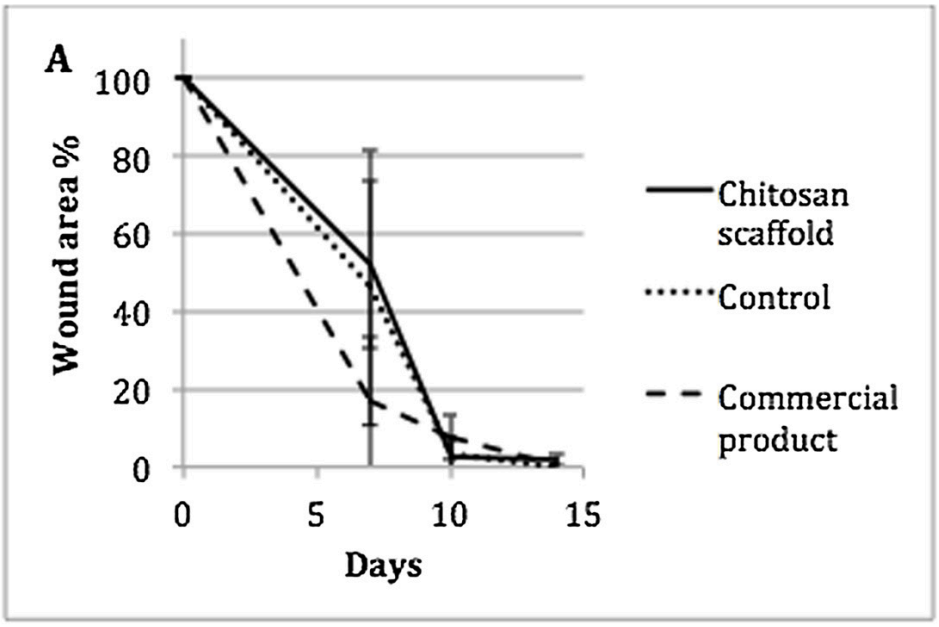

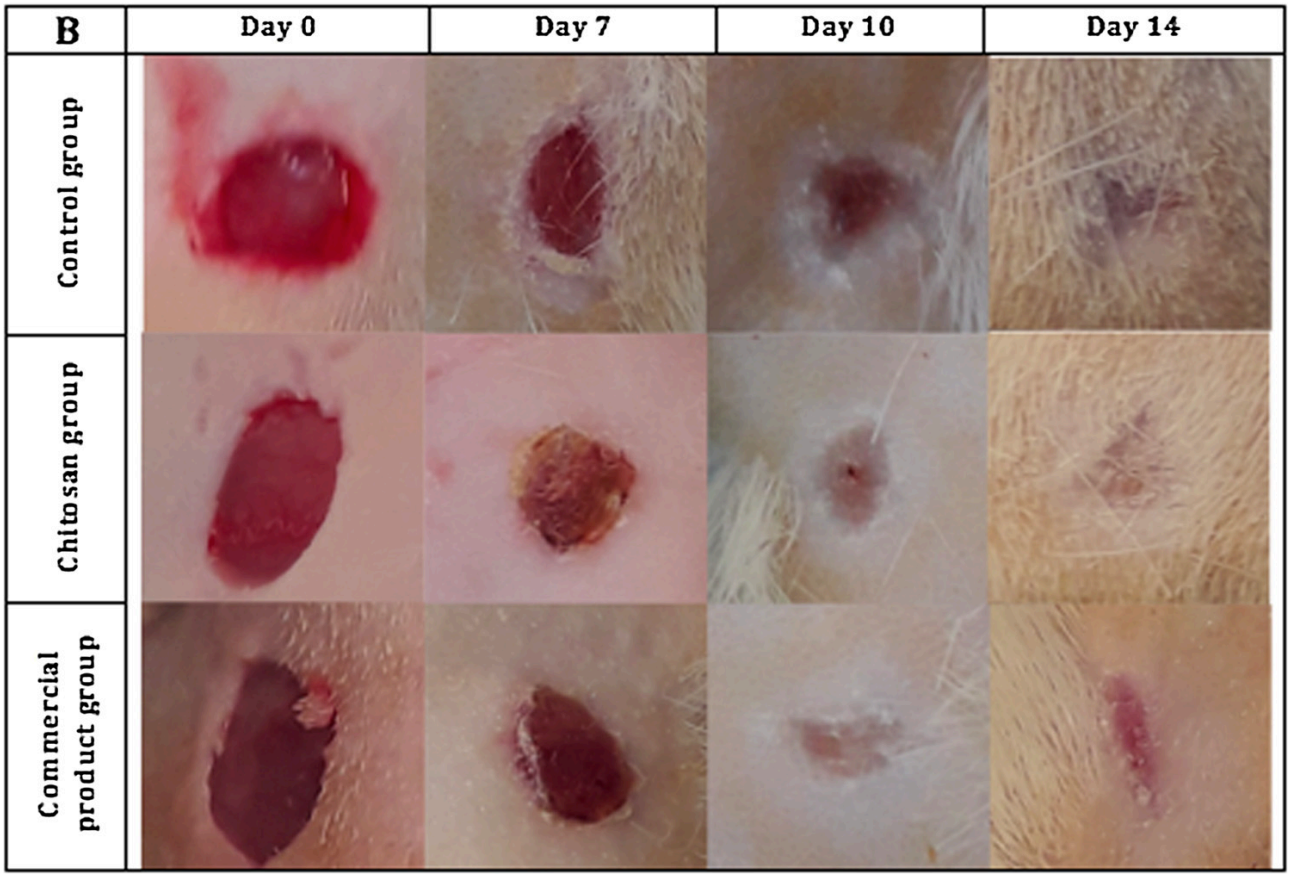

Fig. 7. (A) Contraction of wounds expressed as percent of inital area 7, 10 or 14 days after wound infliction; (B) representative images of wound healing in treated and untreated groups: each photo corresponds to an area of 1 cm^2.

Apart from macroscopic appearance, some differences in the quality of wound healing could be appreciated by histological analysis. Fig. 8 shows the comparison of a wound treated with chitosan hydrogel (left) with respect to spontaneous healing (right), 7 days after wound infliction. The scarlet area on the side of both images marks the limit of original wound, evidencing collagen structure. In figure on the left, the intense purplish red area is indicative of a more intense tissue reorganization, with respect to the pale pink area of the photo on the right, were tissue organization and collagen is very scarce. Epidermis (purple layer up) is present only in the wound treated with chitosan hydrogel. In both images, healing is still ongoing, but the tissue formed on the wound treated with chitosan scaffold has a more mature appearance.

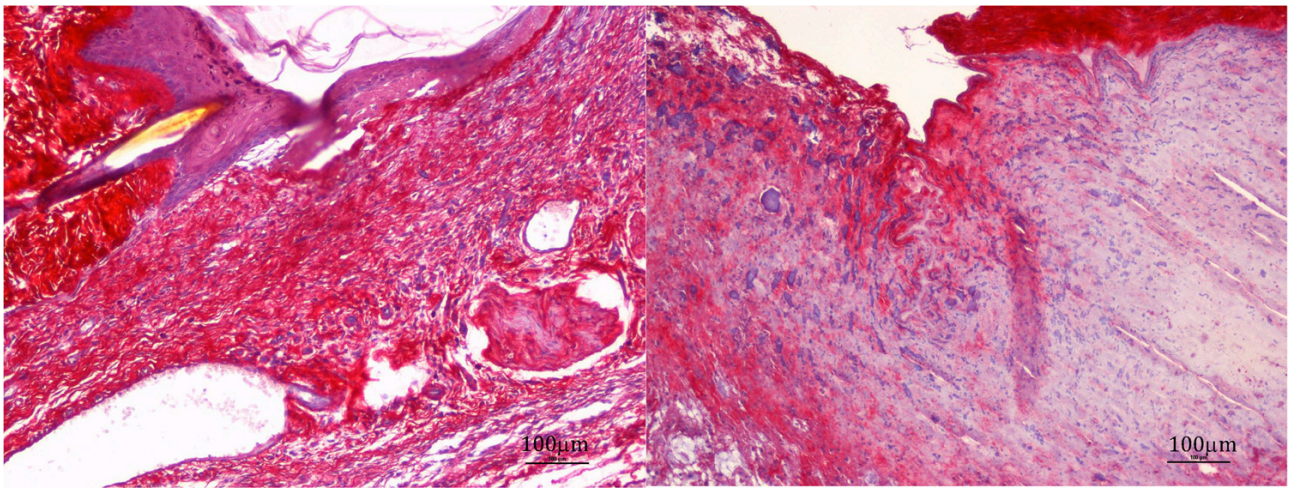

Fig. 8. Histological staining Hematoxylin+picro-sirius red of tissue excised from wounds treated with chitosan scaffolds (left) or spontaneously healed (right) for 7 days. Scalebar 100 µm.

Fig. 9 shows the comparison of a wound treated with chitosan hydrogel (left) with respect to a commercial product (right), 14 days after wound infliction. On the left, it is not possible anymore to distinguish the site of wound infliction, since the tissue is completely reorganized and the epidermis repaired (purple layer up), with a huge amount of collagen (scarlet red) that is not coarse anymore but rather mature and organized into fibrils. Moreover, tissue annexes are present such as blood vessels (v), sebaceous glands (g), hair follicles (p) and arrector pili muscles (m). On the other hand, figure on the right shows a wound treated with the commercial product: resulting tissue shows a non-ordered distribution of loose collagen fibers surrounding an area of tissue, that appears like fat tissue, with a functionality that is still compromised and without evidence of tissue annexes.

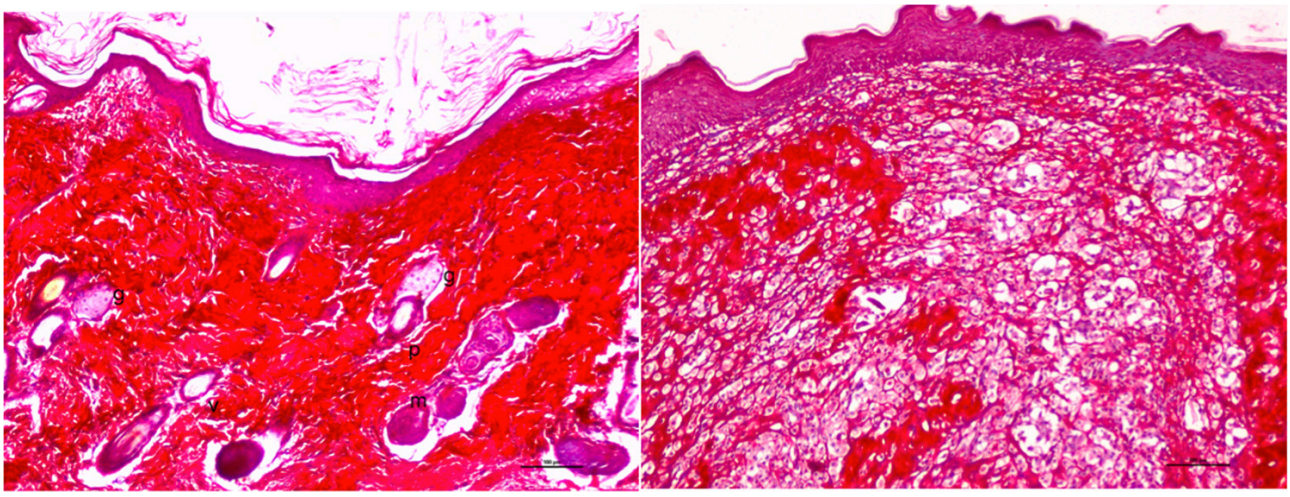

Fig. 9. Histological staining Hematoxylin+picro-sirius red of tissue excised from wounds treated with chitosan scaffolds (left) or a commercial product (right) for 14 days. In left figure, blood vessels (v), sebaceous glands (g) hair follicles (p) and arrector pili muscles (m) are evidenced. Scalebar 100 μm.

6.5 Conclusions

3D chitosan bio-polymeric scaffolds were fabricated using a newly developed extrusion-based 3D printing technique. This system provided a tool for precisely controlling the final shape and spatial distribution of the 3D chitosan structures.

These scaffolds exhibit excellent properties in terms of biocompatibility, cytocompatibility and toxicity toward two different skin associated human cell lines, namely Nhdf and HaCaT. These cell lines successfully attached, grew, and colonized the 3D structures. The best results were obtained when the two cell lines were seeded together onto 3D chitosan scaffolds with chitosan films at the base. The chitosan film provided a boundary to capture seeded cells as opposed to having them fall through. As a result, cells were able to grow up and through the scaffold structure in addition to adhering and growing on the scaffolds themselves.

Scaffolds with chitosan film at the base have a better performance, this is due to the fact that with the chitosan film during seeding cells do not exit from the scaffold holes drawn by the 3D printer so that they can stay *in situ* and have time to attach to the material. Proliferating cells adhere and spread on the chitosan scaffold where interconnected cells form a continuous layer, which is significant for potential application in skin integrity restoration.

Moreover, *in vivo* tests on rat models of diabetes showed that the use of chitosan scaffolds to treat wounds promotes the regeneration of a tissue with an improved functionality with respect to

wounds treated with a commercial product, suggesting the usefulness of chitosan scaffolds for the treatment of chronic dermal wounds.

As conclusion, 3D scaffolds are advantageous as they provide a more representative, biomimetic environment than traditional 2D cultures. They provide more biologically relevant studies and this is reflected in cost effectiveness and faster healing as seen the *in vivo* wound healing model. The cost effectiveness of the product, compared to those available in the market, depends on the low cost of starting material, with respect to biopolymers such as alginate or collagen and on the chance to scale up the process at an industrial level while guaranteeing a high level of reproducibility of critical characteristics such as porosity.

6.6 References

Ahn, J. S., Choi, H. K., & Cho, C. S. (2001). A novel mucoadhesive polymer prepared by template polymerization of acrylic acid in the presence of chitosan. Biomaterials, 22, 923–928.

Ahn, J. S., Choi, H. K., Chun, M. K., Ryu, J. M., Jung, J. H., Kim, Y. U., *et al*. (2002). Release of triamcinolone acetonide from mucoadhesive polymer composed of chitosan and poly (acrylic acid) *in vitro*. Biomaterials, 23, 1411–1416.

Arslan-Yildiz, A., El Assal, R., Chen, P., Guven, S., Inci, F., & Demirci, U. (2016). Towards artificial tissue models: past, present, and future of 3D bioprinting. Biofabrication, 8, 1–8.

Atala, A., Bauer, S. B., Soker, S., Yoo, J. J., & Retik, A. B. (2006). Tissue-engineered autologous bladders for patients needing cystoplasty. Lancet, 367, 1241–1246.

Azhari, A., Toyserkani, E., & Villain, C. (2015). Additive manufacturing of graphene–-hydroxyapatite nanocomposite structures. International Journal of Applied Ceramic Technology, 12, 8–17.

Babich, H., & Borenfreund, E. (1990). Applications of the neutral red cytotoxicity assay to *in vitro* toxicology. Alternatives to Laboratory Animals: ATLA, 18, 129–144.

Barrandon, Y., & Green, H. (1985). Cell size as a determinant of the clone-forming ability of human keratinocytes. PNAS, 82, 5390–5394.

Bello, Y. M., Falabella, A. F., & Eaglstein, W. H. (2001). Tissue-engineered skin. American Journal of Clinical Dermatol, 2, 305–313.

Bettini, R., Romani, A. A., Morganti, M. M., & Borghetti, A. F. (2008). Physicochemical and cell adhesion properties of chitosan films prepared from sugar and phosphatecontaining solutions. European Journal of Pharmaceutics and Biopharmaceutics, 68, 74–81.

Borzacchiello, A., Gloria, A., Mayol, L., Dickinson, S., Miot, S., Martin, I., *et al*. (2011). Natural/synthetic porous scaffold designs and properties for fibro-cartilaginous tissue engineering. Journal of Bioactive and Compatible Polymers, 26, 437–451.

Chen, K. L., Wu, H. C., & Chang, C. H. (2012). Tissue-engineered constructs for urethral regeneration. Urological Science, 23, 42–44.

Elviri, L., Asadzadeh, M., Cucinelli, R., Bianchera, A., & Bettini, R. (2014). Macroporous chitosan hydrogels: Effect of sulfur on the loading and release behaviour of aminoacid based compounds. Carbohydrate Polymers, 132, 50–58.

Elviri, L., Bianchera, A., Bergonzi, C., & Bettini, R. (2016). Controlled local drug delivery strategies from chitosan hydrogels for wound healing. Expert Opinion on Drug Delivery, 14, 897–908.

Elviri, L., Foresti, R., Bergonzi, C., Zimetti, F., Marchi, C., Bianchera, A., *et al*. (2017). Highly defined 3D printed chitosan scaffolds featuring improved cell growth. Biomedical Materials, 12, 045009.

Favari, E., Zanotti, I., Zimetti, F., Ronda, N., Bernini, F., & Rotblath, G. H. (2004). Probucol inhibits ABCA1-mediated cellular lipid efflux. Arteriosclerosis, Thrombosis, and Vascular Biology, 24, 2345–2350.

Galli, C., Parisi, L., Elviri, L., Bianchera, A., Smerieri, A., Lagonegro, P., *et al*. (2016). Chitosan scaffold modified with D-(+) raffinose and enriched with thiol-modified gelatin for improved osteoblast adhesion. Biomedical Materials, 11, 015004.

Gasperini, L., Mano, J. F., & Reis, R. L. (2014). Natural polymers for the microencapsulation of cells. Journal of the Royal Society, Interface, 11 20140817.

Goy, R. C., De Britto, D., & Assis, O. B. G. (2009). A review of the antimicrobial activity of chitosan. Polìmeros: Ciencia & Tecnologia, 19(3), 1–7.

Ho, M. H., Kuo, P. Y., Hsieh, H. J., Hsien, T. Y., Hou, L. T., Lai, J. Y., *et al*. (2004). Preparation of porous scaffolds by using freeze-extraction and freeze-gelation methods. Biomaterials, 25, 129–138.

Karande, T. S., Ong, J. L., & Agrawal, C. M. (2004). Diffusion in musculoskeletal tissue engineering scaffolds: Design issues related to porosity, permeability, architecture, and nutrient mixing. Annals of Biomedical Engineering, 32, 1728–1743.

Karri, V. V., Kuppusamy, G., Talluri, S. A., Mannemala, S. S., Kollipara, R., Wadhwani, A. D., *et al*. (2016). Curcumin loaded chitosan nanoparticles impregnated into collagen alginate scaffolds for diabetic wound healing. International Journal of Biological Macromolecules, 93, 1519–1529.

Khademhosseini, A., Vacanti, J. P., & Langer, R. (2009). Progress in tissue engineering. Science American, 300, 64–71.

Ko, Y. G., Oh, H. H., Kawazoe, N., Tateishi, T., & Chen, G. (2011). Preparation of open porous hyaluronic acid scaffolds for tissue engineering using the ice particulate template method. Journal of Biomaterials Science Polymer Edition, 22, 123–138.

Kumar, M. N., Muzzarelli, R. A., Muzzarelli, C., Sashiwa, H., & Domb, A. J. (2004). Chitosan chemistry and pharmaceutical perspectives. Chemical Reviews, 104, 6017–6084.

Liang, X., & Boppart, S. A. (2010). Biomechanical Properties of *In Vivo* Human Skin From Dynamic Optical Coherence Elastography. IEEE Transactions on Bio-medical Engineering, 57, 953–959.

Macchiarini, P. (2008). Clinical transplantation of a tissue-engineered airway. Lancet, 372, 2023–2030.

Mekhail, M., & Tabrizian, M. (2014). Injectable chitosan-based scaffolds in regenerative medicine and their clinical translatability. Advanced Healthcare Materials, 10, 1529–1545.

Mizuno, K., Yamamura, K., Yano, K., Osada, T., Saeki, S., Takimoto, N., *et al*. (2003). Effect of chitosan film containing basic fibroblast growth factor on wound healing in genetically diabetic mice. Journal of Biomedical Materials Research, 64, 177–181.

Okamoto, Y., Minami, S., Matsuhashi, A., Saimoto, H., Shigemasa, Y., Tanigawa, T., *et al*. (1992). Advances in chitin and chitosan. New York: Elsevier70.

Patil, R. S., Ghormade, V. V., & Deshpande, M. V. (2000). Chitinolytic enzymes: An exploration. Enzyme and Microbial Technology, 26, 473–483.

Patricio, T., Domingos, M., Gloria, A., D'Amora, U., Coelho, J. F., & Bartolo, P. J. (2014). Fabrication and characterisation of PCL and PCL/PLA scaffolds for tissue engineering. Rapid Prototyping Journal, 20, 145–156.

Peluso, G., Petillo, O., Ranieri, M., Santin, M., Ambrosio, L., Calabro, D., *et al*. (1994). Chitosan-mediated stimulation of macrophage function. Biomaterials, 15, 1215–1220.

Rnjak-Kovacina, J., Wise, S. G., Li, Z., Maitz, P. K., Young, C. J., Wang, Y., *et al*. (2011). Tailoring the porosity and pore size of electrospun synthetic human elastin scaffolds for dermal tissue engineering. Biomaterials, 32, 6729–6736.

Schimming, R., & Schmelzeisen, R. (2004). Tissue-engineered bone for maxillary sinus augmentation. Journal of Oral and Maxillofacial Surgery, 62, 724–729.

Stevens, M. M., & George, J. H. (2005). Exploring and engineering the cell surface interface. Science, 310, 1135–1138.

Straccia, M. C., Romano, I., Oliva, A., Santagata, G., & Laurienzo, P. (2014). Crosslinker effects on functional properties of alginate/N-succinylchitosan based hydrogels. Carbohydrate Polymers, 108, 321–330.

Teng, Y. D., Lavik, E. B., Qu, X., Park, K. I., Ourednik, J., Zurakowski, D., *et al*. (2002). Functional recovery following traumatic spinal cord injury mediated by a unique polymer scaffold seeded with neural stem cells. Proceedings of the National Academy of Sciences of the United States of America, 99, 3024–3029.

Ueno, H., Yamada, H., Tanaka, I., Kaba, N., Matsuura, M., Okumura, M., *et al*. (1999). Accelerating effects of chitosan for healing at early phase of experimental open wound in dogs. Biomaterials, 20, 1407–1414.

Warnke, P. H. (2004). Growth and transplantation of a custom vascularised bone graft in a man. Lancet, 364, 766–770.

Weigel, T., Schinkel, G., & Lendlein, A. (2006). Design and preparation of polymeric scaffolds for tissue engineering. Expert Review of Medical Devices, 3, 835–851.

Xue, M., & Jackson, C. J. (2015). Extracellular Matrix Reorganization During Wound Healing and Its Impact on Abnormal Scarring. Advances in Wound Care: The Journal for Prevention and Healing, 4, 119–136.

Yannas, I. V., Lee, E., Orgill, D. P., Skrabut, E. M., & Murphy, G. F. (1989). Synthesis and characterization of a model extracellular matrix that induces partial regeneration of adult mammalian skin. PNAS, 86, 933–937.

Zhang, X., Liu, Z., Yang, Y., Yao, Y., & Tao, Y. (2017). The clinical outcomes of vaginoplasty using tissue-engineered biomaterial mesh in patients with Mayer-Rokitansky-Küster-Hauser syndrome. International Journal of Surgery, 44, 9–14.

Zhao, F., Yin, Y., Lu, W. W., Leong, J. C., Zhang, W., Zhang, J., *et al*. (2002). Preparation and histological evaluation of biomimetic three-dimensional hydroxyapatite/chitosan–gelatin network composite scaffolds. Biomaterials, 23, 3227–3234.

7 Chapter 4: "Design, characterization and antimicrobial activity of 3D printed chitosan/alginate hydrogels with controlled release of silver sulfadiazine"

Lisa Elviri*[1], Carlo Bergonzi[1], Annalisa Bianchera[1], Maria Cristina Ossiprandi[2], Ruggero Bettini[1]

[1] Department of Food and Drug Science, University of Parma, Parco Area delle Scienze 27/A, 43124, Parma, Italy.
[2] Department of Veterinary Science, University of Parma, Via del Taglio 10, 43100 Parma, Italy.

Submitted for revision

Personal contribution

CB performed the experimental work related to drug loading, stability and release studies, analytical characterization, 3D development and contributed to the preparation of the manuscript.

Abstract

The growing demand for personalized medicine requires innovation in drug manufacturing to combine versatility with automation, 3D printing could be a valid solution for the production of drug-loaded medical devices, both for its versatility in the use of different materials and for the possibility to obtain define microporous three-dimensional structures.

Here, freeze-deposition 3D printing is explored for production of hydrogels intended as medicated dressings for wound healing, capable of modulating silver sulfadiazine release (SSD) as a function of the designed architectures. Chitosan and calcium alginate hydrogels were printed and characterized for their water content, elasticity and porosity: all these features were considered determinant for their behavior as drug delivery systems.

SSD-loaded 3D printed alginate hydrogels were associated with 3D printed chitosan hydrogels having different thicknesses and drug release kinetics from different constructs was evaluated *in vitro* using vertical diffusion Franz cells. Moreover, a tangible evaluation of the effectiveness of scaffolds antimicrobial activity was conducted by assaying them on *S. aureus* and *P. aeruginosa* cultures.

All constructs showed different behaviors both in terms of amount and rate of drug released, showing as well a strong antimicrobial activity *in vitro* (100 % of growth inhibition) and offering a proof of concept that 3D printing technique could be efficiently applied to the production of hydrogels for drug delivery.

The technique can be thus exploited for antimicrobial drug release from biocompatible hydrogel dressings, representing the chance to design and realize customized active medications, tunable in terms of dimension, drug quantity and release rate.

Keywords: 3D printed hydrogels, chitosan, alginate, silver sulfadiazine, controlled drug release, antimicrobial activity

7.1 Introduction

Drug manufacturing has a growing demand for personalized medicine and high adaptability, a feature that hardly applies to large-scale production that has characterized so far pharmaceutical industry. From patient's side, differences in age, weight and disease, together with the use of more and more sophisticated diagnostic tools, are leading the way to tailored therapies, which could offer higher drug efficacy as well as higher safety. In order to meet requirements of personalized medicine, drug formulation must rely on manufacturing processes that combine the need of customization to industrial requirements, guaranteeing law-compliant standards of accuracy, flexibility and automation. 3D printing is one of most promising approaches to overcome these issues. The technique leads to the production of three-dimensional objects starting from a digital model, exploiting the precise but versatile deposition of materials with the chance to combine different substances.

A lot of 3D printing techniques have been applied [1-2] to the production of solid dosage forms, mainly intended for oral drug delivery, in substitution of tablets, and, in 2015, the first 3D printed product (Spritam®), based on power bed-inkjet printing, was approved by FDA. Other printing processes commonly applied to pharmaceutical products are stereolithograpy (SLA) and fused-deposition modeling (FDM): in the first technique, a light source causes the polymerization of photocrosslinkable polymers, while the second one relies on the melting of polymers that are then deposited on a build plate layer-by-layer. Both techniques suffer a limit in the availability of polymers that can be applied to photocrosslinking and melting as printable materials and in the potential toxicity of some of those substances. Moreover, these techniques allow the production of solid dosage forms with rigid structures, and cannot be applied to the manufacture of soft products, such as high water content matrices, that are desirable candidates, for example, as wound dressings [3] or for tissue engineering applications. In a recent review by Jang and coworkers [4] advances in 3D printing of hydrogels are described, including low-temperature deposition associated to freeze-drying. In this paper an alternative to this technique, based on cryogenic prototyping followed by ionotropic gelation, previously described by Elviri and colleagues [5], was used to produce drug delivery systems, in the form of gels, from polymeric solutions. Two natural biopolymers, alginate and chitosan, were chosen, having useful characteristics such as safety, biodegradability, biocompatibility and chemical similarity with glycosaminoglycans composing extracellular matrices, that render them ideal as excipients in drug delivery systems and medical devices, including commercially available advanced wound dressings [6]. Ideally, dressings for chronic wounds should be changed less frequently as possible

and a sustained release of antimicrobial agents, such as silver sulfadiazine (SSD), is a desirable feature to control bacterial proliferation for the whole time of contact of the dressing with the wound bed as well as it is the capacity of the medication to be integrated by the tissue. Silver sulfadiazine exhibits fast and broad spectrum antimicrobial activity against both Gram positive and Gram negative bacteria [7-8] and it has been demonstrated to be effective also against multidrug resistant organisms [9-10].

Application of 3D printing to the production of hydrogels based on chitosan and/or alginate reported in literature are mainly conceived for tissue engineering [11] while few reports describe their use as drug delivery systems of SSD, which all rely on classical casting methods. Boateng *et al*. [12] described the development of freeze-dried alginate/gelatin bio-polymeric wafers for potential application on infected chronic wounds capable to release SSD within 7 hours at concentrations higher than the MIC but not in a controlled manner; Shao and colleagues [13] proposed genipin crosslinked chitosan sponges loaded with SSD having excellent antibacterial performances, while Fajardo [14] loaded SSD into chitosan/chondroitin sulphate films, reaching the maximum drug release in about 12 hours.

In this paper we aimed to evaluate both the contribution of 3D printed hydrogel geometries on SSD release and their effectiveness in terms of antimicrobial activity *in vitro* against Staphilococcus aureus (SA) and Pseudomonas aeuriginosa (PA). Different combinations of calcium alginate and chitosan hydrogels loaded with SSD were designed and produced, then constructs were characterized from a physicochemical point of view and their release profiles compared in order to evaluate their suitability as medicated wound dressings. Finally, demonstration of their efficacy was given.

7.2 Materials and methods

7.2.1 Formulation of printable polymeric solutions

Chitosan powder, (ChitoClear® Fg90 TM1874 - CAS 9012-76-4, degree of deacetylation 95%; molecular weight by gel permeation chromatography 150–200 kDa; allergen free, water insoluble, soluble in acid media, Primex, Island), was dispersed in acetic acid solution (2 % v/v) (Flex ultra-pure water, Elga Veolia, Italy) at the concentration of 6% w/v. The suspension was stirred magnetically for 24 h, then, at complete dissolution of the polymer, raffinose pentahydrate (Sigma Aldrich, USA) was added as rheological agent at the final concentration of 290 mM and stirred for further 12 h.

Sodium alginate (Ph.Eur. grade; molecular weight by gel filtration chromatography (GFC) 180–300 kDa; slowly soluble in water, Carlo Erba, Italy) was suspended at the concentration of 6% (w/v) in a mixture of ultrapure water and 28% ammonia 95:5 (v/v) (VWR, Germany) to help polymer dissolution.

7.2.2 Hydrogel design and production by 3D printing

Three-dimensional objects were designed and produced by means of a 3D printer built in house that exploits freeze deposition to give shape to polymeric solutions, as previously described. Briefly, a grid composed of overlapping parallel filaments, having a distance of 200 μm was drawn by Solidworks™ (Dassault Systems, USA) and the file converted by Slic3r™ (RepRap) into a machine code (.gCode) readable by the 3D printer. The 3D printer works by extruding the material loaded on a 5 mL syringe through a 26 G needle (inner diameter 192 μm) layer by layer. Size of hydrogels was customized, and, for following experiments grids of 1.5 x 1.5 cm were chosen; thickness was customized as well, so 5 or 20 layers were printed, resulting in 1 mm- or 4 mm-high hydrogels, respectively.

At the end of each printing process, the frozen polymeric hydrogel underwent an ionotropic gelation to maintain its structure. In the case of chitosan hydrogels, gelation occurred by exposition to ammonia vapors, while sodium alginate hydrogels were gelled by direct immersion in a $CaCl_2$ aqueous solution (3%, w/v).

After gelation, hydrogels were washed twice in 80 mL of ultrapure water for 10 minutes to remove the gelling agent.

7.2.3 Inclusion of SSD in hydrogels for controlled drug delivery

SSD stability was checked in presence of polymers and their co-solvents in solution before printing of hydrogels, revealing drug degradation, for this reason the drug was loaded on printed calcium alginate hydrogels by directly soaking them in a 5% ammonia aqueous solution into which SSD was dissolved at a concentration of 0.75 % (w/v). The choice of using ammonia for the preparation of the loading solution was due to the very low SSD solubility in water and other organic solvents. Each five-layers hydrogel was soaked in 3 mL of drug solution for 3 hours in amber containers on an orbital shaker (IKA, shuttler MTS 4). After soaking, hydrogels were stored in vials until use.

7.2.4 Water content and elasticity

Since water content and hydration state of hydrogels are critical for drug loading and release, the total water content of each kind of hydrogel was measured. 5 replicates of alginate and chitosan hydrogels, 5 layers thick, were produced as described above, washed once with ultrapure water, then gently blotted on filter paper to remove the excess of water present within the pores and finally accurately weighed. Then, hydrogels were totally dehydrated in an oven at 40°C and 200 mbar of pressure (Gallenkam vacuum oven). Once anhydrous, hydrogels were re-weighed and their water content was calculated using the following formula:

$$\% \text{ of water} = 100 - (Wa \times 100) / Ww$$

where:
Wa : Weight anhydrous
Ww: Weight wet

A traction dynamometer (Aquati AG MC1) was used to perform traction tests on alginate and chitosan hydrogels sized 48 x 14 mm and 20 layers-thick. Traction speed was set at 25 mm/min using a 5 daN top head cell and setting a distance between clips of 25 mm. Applied force and movement were digitalized by PowerLab 4/35 software and registered by LabChart®Pro software. Stress applied and elongation of the specimen were registered constantly. Thickness of specimen was measured by a digital thickness feeler (Mitutoyo Corporation) before traction tests.

7.2.5 Scanning Electron Microscopy (SEM) analysis

For a deep morphological characterization, SEM analyses were conducted. 5 layers- chitosan and alginate hydrogels were prepared; in particular, alginate samples with and without SSD were compared. Hydrogels were dehydrated by immersion twice for 10 minutes in increasing grades of ethanol from 50° to absolute. Hydrogels were then dried by the critical point drying technique (Balserz Union, FL) to obtain anhydrous samples avoiding structure deformations. Anhydrous hydrogels were then coated with gold (thickness 60 nm) and observed with the SEM (Philips 501, Holland). Digital photographs of hydrogels were analyzed by means of ImageJ software (NIH, Bethesda, USA) randomly measuring the Feret's diameter of 150 pores and determining their size distribution.

7.2.6 ATR FT-IR spectroscopy

Infrared ATR FT-IR spectroscopy was performed in order to evaluate the presence of the drug and to characterize its interactions with calcium alginate. Spectra were taken by a Nicolet 5700 (Thermo Scientific, USA) in the range 400-4000 wavenumbers (cm^{-1}) with a resolution of 30 scan per second. Spectra of SSD anhydrous powder, dried 3D alginate hydrogels loaded with SSD and dried 3D alginate hydrogel without the drug were collected.

7.2.7 Hydrogel combinations to modify drug release

Different hydrogel combinations were designed and realized with the aim of investigating their influence on the release kinetic of SSD. Drug was loaded only in 5 layers alginate hydrogels, which were then assembled with chitosan hydrogels and stuck together by droplets of sodium alginate solution.

Combinations tested were designed and identified as follows: (1) 3D printed 5 layers alginate loaded with SSD alone (A); (2) 3D printed 5-layers alginate + chitosan film (AF) The film in this construct was prepared by pouring chitosan solution in a mould, freezing it at -20 °C and then immersing it in a 1.5 M KOH solution for gelation [15]; final layer thickness was 3 mm (3) 3D printed 5-layers chitosan hydrogel + 3D printed 5-layers alginate (5CA); (4) 3D printed 20-layers chitosan hydrogel + 3D printed 5-layers alginate (20CA) (Figure 1).

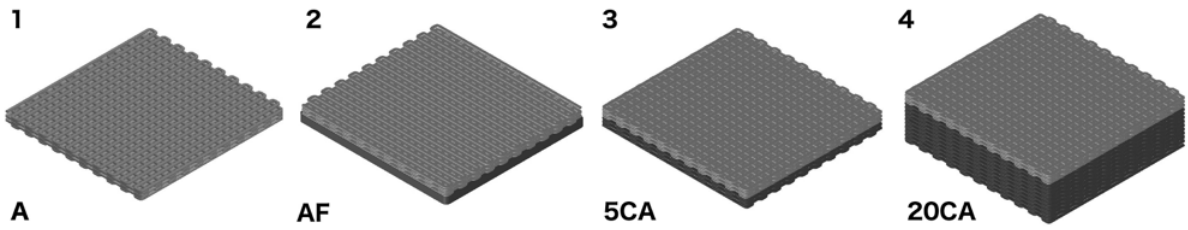

Figure 1. Schematic representation of 3D constructs, where light grey represents SSD loaded alginate hydrogels and dark grey represents chitosan hydrogels: (1) 3D printed 5 layers alginate loaded with SSD alone (A); (2) 3D printed 5-layers alginate + chitosan film (AF); (3) 3D printed 5-layers chitosan hydrogel + 3D printed 5-layers alginate (5CA); (4) 3D printed 20-layers chitosan hydrogel + 3D printed 5-layers alginate (20CA).

7.2.8 *In vitro* release tests

Release tests were performed using vertical diffusion Franz cells having a diffusion area of 3 cm^2 assembled to simulate the behavior of an exudating wound. Donor and receiver parts were separated by a regenerated cellulose membrane (diameter of pores 0.45 μm), previously boiled in ultrapure water for 1 hour to remove the air within the micropores and contingent contaminants: the membrane acted as a physical barrier to support hydrogels; receiver chamber was filled with 20 mL of a degassed buffer whose composition was intended to simulate wound fluid (SWF) composed of $CaCl_2$ anhydrous 0.02 M; NaCl 0.4 M, tris methylamine 0.08 M; pH 7.5. Cells were then placed in a thermostat bath at 37°C under magnetic stirring.

Calcium alginate and calcium alginate-chitosan constructs were placed in the donor chamber of the Franz cell, covering the whole diffusion area with the chitosan side (if present) facing down, in contact with the membrane; no further buffer was added on the donor chamber, that was closed with a waterproof cover to prevent solvent evaporation. At predetermined time points, 400 μL samples were taken from the receiving cell and collected in amber vials; withdrawn volume was restored by the same amount of fresh SWF.

The amount of released drug was evaluated by performing liquid chromatography-ultraviolet/visible (LC-UV/VIS) analysis. An LC Agilent 1200 binary pump (Agilent Technologies, UK) was used. Chromatographic separation was achieved on a C18 (250 x 4.6 mm, 10 μm) column (Supelco). The mobile phase consisted of water, acetonitrile and phosphoric acid in the proportions 90:9.1:0.1 % v/v, the flow rate of the mobile phase was maintained at 1.0 mL/min and detector wavelength at 254 nm. Injection volume was 20 μL volumes. Each sample was analyzed in triplicate. For the quantification of the samples collected from the release experiment standards from 1 to 20 μg/mL prepared in SWF were used to plot a calibration curve [$y = 36{,}42(SD\ 0.04)x$; $r^2 = 0.999$].

7.2.9 Cytotoxicity test

The effect of SSD release from the different assembles was evaluated in terms of cytotoxicity on human fibroblast cells. Human cells were isolated using the technique of explantation from a cutaneous biopsy and maintained in culture inoculating 200,000 cells/flask. Growth of human fibroblasts took place in Dulbecco's minimal essential medium (DMEM, Lonza) with penicillin and streptomycin and completed with fetal bovine serum at 10% (FCV, euroclone).

Assembles A, AF, 5CA and 20CA were prepared following the methods previously described, punched with a 6 mm of diameter circular stamp and subsequently sterilized by immersion in ethanol 70 % v overnight. Cell seeding was performed under laminar flow hood. Each assemble was washed in a PBS solution to bring them at physiological pH and to eliminate ethanol residues. Scaffold were then transferred individually into the wells of a 48 multi well culture plate (Corning). Once fibroblasts were grown, medium was removed and a PBS wash was done. 2 mL of a trypsin solution (Sigma Aldrich) were added to detach cells from the flask and incubated at 37°C for almost 2 minutes to let the enzyme work. Culture medium with serum was added to deactivate the enzyme and cells suspended in the medium were transferred in a sterile 15 mL Falcon tube. A centrifugation was done at 1500 rpm for 5 minutes to concentrate cells in a pellet and the culture medium containing trypsin was removed. The obtained pellet was resuspended in a known volume of fresh culture medium, 10 µL were sampled for the cells count by means of a Burker chamber and the subsequent determination of cells concentration in the suspension. Once the cells number was determined, 75000 cells were seeded in each well, incubated at 37°C for 4 hours in atmosphere containing 5 % of CO_2. After this procedure and once cells attached to the wells bottom, previously prepared scaffolds were transferred in the wells where cells were incubated (each assemble was tested in triplicate). Wells not containing scaffolds were prepared with the same procedure as controls. After 24 hours of incubation cytotoxicity was quantified using the metabolic dye resazurin.

The resazurin test was performed to observe and quantify cells death caused by the different release of SSD from the scaffolds. A resazurin solution 1mg/mL was prepared in PBS, then filtered with a 0.22 µm filter to sterilize it and to eliminate possible precipitates. This stock solution was preserved in the dark at 4°C. Successively, stock solution of resazurin was diluted 1:100 in culture medium serum free, obtaining a concentration of 10 mg/mL. Culture medium present in the multiwell where scaffold where incubated for 24 hours was drawn and a wash with PBS was done. Then, 500 µL of diluted resazurin solution was added into the well containing scaffold and in those that served as controls and incubated for 3 hours at 37°C. After the 3 hours 100 µL was sampled from each well and placed in a black 96 multiwell. Fluorescence measurement took place by means of a fluorimeter set at 560 nm and filter in emission at 590 nm during the analysis. For controls, as mentioned before, cells not in contact with the drug were used.

7.2.10 Antimicrobial activity

Antimicrobial activity evaluation against two strains of bacteria (gram$^+$ and gram$^-$) was assessed. Multi-drug resistant strains of *Staphilococcus aureus* (ATCC 25923) and *Pseudomonas aeruginosa* (ATCC 27853) were considered for such test, since they are responsible of frequent infections in chronic wounds. Kirby-Bauer technique was adopted and *ad hoc* – modified in order to assay 3D printed hydrogel scaffolds as drug-loaded core of biocidal medicated dressings. 6 mm diameter stamps were used to obtain circular drug-loaded alginate scaffolds (same size as the antibiogram discs) and kept in the fridge at 4°C prior to experiment start. At the same time bacteria were seeded in pure culture and inoculated in a Mueller Hinton Broth at 37°C in aerobic conditions for 1-2 hours (0.5 McFarland). Bacterial suspension was seeded through the use of sterile tampons on a Mueller Hinton Agar terrain (carefully covering the entire Petri dish). At this time scaffolds can be applied by the use of sterile forceps. Each test was conducted in duplicate. A negative and positive control were established: a negative one with the only scaffold, to ensure it was not contaminated and a positive one consisting in a Petri dish seeded with bacteria but free of scaffolds. Finally, all the plates were incubated at 37°C for 18-24 hours. Result evaluation was based on inhibition ring presence/absence, followed by its determination in terms of diameter. Bacterial sensibility to antimicrobial specimen was directly proportional to this latter parameter.

7.3 Results and discussion

7.3.1 Characteristics of chitosan and alginate solutions and SSD stability

In this paper, the feasibility of preparing 3D printed polymer-based drug delivery systems was explored.

Chitosan and sodium alginate solutions' viscosity was measured to check their printability: sodium alginate solution had a viscosity of 45875 ± 28 cP at 60 rpm, while the viscosity of chitosan solution resulted 18500 cP ±30 cP at 60 rpm. Rheological tests performed on chitosan and sodium alginate solutions prepared for 3D printing outlined their suitability for cryogenic prototyping, since viscosity is a crucial parameter for the accurate deposition of three-dimensional structures according to the design. These values were adequate for 3D printing by our system.

SSD was chosen as model drug and introduced in hydrogels after the completion of the 3D printing procedure by exploiting a soaking technique. SSD resulted stable in contact with the

alginate hydrogel, in particular, stability was checked in solutions with the polymer up to 21 days, showing a recovery of 102±0.2 %.
Since physico-chemical features of hydrogels could have a determining influence on this process rather than on their behavior as systems for controlling drug delivery, 3D printed hydrogels were deeply characterized.

7.3.2 Physico-chemical characterization of printed hydrogels

7.3.2.1 Evaluation of water content and elasticity

In order to characterize alginate and chitosan hydrogels, water content was measured. Alginate hydrogels resulted to have 93.18 % ± 0.88 % of water in their swollen state. The water percentage present in chitosan hydrogels resulted 92.76 % ± 1.17 %. T-test performed on gravimetric analysis carried out for measuring water content revealed there were not statistical significant differences between hydrogels prepared from the two polymers: this was considered a positive element for their association into drug delivery systems, since a water content imbalance between different types of hydrogels could alter liquid movement within the system, with consequent alteration of drug diffusion through it. Elasticity is another important aspect when designing a drug delivery system, especially for those intended for application on soft tissues such as skin, both in terms of handling and of adaptation to the area of application. Young's modulus of calcium alginate hydrogels reached 0.582 ± 0.019 MPa whereas that of chitosan ones resulted 0.365 ± 0.015 MPa. Student's t-test confirmed that the difference of elasticity values of the different polymeric hydrogels was statistically significant ($p < 0.005$). Traction tests put into evidence a statistically significant smaller elasticity of alginate hydrogels, as testified by the lower value of deformation with respect to chitosan hydrogels, that corresponded to a weaker consistence of gels. For this reason, taking advantage of chitosan mechanical resistance as well as of the possibility of loading SSD on alginate hydrogels, we combined 3D printed scaffolds made from the two biomaterials in order to create tougher structures, easier to handle in view of a possible application as drug delivery systems, for example, for the treatment of infected wounds.

7.3.2.2 Determination of loaded drug

The total amount of drug loaded by alginate hydrogels was estimated by dissolving them and by measuring the drug absorbance at 305 nm. After 1 h each hydrogel had reached its maximum

loading ability with a mean SSD content of 760 μg ± 65 μg (CV 8.7%) no significant differences were found in the estimate of loaded drug after 3 or more hours, suggesting that an equilibrium between absorption and release of the drug by the hydrogel had been reached by 1 hour of soaking. Considering the volume of each hydrogel (0.127 mL) and water content (93.18% corresponding to 0.118 mL) the maximum amount of drug that could be loaded, by complete substitution of water with drug solution, was estimated in 885 μg. The efficiency of loading at equilibrium is 86%.

7.3.2.3 SEM analysis

Calcium alginate hydrogels with and without the drug were characterized morphologically by SEM (Figure 2).

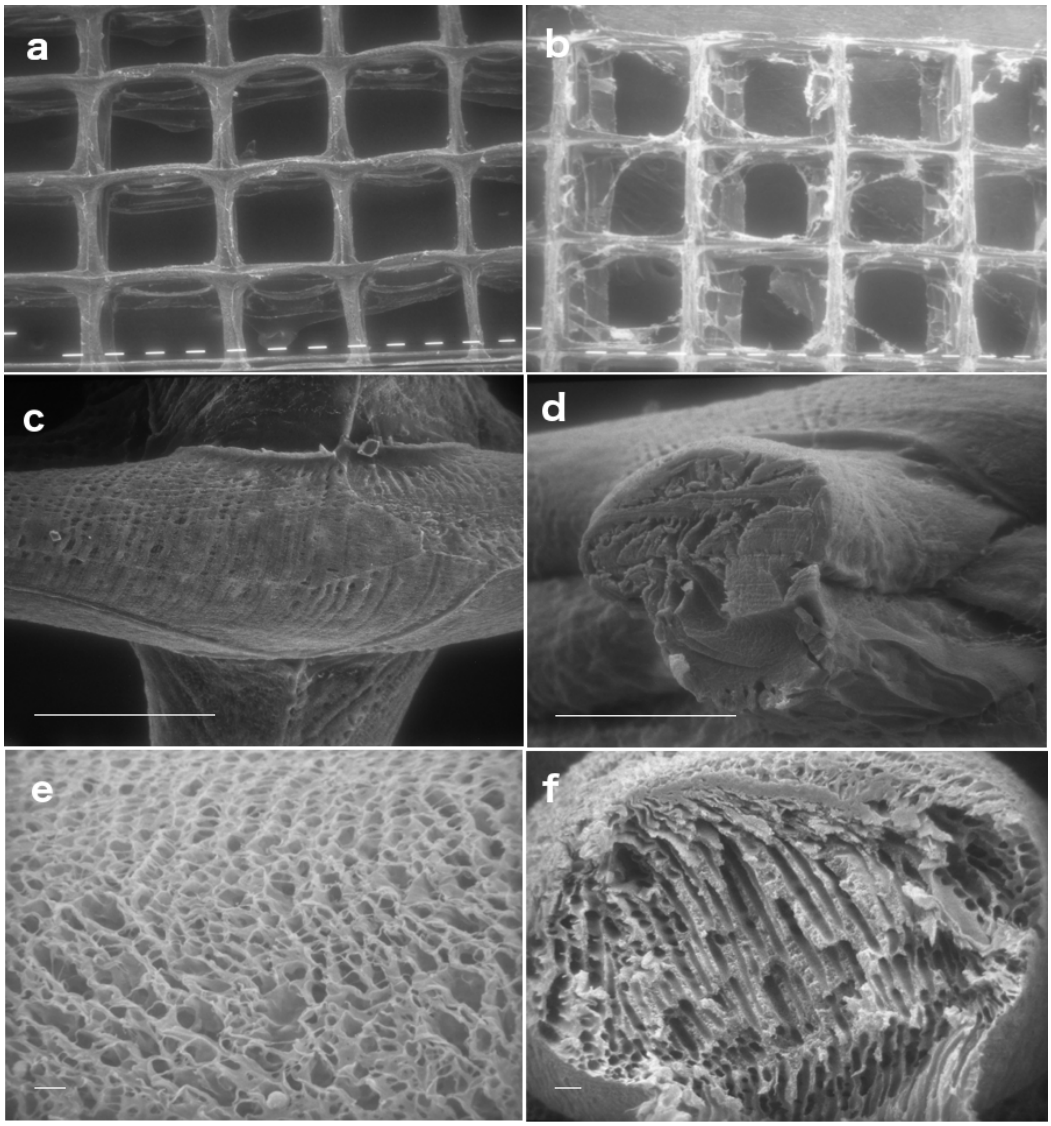

Figure 2. SEM picture of a calcium alginate hydrogel (A) without SSD and (B) containing SSD (magnification 40 X: scale bar: 100µm). Calcium alginate hydrogel surface (C) and cross section (D) (magnification 320 X; scale bar: 100µm). (E) surface (magnification 1250 X) and (F) cross section (magnification 640 X; scale bar: 10µm) of a chitosan hydrogel gelled in ammonia vapors.

By comparing the reported images it is possible to notice that the alginate hydrogel (Figure 2A) presented a well-defined structure with respect to the loaded one (Figure 2B), where surface

precipitation of the drug occurred after dehydration; a partial dissolution of the hydrogel is not excluded, considering the gelation by immersion in $CaCl_2$. In figure 2 C and D calcium alginate hydrogel details are highlighted; with respect to chitosan hydrogel both the surface and the cross section presented a much more compact structure characterized by few and superficial not-interconnected pores.

Chitosan hydrogel gelled in ammonia vapors and dehydrated by Critical Point Drying technique showed a pore size distribution between 0.5 and 13 μm on the surface and between 2 and 38 μm in the cross section (figure 2 D and E); on the other hand the layer of chitosan obtained by freeze-casting showed a compact surface layer, as previously reported [16]. Morphological observation by SEM revealed that drug-loaded hydrogels were subjected to a partial dissolution with a reduction in the amount of alginate. The mechanism of gelation of alginate salts relies on the ionotropic cross-linking mediated by divalent cations, such as Ca^{2+} ions but the stability of these gels in fluids is subject to the presence of other cations: monovalent cations, as silver ions associated to sulfadiazine during the loading procedure, can exchange with Ca^{2+} ions present in the alginic mesh causing a progressive dissolution and loosening of the network [17].

7.3.2.4 ATR FT-IR spectroscopy

To better understand the incorporation of the drug into the hydrogel, the ATR-FTIR spectra of the alginate hydrogel and of the alginate SSD containing hydrogel were compared (Figure 3).

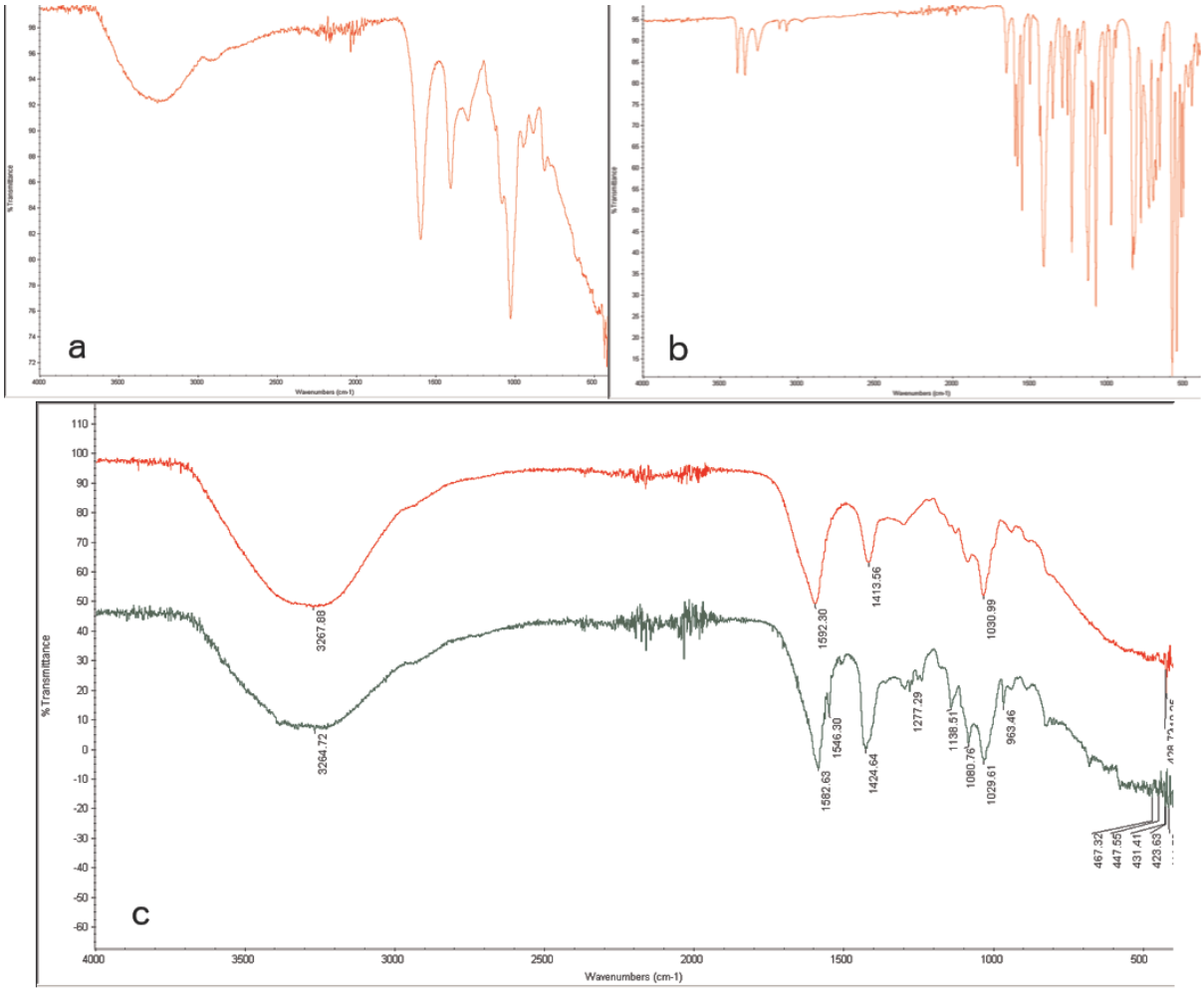

Figure 3. ATR-FTIR spectrum of (A) sodium alginate and (B) silver sulfadiazine powders. Comparison between the AT-FTIR spectra of alginate hydrogel (in red) and the alginate SSD containing hydrogel (in green).

Spectrum of sodium alginate powder (Figure 3A) showed typical signals in the 4000 – 600 cm^{-1} wavelength interval. In particular, a wide peak at 3450 cm^{-1} typical of the -OH group is present, as well as two peaks at 1618 and 1440 cm^{-1} for the -COO- group and an acute peak at 1050 cm^{-1} for the C = O. Analogously, the spectrum of SSD powder (Figure 3B) revealed characteristic absorbance peaks at 3390 and 3340 cm^{-1} referred to the stretching of $-NH_2$ symmetric and asymmetric groups, respectively. The group at 1655 cm^{-1} corresponds to the $-NH_2$ group whereas those at 1595 and 1500 cm^{-1} are related to the phenolic skeleton. Peaks observed at 1230 and 1130

cm^{-1} are characteristic of the asymmetric vibration of SO_2 group. Aromatic vibration appears at 1070 cm^{-1}.

The loading of the drug is demonstrated by the appearance, in the fingerprint zone, of peaks specific of SSD which are not present in the unloaded hydrogel. In particular, peak at 1277.29 cm^{-1} that in SSD powder spectrum appeared at 1230 and 1130 cm^{-1} that was characteristic of the asymmetric stretching vibration group SO_2. Such shift towards lower wavenumbers might suggest the interaction of this SSD functional group with the polymeric matrix. Furthermore, in the SSD-containing hydrogel, two peaks appear compared to the alginate one, at 1139 and at 963 cm^{-1}.

7.3.3 Release tests

Different hydrogel constructs were designed and built in order to modify drug release profile. Chitosan hydrogels were associated to drug loaded alginate hydrogels with the purpose of conferring a tougher consistence to the structure as well as exploiting useful chitosan characteristics in terms of biocompatibility and antimicrobial action. Release tests performed in Franz cells were exploited to evaluate the cumulative drug release with respect to time from different combinations of calcium alginate and chitosan hydrogels. Analyzed samples showed that the four profiles were characterized by different release rates and different amounts of overall released drug.

As it is shown in figure 4, alginate hydrogel shows the fastest release rate and the highest quantity released, with a burst release of the drug.

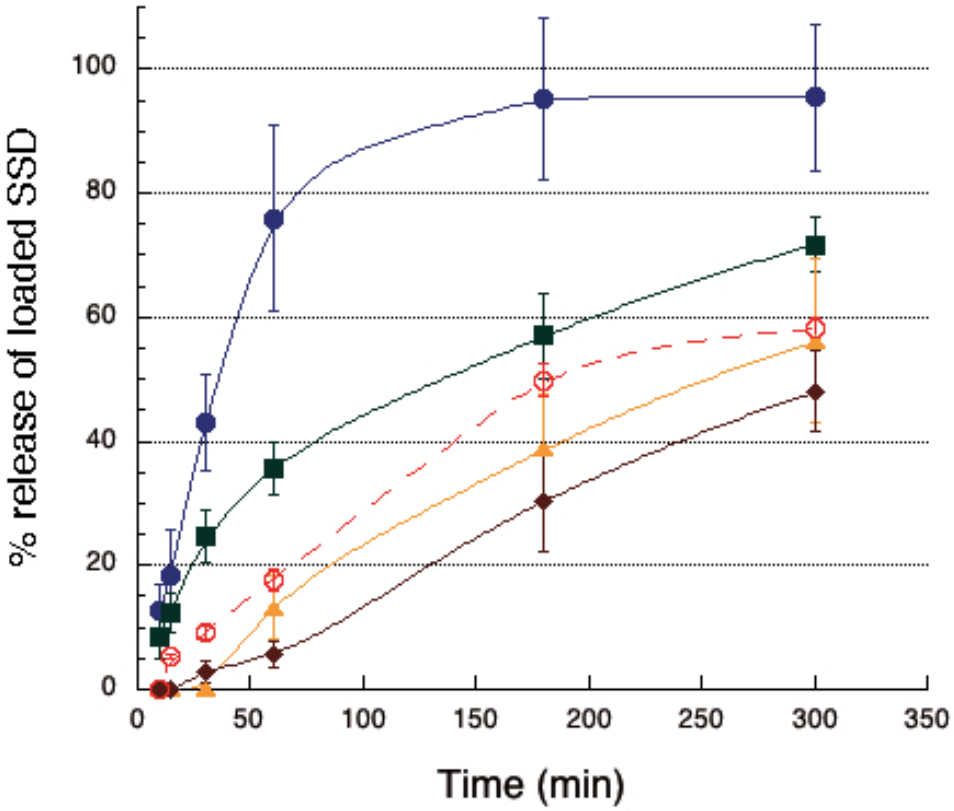

Figure 4. Release profile of SSD from different hydrogel combinations. A (circle), AF (triangle); 5CA (square), 20CA (rhombus).

In particular, during the first 60 minutes the 75.88 ± 14.98 % of loaded drug is released, reaching almost 100 % after 3 hours. The simplest combination of alginate hydrogels we designed was with a thin chitosan film, obtained by direct casting, as described in methods. This construct (AF) showed a maximum drug release of 56.24 ± 13.38 % after 5 hours. Both the rate and cumulative amount of released drug are lower with respect to alginate gels.

The 5CA combination showed a maximum drug release of 71.75 ± 4.40 % at 5 hours. Such difference with respect to alginate gel is attributable to the time needed by the solvent to diffuse through chitosan layers and reach alginate hydrogel. With respect to AF construct, no lag time is observed: no barrier to solvent absorption is exerted by chitosan hydrogel, thanks to macroporosity conferred by 3D printing design, and the release within few minutes, analogously to alginate-only constructs, could be ascribed to the drug located on the surface of alginate hydrogel, which is easily reached by SWF by capillary action. In an attempt to estimate the relation between chitosan hydrogel's thickness and drug release, the 20CA construct was designed: such modification lead to a consistent drop in drug released, 48.02 ± 6.53 % at 5 hours, which was on the whole lower than the AF construct. The release starts after an initial lag time, attributable to the time needed by SWF to wet chitosan layers and reach SDD-loaded alginate gel.

After that an almost linear drug kinetic is observed, characterized by a progressive reduction of the release rate. The rate and amount of drug released from developed prototypes were monitored over time. Calcium alginate scaffolds showed the fastest and highest release of SSD: such speed can be explained by the fact that the hydrogel tested is directly in contact with the membrane, allowing a fast absorption of SWF by capillary action through the whole thickness of the hydrogel, its full hydration and fast release of the drug by diffusion. In particular, macropores formed by 3D deposition constitute a preferential way for SWF to reach the top of the hydrogel, leading to a fast diffusion of the drug that is located on the surface; diffusion of SWF through hydrogel filaments could be responsible for the slower release of drug trapped within the hydrogel observed in the other three constructs, since the drug had to follow a windy path before leaving the polymeric matrix. In the AF construct a lag-time is noticed: this reduction in release rate can be ascribed to the fact that chitosan film is a compact structure acting as a barrier to drug diffusion, also delaying SWF capillary diffusion in alginate hydrogel.

All constructs with chitosan, both films or 3D printed hydrogels, lead to an overall reduction of the final amount of drug released, that decreased increasing chitosan thickness and that resulted statistically different from the loaded alginate scaffold and as well significantly different among them. In all cases a plateau is reached and no further drug release was observed after 5 hours (data not shown): this suggests that the barrier effect created by the presence of chitosan could be attributable not only to a physical segregation, strongly prevailing in chitosan film, but also to molecular interactions occurring between SSD and the polymer that prevents drug release and is proportional to the amount of chitosan encountered by the drug along its diffusion path. Water content analysis reported above lead to exclude that differences in drug delivery could be ascribed to a different hydration state of hydrogels.

From a therapeutic point of view, amounts of drug that are released are all above the reported MIC of SSD, which, depending on the bacterial species, ranges from 50 to 100 microg/ml [18], suggesting that hydrogels could be effective, if applied on wounds, in controlling bacterial proliferation.

7.3.4 Cytotoxicity tests

Cytotoxicity tests were conducted in order to evaluate the effect of SSD on cells vitality and to investigate whether the different releases could determine a difference or not. The results obtained demonstrated that the vitality of cells in contact with the drug loaded assembles is much lower compared to the control. In particular, fluorescence values were 29002 ± 436 units for A scaffold,

23234 ± 7243 for the 20CA, 29074 for AF and 28651 ± 1277 for the 5CA assembles whereas the control showed a fluorescence of 48505 ± 2831 units. Compared to the control the fluorescence of scaffold A showed a reduction of fluorescence of 40.20 ± 1.50 %, 52.10 ± 31.17 % for 5CA, 40.05 % for AF and 40.93 ± 4.45 % for 20CA constructs ($p > 0.05$). The reduced fluorescence values observed for the constructs indicate that already after 24 hours the release of SSD causes suffering to the cells. This data is confirmed from what is reported in literature, in fact, different studies report the cytotoxic effect of SSD on *in vitro* cell cultures. On the basis of the release experiments it was expected that the major cytotoxicity would have been determined by A scaffolds, since it was characterized by the major quantity of SSD released and in the shortest time, as previously described. From the obtained data after 3 hours of incubation the assemble that causes more cytotoxicity is the 5CA, that led to a reduction of fluorescence of 52% compared to the control. To explain these results is necessary to take into consideration that converts resazurin in resafurin is an oxidation reaction, that is also one of the main mechanisms of SSD degradation. The observed cell death is thus probably determined not only by the intrinsic drug cytotoxicity but also by its degradation. By the way it is possible to affirm that independently from the quantity released and from its kinetic SSD is toxic for cells.

7.3.5 Kirby-Bauer antimicrobial activity assay

A further and more concrete demonstration of the potential efficacy of the tested prototypes was given by antimicrobial activity assays. The drug loaded alginate scaffold, that is the core of all constructs developed, was applied as described in material and methods section. The growth inhibition resulted complete (100%) for both the bacteria tested after 18-24 hours of incubation (Figure 5). The inhibition ring was measured, reaching 10 mm diameter, probably due to drug diffusion through agar layer and highlighting high sensibility of bacteria to SSD. It's reasonable to hypothesize their use in combination with chitosan scaffolds could be exploited for the treatment of chronically infected wounds, that can necessitate a slower and more sustained release.

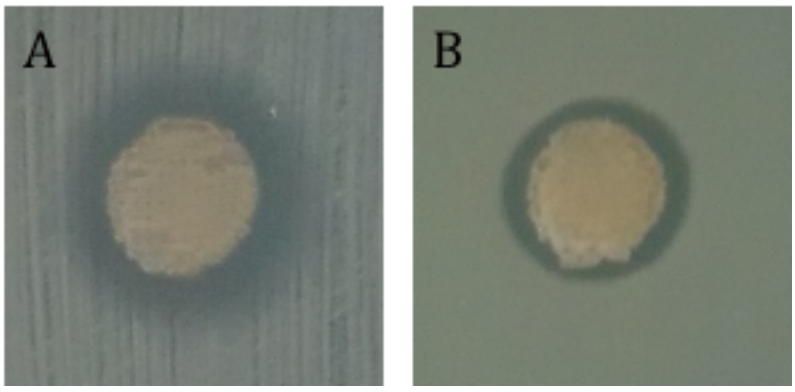

Figure 5. Kirby-Bauer antimicrobial activity assay against multi-drug resistant strains of S. aureus (A) and P. aeruginosa (B).

7.4 Conclusions

In conclusion, an innovative 3D printing technique for hydrogel preparation as drug delivery systems for controlled release of SSD is described. Different constructs were developed: this variable resulted in a dramatic change in terms of rate and amount of drug released, offering a key for the tailoring of drug administration. The versatility of 3D printing, allowing the production of complex structures, enables to explore this route as suggested by Boetker with respect to different excipients [19] and by Goyanes on solid dosage forms [20]. Further experiments on different geometries will prompt the way for a more and more sophisticated control of drug release.

7.5 Acknowledgements

The Authors thank Dr. Fabio Corradini of the University of Parma for providing Figure 1, Mr. Davide Dallatana for his support in SEM analysis, and Cinzia Reverberi from the Department of Veterinary Science, University of Parma, for her kind support in the antimicrobial tests.

7.6 References

[1] Alhnan M.A., Okwuosa T.C. Sadia M., Wan K., Ahmed W., Arafat B. Emergence of 3D Printed Dosage Forms: Opportunities and Challenges Pharmaceutical research 2016; 33: 1817-1832

[2] Lepowsky E. and Tasoglu S. 3D printing for drug manufacturing: A perspective on the future of pharmaceuticals. Int J Bioprint 2018; 4: 119-124.

[3] Paul W. Sharma C.P. Chitosan and Alginate Wound Dressings: A Short Review Trends Biomater. Artif. Organs 2004; 18: 18-23.

[4] Jang T.S., Jung H.D., Pan H.W., *et al*. 3D printing of hydrogel composite systems: Recent advances in technology for tissue engineering. Int J Bioprint 2018; 4: 126.

[5] Elviri, L., Foresti, R., Bergonzi, C., Zimetti, F., Marchi, C., Bianchera, A., *et al*. Highly defined 3D printed chitosan scaffolds featuring improved cell growth. Biomedical Materials 2017; 12: 045009.

[6] Elviri, L., Bianchera, A., Bergonzi, C., & Bettini, R. Controlled local drug delivery strategies from chitosan hydrogels for wound healing. Expert Opinion on Drug Delivery 2016; 14: 897–908.

[7] Castellano J.J., Shafii S.M., Ko F., Donate G., *et al*. Comparative evaluation of silver-containing antimicrobial dressings and drugs. Int. Wound. J 2007; 4: 114–122.

[8] Ip M., Lui S.L., Poon V.K.M., Lung I. and Burd I. Antimicrobial activities of silver dressings: An *in vitro* comparison. J. Med. Microbiol. 2006; 55: 59–63.

[9] Melayie A., and Youngs J.W. Silver and its application on antimicrobial agents. Expert Opin. Ther. Pat 2005; 15: 125–130.

[10] Silvestry-Rodriguez N., Sicairos-Ruelas E.E., Gerba C.P., Bright K.R. Silver as disinfectant. Rev. Environ. Contam. T 2007; 191: 23–45.

[11] Liu Q., Li Q., Xu S., Xheng Q., Cao X. Preparation and Properties of 3D Printed Alginate–Chitosan Polyion Complex Hydrogels for Tissue Engineering Polymers 2018; 10: 664-670.

[12] Boateng J., Burgos-Amador R., Okeke O., Pawar H. Composite alginate and gelatin based bio-polymeric wafers containing silver sulfadiazine for wound healing. International Journal of Biological Macromolecules 2015; 79: 63–71.

[13] Shao W., Wu J., Wang S., Huang M., *et al*. Construction of silver sulfadiazine loaded chitosan composite sponges as potential wound dressings. Carbohydrate Polymers 2017; 157: 1963–1970.

[14] Fajardo A.R., Lopes L.C., Caleare A.O. Britta E.A. *et al*. Silver sulfadiazine loaded chitosan/chondroitin sulfate films for a potential wound dressing application. Materials Science and Engineering C 2013; 33: 588–595.

[15] Bettini R., Romani, A. A., Morganti, M. M., & Borghetti, A. F. Physicochemical and cell adhesion properties of chitosan films prepared from sugar and phosphate- containing solutions. European Journal of Pharmaceutics and Biopharmaceutics 2008; 68: 74–81.

[16] Elviri L, Asadzadeh M, Cucinelli R, Bianchera A and Bettini R. Macroporous chitosan hydrogels: effect of sulfur on the loading and release behaviour of amino-acid based compounds Carbohydrate Polym. 2014; 132: 50–8.

[17] Bajpai S. K., Sharma S. Investigation of swelling/degradation behaviour of alginate beads crosslinked with Ca^{2+} and Ba^{2+} ions. React. Funct. Polym. 2004; 129–140.

[18] Carr H.S., Wlodkowski T.J. and Rosenkranz H.S. Silver sulfadiazine: *In vitro* antibacterial activity. Antimicrobial agents and Chemotherapy 1973; 4: 585-587.

[19] Boetker J., Water J.J., Aho J., Arnfast L. *et al*. Modifying release characteristics from 3D printed drug-eluting products. European Journal of Pharmaceutical Sciences 2016; 90: 47–52.

[20] Robles Martinez, P. Goyanes A., Basit A.W., Gaisford S. Fabrication of drug-loaded hydrogels with stereolitographic 3D printing. International Journal of Pharmaceutics 2017; 532: 313-317.

8 Chapter 5: “Functional Fibronectin Adsorption on Aptamer-Doped Chitosan Modulates Cell Morphology by Integrin-Mediated Pathway”

Ludovica Parisi[1,2,*], Andrea Toffoli[1,2], Massimiliano G. Bianchi[2], Carlo Bergonzi[3], Annalisa Bianchera[3] , Ruggero Bettini[3], Lisa Elviri[3] and Guido M. Macaluso[1,2,4]

[1] Centro Universitario di Odontoiatria, Università degli Studi di Parma, Via Gramsci 14, 43126 Parma, Italy; andrea.toffoli@unipr.it (A.T.); guidomaria.macaluso@unipr.it (G.M.M.)
[2] Dipartimento di Medicina e Chirurgia, Università degli Studi di Parma, Via Gramsci 14, 43126 Parma, Italy; massimiliano.bianchi@unipr.it
[3] Dipartimento di Scienze degli Alimenti e del Farmaco, Università degli Studi di Parma, Parco Area delle Scienze 59/A, 43124 Parma, Italy; carlo.bergonzi@studenti.unipr.it (C.B.); annalisa.bianchera@unipr.it (A.B.); ruggero.bettini@unipr.it (R.B.); lisa.elviri@unipr.it (L.E.)
[4] IMEM-CNR National Research Council, Parco Area delle Scienze 37/A, 43124 Parma, Italy

Published on 8 March 2019, Materials Vol 12, 812; doi:10.3390/ma12050812

OPEN ACCESS

IF 2.972

Personal contribution

CB performed the experimental work related to materials formulation and processing.

Abstract

A decisive step in cell-biomaterial interaction is represented by the adsorption of proteins at the interface, whose fine control may be useful to trigger proper cell response. To this purpose, we can selectively control protein adsorption on biomaterials by means of aptamers. Aptamers selected to recognize fibronectin dramatically enhance chitosan ability to promote cell proliferation and adhesion, but the underlying biological mechanism remains unknown. We supposed that aptamers contributed to ameliorate the adsorption of fibronectin in an advantageous geometrical conformation for cells, thus regulating their morphology by the proper activation of the integrin-mediated pathway. We investigated this possibility by culturing epithelial cells on chitosan enriched with increasing doses of aptamers in the presence or in the absence of cytoskeleton pharmacological inhibitors. Our results showed that aptamers control cell morphology in a dose dependent manner ($p < 0.0001$). Simultaneously, when the inhibition of actin polymerization was induced, the control of cell morphology was attenuated ($p < 0.0001$), while no differences were detected when cells contractility was challenged ($p > 0.05$). Altogether, our data provide evidence that aptamers contribute to control fibronectin adsorption on biomaterials by preserving its conformation and thus function. Furthermore, our work provides a new insight into a new way to accurately tailor material surface bioactivity.

Keywords: DNA aptamers; biomaterials; fibronectin; integrins; cell morphology

8.1 Introduction

Biological tissues are complex systems and their structural and molecular organizations rely on their functions. As such, constructs for tissue engineering (TE), which are designed to restore, replace or regenerate lost damaged tissues, have to be accurately tuned in order to trigger an active dialogue with the surrounding biological milieu, most importantly cells, thus promoting proper healing and regeneration [1,2].

Chitosan is a polysaccharide derived from the partial de-acetylation of chitin, the main component of crustacean and arthropods exoskeleton. Chitin de-acetylation, which occurs through enzymatic or chemical hydrolysis under severe alkaline conditions, confers to chitosan the capacity to be easily protonated and unique structural versatility, thus making it an optimal candidate for TE scaffold fabrication [3,4]. Furthermore, it has been widely described that chitosan possesses high affinity for proteins, which are of the utmost importance in addressing cell response at the interface [4]. However, our previous experiences highlighted a low-supportive capacity of chitosan in term of cell colonization [5]. To justify the mismatch between high protein adsorption and poor cell response, according to Andrade *et al*. we previously hypothesized that the cationic properties of chitosan may induce a shift in protein conformation, that randomly determine which side of the molecule should interact with the material and which with the surrounding milieu, thus potentially influencing the exposure of responsive points for cells [6,7]. Therefore, the preservation of pristine protein conformation functionality at the interface of chitosan is desirable. To address this issue, we have recently conferred to chitosan a selective binding capacity, by means of aptamers (Figure 1) [8]. Aptamers are small oligonucleotides, which are able to recognize, bind and retain target molecules, including proteins, by assuming a high specific three-dimensional conformation [9]. 2 scaffold fabrication [3,4]. Furthermore, it has been widely described that chitosan possesses high affinity for proteins, which are of the utmost importance in addressing cell response at the interface [4]. However, our previous experiences highlighted a low-supportive capacity of chitosan in term of cell colonization [5]. To justify the mismatch between high protein adsorption and poor cell response, according to Andrade *et al*. we previously hypothesized that the cationic properties of chitosan may induce a shift in protein conformation, that randomly determine which side of the molecule should interact with the material and which with the surrounding milieu, thus potentially influencing the exposure of responsive points for cells [6,7]. Therefore, the preservation of pristine protein conformation functionality at the interface of chitosan is desirable. To address this issue, we have recently conferred to chitosan a selective binding capacity, by means of aptamers (Figure 1) [8]. Aptamers are small

oligonucleotides, which are able to recognize, bind and retain target molecules, including proteins, by assuming a high specific three-dimensional conformation [9].

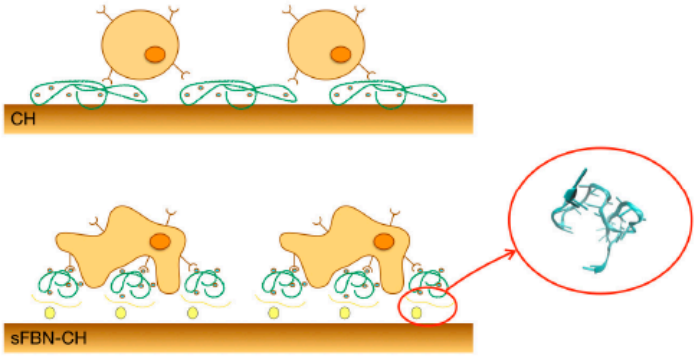

Figure 1. Diagram representing the rationale for the aptamer-coated scaffold to retain fibronectin in a suitable geometric conformation. Un-coated scaffold (CH) adsorbs fibronectin from the surrounding milieu, mostly inducing the masking of cell binding domains. Aptamers specifically lead the adsorption of fibronectin (sFBN-CH) and enrich scaffold with docking points for effective cell adhesion. The 3D rendering of the anti-fibronectin aptamer is a courtesy of Base Pair Biotechnologies (Pearland, TX, USA).

In particular, we have focused our previous efforts on fibronectin (FBN) [8]. FBN has been chosen as a target, because it is a protein abundant in wounded tissues and that plays a pivotal role in cell adhesion thank to the presence of cell binding domains within its structure, including the minimal recognition sequence for cell integrins (Arginine-Glycine-Aspartic Acid-RGD peptide) [10].

Integrins are a large family of homologous transmembrane receptors, constituted of two non-covalently associated glycoprotein subunits, alpha (α) and beta (β). After ECM molecules recognition (e.g., FBN), integrins are activated, α and β parts cluster and the cytoplasmic tail of the β subunit binds intracellular proteins that form mature focal adhesions, which interact with actin bundles to control cytoskeleton organization and thus cell shape [11]. The α5β1 integrin is the isoform known to bind FBN and it is further recognized that a minimal conformational change in FBN tertiary structure greatly diminishes the ability of α5β1 to bind it [12].

Selective FBN chitosan (sFBN-CH) was obtained dressing chitosan by means of aptamers selected for recognizing FBN. Aptamer-modification showed for the first time to dramatically improve murine osteoblasts (MC3T3-E1) colonization on chitosan, as to better preserve pristine FBN conformation once adsorbed on chitosan [8,13].

The aim of the present work is to confirm that the molecular mechanisms behind the amelioration of cell behavior at the interface of sFBN-CH are related to FBN functional adsorption, thus modulating cell shape and spreading by actin modulation. To this purpose, we studied the shape of cells on chitosan modified with increasing amounts of anti-FBN aptamers and under cytoskeleton modulation.

8.2 Materials and methods

8.2.1 Specimens

8.2.1.1 Chitosan preparation

Chitosan discs were prepared as previously described [8]. Briefly, a 2% chitosan solution was prepared by dissolving purified 90% de-acetylated chitosan powder (A.C.E.F., Piacenza, Italy) in a 1% acetic acid solution (Sigma-Aldrich, Saint Louis, MO, USA). D(+)-Raffinose (Sigma-Aldrich) was then added at a final concentration of 290 mM as viscosity modifying agent [14]. The one-milliliter solution was thus spread out onto a glass support to obtain a uniform film 0.25 mm thick and dried at 45 °C for 1 h in a ventilated oven. The film was thus transferred in a 5% potassium hydroxide (Sigma-Aldrich) gelation solution for 24 h and subsequently cut to discs fitting for 48-wells culturing plate. Chitosan discs were rinsed twice in Phosphate Buffer Saline (PBS, Thermo Fisher Scientific, Waltham, MA, USA) and cleaned under UV light for 10 min.

8.2.1.2 Anti-Fibronectin Aptamer

Single-stranded DNA-based aptamers screened against human and bovine FBN were used in this study (Base Pair Biotechnologies, Pearland, TX, USA). Aptamers were modified with a carbon chain containing a disulfide bond on their 3'-end and with a biotin on their 5'-end.
Prior to chitosan functionalization, thiol group at the 3'-end was exposed by reducing the disulfide bond with aptamer reducing buffer (Base Pair Biotechnologies, Pearland, TX, USA) for 10 min. Excess of reducing agent was then removed with a chromatographic column (mini Quick Spin Oligo Columns, Roche Life Science, Branford, CT, USA) and aptamers were finally diluted at their working concentration in aptamer folding buffer (Base Pair Biotechnologies) [8,15].

8.2.1.3 sFBN-CH and CH

The surface of chitosan discs was modified with anti-FBN aptamers by exploiting chitosan capacity to spontaneously adsorb sulfur-containing compounds [16]. Each chitosan disc was incubated with 100 μL of anti-FBN solution for 1 h (sFBN-CH), while unmodified chitosan (CH) was incubated 1 h with 100 μL of aptamer folding buffer and used as a control as previously described [8].
Four different anti-FBN aptamer concentrations were used for the test groups: 0.05, 0.1, 0.2 and 0.4 μg/μL. Previous studies have been conducted to assess the dose of aptamers [8].

8.2.2 Protein adsorption study

8.2.2.1 Bradford assay

Bradford assay was used to study the time-course of blood plasma proteins and of pure FBN adsorption to chitosan with or without aptamers.
To this purpose, discs were soaked for 1 h in 200 μL of PBS supplemented with 2% of human serum (Pooled Normal Human Serum, Innovative Research, Peary Court, FL, USA) either of pure FBN (F0895, Sigma-Aldrich) at a concentration comparable with that present in a 2% human serum solution (0.02 mg/mL). Protein amount in supernatants was quantitated after 5, 15, 30, 45 and 60 min through Bradford assay (BIO-RAD Protein Assay, BIO-RAD, Hercules, CA, USA) according to the manufacturer's recommendations. Ten-μl aliquots were collected at each time point, mixed with 200 μL of Bradford Working Solution and incubated at 37 C for 2 min prior to absorbance assessment at 620 nm with a micro plate photometer (Multiskan™ FC, Thermo Fisher Scientific,Waltham, MA, USA). The number of proteins deposited on the discs was finally calculated by subtracting the residual concentration in supernatant from the initial one.

8.2.2.2 Western Blot

WB was developed at the end of the time-course analysis to assess the selectivity of sFBN-CH for fibronectin.
Samples were briefly rinsed twice in PBS to remove softly bound proteins, incubated with 80 μL of Sample Buffer 1X (Tris-HCl 62.5 mM pH 6.8, SDS 1.5% w/v, DTT 100 mM) and then freeze, thawed sonicated for 15 min and boiled at 95 °C for 10 min to completely recover adsorbed

proteins. Equal volumes of recovered proteins were loaded on a 12% polyacrylamide gel (Acrylamide/Bis-Acrylamide 30%, Sigma-Aldrich), electrophoresed 1 h at 180 V and subsequently blotted on a PVDF membrane (Immobilon-P, Darmstadt, Germany) 1 h at 100 V. Non-specific sites were firstly blocked 1 h at room temperature (RT) in Tris-buffered saline (TBS, Tris-HCl 50 mM pH 7.5 and NaCl 150 mM) containing 10% of blocking reagent (Roche S.p.A., Segrate, Italy). Then, the membrane was prior incubated overnight with an anti-FBN (F3648, Sigma-Aldrich) antibody diluted 1:800 in 0.1% Tween 20 in TBS supplemented with 5% bovine serum albumin (Sigma-Aldrich) and then with an HRP-conjugated secondary antibody (Cell Signalling Technology, Danvers, MA, USA) diluted 1:10,000. Eventually, immunoreactivity was visualized with enhanced chemiluminescence (Immobilon Western Chemiluminescent HRP, Sigma-Aldrich).

8.2.3 Cell Assays

8.2.3.1 Cell Culture

In vitro assays were performed with human cervical cancer (HeLa) cell line (Sigma-Aldrich). Cells were cultured up to 4 days in 48-well plates at a density of 5000 cells/sample and maintained in complete high glucose Dulbecco modified Eagle's medium (DMEM, Thermo Fisher Scientific) supplemented with 10% Fetal Bovine Serum (FBS, Thermo Fisher Scientific) and 1% Penicillin and Streptomycin (PenStrep, Thermo Fisher Scientific).

8.2.3.2 Cytoskeleton Inhibitors Cytotoxicity Analysis

Pharmacological agents cytochalasin-D and blebbistatin were used to inhibit actin polymerization and myosin II contractility respectively.

Experiments were undertaken to define the concentration that did not elicit signs of cytotoxicity and which allowed the spreading of the cells with no changes in their morphology (Figure S1). To this purpose, cells were treated with increasing amounts of cytochalasin-D (0.1, 0.25, 0.5 and 0.75 μM:C8273, Sigma-Aldrich) and blebbistatin (0.1, 0.5, 1 and 1.5 μM: 203390, Sigma-Aldrich) and monitored for viability and morphology up to 4 days. Cell viability was assessed with chemiluminescence (CellTiterGLO, Promega, Milano, Italy).

Briefly, samples were incubated with 100 μL of a 1:1 solution of culturing medium and lysis buffer for 2 min on an orbital shaker, thus stabilized at RT in dark conditions for 10 min.

Eventually, samples were briefly spanned, and luminescence quantitated with a luminometer (GloMax®20/20, Promega, Fitchburg, WI, USA).
Simultaneously, cell morphology was assessed by crystal violet (CV) staining, with an inverted microscope (Eclipse TS100, Nikon, Tokyo, Japan). To this purpose, cells were fixed 20 min at RT in paraformaldehyde 4%, thus stained with a 5 mg/mL solution of CV (491502, Carlo Erba, Cornaredo, Italy) prepared in 20% methanol (Sigma-Aldrich) for 10 min and rinsed twice in distilled water. When samples were completely dried, specimens were observed and microphotographs acquired with a digital camera (Digital Sight DS-Fi2, Nikon).
Cytochalasin 0.1 μM and blebbistatin 1 μM were finally chosen as cytoskeleton inhibitor concentrations for further experiments.

8.2.3.3 Cell Morphology Analysis

To assess the effects of aptamers on cell shape, morphology and adhesion, cells were cultured up to 4 days on CH and sFBN-CH specimens at increasing aptamer concentrations and in the presence or in the absence of cytoskeleton inhibitors. The concentration of the latter substances reflected the previous analysis.
Cells were daily observed with an inverted microscope (Eclipse TS100, Nikon). Photographs were acquired with a digital camera (Digital Sight DS-Fi2, Nikon) and image analysis was performed with the software (Version 4.3, Nikon). In particular, the amount of spread and non-spread cells on chitosan surface was measured after the region of interest identification (ROI). Cells were considered as a spread when philopodia were clearly visible and their circularity coefficient was lower than 0.8.

8.2.4 Statistical Analysis

Data were analyzed using Prism6 (GraphPad, La Jolla, CA, USA) and are reported as the mean ± SD of three repeated experiments performed in triplicates. Differences between groups were evaluated with two-way ANOVA statistical test combined to Sidak multiple comparisons post-hoc test and considered significant when $p < 0.05$. Trends were fitted with linear regression approximation with a 95% interval confidence.

8.3 Results

8.3.1 Anti-FBN Aptamers Interface Modification Induces Firm FBN Adsorption

Serum proteins showed very fast deposition on chitosan both in the presence or in the absence of aptamer functionalization (Figure 2a). As a tendency, slightly more proteins seemed to be adsorbed on CH (39.2 ± 1.0 μg) versus sFBN-CH (34.5 ± 1.4 μg), even though no significant differences were revealed after the statistical analysis (p = 0.2034). The time-courses resulted comparable and estimated to hyperbolic trends (CH R2 = 0.9789; sFBN-CH R2 = 0.9866). Consistently with this, when CH or sFBN-CH specimens were incubated 1h with a solution of pure FBN at serum concentrations, no differences were revealed among the groups (CH 6.6 ± 0.1; sFBN-CH 6.0 ± 0.1 μg; CH vs. sFBN-CH p = 0.2352; CH R2 = 0.9547; sFBN-CH R2 = 0.9755). Furthermore, to investigate whether aptamers enhanced the firm adsorption of FBN a WB analysis was performed. Figure 2b shows that chitosan selectivity for FBN was 34.7-fold promoted by aptamers (O.D. CH = 2.8% vs. O.D. sFBN-CH = 97.2%).

All together, these data indicate that aptamers promote a more fixed adsorption of FBN on the surface.

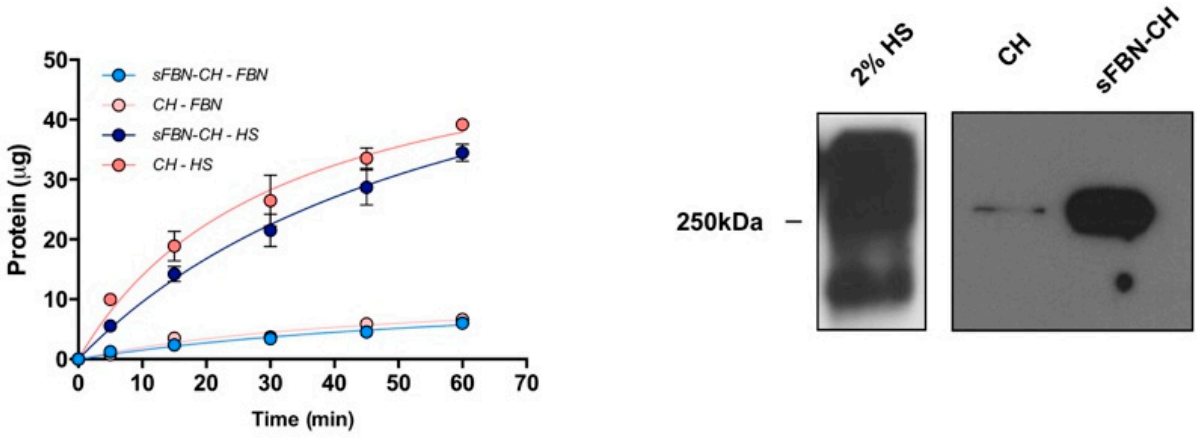

Figure 2. Protein adsorption over time and aptamer-doped chitosan selectivity for FBN. (a) Time-course of serum proteins and of pure FBN deposition on CH and sFBN-CH samples. (b) Western blot analysis of FBN stably adsorbed on CH and on sFBN-CH.

8.3.2 Anti-FBN Aptamers Interface Modification Promotes Epithelial Cells Adhesion in A Dose-Dependent Manner

To investigate if aptamers improve the adhesion of cells to chitosan, the number of flattened cells was monitored over the time up to day 4 and quantitated by image analysis (Representative cell images are reported in Supplementary Materials—Figure S2).

The presence of aptamer dramatically increased the entity of cell spreading starting from day 3 (Figure 3a). After 1 day of culture, no spread cells were found both on CH and sFBN-CH samples, as well as no significant differences were detectable ($p > 0.9999$). However, 6.93-fold more at day 3 and 3.56-fold more cells at day 4 were spread on sFBN-CH, with statistically significant differences (day 3: CH vs. sFBN-CH $p = 0.0002$; day 4: CH vs. sFBN-CH $p < 0.0001$). Additionally, when different doses of aptamers were used, the amount of well-spread cells increased proportionally with the amount of total aptamer used, following linear regression trends (Figure 3b,c—CH $R^2 = 0.5723$; sFBN-CH (5 µg) $R^2 = 0.6621$; sFBN-CH (10 µg) $R^2 = 0.7529$; sFBN-CH (20 µg) $R^2 = 0.7916$; sFBN-CH (40 µg) $R^2 = 0.9068$). After 3 days the differences with the control were significant when high doses of aptamers were used (CH vs. sFBN-CH (10 µg) $p < 0.0001$; CH vs. sFBN-CH (20 µg) $p = 0.0036$; CH vs. sFBN-CH (40 µg) $p < 0.0001$), as well as at day 4 (CH vs. sFBN-CH (10 µg) $p = 0.0004$; CH vs. sFBN-CH (20 µg) $p = 0.0047$; CH vs. sFBN-CH (40 µg) $p < 0.0001$). On the contrary, the minimum dose of aptamer used has never induced any significant change in cell morphology (CH vs. sFBN-CH (5 µg)-day 3 $p > 0.9999$; day 4 $p = 0.8699$). In addition to this, differences were detected also against the minimum amount of aptamer used and the other groups both at day 3 (sFBN-CH (5 µg) vs. sFBN.CH (10 µg) $p < 0.0001$; sFBN-CH (5 µg) vs. sFBN.CH (20 µg) $p = 0.0048$; sFBN-CH (5 µg) vs. sFBN.CH (40 µg) $p < 0.0001$) and at day 4 (sFBN-CH (5 µg) vs. sFBN.CH (10 µg) $p = 0.0022$; sFBN-CH (5 µg) vs. sFBN.CH (20 µg) $p = 0.0458$; sFBN-CH (5 µg) vs. sFBN.CH (40 µg) $p < 0.0001$). Furthermore, at day 4 the maximum amount of aptamer used significantly enhance the cell spreading if compared to low amounts (sFBN-CH (20 µg) vs. sFBN-CH (40 µg) $p = 0.0014$).

The plot of the angular coefficients of the regression lines fitting cells spreading data with different amounts of aptamers revealed a linear regression trend with an estimated R2 value of 0.8322 (Figure 3d).

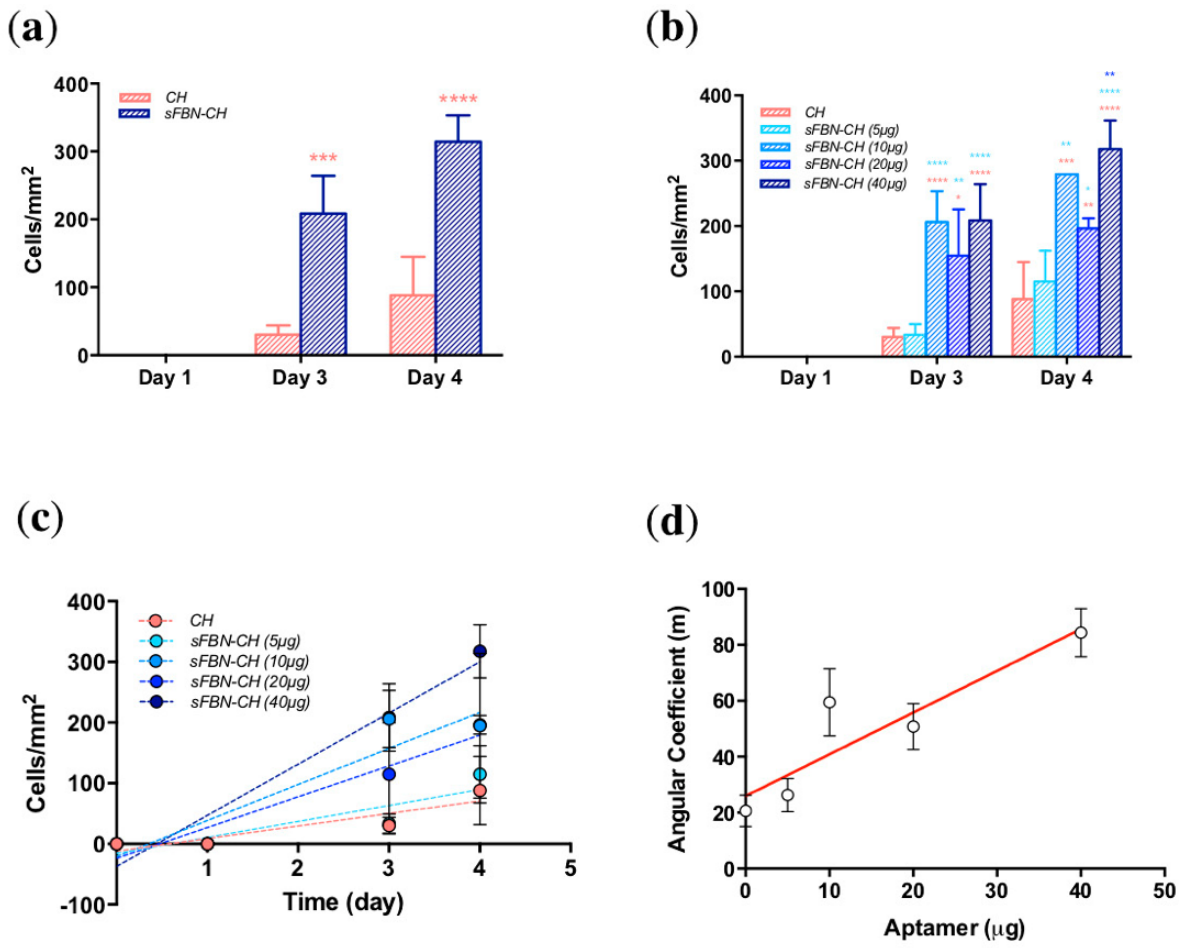

Figure 3. HeLa cells spreading on sFBN-CH. (a) Histograms showing the number of spread cells on CH and sFBN-CH after 1, 3 and 4 days of culture. (b) Histograms the number of spread cells on CH and sFBN-CH enriched with increasing doses of aptamers after 1, 3 and 4 days of culture. (c) The trend of cell spread rate on chitosan discs implemented with increasing aptamer doses. (d) The trend of angular coefficients derived from cell spread on chitosan discs implemented with increasing aptamer doses (* = $p < 0.05$).

8.3.3 Integrin-Mediated Pathway Controls Epithelial Cells Adhesion at the Anti-FBN Aptamers Modified Interface

No differences in morphology of cells exposed to cytochalasin-D or blebbistatin and in untreated cells were detected on bare chitosan (Figure 4a,b). However, when actin polymerization was inhibited with cytochalasin-D on sFBN-CH, we observed a significant 1.29-fold or 1.37-fold reduction in the number of spread cells, when compared to untreated cells ($p = 0.0043$) and to cells cultured with blebbistatin ($p = 0.0007$), respectively. Interestingly, these two conditions did not show the difference between each other ($p = 0.5496$) (Figure 4a,b).

Furthermore, when the angular coefficients of linear regression trends derived from the use of different aptamer doses were compared (Figure 4c,d), a dip of the fitting curve was detected for cytochalasin-D treated group with significant differences to control and blebbistatin group when 20 or 40 µg of aptamers were applied (sFBN-CH (20 µg) control vs. cytochalasin-D $p = 0.0025$, blebbistatin vs. cytochalasin-D $p = 0.0052$; sFBN-CH (40 µg) control vs. cytochalasin-D $p = 0.0279$, blebbistatin vs. cytochalasin-D $p = 0.0002$). On the other hand, strict overlapping of control and blebbistatin group fitting lines was observed.

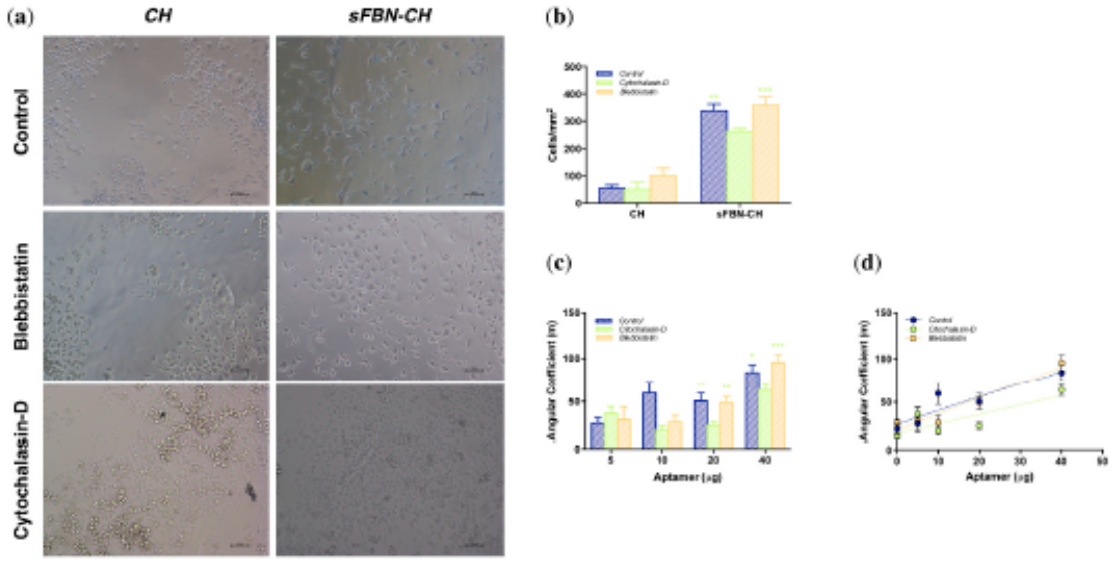

Figure 4. HeLa cells spreading modulation on sFBN-CH by cytochalasin-D and blebbistatin. (a) Representative images acquired with an inverted microscope of cells on CH and sFBN-CH specimens after 4 days of culture in complete medium or in complete medium supplemented with cytochalasin-D 0.1 µM and blebbistatin 1 µM. The magnification in Figure 4a is 10 x. (b) Histograms showing the number of spread cells on CH and sFBN-CH after 4 days of culture in complete medium or in completemedium supplemented with cytochalasin-D 0.1 µM and blebbistatin 1 µM. (c) Histograms reporting angular coefficients derived from cell spread on chitosan discs implemented with increasing aptamer doses and cultured in complete medium or in complete medium supplemented with cytochalasin-D 0.1 µM or blebbistatin 1 µM. (d) The trend of angular coefficients derived from cell spread on chitosan discs implemented with increasing aptamer doses and cultured in complete medium or in complete medium supplemented with cytochalasin-D 0.1 µM and blebbistatin 1 µM (* = $p < 0.05$)

8.4 Discussion

Protein adsorption on biomaterials occurs shortly after scaffold insertion and anticipates cells attachment. Therefore, the control of this phenomenon at the interface is extremely important when seeking to pilot cells fate [17]. Chitosan has been widely recognized as a suitable biomaterial for scaffold production, even if it possesses a scarce ability to support the attachment of mesenchymal, epithelial and osteoblast-like cells. Hence, the presence in the literature of different methods to enhance cell response on chitosan through FBN enrichment [8,18–22]. FBN control cell adhesion, spreading and proliferation on substrates through integrin binding, which is extremely dependant on FBN structural conformation. For examples, the α5β1 integrin recognizes FBN through the interaction with the RGD peptide, which is contained in the 10th type III repeat of FBN structure and that synergizes with a further peptide sequence (proline-histidine-serine-arginine-aspargine—PHSRN peptide) contained in the adjacent 9th type III domain of FBN. In bulk conditions, these two peptides are separated from 32 Å and this distance results to be extremely important for specific recognition between FBN and 51 integrin. It has been indeed demonstrated that a 23 Å removal greatly diminishes the binding capacity among FBN and α5β1 integrin [12]. Therefore, the control of FBN adsorption on biomaterials is important both from a quantitative and qualitative point of view.

In our previous work we proposed a novel method to ameliorate the adsorption of autologous FBN on chitosan through the use of selective binding molecules: Aptamers. We obtained an sFBN-CH that did not influence the amount of FBN adsorbed at the interface, but which induced an impressive amelioration of osteoblasts proliferation, adhesion and morphology [8]. As such, we hypothesized a potential role of aptamers in controlling FBN conformational adsorption. We confirmed this finding in the present experiments (Figure 2a), even though after two rinses in PBS, WB analysis revealed a higher signal of FBN adsorbed on sFBN-CH, showing a much stronger and stable adsorption pattern. Interestingly, these data comply with the results we obtained in a previous work testing a selective FBN hyaluronic acid (sFBN-HA) [15]. The use of anti-FBN aptamers appears therefore a valid general system to obtain materials capable to stably adsorb FBN. However, our recent findings have also confirmed our hypothesis of a different biological activity of FBN once adsorbed on CH or on sFBN-CH [13]. As such, the role of aptamers on chitosan seems to be double and the aim of the present work was thus that of confirming this finding supports the hypothesis of amelioration of FBN activity with biological data.

Our experiments showed striking effects of sFBN-CH on human epithelial cells adhesion. Chitosan modified with the highest dose of anti-FBN aptamers (40 g) dramatically increased the number of well-spread cells with a pancake-like shape on day 3 and 4 (Figure 3a). Furthermore, when increasing the amount of anti-FBN aptamers (0, 5, 10, 20 and 40 g), the rate of cell spreading was progressively enhanced, suggesting an arising presence of functional FBN-related binding domains for cells at the interface (Figure 3b–d). Consistently with this, when cells were cultured in the presence of actin polymerization inhibitor cytochalasin-D, the rate of cell spreading decreased (Figure 4). Interestingly, the effects of cytochalasin-D were more substantial when sFBN-CH with higher doses of anti-FBN aptamers were used. Additionally, when myosin II contractility was inhibited, no significant differences in cell shape were observed. Since myosin II contractility does not directly depend on integrin activation, which is in turn regulated by the proper exposition of FBN RGD binding-motif, these data support the hypothesis that sFBN-CH induces an FBN adsorption pattern that is fully functional to eventually influence actin bundles reorganization and cell shape. It should be stressed that cells were treated with cytoskeleton inhibitors concentrations that did not elicit signs of cytotoxicity and which allowed the complete spreading of the cells on the tissue culture plate (TCPs) with no changes of morphology as reported in the material and methods section. Therefore, any variance of cell morphology can be solely attributed to the functional adsorption of FBN on sFBN-CH.

The hypothesis of an FBN functional adsorption on chitosan is further supported by the literature. For example, observing the preferential adhesion of valve endothelial cells (VEC) on TCPs covered with increasing doses of FBN, Cuy *et al*. tried to ameliorate chitosan bioactivity by an FBN coating [22].

Surprisingly, VEC morphology on FBN-coated chitosan was not different from the control and their growth was lower than the growth on TCPs. Noteworthy, no differences were detected between the amount of FBN adsorbed on TCPs and on chitosan, suggesting a loss in bioactivity of FBN when adsorbed on chitosan with the respect of TCPs. Consistently with this Custodio *et al*. observed that when FBN was covalently immobilized on chitosan via carbodiimide chemistry, the adhesion of SaOS-2 cells was promoted if compared to FBN spontaneous adsorption, confirming the hypothesis of a probable loss in bioactivity when FBN is simply adsorbed on chitosan [21].

To conclude, we demonstrated that sFBN-CH was able to dramatically increase the number of adhering cells. A similar modified hyaluronic acid-based hydrogel (sFBN-HA) [16] showed comparable effects, but, interestingly, different mechanisms appear to be involved. While sFBN-HA quantitatively increased the adsorption of FBN, enhancing cells adhesion, sFBN-CH showed

a similar amount of adsorbed FBN when compared to the control CH, but with great differences in the strength and functionality of the adsorption, as discussed above. Consistent with these findings, additional studies that aimed at directly investigating the structural conformation of FBN on CH and on sFBN-CH have confirmed the role of function-wise conformational differences of adsorbed FBN [13].

8.5 Supplementary Materials

The following are available online at http://www.mdpi.com/1996-1944/12/5/812/s1, Figure S1: Cytochalasin-D and blebbistatin cytotoxicity on human HeLa cells. Figure S2: HeLa cells spreading on CH and on sFBN-CH.

8.6 Author Contributions

This study has been conceptualized by L.P., L.E. and G.M.M. L.P., A.T. and M.G.B. performed the experiments, while C.B. prepared chitosan specimens. Writing and original draft preparation was handled by L.P. and A.B., while the final manuscript was revised and approved for final submission by R.B. and G.M.M.

8.7 Funding

This research was funded by a 2013 Grant from the American Academy of Implant Dentistry Foundation. Acknowledgments: The authors would like to thank Eleonora Maurizi (Dipartimento di Medicina e Chirurgia, Università degli Studi di Parma) for her assistance with cell culture.

8.8 Conflicts of Interest

The authors declare no conflict of interest.

8.9 References

1. Langer, R.; Vacanti, J.P. Tissue engineering. Science 1993, 260, 920–926. 2. Parisi, L.; Toffoli, A.; Ghiacci, G.; Macaluso, G. Tailoring the interface of biomaterials to design effective scaffolds. J. Funct. Biomater. 2018, 9, E50.

3. Pavinatto, F.J.; Caseli, L.; Oliveira, O.N. Chitosan in nanostructured thin films. Biomacromolecules 2010, 11, 1897–1908.

4. Croisier, F.; Jerome, C. Chitosan-based biomaterials for tissue engineering. Eur. Polym. J. 2013, 49, 780–792.

5. Galli, C.; Parisi, L.; Elviri, L.; Bianchera, A.; Smerieri, A.; Lagonegro, P.; Lumetti, S.; Manfredi, E.; Bettini, R.; Macaluso, G.M. Chitosan scaffold modified with D-(+) raffinose and

enriched with thiol-modified gelatin for improved osteoblast adhesion. Biomed. Mater. 2016, 11, 015004.
6. Andrade, J.; Hlady, V. Protein adsorption and materials biocompatibility—A tutorial review and suggested hypotheses. In Advances in Polymer Science; Springer: Berlin/Heidelberg, Germany, 1986; Volume 79, pp. 1–63.
7. Benbow, N.L.; Webber, J.L.; Karpiniec, S.; Krasowska, M.; Ferri, J.K.; Beattie, D.A. The influence of polyanion molecular weight on polyelectrolyte multilayers at surfaces: Protein adsorption and protein-polysaccharide complexation/stripping on natural polysaccharide films on solid supports. Phys. Chem. Chem. Phys. 2017, 19, 23790–23801
8. Parisi, L.; Galli, C.; Bianchera, A.; Lagonegro, P.; Elviri, L.; Smerieri, A.; Lumetti, S.; Manfredi, E.; Bettini, R.; Macaluso, G.M. Anti-fibronectin aptamers improve the colonization of chitosan films modified with D-(+) Raffinose by murine osteoblastic cells. J. Mater. Sci. Mater. Med. 2017, 28, 136
9. Mascini, M.; Palchetti, I.; Tombelli, S. Nucleic acid and peptide aptamers: Fundamentals and bioanalytical aspects. Angew. Chem. Int. Ed. 2012, 51, 1316–1332.
10. Nuttelman, C.R.; Mortisen, D.J.; Henry, S.M.; Anseth, K.S. Attachment of fibronectin to poly(vinyl alcohol) hydrogels promotes NIH3T3 cell adhesion, proliferation, and migration. J. Biomed. Mater. Res. 2001, 57, 217–223.
11. Alberts, B. Integrins. In Molecular Biology of the Cell; Garland Science: New York, NY, USA, 2002; pp. 1227–1242.
12. Krammer, A.; Craig, D.; Thomas, W.E.; Schulten, K.; Vogel, V. A structural model for force regulated integrin binding to fibronectin‘s RGD-synergy site. Matrix Biol. 2002, 21, 139–147.
13. Saccani, M.; Parisi, L.; Bergonzi, C.; Bianchera, A.; Galli, C.; Macaluso, G.M.; Bettini, R.L.E. Surface modification of chitosan films with a fibronectin fragment-DNA aptamer complex to enhance osteoblastic cell activity: A mass spectrometry approach probing evidence on protein behavior. Rapid Commun. Mass Spectrom. 2018, in press.
14. Bettini, R.; Romani, A.A.; Morganti, M.M.; Borghetti, A.F. Physicochemical and cell adhesion properties of chitosan films prepared from sugar and phosphate-containing solutions. Eur. J. Pharm. Biopharm. 2008, 68, 74–81.
15. Galli, C.; Parisi, L.; Piergianni, M.; Smerieri, A.; Passeri, G.; Guizzardi, S.; Costa, F.; Lumetti, S.; Manfredi, E.; Macaluso, G.M. Improved scaffold biocompatibility through anti-Fibronectin aptamer functionalization. Acta Biomater. 2016, 42, 147–156

16. Elviri, L.; Asadzadeh, M.; Cucinelli, R.; Bianchera, A.; Bettini, R. Macroporous chitosan hydrogels: Effects of sulfur on the loading and release behaviour of amino acid-based compounds. Carbohydr. Polym. 2015, 132, 50–58.
17. Morris, A.H.; Kyriakides, T.R. Matricellular proteins and biomaterials. Matrix Biol. 2014, 37, 183–191
18. Huang, G.S.; Dai, L.G.; Yen, B.L.; Hsu, S.H. Spheroid formation of mesenchymal stem cells on chitosan and chitosan-hyaluronan membranes. Biomaterials 2011, 32, 6929–6945.
19. Hsu, S.H.; Huang, G.S.; Feng, F. Isolation of the multipotent MSC subpopulation from human gingival fibroblasts by culturing on chitosan membranes. Biomaterials 2012, 33, 2642–2655.
20. Yeh, H.Y.; Liu, B.H.; Sieber, M.; Hsu, S.H. Substrate-dependent gene regulation of self-assembled human MSC spheroids on chitosan membranes. BMC Genom. 2014, 15, 10.
21. Custodio, C.A.; Alves, C.M.; Reis, R.L.; Mano, J.F. Immobilization of fibronectin in chitosan substrates improves cell adhesion and proliferation. J. Tissue Eng. Regen. Med. 2010, 4, 316–323.
22. Cuy, J.L.; Beckstead, B.L.; Brown, C.D.; Hoffman, A.S.; Giachelli, C.M. Adhesive protein interactions with chitosan: Consequences for valve endothelial cell growth on tissue-engineering materials. J. Biomed. Mater. Res. Part. A 2003, 67A, 538–547.

8.10 Supplementary material

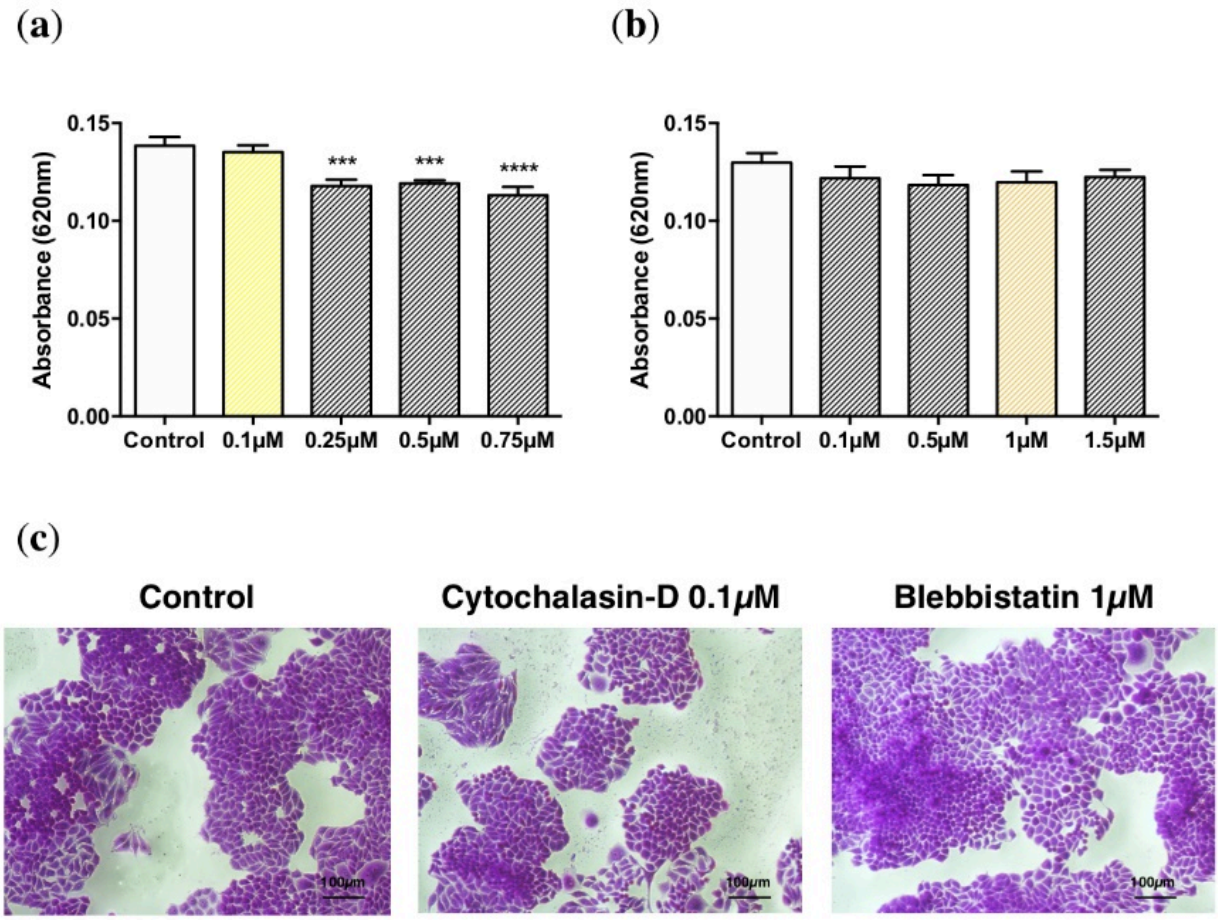

Figure S1. Cytochalasin-D and blebbistatin cytotoxicity on human HeLa cells. (a) Cell viability of HeLa cells up to 4 days treating with cytochalasin-D at increasing concentrations. (b) Cell viability of HeLa cells up to 4 days treating with blebbistatin at increasing concentrations. (c) Representative images acquired with an inverted microscope of HeLa cells stained with CV after 4 days of culture in complete medium or in complete medium supplemented with cytochalasin-D 0.1µM and blebbistatin 1 µM. (* = $p < 0.05$). Cytochalasin-D showed a negative effect on cell viability, which was significantly reduced at concentrations higher than 0.1 µM (Day 4: Control vs. 0.25 µM $p = 0.0002$; Control vs. 0.5 µM $p = 0.0003$; Control vs. 0.75µM $p < 0.0001$). Consistently, after CV staining cell morphology was severely affected by cytochalasin-D. With increasing amount of cytochalasin-D used, cells appeared more elongated, they lost contacts and adhesion among them when organized in cluster and finally they fused forming structures like syncytiums. On the counterpart, blebbistatin did not show negative effects on cell viability up to 1.5 µM. However, cell morphology was affected when doses higher than 1 µM were applied.

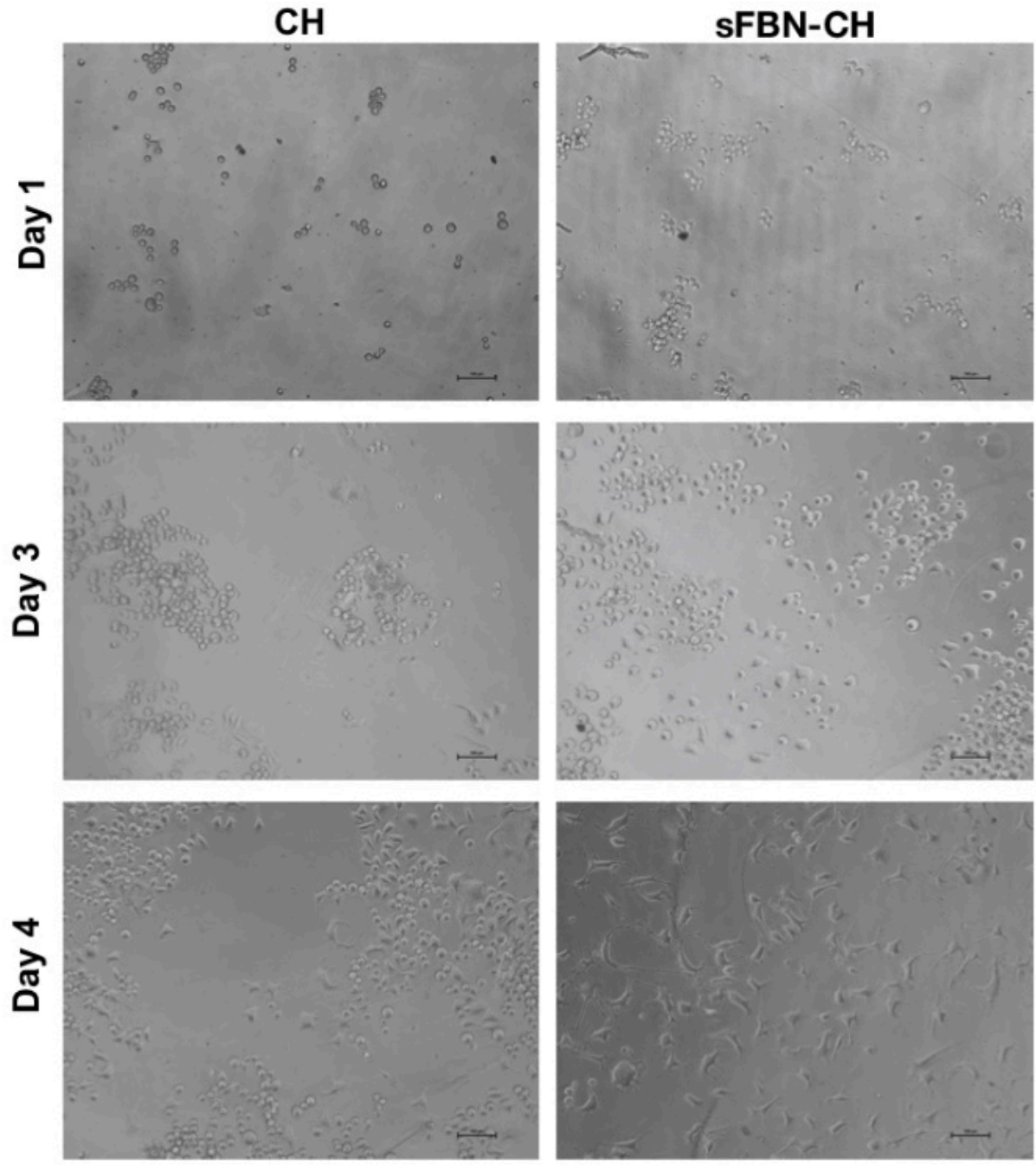

Figure S2. HeLa cells spreading on CH and on sFBN-CH. Representative images acquired with an inverted microscope of cells on CH and sFBN-CH specimens after 1, 3 and 4 days of culture.

9 Chapter 6: “Surface modification of chitosan films with a fibronectin fragment-DNA aptamer complex to enhance osteoblastic cell activity: A mass spectrometry approach probing evidence on protein behavior”

M. Saccani[1], L. Parisi[2], C. Bergonzi[1], A. Bianchera[3], C. Galli[2], GM. Macaluso[2], R. Bettini[1], L. Elviri[1*]

[1]Department of Food and Drug Science, University of Parma, Parco Area delle Scienze 27/A, 43124, Parma, Italy.
[2]Department of Biomedical, Biotechnological and Translational Sciences, University of Parma, Parma, Italy; Centro Universitario di Odontoiatria, Via Gramsci 14, 43126, University of Parma, Parma, Italy.
[3]Interdepartmental Centre Biopharmanet-Tec, University of Parma Parco, Area delle Scienze 27/A, 43124, Parma, Italy.

Published on 28 February 2019, Rapid Commun Mass Spectrom. Vol 33 (4), 336-342; doi: 10.1002/rcm.8335

IF 2.045

Personal contribution

CB performed the experimental work related to materials formulation and processing, analytical characterization and contributed to the preparation of the manuscript.

Abstract

Rationale: Protein dynamics are fundamental for biological activity. Direct surface functionalization with these biomolecules often creates regions presenting non-homogeneous and altered protein functionality. Aptamers have been shown to be an effective method to enhance the biocompatibility of biomaterials by acting as docking points for biomolecules capable to improve cell responses and the colonization/proliferation processes. Here mass spectrometry (MS) was successfully applied as an analytical approach to study the interactions between a fibronectin fragment (FN) and anti-fibronectin aptamers in solution and on a chitosan film.

Methods: A thirty kDa N-terminal fibronectin fragment, a ssDNA anti- fibronectin 40 nucleotide long aptamer and chitosan 95/50 (degree of deacetylation 92.6-97.5%; molecular weight 80-220 kDa) were used. First, the dynamics of FN in aqueous solution, in the presence or absence of anti-FN specific DNA aptamers, were described. Thus, the same study was carried out on 2% (w/w) chitosan-based films, functionalized with FN alone or through aptamers as selective spacers.

Results: Amide hydrogen/deuterium mass spectrometry exchange (HDX-MS) analysis identified the SYRIGDTWSKKDNRGNL and YRVGDTYERPKDSMI, YVVGETWEKPYQGWMM and WERTYLGNAL fragments as presumably involved in the interaction of FN with aptamers. MS findings indicated the improved functionality of FN on chitosan when aptamers were used as selective spacer, and this may explain why cells preferentially attached to aptamer-bound FN rather than on chitosan-FN films.

Conclusions: Aptamers did not affect the amount of adsorbed FN, but influenced its conformation enhancing its biological activity toward osteoblasts adhesion and growth. HDX-MS data allowed to identify the FN/aptamer interaction regions. The differences in FN flexibility on the chitosan film in the presence or absence of the aptamer were established providing insights at the molecular level to better understand the protein biological functionality on cell proliferation.

Keywords: Fibronectin, aptamer, mass spectrometry

9.1 Introduction

Biomaterials are widely used to develop active medical devices capable of promoting tissue regeneration and functional restoration.[1,2] During these processes, the extra cellular matrix (ECM) with its complex and dynamic microenvironment plays a pivotal role in regulating cell adhesion, growth and proliferation.[3-4] Thus, the direct combination of scaffolds functionalized with simplified ECM proteins is widely studied as a promising approach for a broad range of biomedical applications. Biomaterials functionalized with ECM-derived proteins were demonstrated to significantly affect cell behavior.[5] However, direct functionalization of a surface with an active molecule (i.e. a protein) could result in random non-specific adsorption, loss of functionality or triggering of undesired reactions. Therefore, biomaterial functionality is strictly related to the control of protein adsorption. For these reasons, advances in understanding dynamic interaction mechanisms represent an important step to design substrates with improved efficacy in tissue regeneration.

Chitosan is a natural polymer derived from the alkaline N-deacetylation of chitin, which is widely used in pharmaceutical and biomedical applications thanks to its useful characteristics of biodegradability, biocompatibility, low toxicity and moldability.[6-8] Its molecular structure is very close to that of the glycosaminoglicans that compose the ECM, which renders it an ideal candidate as supportive material for the preparation of scaffolds intended for tissue engineering.[9,10] In particular, the use of chitosan in oral and maxillofacial applications is particularly interesting because of its contribution to wound healing,[11,12] and its intrinsic antibacterial activity against some common oral pathogens.[13] In order to improve the ability of chitosan to act as a substrate for cell growth,[14] described the preparation of chitosan films in the presence of phosphates and D-(+)-raffinose, which positively contributed to the growth of WI-38 and HUVEC cells on this biomaterial. The same model however was not very efficient in supporting the growth of osteoblastic cells, so further functionalization of these hydrogels was performed to improve their biocompatibility by exploiting the binding affinity of chitosan for sulfur-containing components,[15] such as thiol-modified gelatin,[16] or by means of aptamers.[17]

A previous work by Parisi *et al*.,[17] described the positive effect of the functionalization of chitosan films with anti-fibronectin aptamers on their colonization by murine osteoblastic cells. Aptamers significantly increased the selective adsorption of fibronectin on chitosan hydrogels, which resulted in improved adhesion and growth of MC3T3-E1 cells. This effect was probably due to the contribution of aptamers in preserving the natural conformation of fibronectin without unfolding it and maintaining a favorable exposure of adhesion sequences for cells (Figure 1),

because the amount of adsorbed fibronectin did not appear to be affected by the presence of aptamers.

Fibronectin is a high molecular weight glycoprotein (MW ~ 440 kDa) composed of two dimeric chains interconnected by disulfide bonds located at the end of each chain. Such protein is able to bind several different ligands mainly involving the charged residues present on the surface of the molecule.[18]

To provide a complete insight into the complex polysaccharide surface functionalization and thus cell activity even at the molecular level, in this paper, we delved into the type of interactions that are established between fibronectin and chitosan, fibronectin and anti- fibronectin aptamer or in the system with the three elements together with the help of Hydrogen Deuterium Exchange-Mass Spectrometry (HDX-MS) high resolution mass spectrometry (HRMS). For this purpose, a 30kDa N-terminal fibronectin fragment (FN) was used as proteins domain involved in ligand interactions. HDX-MS offers a useful approach to study protein-ligand interactions, or protein dynamics.[19] The H/D exchange is monitored by measuring protein molecular weight in aqueous and deuterium solutions at different incubation times. Ligand-protein interactions cause local and global conformational changes that induce the stabilization of new secondary structure elements and differences in H/D exchange rate and number.

This paper focuses on the application of HDX-MS to study FN-aptamer interactions in solution and the dynamics of FN bound on the surface of chitosan films with or without aptamers.

9.2 Materials and Methods

9.2.1 Chemicals

Thirty kDa N-terminal fibronectin fragment (powder), trypsin and pepsin were obtained from Sigma-Aldrich (St. Louis, MO, USA). Chitosan 95/50 (CAS 9012-76-4, degree of deacetylation 92.6-97.5%; molecular weight by gel permeation chromatography 80-220 kDa; water insoluble, soluble in acid media) was purchased from HEPPE MEDICAL CHITOSAN GmbH (Halle, Saale, Germany). A ssDNA, anti- fibronectin, 40 nucleotide long aptamer (MW 12597 g/mol) (ATW008, Base Pair Biotechnologies, Pearland, TX) was used.

Formic acid was from J.T. Baker (Deventer, Netherland). Water was obtained with a MilliQ element A10 System (Millipore, S. Francisco, CA, USA). Deuterated water, deuterated ammonium acetate and hydrochloric acid were provided by Sigma-Aldrich.

9.2.2 MS and HDX-MS experiments

An aliquot of aqueous solution of human plasma 30kDa N-terminal fibronectin fragment (conc. 16.7 μM) was diluted with ultrapure water (final concentration 1.67μM) and analyzed by high resolution mass spectrometry to evaluate the protein molecular weight and charge distribution spectrum. An Orbitrap (Thermo Scientific, San Jose, CA, USA) instrument equipped with a pneumatically assisted ESI interface was used. In the ESI experiments, the desolvation gas (nitrogen, 99.999% pure) was delivered at 820 kPa. Direct infusion mode, operating with a syringe pump at a flow rate of 1 μL/min, was used to evaluate the influence of the ESI interface parameters on the MS response of FN. MS data were acquired in positive ion mode over the m/z 500–2000 range. The interface parameters were as follows: capillary voltage 40 V, electrospray voltage 3,5 kV, capillary temperature 150°C.

HDX experiments were performed by diluting an aliquot of FN solution (final concentration 1,67 μM) in deuterated water and analyzed at different time points (t 2, 10, 30, 60 and 120 min). All the reagents and the solutions were maintained hermetically sealed under nitrogen atmosphere.

The same experiments were performed on a FN aqueous solution in presence of anti-fibronectin aptamers. An aliquot of ATW008 solution was diluted with ultrapure water to a final concentration of 10 μM and analyzed in ion negative mode for direct infusion with MS in order to confirm the MW.

An aliquot of FN and ATW008 in a [1:5] v/v ratio were incubated for 1 hour and then diluted with water and analyzed. For the HDX experiment, the FN-aptamer sample was diluted, after 1h of incubation, in deuterated water and analyzed at different time points (t 2, 10, 30, 60 and 120 min).

9.2.3 Pepsin digestion and HPLC-MS analysis

Aqueous and deuterated solutions of FN alone and in presence of ATW008 were digested with a 5 μM pepsin solution (4h, 37°C) and analyzed by HPLC-MS. For samples in deuterated water a 1 hour incubation was established as a suitable time to perform the exchange reactions. The quenching of HD exchange was at pH 2.5 and 0°C.

Peptide separation was carried out on a Kinetex C18 column (75x2.1mm, 2.6μm) (Phenomenex, Torrance, CA, USA) under the following [(A) aqueous formic acid 0.1% v/v: (B) acetonitrile] gradient conditions: 0-2 min 2% (B), 2-30 min 80% (B) at a flow-rate of 0.2 mL/min. Data dependent acquisition (DDA) mode was used to analyse proteolytic fragments identified by

Proteome Discoverer™ software (ThermoScientific). Analysis were performed in triplicate and data were expressed as mean +/- standard deviation. The isoform 12 of human fibronectin (GN1 HS) was considered for data analysis; structure was from NCBI protein database (www.ncbi.nlm.nih.gov) and elaboration was performed by Chimera Molecular Modeling software v.10.1.[24]

9.2.4 Chitosan scaffold preparation and analysis

A 2% p/v chitosan solution was prepared by dissolving purified chitosan powder in 1% v/v acetic acid; D(+)-raffinose (Sigma-Aldrich, Saint Louis, MO, USA) was then added at the final concentration of 290 mM as viscosity modifying agent. One milliliter of each solution was spread out onto a microscope slide (12x25 mm) to obtain a film with uniform thickness of 0.25mm and dried at 45°C in a ventilated oven for 1 hour. Films were then transferred in a 5% p/v NaOH gelation solution for 24 hours. Chitosan gel discs were cut off from the 2% p/v films for 96-multi well plates, rinsed in double distilled water and sterilized under UV light for 10 minutes, before use.

ATW008 were modified with a short carbon chain containing a disulphide bond on their 3' end and with a biotin on their 5'-end. Disulphide bonds at the 3'-ends of the strands were reduced with a 2 mM, pH 7,8 solution of Tris(2-carboxyethyl)phosphine hydrochloride (TCEP, Sigma Aldrich) for 2 hours prior to use, in order to free thiol-groups able to bind chitosan without the need for any other cross linker molecule. TCEP excess was subsequently removed through a chromatographic column (mini Quick Spin Oligo Columns, Roche Life Science, Branford, CT, USA).

Chitosan discs were enriched with FN directly or indirectly using aptamers as selective spacers. In the former case, chitosan discs were functionalized by incubation with 50 µL of FN solution for 1 hour. FN solution was then removed, chitosan discs were rinsed with 100 µL of PBS for three times and stored in PBS until use. In the latter case, chitosan discs were functionalized by incubation with 50µl of anti-fibronectin aptamer solution for 1 hour. Aptamer solution was then removed and chitosan discs were washed three times with PBS. Chitosan discs functionalized with aptamers were incubated with 50µL of human fibronectin from human plasma solution. After 2 hours, the fibronectin solution was removed and discs were washed with 100µL of PBS for three times. Chitosan discs functionalized with the aptamer-fibronectin complex were stored in PBS until use.

Chitosan discs enriched with only fibronectin and chitosan discs enriched with fibronectin through aptamers, were digested with pepsin as described above. HDX exchange and peptide separation was carried out as described above. The obtained peptides were analyzed with HPLC-MS.

9.3 Results and Discussion

9.3.1 Qualitative Analysis of Fibronectin fragment and Anti-Fibronectin Aptamers with ESI-HRMS

HRMS is a leading analytical technique to investigate biomolecules. Proteins can be accurately identified and characterized in terms of covalent structures, dynamics and non-covalent interactions using a very low amount of sample. Here, an aqueous solution of FN (conc. 1.67 μM) was initially analyzed by direct infusion in the ESI-HRMS system to accurately establish its molecular weight (MW). The positive ion full-scan spectrum presented a charge state distribution centered on +21 at m/z 1376.39 (Fig. 2A), with a calculated average molecular mass of 28884 (± 2) Da (n=3). In the same way, the aptamer aqueous solution was analyzed by acquiring negative ions at low resolution. The charge state distribution was centered at following values: 901.35 m/z; 970.92 m/z; 1048.84 m/z, which correspond to -14; -13; -12 charge states, respectively (Fig. 2B). The calculated average MW was 12631 (± 2) Da.

9.3.2 HDX MS experiments on FN aqueous solutions

The H/D exchange mass spectrometry approach was used to prove interactions between FN and the DNA aptamers in aqueous solution. Figure 3 shows the full scan spectrum of FN alone in heavy water, after 1 hour of exchange. The multi charge distribution of proteins was preserved, but the m/z value was centered on 1933,78 m/z, indicating an average exchange of 75 H (± 10). It is well know[21] that the ESI study of protein/DNA interactions can be challenging: source parameters suitable to retain non-covalent interactions should be selected, an adequate in solution protein:aptamer ratio should be evaluated to avoid non-specific binding or ESI protein signal suppression. For this reason, different initial test were performed on the protein:aptamer ratio to establish a suitable 1:5 ratio (data not shown). In the presence of aptamers, HDX-MS analysis showed that FN exchanged fewer H^+ atoms, indicating that some of the H^+ ions initially available for exchange were engaged in protein-aptamer interactions (Figure 4A). Kinetic studies

demonstrated that FN alone and in the presence of aptamers exhibited two different trends both in terms of number of exchanged hydrogens and relative rate constants (Figure 4A). In the case of FN alone, after a very fast initial exchange involving approximately 55 H atoms in 0.5 min ($k \approx 4.1 \pm 0.8$ min^{-1}), a second group of hydrogens exchanged up to ≈75 H atoms in 60 min with a reduced rate ($k \approx 0.29 \pm 0.13$ min^{-1}). In the presence of aptamers, an initial fast exchange involved approximately 28 H atoms in 0.5 min ($k \approx 3.1 \pm 0.8$ min^{-1}) and a second group of hydrogens exchanged up to ≈55 H atoms in 60 min with a reduced rate ($k \approx 0.39 \pm 0.13$ min^{-1}).

FN-aptamer complexes could be present in solution at different strength mainly as a result of H-bonding and electrostatic interactions. Additional experimental tests at the peptide level were carried out to improve the understanding of the interaction phenomenon.

By performing the ESI-MS/MS analysis of the peptic digests of FN and FN-aptamer aqueous solutions, extended FN sequence coverage was obtained by DDA analysis as depicted in Figure S1 (Supplementary material). Differences in the peptide signals in terms of absolute and relative peptide ion intensities were observed and resulted significantly ($p<0.05$) affected by the presence of the aptamer (Table 1). ESI matrix effect could be involved in these data distribution, HDX experiments were thus carried out, as reported in the Experimental section, on peptides fragments obtained by proteolytic digestion of FN with pepsin. After identification, the relative intensity of peptides and the number of exchanged deuterium ions were calculated. By comparing the peptides generated by digestion of fibronectin alone and in the presence of aptamers, possible interaction regions were identified at the level of the following residues SYRIGDTWSKKDNRGNL and YRVGDTYERPKDSMI, YVVGETWEKPYQGWMM and WERTYLGNAL. HDX data were reported in Figure 4B and show differences both in terms of number and kinetic of exchanged hydrogens. Three of these sequences carry charged residues (L-Lys,R-Arg and H-His), whereas all the four peptides contain polar residues. These finding could suggest that the aptamer/protein interactions are not driven only by electrostatic binding, but even by polar groups all along the FN structure.

9.3.3 ESI-MS and MS/MS analysis of functionalized chitosan films

Chitosan discs enriched with only fibronectin, and chitosan discs enriched with fibronectin through aptamers were digested by pepsin and the obtained fragments were analyzed with HPLC-MS. The peptides obtained from chitosan film enriched with only fibronectin and from chitosan film enriched with fibronectin through aptamers were reported on Table 2.

A lower number of peptides were obtained from FN directly bound to chitosan with respect to FN in solution and FN bound to chitosan disc through the aptamer, to suggest a reduced FN conformational mobility or availability to the in-solution proteolytic activity. It is interesting to notice that the number and type of peptides generated from FN bound to chitosan film in the presence of aptamers were comparable to those obtained with FN in solution (Table 1). Thus the protein, when bound to the film through aptamers, maintains greater exposure to the solvent and to the enzymatic activity. These data confirm that aptamer act as a spacer and allows to preserve the pristine conformation of FBN, once adsorbed on chitosan.

9.4 Conclusions

Over the last two decade several refined HDX MS techniques have been developed to study proteins dynamics, making this approach widely exploited for many applications.
As in the field of biomaterials, the ESI-MS and MS/MS data here obtained presented, as key feature, the ability of a simple HDX approach to provide useful and direct insights on the structural dynamics of a FN fragment involved in chitosan surface functionalization in the presence or absence of a selective aptamer. As previously reported[17] aptamers did not affect the amount of adsorbed FN, but presumably influenced its conformation enhancing its biological activity toward osteoblasts adhesion and growth. Here, FN peptides involved in the interaction with aptamers were identified and MS findings indicated the improved functionality of FN on chitosan when aptamers were used as selective spacer. These results support the *in-vitro* experiments carried out on osteoblastic cells and could explain why cells preferentially attached and proliferated on the aptamer-bound FN rather than on chitosan-FN films.[17]

9.5 References

[1] Cooke M.E., Jones S.W., Ter Horst B., *et al.* Structuring of hydrogels across multiple length scales for biomedical applications. Adv. Mater. 2018; 30(14): e 1705013 doi: 10.1002/adma.201705013.
[2] Tang Z., Li X., Tan Y., Fan H., Zhang X. The material and biological characteristics of osteoinductive calcium phosphate ceramics. Regen. Biomater. 2018; 5(1): 43-59.
[3] Walraven M., Hinz B.. Therapeutic approaches to control tissue repair and fibrosis: extracellular matrix as a game changer. Matrix Biol. 2018; (71-72): 205-224pii: S0945-053X(17)30490-0

[4] Huang G., Li F. , Zhao X., *et al*. Functional and biomimetic materials for engineering of the three-dimensional cell microenvironment. Chem. Rev. 2017; 117,(20): 12764-12850.
[5] Spang M.T., Christman K.L.. Extracellular matrix hydrogel therapies: *in vivo* applications and development. Acta Biomater. 2018; 1(68): 1-14.
[6] Lee Y.E., Kim H., Seo C., *et al*. Marine polysaccharides: therapeutic efficacy and biomedical applications. Arch. Pharm. Res. 2017; 40(9): 1006-1020.
[7] Husain S., Al-Samadani K.H., Najeeb S., *et al*. Chitosan biomaterials for current and potential dental applications. Materials. 2017; 10(6): 602.
[8] Bianchera A., Salomi E., Pezzanera M., Ruwet E., Bettini R., Elviri L. Chitosan hydrogels for chondroitin sulphate controlled release: an analytical characterization. J. Anal. Methods Chem. 2014; 2014, 808703.
[9] Oryan A., Sahvieh S. Effectiveness of chitosan scaffold in skin, bone and cartilage healing. Int. J. Biol. Macromol. 2017; 104(Pt.A): 1003-1011.
[10] Ribeiro J.C.V., Vieira R.S., Melo I.M., Araújo V.M.A., Lima V. Versatility of chitosan-based biomaterials and their use as scaffolds for tissue regeneration. Sci World J. 2017; 2017:8639898. doi: 10.1155/2017/8639898.
[11] Elviri L., Bianchera A., Bergonzi C., Bettini R.. Controlled local drug delivery strategies from chitosan hydrogels for wound healing. Exp. Opin. Drug Deliv. 2017; 14(7), 897-908.
[12] Napavichayanun S., Aramwit P. Effect of animal products and extracts on wound healing promotion in topical applications: a review. J. Biomater. Sci. Polym. Ed. 2017; 28(8): 703-729.
[13] Costa E., Silva S., Pina C., Tavaria F., Pintado M. Evaluation and insights into chitosan antimicrobial activity against anaerobic oral pathogens. Anaerobe. 2012; 18(3): 305-309.
[14] Bettini R., Romani A., Morganti M., Borghetti A.F. Physicochemical and cell adhesion properties of chitosan films prepared from sugar and phosphate-containing solutions. Eur. J. Pharm. Biopharm. 2008; 68(1): 74-81.
[15] Elviri L., Asadzadeh M., Cucinelli R., Bianchera A., Bettini R. Macroporous chitosan hydrogels: Effects of sulfur on the loading and release behaviour of amino acid-based compounds. Carbohydr. Polym. 2015; 132: 50-58.
[16] Galli C., Parisi L., Elviri L., *et al*. Chitosan scaffold modified with D-(+)-raffinose and enriched with thiol-modified gelatin for improved osteoblast adhesion. Biomed. Mater. 2016; 11(1): 015004.
[17] Parisi L., Galli C., Bianchera A., *et al*. Anti-fibronectin aptamers improve the colonization of chitosan films modified with D-(+) Raffinose by murine osteoblastic cells. J. Mater. Sci: Mater. Med. 2017; 28(9): 136. [18] Cheng S.S., Chittur K.K., Sukenik C.N., Culp L.A., Lewandowska

K. The conformation of fibronectin on self-assembled monolayers with different surface composition: an FTIR/ATR study. J. Colloid Interface Sci. 1994; 162: 135-43.
[19] Pirrone G.F., Iacob R.E., Engen J.R.. Applications of hydrogen/deuterium exchange MS from 2012 to 2014. Anal. Chem. 2015; 87(1), 99-118.
[20] Wang L., Chance M.R.. Protein footprinting comes of age: mass spectrometry for biophysical structure assessment. Mol. Cell Proteomics. 2017; 16(5): 706-716.
[21] Chengjie J., Gary W.. Deglycosylation induces extensive dynamics changes in □-amylase revealed by hydrogen/deuterium exchange mass spectrometry. Rapid Commun. Mass Spectr. 2013; 27(23): 2625-30.
[22] Dey B., Thukral S., Krishnan S., *et al*. DNA-protein interactions: methods for detection and analysis Mol. Cell Biochem. 2012; 365(1-2): 279-99.
[23] Zhang Q., Chen J., Kuwajima K., *et al*. Nucleotide-induced conformational changes of tetradecameric GroEL mapped by H/D exchange monitored by FT-ICR mass spectrometry, Sci. Rep., 2013; 3, 1247 doi:1038/srep01247.
[24] Pettersen E.F., Goddard T.D., Huang C.C., *et al*. UCSF Chimera-A visualisation system for exploratory research and analysis. J. Comput. Chem. 2004, 25(13): 1605-12.

Peptide sequence	m/z	FN	FN+aptamer
		Ion intensity (cps) (RSD%)	Ion intensity (cps) (RSD%)
QAQQMVQPQSPVAVSQ	864	-	3,90E+04 (3%)
WERTYLGNAL	408	1,17E+03 (3%)	2,50E+04 (3%)
YRVGDTYERPKDSMI	916	1,08E+05 (1%)	3,20E+04 (3%)
YKIGDTWRRPHETGGYM	1035	3,00E+05 (5%)	1,80E+04 (6%)
YVVGETWEKPYQGWMM	669	2,80E+05 (2%)	1,90E+02 (4%)
QTTSSGSGSPFTDVR	510	-	6,00E+05(2 %)
TRTSYRIGDTWSKKDNRG NLL	1242	-	9,70E+04(3 %)

Table 1. Significantly different ($p<0.05$) peptic fragments identified from the FN (conc. 1.67 μM) and the FN/aptamer (1:5) aqueous solutions (n=3).

Peptide sequence	Chitosan disc+FN	Chitosan disc+aptamer+FN
	Ion intensity (cps)(RSD%)	Ion intensity (cps)(RSD%)
QAQQMVQPQSPVAVSQ	-	6,70E+04 (3%)
WERTYLGNAL	-	1,90E+04 (3%)
YRVGDTYERPKDSMI	2,45E+04 (3%)	4,50E+04 (3%)
YKIGDTWRRPHETGGYM	2,83E+04 (6%)	2,10 +05 (6%)
YVVGETWEKPYQGWMM	3,87E+03 (3%)	3,65E+04 (3%)
QTTSSGSGSPFTDVR	-	-
TRTSYRIGDTWSKKDNRGNLL	-	3,30E+04(2%)

Table 2. Significantly different ($p<0.05$) peptic fragments identified from the FN and the FN/aptamer bound to chitosan disc (n=3).

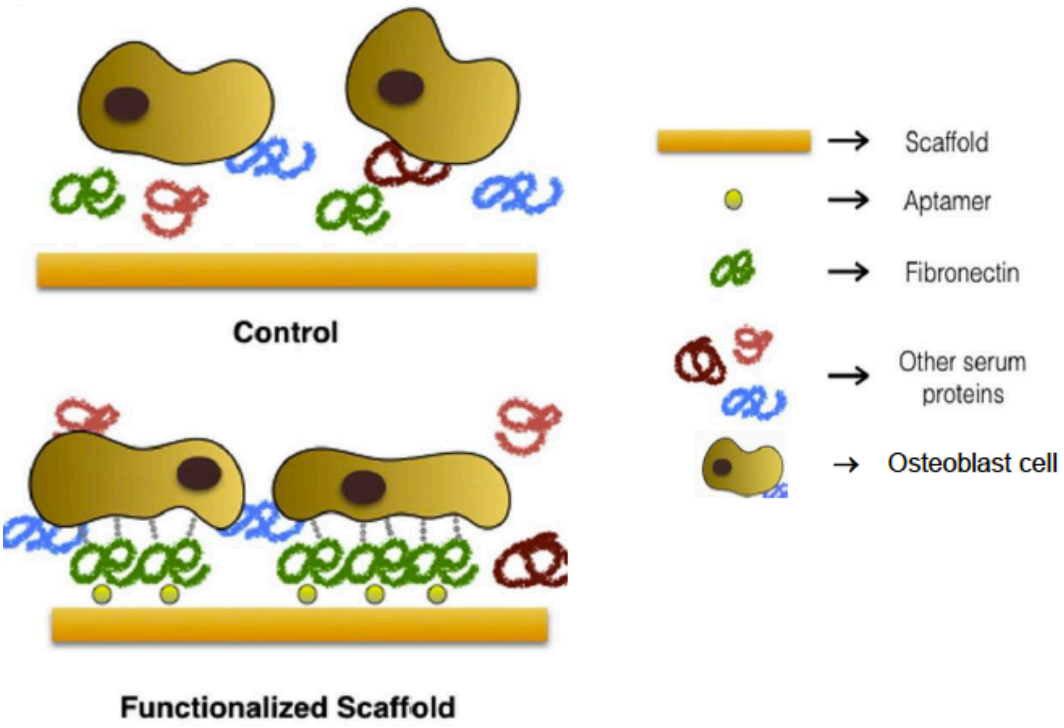

Figure 1. Scheme of the interaction of fibronectin on the chitosan disk surface in presence or absence of the selective binding aptamer.

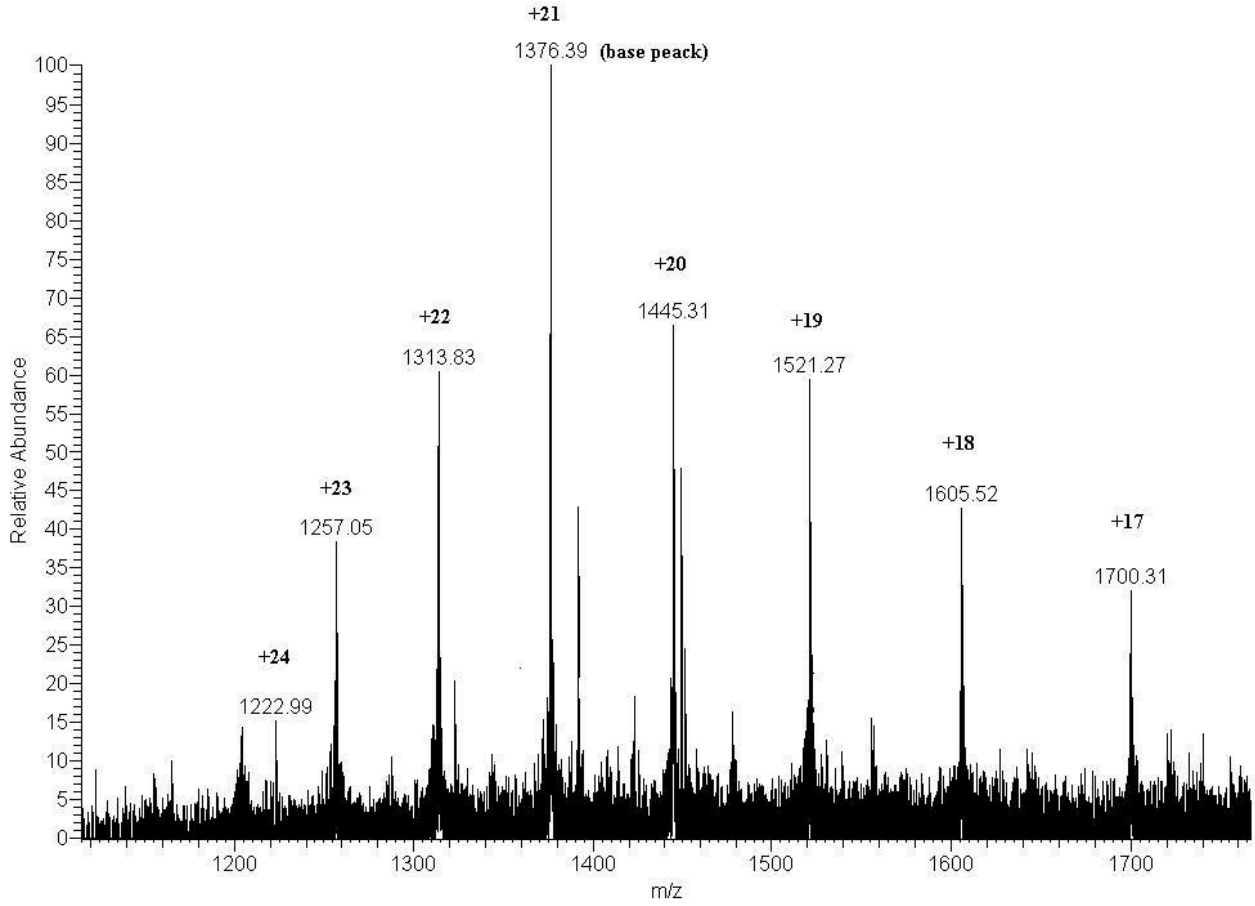
+21
1376.39 (base peack)
+20
1445.31
+22
1313.83
+19
1521.27
+23
1257.05
+18
1605.52
+17
1700.31
+24
1222.99
Relative Abundance
m/z

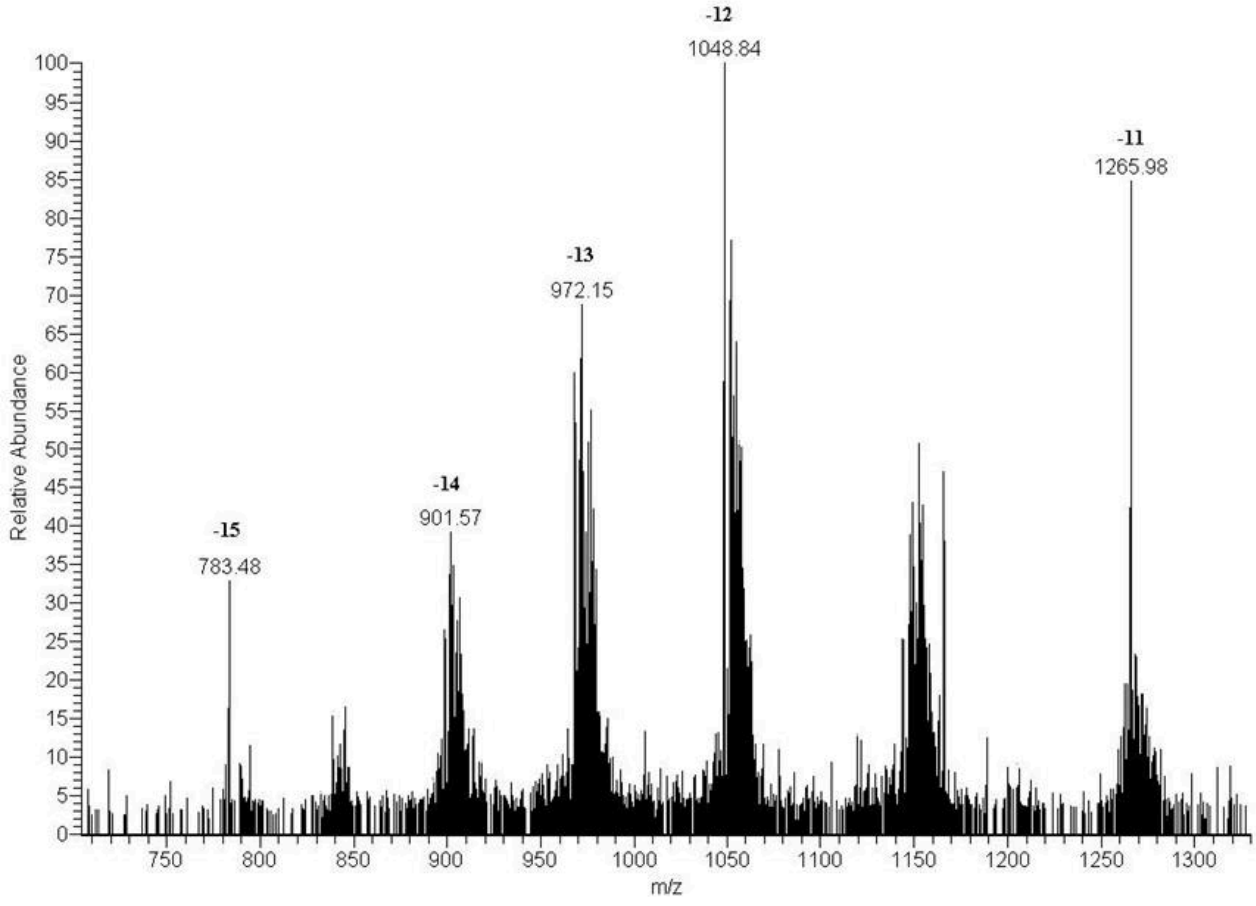
-12
1048.84
-11
1265.98
-13
972.15
-14
901.57
-15
783.48
Relative Abundance
m/z

Figure 2. ESI-MS full scan mass spectra of (A) the FN (conc. 1.67 μM) and (B) the aptamer (conc. 10 μM) aqueous solutions.

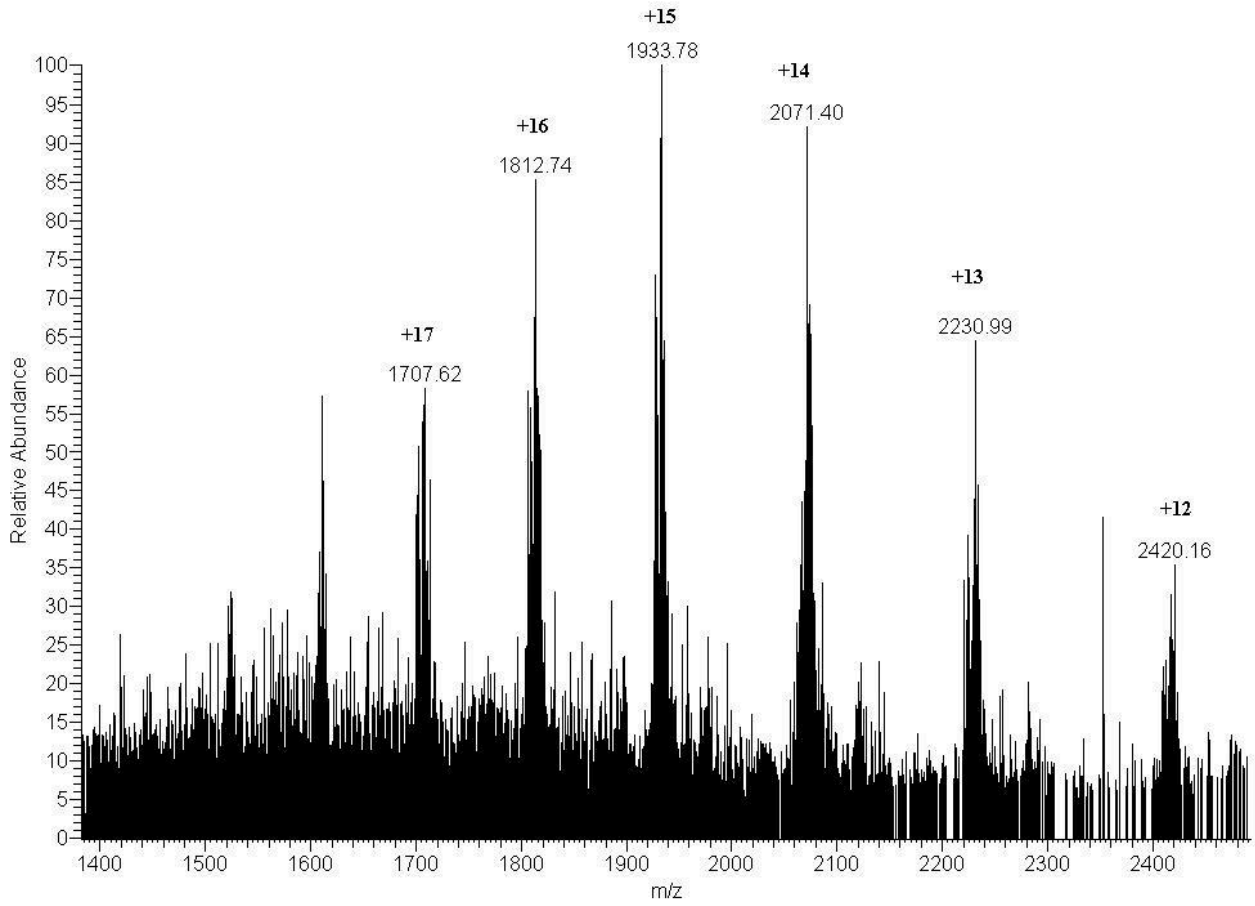

Figure 3. ESI-(PI)MS mass spectrum of FN after 60 min HDX.

(A)

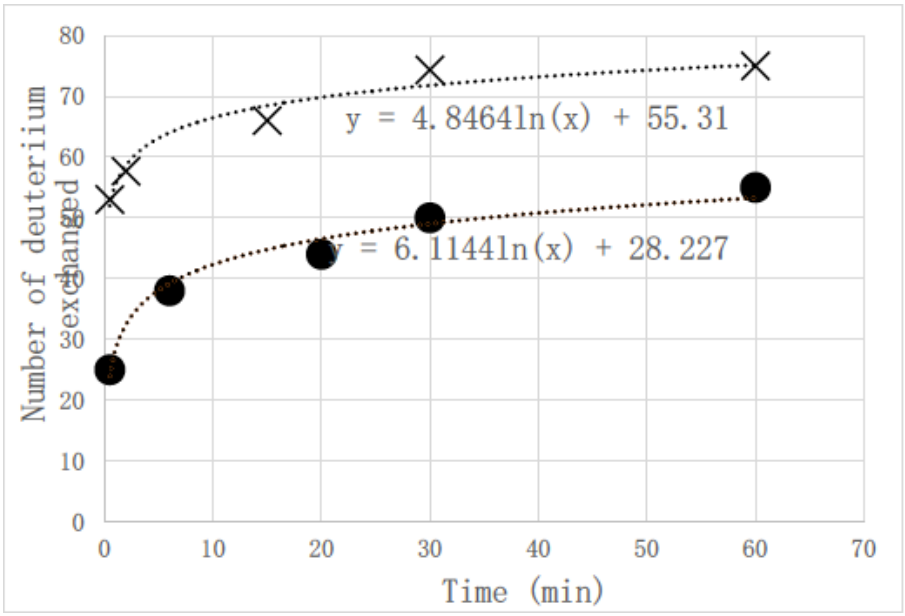

(B)

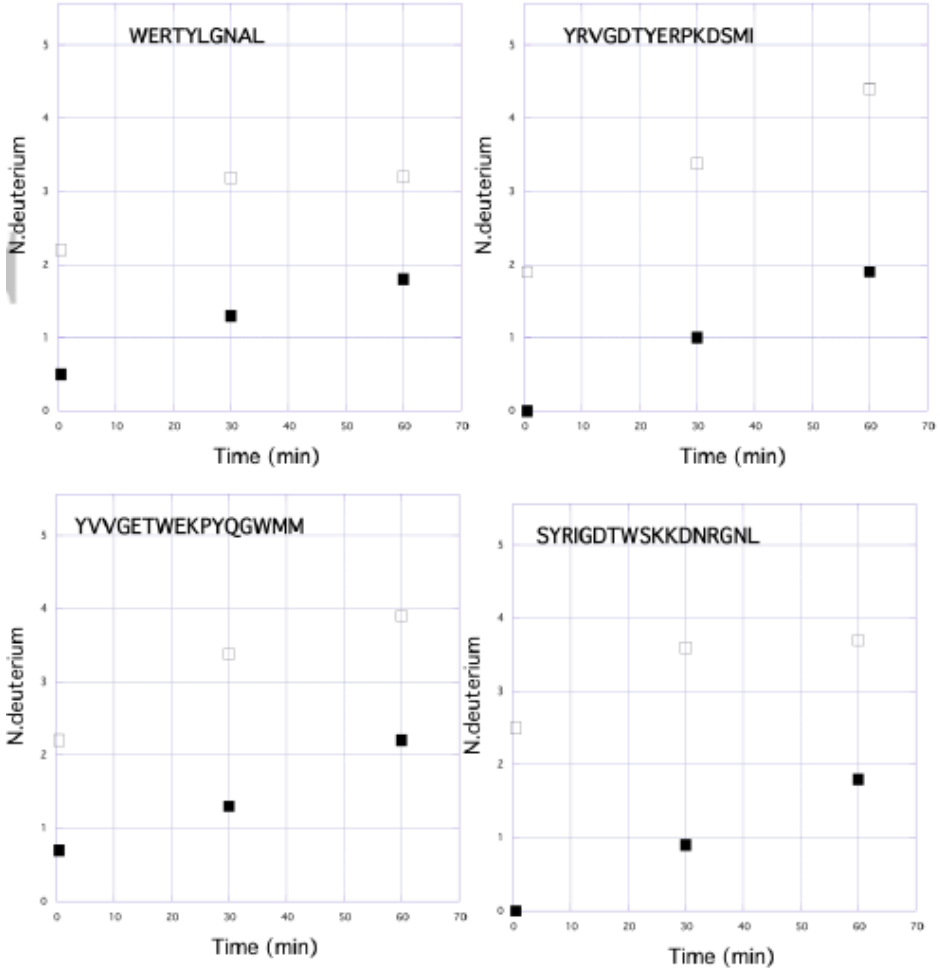

Figure 4. (A) Number of deuterium exchanged in solution by FN (cross) and FN in the presence of aptamer (dot). (B) Time course of deuterium incorporation by FN peptic peptides in D_2O as a

function of time (average of triplicates, RSD<3%). FN alone (empty square), FN in the presence of aptamer (black square).

10 Chapter 7: “3D-printed Chitosan scaffolds modified with D-(+) Raffinose and enriched with type IV Collagen to improve epithelial cell colonization”

Maria Teresa Colangelo(ORCID: 0000-0002-4664-5766) [1*], Lisa Elviri(ORCID: 0000-0002-5988-618X)[2*], Silvana Belletti(ORCID: 0000-0003-0262-4485)[1], Monica Mattarozzi(ORCID: 0000-0002-6766-4616)[3], Paolo Govoni(ORCID: 0000-0002-7596-6251)[1], Carlo Bergonzi(ORCID: 0000-0001-9623-7296)[2], Maria Careri(ORCID: 0000-0002-4558-5001)[3], Ruggero Bettini(ORCID: 0000-0002-3857-7476)[2], Stefano Guizzardi(ORCID: 0000-0003-2395-8767)[1], Carlo Galli (ORCID: 0000-0001-7476-7181)[1]

[1] Dep. Medicine and Surgery, University of Parma, [2] Food and Drug Department, University of Parma, [3] Department of Chemistry, Life Sciences, and Environmental Sustainability, University of Parma, Parma, Italy [*]These authors contributed equally to the work

Manuscript submitted on Biomedical Materials to be considered for publication

Personal contribution

CB performed the experimental work related to 3D development and scaffold analytical characterization and contributed to the preparation of the manuscript.

Abstract

Tissue regeneration often requires the use of biocompatible resorbable scaffolds to support the ingrowth of cells from neighboring tissues into a localized tissue defect. Such scaffolds must possess surface molecular cues that stimulate cells to populate the device, the first necessary condition for the formation of a healthy tissue. Chitosan is a natural polymer that has long been tested in biomedical applications because of its high biocompatibility, which can be further increased by modifying its formulation, e.g. adding D-(+) Raffinose. We used this formulation in an *ad hoc* designed 3D-printer to create regularly ordered scaffolds, which we then enriched with type IV Collagen, an isoform of Collagen that is exclusively found in Basement Membranes. Human epithelial A549 cells were then seeded on control scaffolds or on scaffolds coated with Collagen, which was then either precipitated or exposed to UVB or UVC radiation. Observations at the transmission microscope, confocal microscope after staining with Calcein-AM/Propidium Iodide, and by Environmental Scanning Electron Microscope revealed that collagen-enriched UV-treated scaffolds promoted the attachment of a higher number of cells, which covered a more extensive area of the scaffold, as also confirmed by Alamar blue viability assay.
Together these data confirm that coating 3D-printed scaffolds made of D-(+) Raffinose-modified Chitosan with type IV Collagen and exposing them to UV light sensibly increases the cell compatibility of scaffolds, making them a better candidate to serve as a tool for the regeneration of epithelia.

Keywords: Chitosan, Collagen, Epithelial cells

10.1 Introduction

The repair and regeneration of damaged tissues are complex phenomena that involve the coordinated action of several processes, including hemostasis, cell proliferation, differentiation and the formation of extracellular matrix [1]. Epithelia in mammals have a marked self-healing potential, but there are numerous clinical situations where healing is impaired, thus resulting in scar formation and, eventually, functional alterations. This may happen, for instance, in the case of severe tissue destruction, as after extensive trauma or burn, on in the presence of metabolic diseases that affect and hinder normal tissue functionality, e.g. diabetes [2]. Biocompatible scaffolds are often inserted into tissue defects to support the ingrowth of cells from neighboring healthy tissues [3]. One of the best known and exploited materials to this purpose is Chitosan (CH), which is obtained by de-acetylating Chitin, a common component found in the exoskeleton of arthropods and in molds [4]. Chitosan has long been proposed for biomaterial diverse engineering applications, due to its high compatibility, low toxicity and cost [5]. Chitosan can also be easily manipulated into medical devices of different shapes and functionalized [6], as it will promptly bind proteins and negatively-charged macromolecules, e.g. chondroitin sulphate [7], thus proving to be a flexible multi-role platform for tissue engineering. Furthermore, CH has been extensively investigated as a support for epithelial regeneration in numerous studies conducted with a vast array of models [8,9].

Bettini et al. have reported that using D-(+) Raffinose during the preparation of the scaffold improved material hydrophilicity and increased its water content, possibly by acting as a spacer between CH chains[10]. Moreover, the same authors have used this modified formulation to create CH scaffolds through freeze-deposition by a dedicated 3D printer. In this system, CH is deposited on a cooled surface and immediately frozen to help maintain the desired scaffold geometry while the gelation process occurs [11,12]. These scaffolds have been successfully tested with fibroblasts and keratinocytes *in vitro* and in an *in vivo* diabetic rat model [13]. We have previously reported on the functionalization of D-(+) Raffinose-modified CH discs with thiol-modified gelatin [14] or with anti-fibronectin single strand DNA aptamers [15,16] to improve the attachment of murine calvaria osteoblastic MC3T3-E1 cells and have shown how D-(+) Raffinose-modified Chitosan readily allowed for easy functionalization, which in turn enhanced they cytocompatibility. In the present report, human epithelial cells were cultured on 3D printed D-(+) Raffinose-modified CH scaffolds enriched with type IV Collagen, a network/sheet-forming, non fibrillar isoform of Collagen [17] which is abundant and exclusive in basement membranes, structures that support and orient the overlying epithelia [18]. The purpose of the

present study was therefore to investigate whether epithelia-targeting type IV Collagen coating could improve the adhesion and proliferation of epithelial cells on 3D printed Chitosan.

10.2 Materials and methods

10.2.1 Scaffold preparation

We used 3D chitosan scaffolds of 15 mm diameter, 1-2 mm thickness, with 200 µm pores and a variable number of layers (5-10). Chitosan scaffolds were prepared according to the method reported by Bettini et al. and printed using a Low Temperature Manufacturing system designed and implemented by Elviri *et al.* [11,12] The bottom of the scaffolds was sealed by a continuous layer of Chitosan, unless specified. Briefly, a 6% w/v solution of chitosan –modified with D-(+) Raffinose was prepared in 2% w/v acetic acid. D-(+) Raffinose pentahydrate (290mM) was used as a viscosity modifier agent in order to obtain more hydrophilic hydrogels. This solution was used to develop the 3D chitosan scaffolds by extrusion-based 3D printing using a syringe pump and a cooling system combining air–liquid exchangers and Peltier plates that to control the scaffold porosity. Subsequently, frozen scaffolds were transferred to aqueous KOH (8% w/v) for 10 min for gelation. Scaffolds were then rinsed in deionized water for 10 min to remove the sugar and stored in deionized water at 4°C.

10.2.2 Type IV collagen coating

Chitosan scaffolds were enriched with type IV Collagen (Merck KGaA, Darmstadt, Germany). Briefly, we dissolved type IV collagen with buffer HBSS (Hank's Balanced Salt Solution, Merck KGaA) at final concentration of 0.1 µl/ml and 1ml of the above-mentioned solution was added to chitosan scaffolds in a 24-well plate. Then, 100 µl NaOH 1N (Merck KGaA) was added and samples were incubated at 37°C over-night. The type IV collagen-coated chitosan was washed with PBS (Gibco, ThermoFisher Scientific, Waltham, Massachussetts, USA) and used directly as cell culture substrate or exposed to UVB and UVC light to induce cross-linking collagen before the seeding of the cells. For this purpose, scaffold coated with type IV Collagen were irradiated for 30 minutes at room temperature in a custom-made exposure chamber equipped with a TL20W/12 RS (Philips) neon lamp emitting in the 290-315 nm, with a power of 2.4 W. UVC were administered with a Stratalinker UV 1800 (Stratagene, La Jolla, CA, USA), set at 20 mJ, according to the manufacturer's recommendations.

10.2.3 Cell culture

The cells used in the experiments were A549 human lung adenocarcinoma cell line. The cells were maintained in complete Dulbecco′s Modified Medium (DMEM, ThermoFisher Scientific), with 10% fetal bovine serum (Gibco, ThermoFisher Scientific) and supplemented with 1% L-glutamine (Merck KGaA) and 1% penicillin and streptomycin (PenStrep, Merck KGaA). The cells were plated in 75-cm^2 cell culture flasks and sub-cultured before reaching confluence using a 0.1% trypsin solution in EDTA (Merck KGaA). The culture medium was replaced every 2 days. For the experimental assays, cells were plated on CH scaffolds in complete culture medium at the density of 60000 cells/well, with the only exceptions of ESEM observations, where 200000 cells/well were used.
Cell cultures on CH scaffolds, collagen-coated CH scaffolds and irradiated collagen-coated CH scaffolds were monitored by inverted optical microscope (Nikon, Tokyo, Japan) in phase contrast for morphological characterization. The microscope was equipped with a digital image acquisition system (Nikon).

10.2.4 Histology

Chitosan scaffolds were fixed in PBS-buffered 4% paraformaldehyde (pH 7.4) and then embedded in paraffin. Six μm-thick slices were cut with a microtome and stained with hematoxylin-eosin, with the addition of picro-sirius red F3BA for collagen detection. Slices were then observed with an optical microscope Nikon Eclipse 80i (Nikon), equipped with a Nikon Digital Sight DS-2Mv camera and imaged with NIS Elements F control software (Nikon).

10.2.5 LIVE/DEAD assay

The viability of A549 cultured on chitosan scaffolds, collagen-coated chitosan scaffolds and irradiated collagen-coated chitosan scaffolds was determined using a LIVE/DEAD assay. Cells were seeded on the scaffolds at a concentration of 60000 cells/well in a 24-well plate. Cells were cultured in complete medium. After 24h the medium was replaced with PBS $Ca^{2+}Mg^{2+}$ and the cells were stained with 1 μl Calcein AM solution (Invitrogen, ThermoFisher) and 2 μl of Propidium Iodide solution (PI, Invitrogen, ThermoFisher), incubated at 37°C for 30min and observed with a Confocal Laser Scanning Inverted Microscope (CLSM, LSM 510 Meta, Zeiss,

Oberkochen, Germany). For 3D reconstruction, stacks of digital images were processed employing the Axiovision (release 4.5) software (carl Zeiss, Jena Germany).
To quantitate viable cells, images were processed with ImageJ freeware software [19]. Data were obtained as the average of 5 images per condition and normalized by area.

10.2.6 Alamar Blue assay

Cell viability and cytotoxicity were evaluated with the Alamar Blue assay. Cells were seeded at a concentration of 60000 cells/well on chitosan scaffolds, collagen-coated chitosan scaffolds and irradiated collagen-coated chitosan scaffold. Cell growth was monitored at 24,48, 72 and 96 h after seeding. Briefly, at each experimental time point the culture medium was replaced with DMEM and Resazurin (Merck KGaA) in a 1:5 ratio. Cells were then incubated for 4 h at 37°C. The fluorescence was read at 535 and 595 nm using a spectrophotometer (Infinite F200, Tecan, Männedorf, Switzerland). The samples were then washed with DMEM and fresh culture medium was added.
As for statistical analysis, Alamar Blue assay was performed in triplicate and results were expressed as mean±SD. The significance of the differences between groups were determined by two-way analysis of variance (ANOVA) and by Bonferroni post hoc test; p values of less than 0.05 were considered statistically significant. Data analyses were performed using the software Prism v5.00 (GraphPad, La Jolla , CA).

10.2.7 Environmental Scanning Electron Microscopy (ESEM) analysis

Cells were seeded at a concentration of 200000 cells/well on chitosan scaffolds, collagen-coated chitosan scaffolds and irradiated collagen-coated chitosan scaffolds and after 24h were observed by Environmental Scanning Electron Microscopy (ESEM Quanta™ 250 FEG instrument, FEI, Hillsboro, OR) to evaluate the cytocompatibility of the different types of scaffolds. Samples were washed with PBS $Ca^{2+}Mg^{2+}$, immersed in 4% PFA (Merck KGaA) for 15 min and rinsed in PBS and water. Then, scaffolds were cut to a proper size to be placed on a pre-cooled metallic plate in thermal contact with a Peltier water-cooling stage, maintained at 3°C. The relative humidity (RH) was initially set to 100%, then it was slowly decreased, until the working value of 70% was reached. Gaseous secondary electron detector (GSED) was used for morphological investigation working with an accelerating voltage of 10 kV.

10.3 Results

10.3.1 Adhesion of A549 epithelial cells is impaired on not functionalized chitosan

As a first step, lung carcinoma-derived A549 epithelial cells grown in complete DMEM were cultured on 3D-printed D-(+) Raffinose-modified CH scaffolds (Figure 1, 2A) without a bottom layer.

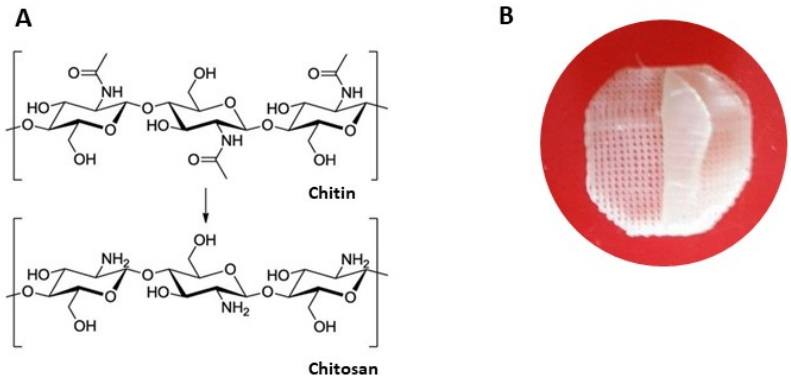

Figure 1: A) Diagram representing the structure of Chitin and its derivative Chitosan. Chitosan is obtained by de-acetylation of Chitin. B) The scaffolds used in the present study were obtained by 3D printing as 10 superimposed layers of Chitosan.

Cells therefore grew on culture plastic and contacted the CH scaffold only peripherally (Fig. 2B). Cell morphology appeared elongated, tending to a squared shape in areas of high cell density, when observed at the transmission microscope. Under these conditions, cells spread evenly on the culture surface and without displaying signs of toxicity in the areas of contact with the CH scaffolds. Consequently, to better visualize cells' behavior on CH, we seeded A549 cells on scaffolds with a chitosan bottom layer avoiding their direct contact with the plastic well (Fig. 2C, D). This kind of bottom-closed scaffold was used for all the following experiments. When cultured on CH, cells appeared quite different than they did on culture plastic: they were mostly rounded, small and formed clusters, gathering mostly at the corners between the bottom and the scaffold walls (Fig. 2D). This morphology is highly suggestive of reduced adhesion, as cells are not able to maintain their normal spread shape.

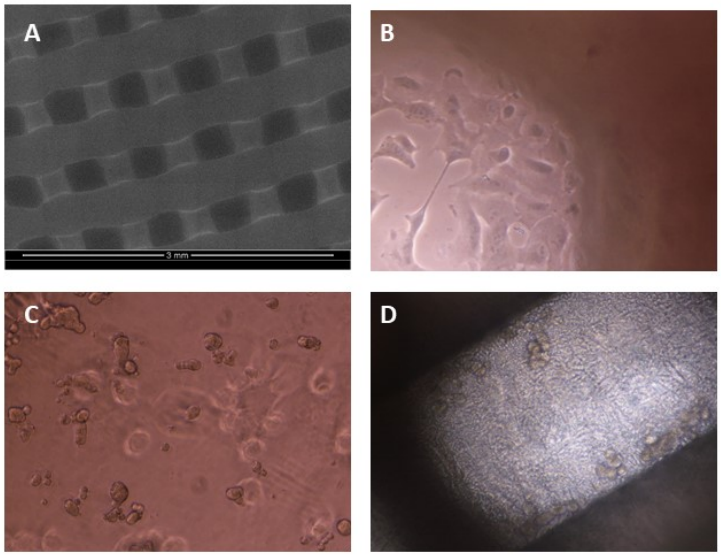

Figure 2: (A) SEM microphotograph of CH scaffold showing its ordered structure. Microphotographs of A549 epithelial cells cultured on plastic wells in the presence of Chitosan scaffolds at B) 40 X magnification. Cells have normal morphology and do not present signs of toxicity. (C, D) A549 cells growing on Chitosan scaffolds with a Chitosan bottom layer. Higher magnification (C, 40 X) shows that cells are mostly rounded and tend to grow in clusters along the scaffold edges (D, 20 X).

10.3.2 Chitosan scaffolds can be enriched with type IV Collagen for improved cell adhesion

The strategy proposed in the present work to improve epithelial cell attachment on D-(+) Raffinose-modified CH was to coat the chitosan scaffolds with type IV Collagen, as described in the experimental section. At SEM observation, the scaffold structure appeared morphologically unaffected by Collagen coating, neither in shape, nor in size (data not shown). The presence of Collagen was verified by Sirius Red staining (Fig. 3A), and it was observed to be evenly distributed along the surface of the scaffold. Fluorescence microscopy was used to quantitate cells on scaffolds and proved that Collagen increased the number of adhering cells (Fig. 3B). Moreover, the effect of Collagen appeared to depend on its concentration, as more cells were found to be adhering to CH after coating with 1% type IV Collagen than with 0.0001% Collagen (Fig. 3B). Although Collagen promoted a better cell adhesion (Fig. 4A, B) their morphology still tended to be round as in uncoated scaffolds.

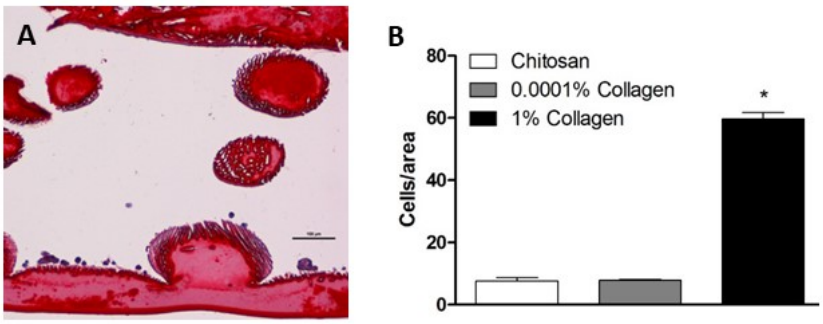

Figure 3: Collagen coating formed a uniform layer on the scaffold (A) and significantly increased the number of adhering cells, as quantified at fluorescence microscopy (B).

As crosslinking is a common method to stabilize Collagen both in tissues and on scaffolds, we treated type IV Collagen-coated CH scaffolds with UVB or UVC light. UVC is a more common approach, because it has been shown to possess the energy required to cross-link Collagen. We decided, however, to compare UVC with a radiation with lower energy, namely UVB, to reduce potential molecular alterations. Cell observation at transmission microscopy showed a higher number of cells on UV-treated samples compared to the control group (Fig. 4C, D).

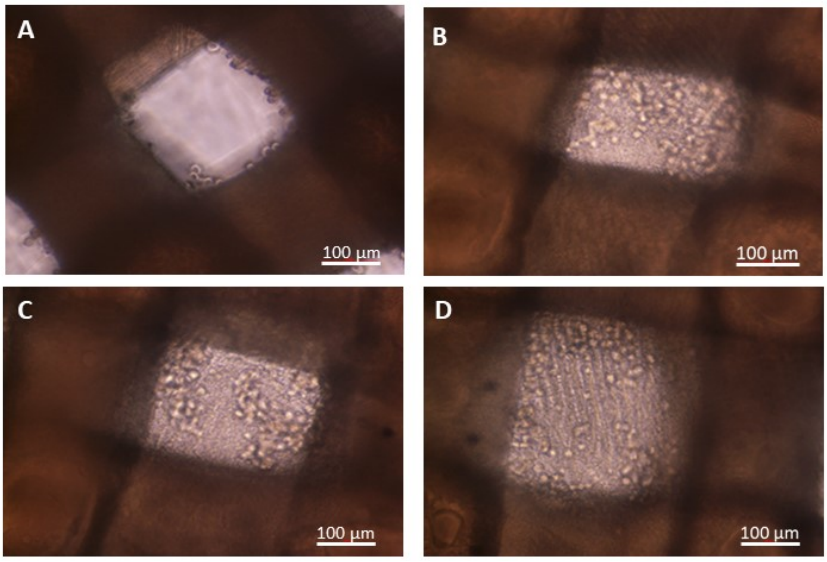

Figure 4: (A) Microphotographs of A549 cells on control scaffolds at transmission microscopy. (B-D) Cells growing on Collagen-coated alone (B) or after UVB (C) or UVC (D) treatment scaffolds were visibly more numerous than cells in the control group (A). Exposure to UVB or UVC light did not apparently impact on cell morphology or cell distribution. Magnification 20 X, bar= 100 µm

10.3.3 Cell growth is increased on Collagen-coated Chitosan after UV treatment

The investigation of cell growth on chitosan samples assessed by Alamar blue staining demonstrated how the highest cell number was detected on UV-irradiated collagen-coated scaffolds after 48 hours of culture. By that time a significantly lower level of cell viability was detected on control samples than UVB-treated samples ($p<0.05$, Fig. 5). Interestingly, cell viability on Collagen-coated CH was comparable to Control at that time-point. The levels of cell viability on Collagen-coated samples, however, increased after 72 hours of culture, and reached similar levels to UV irradiated scaffolds (Fig. 5). Therefore, at that time point, viability levels on control samples were significantly lower than on Collagen-coated samples ($p<0.05$), UVB-treated samples ($p<0.01$) and UVC-treated samples ($p<0.05$). The situation did not substantially change after 96 h of culture, when the levels of cell viability on UVB-treated samples were still significantly higher than in the control group ($p<0.05$).

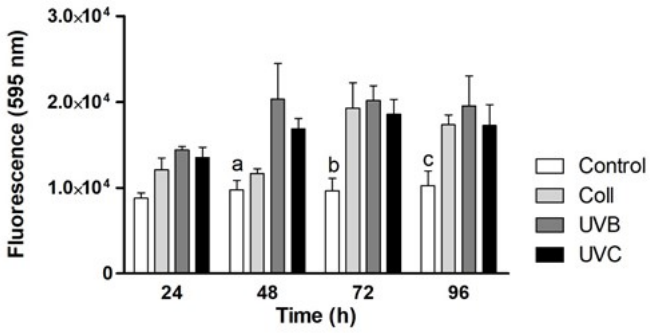

Figure 5: Diagram representing cell viability on Control or Collagen-coated scaffolds as assessed by Alamar Blue assay 24, 48, 72 or 96 hours after seeding. Cell viability levels on Control scaffolds were always significantly lower than viability levels on UVB-treated scaffolds. a= $p<0.01$ vs UVB samples; b=$p<0.01$ vs Collagen-coated (Coll), $p<0.01$ vs UVB, $p<0.05$ vs UVC samples; c=$p<0.01$ vs UVB samples.

10.3.4 Collagen increases cell viability on Chitosan

These results were confirmed by observation with confocal microscope after staining with Calcein-AM and Propidium Iodide (Fig. 6). A higher number of cells is visible in the scaffolds after Collagen functionalization (Fig. 6B), not only on the bottom of the scaffold, as observed in most cases on the control samples (Fig. 6A), but cells were seen colonizing the whole Chitosan samples. Irradiation again increased cell adherence on the scaffolds.

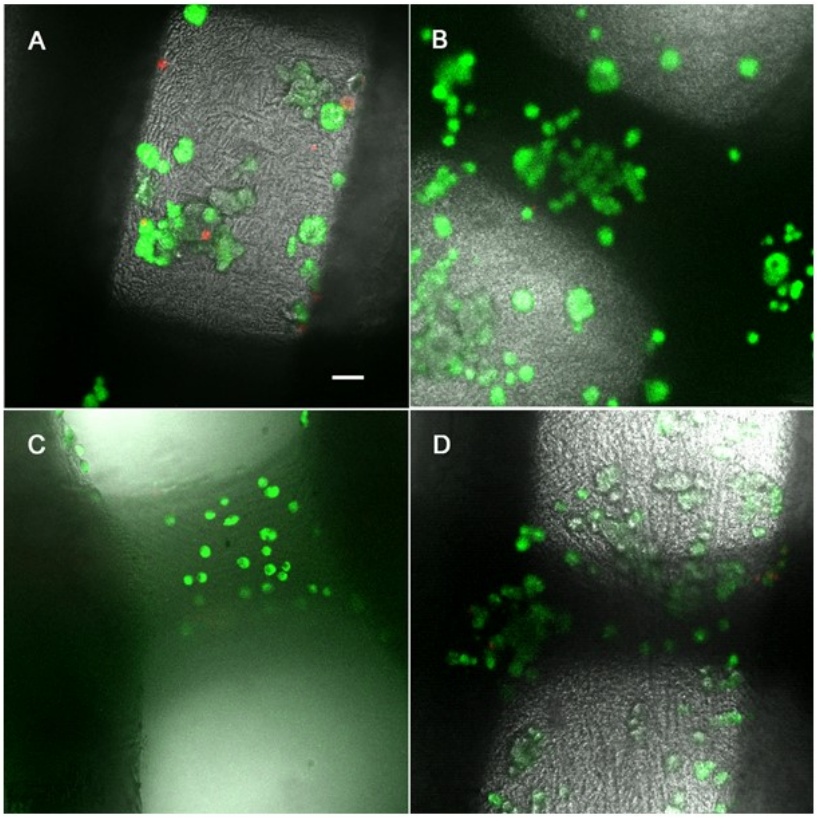

Figure 6: Microphotographs of A549 cells on Control (A) or Collagen-coated (B) UVB-treated (C) or UVC-treated (D) Chitosan scaffolds, stained with Calcein-AM (green) for viable cells or Propidium Iodide (red) for dead cells at Confocal Laser Microscope. Magnification = 20X, Bar = 50 μm. The presence of Collagen increased the number of cells adhering on the actual scaffolds.

The effects of UV light on the scaffold were made more clear by 3D reconstruction (Fig. 7), where cells were observed coating the Chitosan walls. In particular cells on UVB-treated scaffolds were seen to form an almost continuous layer along some areas of the scaffold, as seen in Fig. 7A, B.

10.3.5 Collagen coating promotes a more even cell spreading

Control and functionalized samples incubated with A549 epithelial cells were observed with ESEM microscope after 24 hours of culture (Fig. 8A-H), exploiting ESEM potentialities for *in vivo* characterization of biological samples without any previous dehydration, fixation and conductive coatings[20].

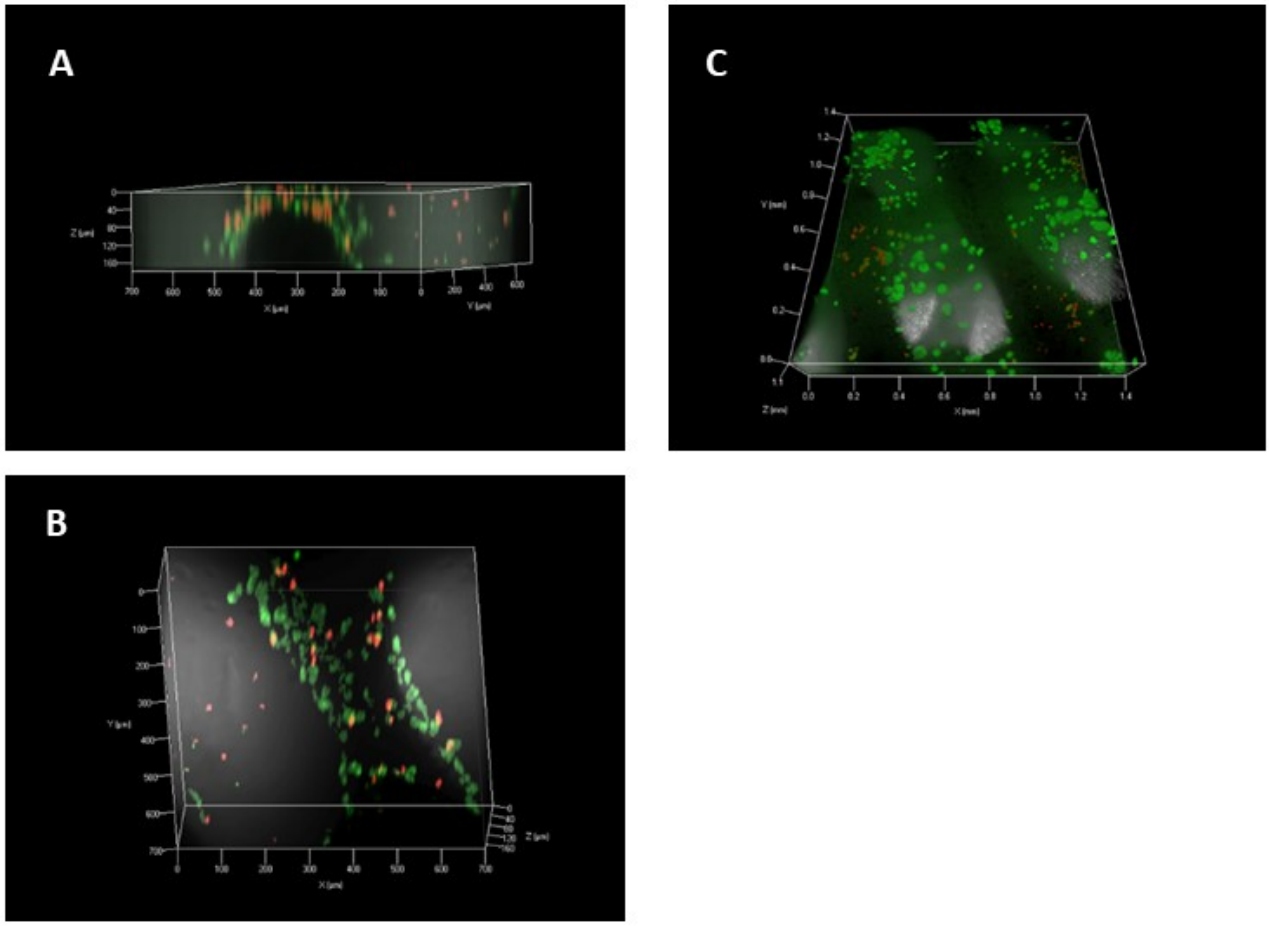

Figure 7: Three-dimensional reconstruction of A549 cells on Collagen-coated, UVB- (A, B) or UVC-treated (C) Chitosan scaffolds after staining for Calcein-AM (green) or Propidium Iodide (red) for cell viability at Confocal Laser Microscope.

Since its introduction, ESEM has represented a very attractive innovation in biological and medical research because it permits the imaging of wet specimens with no need for the conventional Scanning Electron Microscope (SEM) preparation, which may introduce artifacts. Cells on control scaffolds appeared rare and formed small clusters, as minimizing their contact to the surface. Addition of Collagen visibly improved the number of adhering cells and improved their distribution on the scaffold, which appeared more uniform. Although cell shape was still mostly rounded, some cells appeared to display cytoplasmic projections on UV-treated samples (Fig. 8H).

10.4 Discussion

The scaffolds used in the present study were based on a modified Chitosan formulation, with higher water content, due to the use of D-(+) Raffinose as a chain spacer during gelation [10].

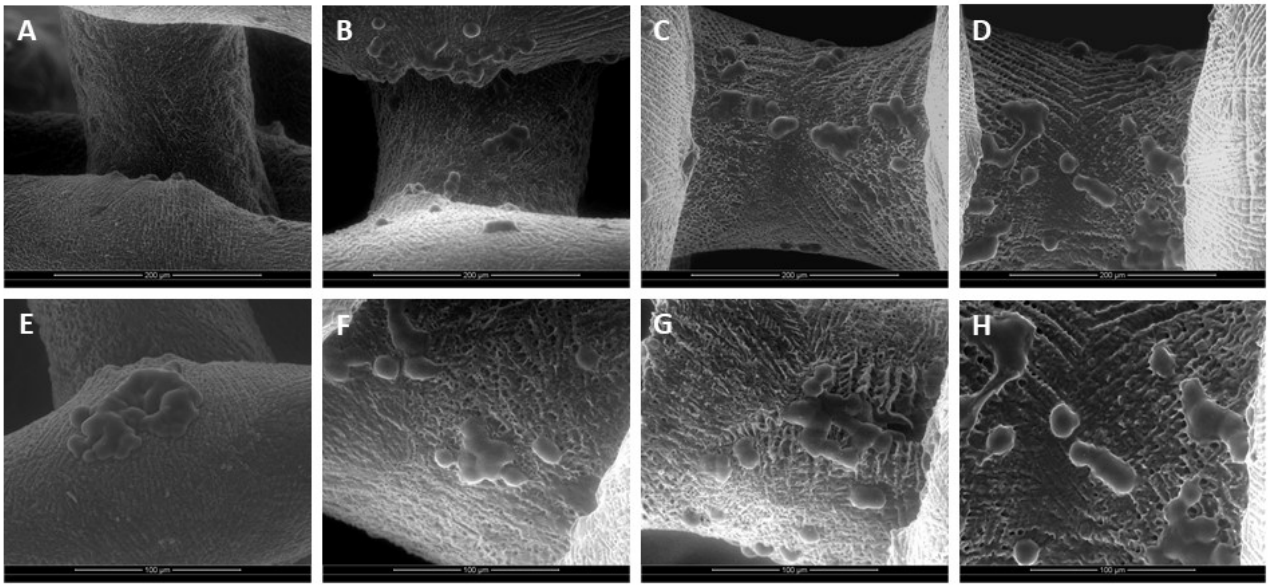

Figure 8: Microphotographs of A549 cells on Control (A, E), Collagen-coated scaffolds (B, F), Collagen-coated and UVB-treated scaffolds (C, G) or Collagen-coated, UVC-treated scaffolds (D, H), observed at Environmental Scanning Electron Microscope at 1000 X magnification (A-D) or 1500 X magnification (E-F).

It must be noted that D-(+) Raffinose gets washed out of the scaffold prior to use, so no additional component is present in the formulation besides Chitosan. Moreover, Chitosan, due to its net electrical charge, is easily functionalized [7] and we relied on this property of CH to enrich it with type IV Collagen, which was then precipitated on the scaffold and UV-treated, with either UVB or UVC radiation. Type IV Collagen is a Basement Membrane-specific form of Collagen, which shares extensive similarities with the primary structure of other, more abundant Collagen types, e.g. type I Collagen, but, unlike the latter, does not form fibrils [18]. Due to its localization, type IV Collagen is one of the main support structures found in Basement Membranes, which provide anchorage to epithelial cells. The rationale behind the use of type IV Collagen, therefore, is to try and create a 3D structure that can act as a support for epithelia, just like a connective tissue-supported Basement Membrane would do.

The cell model we adopted reflected the preliminary nature of this study, as a multi-layered CH scaffold could be possibly used with skin lesions but also to help promote the healing of parenchymal tissues in other organs, such as the lungs. What we were mostly interested in was therefore to investigate whether type IV Collagen coating increased cell adhesion on the scaffold and possibly promoted the formation of a continuous cell layer. Although Chitosan has been repeatedly shown to possess a good biocompatibility, and some reports showed a stronger cell adhesion on Chitosan [8], our investigation revealed that few A549 cells actually attached on the

walls of the scaffold. Most cells were instead observed along its internal edges, where they were presumably retained by mechanical factors. Furthermore, cells were mostly observed in clusters. This may be interpreted as a sign of reduced adhesion: clustering helped cells increase their cell-to-cell adhesions, and therefore *in situ* retention. Cells may also have deposited some matrix proteins, thus creating a more favorable microenvironment in the direct proximity of the cluster. Finally, cell shape was markedly rounded on Chitosan and this finding requires a more detailed explanation. Cell shape is associated to the equilibrium of forces within a cell and between a cell and its extracellular matrix (ECM). According to the Tensegrity theory, cells possess an internal pre-stress, a mechanical tension that is generating by myosin molecules pulling on actin microfilaments [21]. Unless they adhere to a substrate, cells are as round as a drop of liquid, as it is observed with blood cells, which actually do not adhere to their liquid ECM. When cells attach to a firm substrate, however, they form focal adhesions (FAs) and start to pull on these FAs, stretching their cell bodies and achieving an elongated shape [22]. Cell shape is therefore function of its capability to form FAs, as demonstrated by integrin inhibition with specific antibodies and the rigidity of the substrate material [23,24]. We chose to enrich the scaffold with Collagen to provide more numerous attachment sites to cells, and this resulted in a visible increase in the number of adhering cells, as expected regardless of the Collagen isoform used. Cell morphology remained however mostly rounded, with few visible exceptions. It is possible that the mechanical properties of the outmost layer of the substrate, including the Collagen coating, did not allow for further cell spreading.

Collagen has long been investigated as a coating for scaffolds, because it is ubiquitous in the ECM and not only provides multiple attachment sites to cells but can coordinate the assembly of other extracellular proteins [25]. To improve its stability, numerous protocols have been proposed, including cross-linking via short wave ultraviolet radiation (UVC, $\lambda = 254$ nm), which possesses also a marked and useful anti-bacterial activity. It has been shown that UVC is capable of forming radicals on tyrosine and phenylalanine aminoacids [26], which then create cross-links [27]. At the same time, UV radiation can also degrade Collagen, and the outcome of the treatment possibly depends on these two conflicting effects [28]. It has been recently shown that UVC, used in combination with chemical cross-linking by 1-ethyl-3-(3-dimethylaminopropyl)-carbodiimide hydrochloride selectively inhibited □2-I-domain integrin binding[29] and this suggests that each treatment should be specifically tailored to meet the requirements of the cell model used. Longer UV wavelengths ($\lambda = 365$ nm) or even blue light ($\lambda = 436$ nm) have also been shown to act on Collagen, possibly in combination with photosensitizers such as riboflavin and are commonly used as a treatment in ophthalmologic diseases such as keratoconus 30. As longer wavelengths

have a lower energy content, their detrimental effect on the stability of Collagen may be reduced, although most studies available in the literature focus on type I Collagen, due to its relative abundance in tissues, and the effects of UV may differ in type IV Collagen. UVC have been actually shown to degrade Triptophan [30] specifically in type IV Collagen. In the present study we used two irradiation protocols that relied on different wavelengths, UVB and UVC, and were able to observe a marked increase in cell attachment after either one of them, even when compared to untreated Collagen coating. The viability assay showed that cell viability was statistically higher in the presence of UVB-treated Collagen than on controls or Collagen-coated samples, which did not differ, up to 48 h of culture. However, cells on Collagen-coated scaffolds caught up by 72 hours of culture and reached comparable levels to UV-treated samples, suggesting that the Collagen coating provided a more viable substrate for cell growth, although it may have negligibly impacted the initial cell attachment. Given the distinct effects of these treatment conditions, future studies will have to characterize the changes in the structure of type IV Collagen brought around by UV treatment.

In no case cells were able to completely populate the scaffolds, although some areas of complete coverage were observed after UV-treatment. It must be remembered, however, that the static culture conditions that were employed in this study may have hindered a more complete diffusion of cells along all the walls of the scaffold and other culture models should be adopted to further characterize cell growth on these scaffolds.

10.5 Conclusions

Within the limits of this *in vitro* model, coating 3D-printed, D-(+) Raffinose-modified Chitosan scaffolds with type IV Collagen drastically increase cell compatibility, especially after treatment with UVB light.

10.6 References

[1] Chouhan D, Dey N, Bhardwaj N and Mandal B B 2019 Emerging and innovative approaches for wound healing and skin regeneration: Current status and advances Biomaterials 216 119267

[2] Rodrigues M, Kosaric N, Bonham C A and Gurtner G C 2019 Wound Healing: A Cellular Perspective Physiol. Rev. 99 665–706

[3] Bhardwaj N, Chouhan D and Mandal B B 2018 3D functional scaffolds for skin tissue engineering Funct. 3D Tissue Eng. Scaffolds 345–65

[4] Gasperini L, Mano J F and Reis R L 2014 Natural polymers for the microencapsulation of cells. J. R. Soc. Interface 11 20140817

[5] Kumar M N V R, Muzzarelli R A A, Muzzarelli C, Sashiwa H and Domb A J 2004 Chitosan Chemistry and Pharmaceutical Perspectives Chem. Rev. 104 6017–84

[6] Kardas I, Struszczyk M H, Kucharska M, van den Broek L A M, van Dam J E G and Ciechańska D 2012 Chitin and Chitosan as Functional Biopolymers for Industrial Applications The European Polysaccharide Network of Excellence (EPNOE) (Vienna: Springer Vienna) pp 329–73

[7] Bianchera A, Salomi E, Pezzanera M, Ruwet E, Bettini R and Elviri L 2014 Chitosan hydrogels for chondroitin sulphate controlled release: an analytical characterization. J. Anal. Methods Chem. 2014 808703

[8] Patil S V and Nanduri L S Y 2017 Interaction of chitin/chitosan with salivary and other epithelial cells—An overview Int. J. Biol. Macromol. 104 1398–406

[9] Sandri G, Rossi S, Bonferoni M C, Miele D, Faccendini A, Del Favero E, Di Cola E, Icaro Cornaglia A, Boselli C, Luxbacher T, Malavasi L, Cantu' L and Ferrari F 2019 Chitosan/glycosaminoglycan scaffolds for skin reparation Carbohydr. Polym. 220 219–27

[10] Bettini R, Romani A A, Morganti M M and Borghetti A F 2008 Physicochemical and cell adhesion properties of chitosan films prepared from sugar and phosphate-containing solutions Eur. J. Pharm. Biopharm. 68 74–81

[11] Bergonzi C, Di Natale A, Zimetti F, Marchi C, Bianchera A, Bernini F, Silvestri M, Bettini R and Elviri L 2019 Study of 3D-printed chitosan scaffold features after different post-printing gelation processes. Sci. Rep. 9 362

[12] Elviri L, Foresti R, Bergonzi C, Zimetti F, Marchi C, Bianchera A, Bernini F, Silvestri M and Bettini R 2017 Highly defined 3D printed chitosan scaffolds featuring improved cell growth Biomed. Mater. 12 045009

[13] Intini C, Elviri L, Cabral J, Mros S, Bergonzi C, Bianchera A, Flammini L, Govoni P, Barocelli E, Bettini R and McConnell M 2018 3D-printed chitosan-based scaffolds: An *in vitro* study of human skin cell growth and an *in-vivo* wound healing evaluation in experimental diabetes in rats Carbohydr. Polym. 199 593–602

[14] Galli C, Parisi L, Elviri L, Bianchera A, Smerieri A, Lagonegro P, Lumetti S, Manfredi E, Bettini R and Macaluso G M 2016 Chitosan scaffold modified with D-(+) raffinose and enriched with thiol-modified gelatin for improved osteoblast adhesion Biomed. Mater. 11

[15] Parisi L, Galli C, Bianchera A, Lagonegro P, Elviri L, Smerieri A, Lumetti S, Manfredi E, Bettini R and Macaluso G M 2017 Anti-fibronectin aptamers improve the

colonization of chitosan films modified with D-(+) Raffinose by murine osteoblastic cells J. Mater. Sci. Mater. Med. 28 136

[16] Saccani M, Parisi L, Bergonzi C, Bianchera A, Galli C, Macaluso G M, Bettini R and Elviri L 2018 Surface modification of chitosan films with a fibronectin fragment-DNA aptamer complex to enhance osteoblastic cell activity: a mass spectrometry approach probing evidence on protein behavior Rapid Commun. Mass Spectrom.

[17] Wells R G 2008 Cellular sources of extracellular matrix in hepatic fibrosis. Clin. Liver Dis. 12 759–68, viii

[18] Mak K M and Mei R 2017 Basement Membrane Type IV Collagen and Laminin: An Overview of Their Biology and Value as Fibrosis Biomarkers of Liver Disease Anat. Rec. 300 1371–90

[19] Schneider C A, Rasband W S and Eliceiri K W 2012 NIH Image to ImageJ: 25 years of image analysis Nat. Methods 9 671–5

[20] Mattarozzi M, Visioli G, Sanangelantoni A M and Careri M 2015 ESEM-EDS: *In vivo* characterization of the Ni hyperaccumulator Noccaea caerulescens Micron 75 18–26

[21] Ingber D E, Wang N and Stamenovic D 2014 Tensegrity, cellular biophysics, and the mechanics of living systems. Rep. Prog. Phys. 77 046603

[22] Atherton P, Stutchbury B, Jethwa D and Ballestrem C 2016 Mechanosensitive components of integrin adhesions: Role of vinculin. Exp. Cell Res. 343 21–7

[23] Engler A J, Sen S, Sweeney H L and Discher D E 2006 Matrix Elasticity Directs Stem Cell Lineage Specification Cell 126 677–89

[24] Kilian K A, Bugarija B, Lahn B T and Mrksich M 2010 Geometric cues for directing the differentiation of mesenchymal stem cells. Proc. Natl. Acad. Sci. U. S. A. 107 4872–7

[25] Ramshaw J A M 2016 Biomedical applications of collagens J. Biomed. Mater. Res. Part B Appl. Biomater. 104 665–75

[26] Metreveli N, Namicheishvili L, Jariashvili K, Mrevlishvili G and Sionkowska A 2006 Mechanisms of the Influence of UV Irradiation on Collagen and Collagen-Ascorbic Acid Solutions Int. J. Photoenergy 76830 1–4

[27] Lew D-H, Liu P H-T and Orgill D P 2007 Optimization of UV cross-linking density for durable and nontoxic collagen GAG dermal substitute J. Biomed. Mater. Res. Part B Appl. Biomater. 82B 51–6

[28] Davidenko N, Bax D V, Schuster C F, Farndale R W, Hamaia S W, Best S M and Cameron R E 2016 Optimisation of UV irradiation as a binding site conserving method for crosslinking collagen-based scaffolds. J. Mater. Sci. Mater. Med. 27 14

[29] Bax D V., Davidenko N, Hamaia S W, Farndale R W, Best S M and Cameron R E 2019 Impact of UV- and carbodiimide-based crosslinking on the integrin-binding properties of collagen-based materials Acta Biomater.

[30] Kato Y, Nishikawa T and Kawakishi S 1995 Formation of protein-bound 3,4-dihydroxyphenylalanine in collagen types I and IV exposed to ultraviolet light Photochem. Photobiol. 61 367–72

11 Chapter 8: “Mapping insulin non-covalent interactions with natural polysaccharides by hydrogen/deuterium exchange mass spectrometry”

[1]Lisa Elviri*, [1]Carlo Bergonzi, [2]Annalisa Bianchera, [1]Ruggero Bettini

[1]Department of Pharmacy, University of Parma, Parco Area delle Scienze 27/A, 43124, Parma, Italy.
[2]Interdepartmental Centre Biopharmanet-Tec, University of Parma Parco, Area delle Scienze 27/A, 43124, Parma, Italy.

Published on 15 November 2016, Rapid Commun Mass Spectrom. Vol 30(21):2323-2330. doi: 10.1002/rcm.7708.

IF 2.045

Personal contribution

CB performed the experimental work related to ATR FT-IR analytical characterization and mass spectrometry analysis.

Abstract

Rationale

Drug development efforts involving therapeutic peptides or proteins strongly lead optimization of drug delivery, drug stability, solubility and functionality. Key feature of controlled drug delivery is the use of biocompatible polymers able to interact via non-covalent bonds with an active principle through multiple functional groups. Here amide hydrogen/deuterium exchange (HDX) mass spectrometry was employed to localize insulin dynamics induced by interactions with three natural polysaccharides, i.e. chitosan (CH), sodium alginate (ALG) and chondroitin sulfate (CS).

Methods

LTQ-Orbitap continuous-labelling mass spectra were collected by diluting insulin stock solution (10 mM in 0.1% formic acid) to a final concentration of 0.1 mM in D_2O containing 1 mM deuterated ammonium acetate (final pH 5.6) (insulin:polysaccharide ratio 1:2, w/w). For peptide mapping, deuterated samples were quenched after 0.5, 30, 60, 120 minutes exchange by adding HCl (pH 2) and digested with pepsin before LC-MS/MS analysis.

Results

Differences in the insulin backbone dynamics in presence of the three polysaccharides were highlighted by monitoring peptic peptides at different time points. No significant differences were observed in the presence of CH, whereas the negatively charged ALG and CS were able to induce significant conformational variations at the B-chain level resulting more protected against H/D exchange. The A-chain interacted only with CS reducing the protein mobility in a long time scale (120 min). HDX data evidenced heterogeneous insulin dynamics in the presence of ALG and CS.

Conclusions

The studies here reported demonstrated the capabilities of mass spectrometry techniques and HDX methods to obtain useful information toward the flexibility and the behavior of native

insulin in the presence of natural polysaccharides, and could provide insights to study the behavior of pharmaceutical formulations.

11.1 Introduction

Protein and peptide therapeutics have assumed a central role in pharmaceutical R&D for their great clinical potential and promise to play a main role in the future pharmaceutical market [1,2]. Compared to small molecules, peptides have the advantage of high specificity and selectivity as well as of low toxicity; they can provide effective replacement treatment in genetic disorders and, from a regulatory point of view, require a relatively shorter approval time [3]. The main limits for protein therapeutics lie in a poor bioavailability, due to their hydrophilicity, and a remarkable susceptibility to proteases that leads to their degradation inside the gastrointestinal tract, and results in a strong limiting the their efficacy upon oral administration [4]. Parenteral remains the main route of administration of this category of drugs, although this often implies a very poor patient compliance. For this reason, strategies that could promote the development of non-invasive alternative routes of administration, such as the trans-mucosal (oral, buccal, nasal pulmonary, rectal and vaginal) or the transdermal are nowadays intensively investigated. Apart from solutions offered by combinatorial chemistry, also formulative strategies can be useful to amend peptides administration issues while ensuring the desired safety and efficacy.

Polysaccharides constitute a valid tool for the formulation of peptide products, as they are generally stable, nontoxic, hydrophilic and biodegradable and can improve the physical properties and pharmacological performance of protein drugs, provided that their interaction with them does not alter peptide conformation [5]. Their property as excipients, coating materials and their ability to create non-covalent interaction with active ingredients to obtain controlled release system are well known [6-8]. The three-dimensional organization of proteins is vital both for their function and for their behavior, and any conformational alteration can negatively impact on drug efficacy [9]. For this reason, the investigation of the interaction of peptide drugs with such pharmaceutical excipients is of primary importance in order to get awareness of their possible activity in a formulation.

In this work we selected insulin as a model protein drug to study its conformational dynamics induced by the interaction with three common polysaccharides, namely chitosan, sodium alginate and chondroitin sulfate.

Insulin was the first commercially available recombinant protein therapeutic approved by FDA in 1982 and has been the major therapy for diabetes mellitus type I ever since [3]. Conventional insulin administration involves subcutaneous injection and, despite many attempts to find an alternative route, the results have so far been elusive or not completely satisfactory. Present

formulation research is focusing on the association of insulin with specific excipients, or combination of them, in many forms such as micro or nanoparticles, etc.

Chitosan (CH) is a nontoxic, biocompatible linear copolymer consisting of (1-4)-linked 2-amino-2-deoxy–D-glucose (D-glucosamine) and 2-acetamido-2-deoxy-D-glucose (N-acetyl-D-glucosamine) units. It is obtained by the alkaline N-deacetylation of chitin, which is the primary structural component of the outer skeletons of crustaceans. This excipient is commonly used in the administration of hydrophilic macromolecule drugs since it acts as an absorption and permeation enhancer: the molecule is very mucoadhesive, thanks to its ability to interact with mucin and increases paracellular permeability by loosening epithelial tight junctions [10]. Chitosan was already assayed for the administration of peptides [11], including insulin [12], alone or in association with other polysaccharides such as, among many, pectin [13], chondroitin sulfate or sodium alginate.

Alginate (ALG) is a naturally occurring polysaccharide obtained from marine brown algae [14]. It is a linear copolymer composed of 1,4-linked-β-D-mannuronic acid and α-L-guluronic acid residues that gel in the presence of divalent cations. It is a nontoxic and biodegradable polyanion that, like chitosan, is biocompatible, GRAS and has the highest mucoadhesive strength compared to polymers such as polystyrene, chitosan, carboxmethylcellulose and polylactic acid, thus it may be useful for improving drug bioavailability and effectiveness [15]. Thanks to its mild gelation conditions, alginate has been intensively used for the incapsulation of proteins, including insulin [16].

Chondroitin sulfate (CS) is a glycosaminoglycan composed of repeating units of b-1,3-linked-N-acetyl galactosamine and b-1,4-linked D-glucuronic acid which are sulfated in certain positions [17]. Such positions determine the classification of chondroitin sulfate types in A (chondroitin-4-sulfate), C (chondroitin-6-sulfate), D (chondroitin-2,6-sulfate), or E (chondroitin-4,6-sulfate). Chondroitin sulfate has been mainly used in the therapy of osteoarthritis and cartilage damage diseases but it has also applications as component of drug delivery systems, especially in association with other excipients [18].

In past years, the study of protein conformation and dynamics was approached through different experimental techniques, such as X-ray crystallography and high resolution nuclear magnetic resonance, but those methods suffer inherent limitations in terms of sample amount, evaluation of production, storage or physiological conditions, especially for high molecular weight proteins [19, 20]. On the other hand, mass spectrometry (MS) is a powerful technique that can be applied to protein conformational analysis [21]. In particular hydrogen/deuterium exchange (HDX) in association with MS is a reliable, robust and sensitive technique that can detect structural

variations of proteins even in highly complex matrices [22]. The technique exploits the feature of hydrogen atoms to exchange with water. Exchange occurs in a conformational sensitive manner [23]: hydrogen atoms either involved in secondary structures or buried in a protein's core exchange with water more slowly than hydrogen atoms in solvent-exposed regions and not H-bonded. Differences can be associated with ligand binding, formation of protein-ligand interactions, and/or formation of more stabilized secondary structure elements throughout the protein.

The combination of MS techniques and hydrogen exchange, coupled with proteolytic fragmentation of a partially labeled protein, allows identification of the extent of deuterium exchange in specific regions of the protein as a function of time.

Several papers dealing with the insulin HDX were published [24-26]. However, HDX results dealing with the insulin-polysaccharide interactions are still lacking in the literature.

Here we report the investigation of insulin behavior in the presence of CH, ALG and CS by HDX high resolution mass spectrometry, with the aim to put into evidence the possible influence of different polysaccharides on the peptide dynamics and to localize the regions involved in such interactions.

11.2 Experimental

11.2.1 Chemicals

Insulin (powder) from bovine pancreas, trypsin, pepsin and tris(2-carboxyethyl)phosphine hydrochloride (TCEP□HCl, purity >98%) were from Sigma-Aldrich (St. Louis, MO, USA). Chitosan 95/50 (CAS 9012-76-4, degree of deacetylation 92.6-97.5%; molecular weight by gel permeation chromatography 80-220 kDa; water insoluble, soluble in acid media) was from HEPPE MEDICAL CHITOSAN GmbH (Halle, Saale, Germany). Sodium alginate Ph.Eur. grade (molecular weight by gel filtration chromatography (GFC) 180-300 kDa; slowly soluble in water) was from Carlo Erba (Milan, Italy). Chondroitin sulphate 90% purity (molecular weight by GFC 150-280 kDa; water soluble) was from ACEF (Fiorenzuola d'Arda, Italy).

Formic acid was from J.T. Baker (Deventer, Netherland). Water was obtained with a MilliQ element A10 System (Millipore, S. Francisco, CA, USA). Deuterated water, deuterated ammonium acetate and hydrochloric acid were from Sigma-Aldrich.

11.2.2 ESI-MS system

An LTQ-Orbitap (Thermo Scientific, San Jose, CA) instrument equipped with a pneumatically assisted ESI interface was used. In the ESI experiments, the desolvation gas (nitrogen, 99.999% pure) was delivered at 820 kPa. Direct infusion mode, operating with a syringe pump at a flow rate of 1 μL/min, was used to evaluate the influence of the ESI interface parameters on the MS response of insulin.

MS experiments were performed by operating the mass spectrometer in positive ion mode. The conditions of the interface were as follows: capillary voltage 40 V; electrospray voltage 3.5 kV; capillary temperature 150°C. Full-scan mass spectra were acquired over the range m/z 500–2000. Data dependent acquisition (DDA) mode was used to analyse proteolytic fragments identified by Proteome DiscovererTM software (ThermoScientific). Bovine insulin structure was from NCBI protein database (www.ncbi.nlm.nih.gov, Accesion N. 550085A) and elaboration was performed by Chimera Molecular Modeling software v.10.1 [27].

11.2.3 Preparation of the solutions for the ESI HDX experiments

All the reagents and the solutions were maintained hermetically sealed under nitrogen atmosphere.

Insulin stock solution (10 mM) was prepared in aqueous formic acid solution (0.1% v/v). An initial dilution (1:10) in aqueous ammonium acetate buffer (1mM, pH 5.6) was performed to equilibrate protein dynamics upon pH change before HDX. Continuous-labeling mass spectra were then collected by diluting (1:10 v/v) insulin solution (10 mM in 0.1% formic acid) to a final concentration of 0.1 mM in D_2O containing 1 mM deuterated ammonium acetate (final pH 5.6). The insulin:polysaccharide solution was prepared in a 1:2 (w/w) ratio in 0.1% formic acid solution and diluted first in aqueous ammonium acetate buffer for pH equilibration and then in D_2O containing 1 mM deuterated ammonium acetate immediately before analysis. Since HDX is affected by pH, all solutions were at pH 5.6. Direct infusion of the solution was performed into the ESI interface at a flow rate of 1 μL/min. Starting from the beginning of the exchange reaction, mass spectra were recorded for 120 min. The signal for the +5 charge-state ion (base peak) was monitored, and the total number of exchanged hydrogen atoms was calculated as the difference between the molecular mass of the neutral protein after exchange reaction and that before exchange. The lowest centroid mass of the isotopic envelope was used to calculate the number of exchanged hydrogens. Analyses were performed in triplicate. A rough estimation of the relative

exchange rate constants was obtained by fitting data by the sum of two exponentials. To correct for back exchange a nondeuterated control and a fully deuterated control at all time points were considered as reported in the literature [28].

11.2.4 Proteolytic digestion and LC-MS/MS analysis

Tryptic digestion of insulin was performed in aqueous solution for 4 hours at 37°C by adding a trypsin solution in a 1:50 ratio.
Deuterated samples were quenched after 0.5, 30, 60, 120 minutes exchange by adding HCl to pH 2, TCEP□HCl (50mM) and digested with pepsin (1:50) for 5 min in ice bath before LC-MS/MS analysis. Peptide separation was carried out on a Kinetex C18 column (75x2.1mm, 2.6μm) (Phenomenex, Torrance, CA, USA) under gradient conditions [(A) aqueous formic acid 0.1% v/v: (B) acetonitrile] as follows: 0-2 min 2% (B), 2-30 min 80% (B) at a flow-rate of 0.2 mL/min. Data were processed by Proteome DiscovererTM software (ThermoScientific). Analysis were performed in triplicate and data expressed as mean and standard deviation. To determine significance between groups, a two-tailed t-tests was performed at the 95% significant level.

11.3 Results and Discussion

11.3.1 ESI-HRMS and MS/MS analysis

As first step, insulin peptide was characterized by high resolution MS and MS/MS analysis. The ESI(+) full scan mass spectrum of the standard solution of insulin resulted in four multiply-charged ions at m/z 956.60774, m/z 1147.52759 (base peak), m/z 1434.15805 and m/z 1911.87472 corresponding to +6, +5, +4 and +3 charge states, respectively.
By using a bottom-up approach followed by a DDA analysis insulin was sequenced and the heterodimer of the A chain and B chain was entirely identified (Figure 1).
By performing the ESI-MS analysis of the tryptic digests of insulin aqueous solution and insulin-polysaccharide aqueous solutions, differences in the peptide signals were observed. Both the absolute and relative peptide ion intensities were significantly ($p<0.05$) affected by the presence of the polysaccharide (Table 1). The observed signal intensity decreased for all the peptides in the presence of the polysaccharides (52-100% decrease), in particular in the presence of chitosan (52-55% signal intensity decrease), sodium alginate (80-86% signal intensity decrease) and chondroitin sulfate (94-100% signal intensity decrease). These decreases could be ascribable to

the presence of an ESI matrix effect that might differ for each kind of polysaccharide tested as a function of their molecular size distribution and functional groups. However, the presence of a matrix effect could not be sufficient to completely describe the data observed. The relative ratio between the insulin peptides was very similar to the control sample when chitosan was present, whereas it resulted significantly altered in the presence of the other two polysaccharides (Table 1). At the operative pH (5.6) insulin is close to its isoelectric point (pH 5.3), whereas sodium alginate and chondroitin sulfate are negatively charged, and chitosan is positive charged. Insulin interactions involving positive and polar residues could be present with CS or ALG as a function of the protein orientation. As a matter of fact, in the presence of CS, the signal relevant to the two chain residue of insulin disappeared from the chromatogram, and the B-chain fragment peptide observed showed modest signal intensity.

These preliminary results could indicate the presence of non-covalent interactions, between insulin and the polysaccharides investigated, able to change the insulin availability to trypsin activity. Insulin-polysaccharide complexes could be present in solution at different strength as a result of H-bonding, electrostatic or dipole-dipole interactions. Reasonably, the peptide localization and intensity of these interactions is correlated with the functional groups present on the polysaccharide under investigation. Thus, in order to understand if these findings are consistent with the presence of insulin-polysaccharide non-covalent interactions, their dynamics and which residues could be possibly involved in the interactions further MS experiments based on an HDX process were carried out.

11.3.2 HDX ESI-HRMS analysis

Bovine insulin is a two-chain small protein containing 50 amino acid residues; one intra-chain disulfide bond is present on the A-chain and two disulfide bonds join the A and B chains (Figure 1). In neutral pH solution, insulin mainly presents two helices located in the A-chain (AA 2-8 and AA 13-20) and one helix located in the B-chain (AA 9-19). A loop (AA 1-8), a β -turn (AA 20-23) and an extended strand (AA 24-30) are also present on the B chain. Positive charges are mainly located on the B-chain, whereas negatively charged residues are located on both chains as well as the polar and hydrophobic residues (Figure 1 A-C) [29, 30].

Here, HDX experiments were carried out to evaluate the behavior of insulin in the presence of chitosan, chondroitin sulfate and sodium alginate. The time-plot of insulin deuterium incorporation is reported in Figure 2.

Insulin alone and insulin in presence of CH exhibited an analog trend in terms of both number of hydrogens and relative rate constants. After an initial very fast exchange involving approximately 7 H atoms in 0.5 min ($k \approx 3.7 \pm 0.9$ min^{-1}), a second group of hydrogens exchange with a reduced rate ($k \approx 0.34 \pm 0.02$ min^{-1}) up to ≈18 H atoms in 120 min. These findings indicate that the presence of the polysaccharide in the solution did not affect in a significant manner ($p > 0.05$) the insulin behavior. Notably, the solution containing CS and ALG induced a significant ($p < 0.05$) reduction in the insulin deuterium uptake and kinetic parameters for the second group of hydrogens, denoting the presence of dynamic differences between free insulin and insulin in the presence of possible binding systems. The significant reduction in the exchange rate ($k_{ALG} \approx 0.17 \pm 0.01$min^{-1}; $k_{CS} \approx 0.20 \pm 0.03$ min^{-1}) and lower level of incorporated deuterium number (≈13 H atoms at 120 min) suggest that insulin could be shielded by peptide-polysaccharide interactions. Additional emphasis should be placed on the full-scan mass spectrum of insulin during HDX. In the presence of ALG and CS the signal of insulin at the +6 charge state exchanged in a non homogeneous manner. The mass spectra of insulin and insulin incorporating deuterium in the presence of ALG are shown, as an example, in Figure 3. The presence of two intense signals, one at lowest m/z and one at highest m/z, were distinguishable just because of their different rates of isotopic replacement. These findings could be ascribed to heterogeneity in the insulin conformational distribution in solution when CS and ALG are present. Some interactions of insulin with the negatively charged CS and ALG could induce a decrease of the insulin stability with partial unfolding, for a part of insulin population at the +6 charge state, evidenced by and an increase in the HDX extent. The molecular size distribution of the polysaccharides could result in different abilities of interaction with the insulin molecule, inducing a variety of conformational dynamics. A complete understanding of the phenomenon would require additional experimental tests. However, continuous-labeling experiments allowed to obtain information about the lifetime of the different conformational states. In particular in the presence of both CS and ALG, insulin, monitored at the +6 charge state, behaved as one single conformation for the first 20 min, and progressively split in at least two different conformational states up to 60 min (data not shown). At the equilibrium these two conformational states were present at the 50% abundance (Figure 3B).

Having demonstrated above the different behavior of insulin in the presence of polysaccharides, the study was extended to the localization of the amino acid segments involved in the interactions. HDX experiments were thus carried out, as reported in the Experimental section, on peptides fragments obtained by proteolytic digestion with pepsin. Extended sequence coverage was

obtained and the peptide primary sequence coverage is depicted in Figure S1 (Supplementary material).

HDX data obtained for four peptides are reported in Figure 4. In the presence of chitosan the data were almost analogous to those obtained for insulin only for all the investigated segments. These findings suggest the absence of significant interactions between CH and insulin under the operative conditions adopted. When sodium alginate and chondroitin sulfate were used, perturbations in the amide HDX were observed (Figure 4).

In the presence of CS the segment A1-11 is overlapped to insulin only nearly for 60 min, the difference increased ($p<0.05$) with increased incubation time (Fig. 4). This finding indicated that part of the A-chain could be able to interact with CS reducing the protein mobility in a long time scale (120 min). No significant differences ($p>0.05$) were observed in the HDX behavior of the A-chain of insulin in the presence of ALG. In the presence of ALG and CS, the B-chain region resulted more protected against H/D exchange than other H-bound amide protons. A reduced structural flexibility of insulin interacting with both polysaccharides could occur. The polar and positive AA residues are mainly localized on the B-chain and they could be able to form H-bonds and electrostatic interactions with the negatively charged CS and ALG polysaccharides. The segment B5-13 contains four basic and one acid residues (2 Lys, pka=10.79; 2His, pka=6.04; Glu, pka=4.07) and behaved in the same manner for both CS and ALG as a function of time (Figure 4). Notably, the B14-24 segment, containing three positively charged basic residues (2 Lys, pka=10.79; 1Arg, pka=12.48) and an acid residue (Glu, pka=4.07), showed appreciable differences between ALG and CS as the incubation time increase (Figure 4). These data could suggest that, under the operative conditions adopted, CS is the polysaccharide, among those investigated, able to form the more intense network of ionic and H-bond interactions with this region of insulin.

11.4 Conclusions

The studies here reported demonstrated the capabilities of mass spectrometry techniques and HDX methods to obtain useful information toward the flexibility and the behavior of native insulin in the presence of natural polysaccharides, like chitosan, chondroitin sulfate and sodium alginate.

Data demonstrated that the insulin conformational dynamics are mainly influenced by the negatively charged polysaccharides ALG and CS. The positively charged CH did not affect significantly the protein HD exchange. The interactions occurring between CS, ALG and insulin,

are mainly driven by H-bonds and electrostatic forces occurring at different time scales. In agreement with this hypothesis the insulin B-chain, containing the positively charged residues, seemed to be mostly involved in these interactions in a targeted manner. Furthermore, the HDX data obtained on the intact insulin put in evidence the presences of at least two protein conformational states in solution, arising from differences both in structure and dynamics of the free protein versus a bound state. This interesting finding could be unravel in a further experimental work.

11.5 References

[1] D.J. Craik, D.P. Fairlie, S. Liras, D. Price. The Future of Peptide-based Drugs, Chem. Biol. Drug Design. 2013, 81, 136.

[2] T. Uhlig, T. Kyprianou, F.G. Martinelli, C.A. Oppici, D. Heiligers, D. Hills, X. Ribes Calvo, P. Verhaert. The emergence of peptides in the pharmaceutical business: From exploration to exploitation, EuPA Open Proteom. 2014, 4, 58.

[3] B. Leader, Q.J. Baca, D.E. Golan. Protein therapeutics: a summary and a pharmacological classification. Nat. Rev. Drug Discov. 2008, 7, 21.

[4] L. Otvos, D. Wade. Current challenges in peptide-based drug discovery. Front. Chem. 2014, 2, 62.

[5] J.P. Fuenzalida, F.M. Goycoolea. Polysaccharide-protein nanoassemblies: novel soft materials for biomedical and biotechnological applications. Curr. Prot. Pept. Sci. 2015, 16, 89.

[6] Z. Liu, Y. Jiao, Y. Wang, C. Zhou, Z. Zhang. Polysaccharides-based nanoparticles as drug delivery systems. Adv. Drug Del. Rev. 2008, 60, 1650.

[7] L. Elviri, M. Asadzadeh, R. Cucinelli, A. Bianchera, R. Bettini. Macroporous chitosan hydrogels: effects of sulfur on the loading and release behavior of amino acid-based compounds. Carbohydr. Polym. 2015, 132, 50.

[8] T. Coviello, P. Matricardi, F. Alhaique. Drug delivery strategies using polysaccharidic gels. Exp. Opin. Drug Deliv. 2006, 3, 395.

[9] I.A. Kaltashov, C.E. Bobst, R.R. Abzalimov, S.A. Berkowitz, D. Houde. Conformation and Dynamics of Biopharmaceuticals: Transition of Mass Spectrometry-Based Tools from Academe to Industry. J. Am. Soc. Mass Spectrom. 2010, 21, 323.

[10] B. Menchicchi, J.P. Fuenzalid, K.B. Bobbili, A. Hensel, M.J. Swamy, F.M. Goycoolea. Structure of Chitosan Determines Its Interaction with Mucin. Biomacromol. 2014, 15, 3550.

[11] M. Amidi, E. Mastrobattista, W. Jiskoot, W. Hennink. Chitosan-based delivery systems for protein therapeutics and antigens. Adv. Drug Del. Rev., 2010, 62, 59.
[12] Y. Pan, Y. Li, H. Zhao, J. Zheng, H. Xu, G. Wei, J. Hao, F. Cui. Bioadhesive polusaccharide in protein delivery system: chitosan nanoparticles improve the intestinal absorption of insulin *in vivo*. Int. J. Pharm. 2002, 249, 139.
[13] S.O.S.M. Al-Azi, Y.T.F. Tan, T.W. Wong. Transforming large molecular weigh pectin and chitosan into oral drug protein nanoparticulate carrier. React. Funct. Polym., 2014, 84, 45.
[14] H. Andriamanantoanina, M. Rinaudo. Characterization of the alginates from five madagascan brown algae. Carbohy. Polym. 2010, 82, 555.
[15] M. George, T.E. Abraham. Polyionic hydrocolloids for the intestinal delivery of protein drugs: Alginate and chitosan- a review. J. Contr. Rel. 2006, 114, 1.
[16] W.R. Gombotz, S.F. Wee. Protein release from alginate matrices. Adv. Drug Deliv. Rev. 1998, 31, 267.
[17] F. Maccari, F. Galeotti, N. Volpi. Isolation and structural characterization of chondroitin sulfate from bony fishes. Carbohy. Polym. 2015, 129, 143.
[18] L. Zhao, M. Liu, J. Wang, G. Zhai. Chondroitin sulfate-based nanocarriers for drug/gene delivery. Carbohy. Polym. 2015, 133, 391.
[19] L.E. Kay. New Views of Functionally Dynamic Proteins by Solution NMR Spectroscopy. J. Mol. Biol. 2015, doi: 10.1016/j.jmb.2015.11.028.
[20] R. Neutze, Opportunities and challenges for time-resolved studies of protein structural dynamics at X-ray free-electron lasers. Philosoph. Transact. B Royal Soc. 2014, 369, 20130318.
[21] H. Wei, A.A. Tymiak, G. Chen. High-resolution MS for structural characterization of protein therapeutics: advances and future directions. Bioanal. 2013, 5, 1299.
[22] R.Y. Huang, G. Chen. Higher order structure characterization of protein therapeutics by hydrogen/deuterium exchange mass spectrometry. Anal. Bioanal. Chem. 2014, 406, 6541.
[23] L. Konermann, X. Tong, Y. Pan. Protein structure and dynamics studied by mass spectrometry: H/D exchange, hydroxyl radical labelling, and related approaches. J. Mass Spectrom. 2008, 43, 1021.
[24] W. Dzwolak, A. Loksztejn, V. Smirnovas. New insights into self-assembly of insulin amyloid fibrils: an H-D exchange FT-IR study. Biochem. 2006, 45, 8143.
[25] J. Buijs, C.C. Vera, E. Ayala, E. Steensma, P. Hakansson, S. Oscarsson. Conformational stability of adsorbed insulin studied with mass spectrometry and hydrogen exchange. Anal. Chem. 1999, 71, 3219.

[26] S. Nakazawa, J. Ahn, N. Hashii, K. Hirose, N. Kawasaki. Analysis of the local dynamics of human insulin and a rapid-acting insulin analog by hydrogen/deuterium exchange mass spectrometry. Biochim. Biophy. Acta. 2013, 1834, 1210.
[27] E.F. Pettersen, T.D. Goddard, C.C. Huang, G.S. Couch, D.M. Greenblatt, E.C. Meng, T.E. Ferrin. UCSF Chimera-A visualisation system for exploratory research and analysis. J. Comput. Chem. 2004, 25, 1605.
[28] D.D. Weis, Hydrogen exchange mass spectrometry of proteins, 2016, Ed. Wiley & Sons.
[29] Q. Hua, M.A. Weiss. Toward the solution structure of human insulin: sequential 2D 1H NMR assignment of a des-pentapeptide analogue and comparison with crystal structure. Biochem. 1990, 29, 10545.
[30] S. Ludvigsen, M. Roy, H. Thøgersen, N.C. Kaarsholm. High-resolution structure of an engineered biologically potent insulin monomer, B16 Tyr-->His, as determined by nuclear magnetic resonance spectroscopy. Biochem. 1994, 33, 7998.

Peptide	m/z (charge state)	Insulin	Insulin + chitosan	Insulin + sodiumalginate	Insulin + chondroitin sulfate
GIVEQccASV cSLYQLE NYcN (A chain; AA 1-21)	856.36 (+3)	$8.0\ 10^3$ (±400)	$3.6\ 10^3$ (±120)	$1.6\ 10^3$ (±100)	
GFFYTPK (B chain; AA 23-29)	430.22 (+2)	$2.5\ 10^3$ (±320)	$1.2\ 10^3$ (±90)	$8.0\ 10^2$ (±20)	$4.0\ 10^2$ (±40)
AFVNQHLcG SHLVEAL YLVcGERGFF YTPK (B chain; AA 1-29)	878.96 (+4)	$2.8\ 10^3$ (±360)	$1.3\ 10^3$ (±110)	$4.0\ 10^2$ (±20)	
		Signal relative ratio	Signal relative ratio	Signal relative ratio	Signal relative ratio
		1:0.31:0.35	1:0.33:0.36	1:0.5:0.25	00:01:00

Table 1. Relative intensity of insulin peptides obtained after tryptic digestion (4 hours, 37 °C). Standard deviation in parenthesis (n=4).

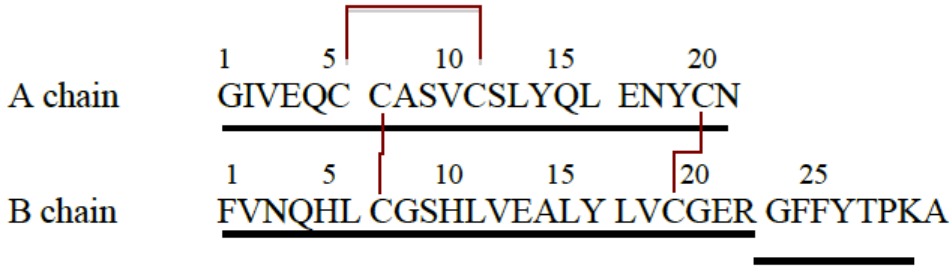
1 5 10 15 20
A chain GIVEQC CASVCSLYQL ENYCN
1 5 10 15 20 25
B chain FVNQHL CGSHLVEALY LVCGER GFFYTPKA

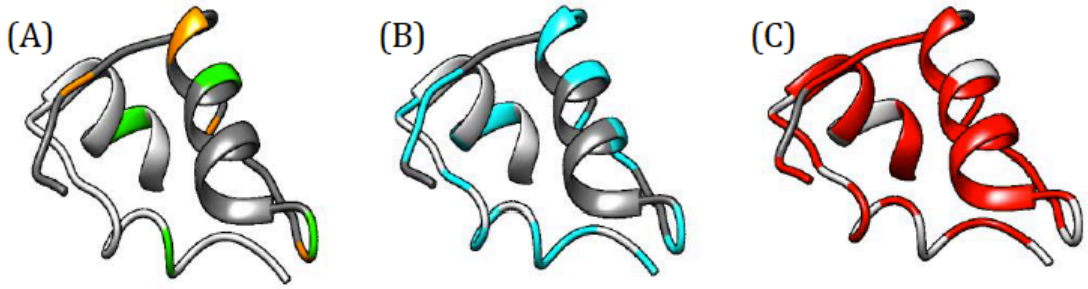
(A)
(B)
(C)

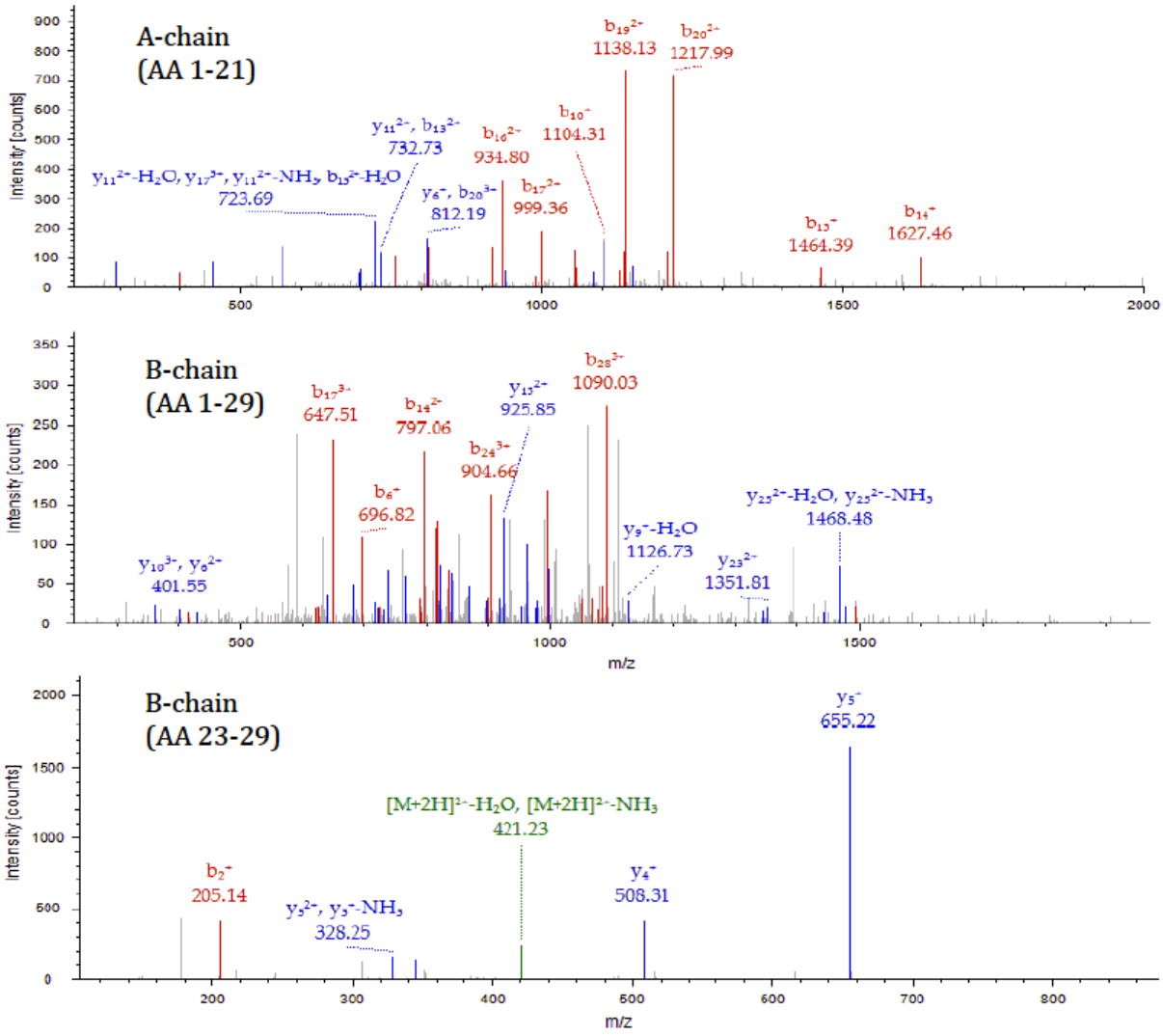
A-chain
(AA 1-21)
Intensity [counts]
b19 2+ 1138.13
b20 2+ 1217.99
y11 2+, b13 2+ 732.73
b16 2+ 934.80
b10+ 1104.31
y11 2+-H2O, y17 3+, y11 2+-NH3, b15 2+-H2O 723.69
y6+, b20 3+ 812.19
b17 2+ 999.36
b13+ 1464.39
b14+ 1627.46
B-chain
(AA 1-29)
b28 3+ 1090.03
b17 3+ 647.51
b14 2+ 797.06
y13 2+ 925.85
b24 3+ 904.66
b6+ 696.82
y23 2+-H2O, y23 2+-NH3 1468.48
y9+-H2O 1126.73
y10 3+, y6 2+ 401.55
y23 2+ 1351.81
m/z
B-chain
(AA 23-29)
y5+ 655.22
[M+2H]2+-H2O, [M+2H]2+-NH3 421.23
b2+ 205.14
y4+ 508.31
y3 2+, y3+-NH3 328.25
m/z

Figure 1. Bovine insulin monomer sequence and structure (A chain in light gray and B-chain in dark gray) : (A) positively (orange) and negatively (green) charged residue, (B) polar (light blue) residues, (C) hydrophobic (red) residues. ESI-MS/MS tryptic peptide mapping of A- and B- chains.

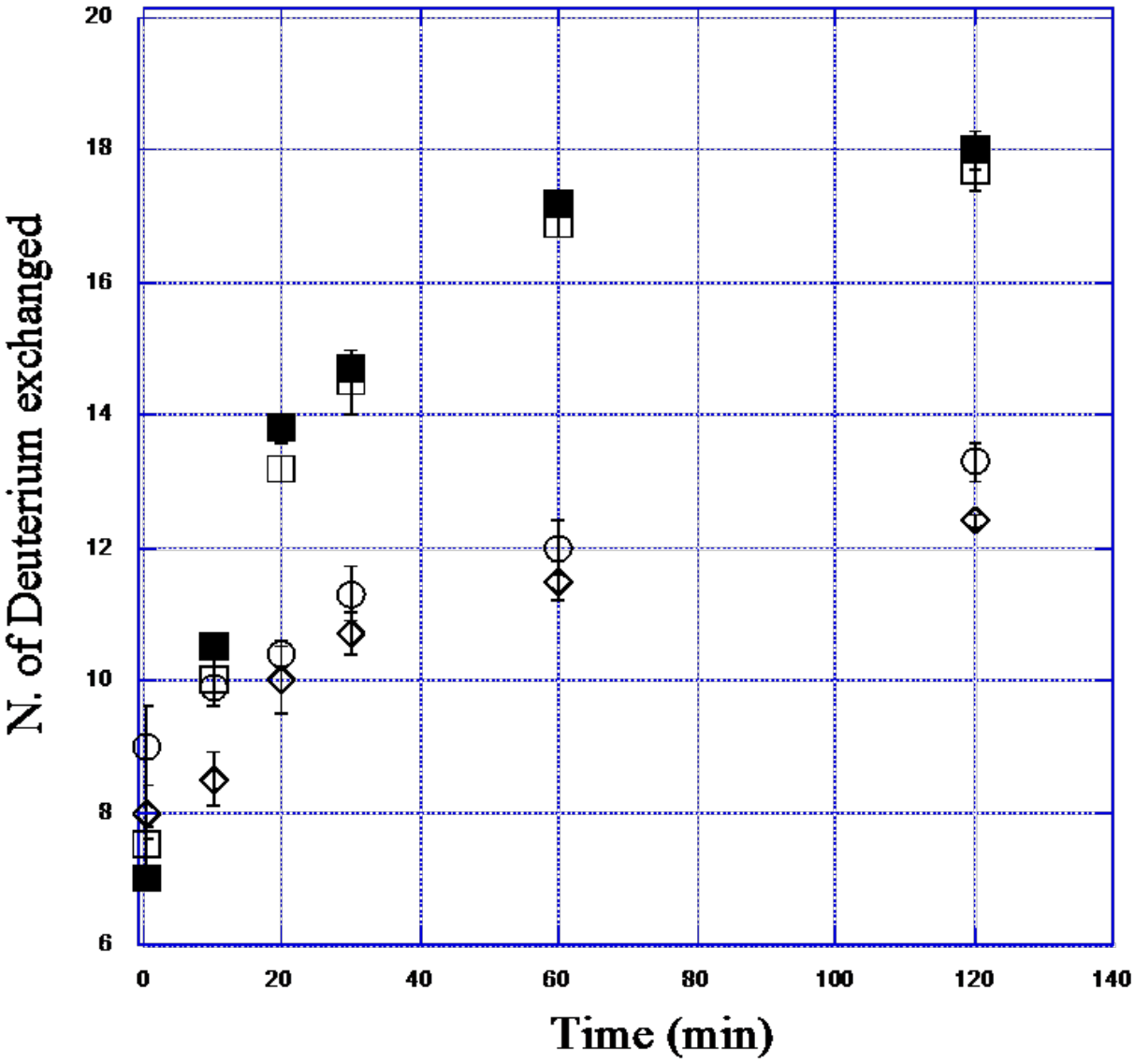

Figure 2. Number of deuterium exchanged (monitored on the +5 charge state) in solution by insulin (solid square), insulin in the presence of chitosan (empty square), insulin in the presence of alginate (diamond) and insulin in the presence of chondroitin sulfate (circle). The bars represent the standard deviation (n= 3).

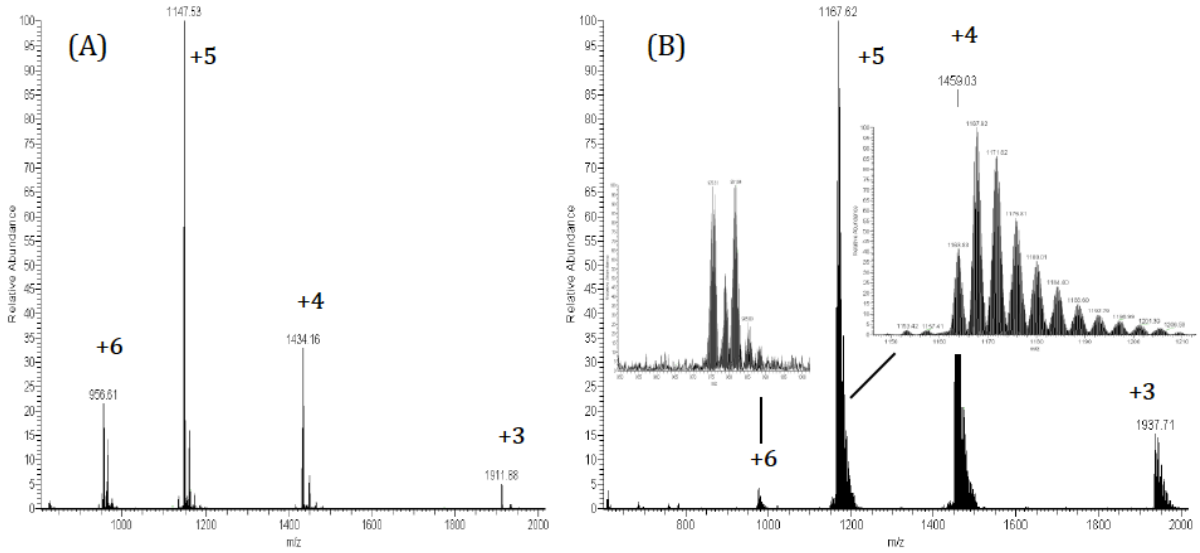

Figure 3. (A) ESI-(PI)MS mass spectrum of insulin; (B) ESI-(PI)MS mass spectrum of insulin after 60 min HDX.

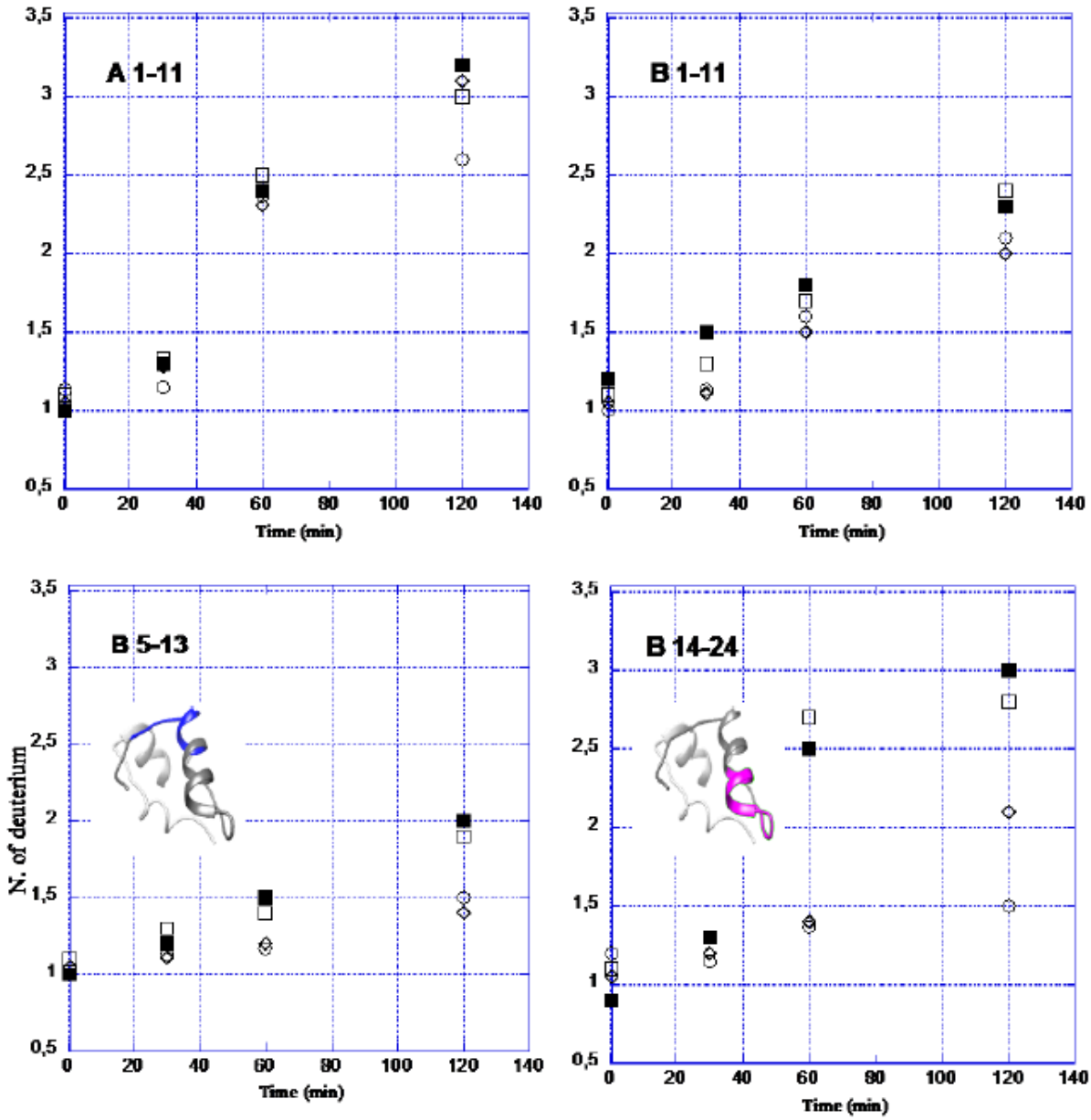

Figure 4. Time course of deuterium incorporation by insulin peptic peptides in D_2O (0.1 mM in 1 mM deuterated ammonium acetate, pH 6.9) as a function of time (average of triplicates). Insulin region A 1-11 (upper panel left), B 1-11 (upper panel right), B5-13 (lower panel left) and B 15-24 (lower panel right). Insulin alone (solid square), insulin in the presence of chitosan (empty square), insulin in the presence of alginate (diamond) and insulin in the presence of chondroitin sulfate (circle). Inset: insulin region involved in dynamic variations.

12 Chapter 9: “A targeted mass spectrometry method to screen collagen types I-V in the decellularized 3D extracellular matrix of the adult male rat thyroid”

Marco Alfieri[a], Fulvio Barbaro[a], Elia Consolini[a], Elena Bassi[a], Davide Dallatana[a], Carlo Bergonzi[b], Annalisa Bianchera[c], Ruggero Bettini[b], Roberto Toni[a,d,e], Lisa Elvirib[,c,d,*]

[a] Laboratory of Regenerative Morphology and Bioartificial Structures (Re.Mo.BIO.S.), Unit of Biomedicine, Biotechnology, and Translational Sciences – Section of Human Anatomy, Di.ME.C., University of Parma School of Medicine, 43124 Parma, Italy

[b] Food and Drug Department, University of Parma, V.le delle Scienze 27/A, 43124 Parma, Italy

[c] Interdepartmental Centre Biopharmanet-Tec, University of Parma, Parco Area delle Scienze 27/A, 43124 Parma, Italy

[d] Interdepartmental Center for Sport and Exercise Medicine (SEM), University of Parma, 43100 Parma, Italy

[e] Division of Endocrinology, Diabetes, and Metabolism, Tufts Medical Center and Tufts University School of Medicine, Boston, MA 02111, USA

Published on 1 February 2019, Talanta Vol 193:1-8. doi: 10.1016/j.talanta.2018.09.087. Epub 2018 Sep 25.

IF 4.916

Personal contribution

CB performed the experimental work related to SEM analysis and material preparation.

Abstract

Here we have developed and validated an original LC-MS/MS SRM procedure flexible enough to quantitatively screen collagen types I-V in copies of the same type of stromal matrix prepared with different protocols of cell removal to retain the native 3D architecture of the ECM. In a first step, identification of tryptic sequences exclusive to specific chains (either α1 or α2) of mammalian collagen standards types I-V was pursued using a combination of LC-LIT-Orbitrap XL and LC-MS/MS SRM analyses. In a second step, the adult male rat thyroid was decellularized using three different protocols specifically set for engineering of bioartificial 3D thyroid organoids. In a third step, DNA analysis of the decellularized 3D thyroid stroma was pursued to exclude contamination by cell nuclear debris. In a final step, collagen standards and 3D thyroid matrices were digested using the same mechanical / enzymatic protocol, and quantitative profiles of collagen types I-V ensued using comparisons of ionic intensities between tryptic peptides of collagen standards and matrices, as derived from targeted LC-MS/MS SRM analysis. Collectively, the procedure allowed for detection and quantitation of collagen types I-V at a femtomolar level in thyroid gland stromal matrices initially maintaining their original 3D architecture, tryptically digested through a method common to collagen standards and thyroid ECM, with satisfactory reproducibility of results, moderate procedural cost, and limited analytical time.

Keywords: liquid chromatography-mass spectrometry, collagen, thyroid, decellularization, organ matrix

12.1 Introduction

Relative or absolute quantification of extracellular matrix (ECM) proteins including collagens in normal and neoplastic, rodent and human viscera (e.g. skin, tail tendon, aorta, heart, mammary gland, liver, thyroid) has been achieved associating liquid chromatography to mass spectrometry (LCMS/MS), to yield variably sensitive, specific, and accurate results [1–4]. A mainstay of all these methods is an immediate and/or substantial disruption of the original three-dimensional (3D) structure of the organ-specific stroma that is rapidly extracted, and/or solubilised, and/or fractionated. In addition, although most recent LC-MS/MS techniques based on isotope labelling provide high analytical specificity and accuracy, they imply a quite high preparative cost, and a long procedural time [5].

Integrity of the 3D architecture of the ECM, collectively known as "stromal matrix" when including both interstitial and basement membrane ECM [6], is considered a key factor in tissue engineering for organ reconstruction based on re-cellularization with stem cells / progenitors [7–9]. Indeed, a de-cellularized organ-specific 3D stromal matrix may act as an ideal biocompatible scaffold for 3D organ reconstruction [10] including innovative engineered biostructures like 3D organoids and organs-on-chip, whose potential as laboratory tools for pharmacological / toxicological screening and diagnostic purposes is under active investigation [11,12]. Finally, 3D bio-artificial organs engineered on the laboratory bench (i.e. ex situ) promise to become a feasible therapeutic option in the clinical setting, where they may substitute malfunctioning native organs through transplantation, and thus provide a definitive solution to the paucity of organ donations [13].

Therefore, to have an LC-MS/MS procedure aimed at quantitatively screen the protein composition of the de-cellularized stromal matrix starting directly from the same type of 3D matrix preparations eventually used for re-cellularization protocols might be very useful. It would allow for comparison of the role of different amounts of specific stromal proteins with the capacity of the matrix to act as a 3D guide to induce *in vitro* / ex situ 3D self-assembly of cells. Indeed, changes in amounts of a specific collagen type within the same 3D environment has been shown to be critical for *in vitro* self-assembly of ovarian cells [14], and we have predicted through theoretical modelling that this phenomenon might play a critical role also for ex situ formation of thyroid follicles [9]. In addition, a similar LC-MS/MS approach could eventually be applied to a real-time quantitation of stromal collagen breakdown from 3D organs-on-chip during their medium and long-term maintenance in micronized circuitries [12]. This, particularly when using

endocrine cells like those of the thyroid gland whose follicular stability is ensured by a complex 3D network of different collagens [8,15,16].

Finally, tissue engineering increasingly search for standardization of production chains, and for technical procedures with moderate cost and a limited analytical time [17]. An LC-MS/MS procedure simple to standardize, of contained analytical cost, and limited procedural time but retaining sensitivity, specificity, and accuracy enough to provide a reliable quantitation of the relevant ECM proteins would be of great help, primarily to set strategies for 3D bio-printing of copies of the organ-specific, stromal matrix using biomaterials functionalized with organ-specific collagens, as in the case of a bio-artificial thyroid gland [18,19].

To these purposes, we have applied a combination of mass spectrometry approaches (LC-LIT-Orbitrap XL and LC-MS/MS Selective Reaction Monitoring, SRM) to identify and quantitate the five most relevant types of collagen (I to V) in the stromal matrix of the adult, male rat thyroid gland [16]. The glands were de-cellularized using protocols specifically developed by our group for preparation of 3D bioartificial thyroid organoids [8,20,21] and, thus initially retaining a thyroid-specific 3D architecture ideal for re-cellularization [9,15,17]. Only in final stages, the 3D stromal matrix was disrupted using standard solubilisation methods, and accurate quantitation of the five collagen types studied was achieved retaining an analytical sensitivity up to the femtomolar level.

12.2 Materials and methods

12.2.1 Animals

Seven adult Sprague Dawley male rats weighting 50–75 g (3 animals, 3–4 weeks old) and 225–250 g (4 animals, 8 weeks old) were purchased from Harlan Labs (Udine) and Charles River Labs (Lecco), respectively and housed in temperature-controlled rooms (22 °C) with a humidity of 50% and a 12:12 h light–dark cycle, according to the stabulary rules. All animal procedures were conducted in accordance with the current European Community Council Directives, and approved by the Ethical Committee for Animal Care of the University of Parma, Parma, Italy (approval code n. 18/2016-PR released on 12/01/2016).

12.2.2 Decellularization of the rat thyroid gland

All rats were deeply anesthetized with intraperitoneal tiletaminezolazepam (40 mg kg^{-1}), and sacrificed by cervical dislocation. The thyroids were surgically removed and cleaned from the capsule and adjacent parathyroid glands, the two lobes of each gland separated at the level of the isthmus, each lobe put into plastic vials containing phosphate-buffered saline 0.1MpH 7.4 (PBS), rapidly frozen in liquid nitrogen, and stored at −80 °C until use. Four lobes coming from the thyroids of two 225–250 g rats, and 6 lobes coming from the thyroids of three 50–75 g rats were de-cellularized using three different de-cellularization protocols as follows:

– protocol 1 (two lobes from one 225–250 g animal, 2 lobes from one 50–75 g animal): thawing of the thyroid lobes at 4 °C for 24 h, followed by 0.02% Trypsin EDTA 0.25% (Sigma Aldrich p.n. T4049) in PBS for 1 h at 37 °C, 3% Triton X-100 (Sigma Aldrich p.n. T8532) in PBS for 48 h at 4 °C, and 0.03% sodium deoxycholate (Sigma Aldrich p.n. 30970) in PBS for 24 h at 4 °C;

– protocol 2 (one lobe for one 225–250 g animal, 2 lobes from one 50–75 g animal): thawing of the thyroid lobes at 4 °C for 24 h, followed by 0.01% Trypsin EDTA 0.25% (Sigma Aldrich p.n. T4049) in PBS for 1 h at 37 °C, 3% Triton X-100 (Sigma Aldrich p.n. T8532) in PBS overnight (ON) at 4 °C, and 0.3% sodium deoxycholate (Sigma Aldrich p.n. 30970) in PBS ON for 24 h at 4 °C;

– protocol 3 (one lobe for one 225–250 g animal, 2 lobes from one 50–75 g animal): thawing of the thyroid lobes at 4 °C for 5 h, followed by 0.01% Trypsin EDTA 0.25% (Sigma Aldrich p.n. T4049) in PBS for 1 h at 37 °C, 0.1% Triton X-100 (Sigma Aldrich p.n. T8532) in PBS for 24 h at 4 °C, 2% sodium deoxycholate (Sigma Aldrich p.n. 30970) in PBS for 24 h at 4 °C, sodium chloride (NaCl) 1M in PBS for 1 h at room temperature (RT), and 30 μg mL−1 DNAase (Sigma Aldrich p.n. D4263) +1.3mM $MgSO_4$ +2mM $CaCl_2$ in distilled H_2O (dH_2O) for 1 h at RT.

SEM has been used to investigate differences in the morphological architecture between the three decellularization protocols. After decellularization, 3 thyroid lobes coming from two 225–250 g rats have been fixed in glutaraldehyde 4% (in cacodylate sodium buffer 0,1 M) O/N at 4 °C, then dehydrated with several rinses of a growing percentage of ethanol, starting from 30% (v/v in dH_2O) to 100% v/v and subjected to Critical Point Drying (Balzers) with 100% ethanol / liquid CO2 exchange system. Dried samples have been mounted on aluminium stubs and metallized (Balzers) to cover scaffolds with a 60 nm gold film. Samples have been observed with a Philips SEM501.

After each treatment, samples were washed at least 5–10 min two times with PBS. De-cellularized matrices were sterilized under an UV laminar flow hood using 0.1% peracetic acid in sterile PBS for 3 h at RT. Finally, samples were rinsed with sterile dH2O two times for 5–10 min, and stored in 0.01 mg mL−1 gentamicin (Sigma Aldrich p.n. G1297) in PBS at 4 °C until analysis.

12.2.3 Analysis of the residual DNA content by CyQUANT® cell proliferation assay kit

In a first step, the wet weight of 3 intact thyroid lobes coming from two 225–250 rats and that of 4 de-cellularized thyroid lobes coming from the other two 225–250 g rats was determined using an analytical balance. Then, each lobe was digested in 1 mL of Lysis Solution (LS) at 56 °C ON. The LS was composed by 1 mg mL^{-1} proteinase K (Sigma Aldrich p. n. P2308) in 50mM Tris (Sigma Aldrich p.n. A5456-3) pH 7.6 and a protease inhibitor cocktail made with 1mM EDTA +1mM iodoacetamide +10 μg/mL Pepstatin A (Sigma Aldrich p. n. P5318) diluted in DMSO (FLUKA p. n. 41640).

For DNA measurements, a calibration curve was prepared in a 96 multiwell plate using 200 μL serial dilutions (0, 50, 200, 600, 1000 ng mL−1) of the bacteriophage λ DNA in CyQUANT dye solution. The latter was prepared by mixing the Working Buffer with the CyQUANT® GR dye 400X supplied by the kit. For analysis, 5 μL of each digested sample (control thyroid and de-cellularized matrices) were dissolved in 195 μL of CyQUANT dye solution, and three replicates were prepared for each sample. Analysis of the calibration curve and samples were performed using a Victor 3 V Multilabel Plate Readers (Perkin Elmer) set at the Fluorescein protocol (485/535 nm of wavelength – λ). The calibration curve gave an interpolation (y=1923x+77,356) with an R^2 =0,9986. For each sample, the amount of DNA was normalized to the dilution factor and wet weight of the native tissue (intact thyroid and de-cellularized matrix), and expressed as ng DNA/mg wet tissue.

12.2.4 Collagen standards and reagents

Standards of collagen type I (Bovine, COL I, heterotrimer α1α1α2, mw: α1=137,953 Da; α2=129,564 Da), type II (Bovine tracheae, COL II, homotrimer α1α1α1, mw: α1=134,570 Da), type III (Human, COL III, homotrimer α1α1α1, mw: α1=138,936 Da), type IV (Human, COL IV, heterotrimer α1α1α2, mw: α1=160,613 Da; α2=160,757 Da), and type V (Human placentae, COL V, heterotrimer α1α1α2, mw: α1=183,987 Da; α2=145,202 Da), trypsin, iodoacetamide (IAA) and dithiotreitol (DTT) were all purchased from Sigma Aldrich (St. Louis, MO, USA). LC-grade

water, acetic acid, acetonitrile, and analytical reagent grade formic acid (FA) were purchased from Carlo Erba (Milan, Italy).

12.2.5 Preparation and trypsin digestion of 3D stromal matrices and collagen standards for mass spectrometry analysis

Initially, the 3D structure of the de-cellularized thyroid lobes was disrupted by immersion in liquid nitrogen and mechanical breaking using a pestle. Then, tissue samples and collagen standards (types I to V) were separately suspended in 500 μL of Trizma HCl 0.1 M +NaCl 0.1 M at pH 7.8 in plastic vials. Then, thyroid matrices and collagen standards were immersed in an ultrasonic bath at 60 °C for 24 h, using a Bransonic ultrasonic cleaner 2510E – DTH sonicating at 42 kHz. Proteins in the sonicated material were reduced and alkylated using 5 mM DTT for 55 min at 37 °C, followed by 10 mM IAA for 30 min at RT in the dark, and addition of DTT to a final concentration of 2 mM at 37 °C for 15 min. Finally, all samples (thyroid matrices and collagen standards) were separately digested by incubation with trypsin (1:50 enzyme/substrate ratio) at 37 °C for 24 h. To stop the digestion, 3 μL of acetic acid 98% v/v were added to each sample, all samples dried in a stream of nitrogen, and the pellet re-suspended to a final volume of 100 μL in a water/acetonitrile mixture (50/50, v/v).

12.2.6 LC-LIT-Orbitrap XL analysis

Analysis of tryptic sequences exclusive to specific chains (either α1 or α2) of collagen standards types I-V was carried out by LC using a capillary column Jupiter® 5 μm C18 300 Å, 150×0.3mm (Phenomenex), with pre-filtering column at a flow-rate of 5 μL min^{-1}. Eluting mixtures included solvent A (0.1% aqueous formic acid, v/v) and B (0.05% formic acid, 100% acetonitrile, v/v). Gradients were set as follows: 5 min with the 2% solution B, then a graded increase of 2% solution B/min for 15 min, cleaning for 3 min with 85% solution B, and column re-conditioning for 11 min with 2% solution B. The mobile phase was delivered by a Dionex Ultimate 3000 chromatographic system (Dionex Corporation, San José, CA, USA) equipped with a 200-vial capacity sample tray. Volume of the injected samples (collagen standards) was 5 μL, with a collagen standard concentration of 1 μg μL^{-1} (total protein injected = 5 μg). Identification of m/z values characteristic of each tryptic sequence of selected α1 or α2 chains of collagen standards was obtained by mass spectrometry using an LTQ linear ion trap-Orbitrap instrument

(ThermoScientific Corporation, San José, CA, USA), equipped with ESI interface and controlled by Xcalibur software.

Optimized conditions of the interface were as follows: ESI (ionization electrospray source) voltage 3.5 kV, capillary voltage 13 V, capillary temperature 275 °C, tube lens 85 V. In the first scan event (full scan) the m/z window was 200–1800 with a resolution of 60.000. The four highest mass-to-charge ratios over a threshold of 100.000 counts were selected for collision-induced dissociation (CID) in the ion trap, with normalized collision energy of 35% and collision gas pressure of 2.3×10^{-3} mbar in the collision cell.

12.2.7 LC-MS/MS SRM analysis

To quantitate the presence of collagens types I-V, an identification of the various peptides raising from disruption and digestion of either collagen standards type I-V or de-cellularized 3D matrices of the rat thyroid gland was pursued by LC, equipped with a narrow-bore C18 Sunshell, 100×2.1 mm, 2.6 μm column (Chromanik, Sunshell, Japan), and a pre-filtering column at a flow-rate of 0.2 mL min^{-1}, thermostated at 25 °C. An elution system based on a solvent gradient [solution A: 0.1% aqueous formic acid (v/v) / solution B: 0.08% formic acid in acetonitrile (v/v)] was delivered at 0.2 mL min−1. The mobile phase was delivered by the Agilent HP 1260 chromatographic system (Agilent Technologies, USA) equipped with a 200-vial capacity sample tray. Volume of the injected unknown sample (de-cellularized thyroid matrix) was 5 μL, whereas that of the injected reference sample (collagen standard) was 10 μL, with a 1 μg μL^{-1} concentration for each of the five collagen standards (10 μg of each collage type). Using LC-MS/MS SRM analysis, identification of the ionic intensity characteristic of each peptide selected from the corresponding collagen standard (either α1 or α2 chain) and of that of the peptide with identical m/z value in the matrix sample of unknown concentration was achieved based on a QTRAP 4000 triple quadrupole instrument (ABSCIEX), equipped with a pneumatically assisted ESI interface. The sheath gas (nitrogen, 99.999% purity) and the auxiliary gas (nitrogen, 99.998% purity) were delivered at flow-rates of 45 and 5 arbitrary units, respectively. Optimized conditions of the interface were as follows: ESI voltage 4.5 kV, capillary voltage 50 V, capillary temperature 350 °C. MS2 experiments were performed under SRM conditions with a collision gas (N_2) pressure of 2.1×10^{-3} mbar in the collision cell. To avoid any potential “matrixeffect” of interference with the SRM signals, calibration curves of the tryptic products of the collagen standards (data not shown) were performed using the same disruption procedure and the same solvents applied for solubilisation of the stromal matrix. Several dilutions of the same tryptic

product for each collagen standard were used. Detection and quantitation limits were calculated in the low fmol/mL concentration range. Method validation was carried out by calculating limits of detection (LODs, as signal to noise ratio, S/N=3), limits of quantitation (LOQs, as signal to noise ratio S/N=10), repeatability expressed as relative standard deviation (RSD%) for n=6, (corresponding to the number of tryptic peptides used), lack of missed cleavages, linearity, recovery, and selectivity.

12.2.8 Data analysis, bioinformatics, and quantitative evaluation of collagen types

LC-LIT-Orbitrap XL data were processed using Proteome Discoverer (ThermoScientific) with SEQUEST as search algorithm. RAW files were processed using precursor ion tolerance at 0.1 amu (AMU), and fragment tolerance at 0.5 AMU. Processed files were then searched against a custom database, in which all known and hypothetical collagen forms, digestion enzymes, and every possible contaminant (e.g. keratine) were considered. Cysteine carbamidomethylation was selected as fixed modification. Confident identification was obtained using stringent filter criteria: DeltaCN was set at 0.1, XCorr vs. charge state was set at 1.5 (1+) and 2 (2+). Peptide probability was set at 0.05 (5%). Every spectrum was then manually validated to avoid false positives. In order to verify possible false negatives, manual search on some discarded results was performed. BLAST (Basic Local Alignment Search Tool; www.ncbi.nml.nih.gov link NCBI BLAST) search (algorithm: blastp; MATRIX PAM 30; GAP COASTS: existence 10, extension 1; DATABASE: non redundant protein sequences) analysis was performed to assess targeted peptide uniqueness. In contrast, LC-MS/MS SRM data were analyzed using the Analyst v 1.4 software.
Tryptic peptides derived from Bovine (Bos taurus, Uniprot id: 9913) and Human (Homo sapiens, Uniprot id: 9606) collagen standards and choosen for quantitative comparison with tryptic peptides recognized in the rat thyroid matrix exhibited 100% identity at the aminoacidic level with corresponding collagen tryptic peptides of Rattus norvegicus (Uniprot id:10116). Quantitation of collagen types I-V in the matrix samples was achieved through proportion, by comparing the ionic intensity corresponding to a known concentration of the selected tryptic peptide of each collagen standard with that of the corresponding peptide in the volume of solubilized matrix with unknown concentration. To this aim, the value of ionic intensity corresponding to the SRM transition identifiable as product-ion was preliminary selected for each sample (collagen standards and de-cellularized thyroid matrix).

12.3 Results

Table 1 reports the most distinguishing values of specificity, signal intensity, sensitivity, and repeatability of each collagen standard sequence analyzed by LC-MS/MS SRM, indicating their uniqueness to identify each specific collagen type. Repeatability expressed at RSD% was in the 1.5–4% range, accompanied by an excellent linearity. In particular, the peptide at m/z 414 selected for collagen II provided the highest sensitivity comparable to that observed for all other peptides (32% improvement in ionization efficiency).

Fig. 1 shows the chromatograms of the collagen standard types I-V characterized by LC-MS/MS SRM analysis. Each tryptic sequence identifying each specific collagen type (including both α1 and α2 chains for collagen type 1) corresponded to a single peak with the highest ionic intensity and a specific retention time (i.e. reference peptide providing signal), variably flanked by fragment ions distributed under and above each selected precursor ion mass (i.e. noise). The six selected collagen peptides exhibited excellent stability of the retention times (RSD<1.8%, n=10).

Table 2 shows the DNA amount detected in 3 intact, rat thyroid lobes used as controls (Ctrl 1, Ctrl 2 and Ctrl 3) and 4 rat thyroid lobar matrices de-cellularized with different protocols. Remarkably, protocol 1 removed all DNA residues from the lobar matrix; in contrast, protocols 2 and 3 retained DNA contamination ranging from 9% to 17% of the averaged DNA content detected in the three controls.

Fig. 2 depicts the 3D morphology of decellularized matrices evaluated by SEM. All three decellularization protocols seem to preserve both the outer fibrous rat thyroid capsule and the 3D internal structure of the lobes.

Collagen type	Peptide sequence	Peptide probability	Xcorr	SRM transition (m/z)	LOD (fmol mL^{-1})	LOQ (fmol mL^{-1})	RSD%
Iα1	GSEGPQGVR	37.77	2.14	443/613	6	15	2
Iα2	GDQGPVGR	23.34	2.20	393/485	20	35	1.5
IIα1	TGPAGAAGAR	83.4	2.43	414/335	0.4	1	3
IIIα1	GNDGAR	9.61	1.35	498/377	20	40	1.9
IVα1	GPPGGVGFPGSR	72.13	2.29	558/962	10	28	4
Vα1	AGSDGAR	9.59	0.88	504/853	7	19	3

Table 1. Peptide sequences of each collagen type selected by LC-LIT-Orbitrap XL analysis for targeted LC-MS/MS SRM analysis.

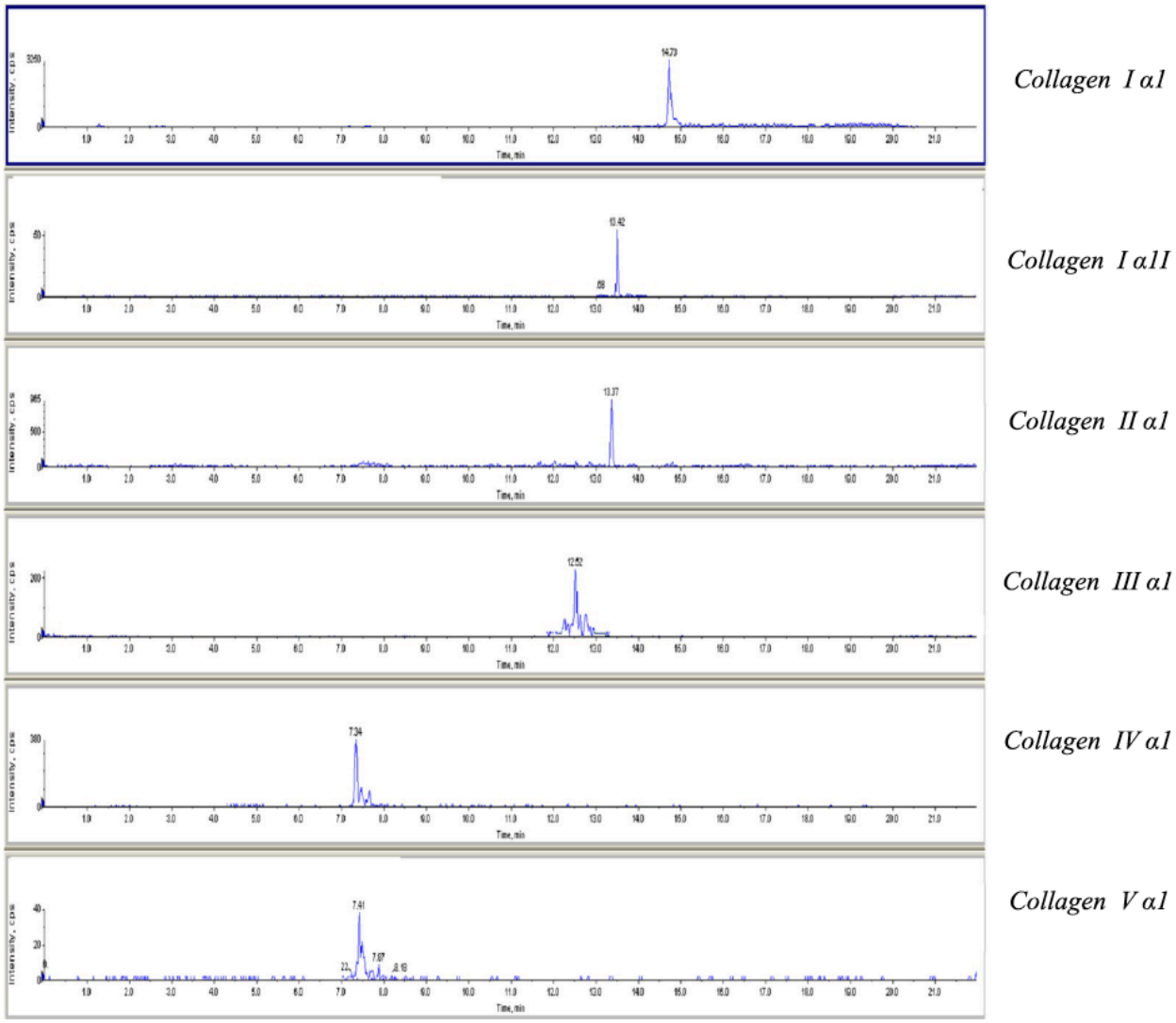

Fig. 1. LC-MS/MS SRM chromatograms obtained from each of the five collagen standards (including α1 and α2 chains of collagen type I) under investigation. Collagen concentration in the injection volume was 1 μg μL^{-1}.

Sample (wet weight)	DNA concentration on interpolation (ng mL^{-1}	DNA concentration after dilution factor correction (ng mL^{-1})	DNA concentration in the thyroid gland (ng mg^{-1} wet tissue)
ctrl 1 (3 mg)	114.84 ± 8,28	4593.49 ± 331.26	1531.16 ± 110.42
ctrl 2 (5 mg)	90.43 ± 13,06	3617.03 ± 522.57	723.40 ± 104.51
ctrl 3 (2 mg)	89.56 ± 10,85	3582.38 ± 434.18	1791.19 ± 217.09
protocol 1 matrix 1 (5 mg)	n.d.	n.d.	n.d.
protocol 1 matrix 2 (3 mg)	n.d.	n.d.	n.d.
protocol 2 matrix (4.5 mg)	13.89 ± 2.88	555.60 ± 115.12	122.70 ± 25.36
protocol 3 matrix (3.9 mg)	23.14 ± 3.77	925.50 ± 150.73	236.70 ± 38.55

Table 2. DNA quantification by CyQUANT analysis. n.d. not detected.

The structure of the decellularized follicles resulted surrounded by stromal proteins, visible after cutting the thyroid lobe capsule before starting the decellularization process to facilitate the removal of cells and the penetration of enzymatic and chemical agents. SEM results showed that were no cellular residues both in the stroma and in the follicles cavities, demonstrating that no substantial structural/morphological differences were apparent between the three decellularization methods.

Fig. 3 show two example of the chromatograms of the five collagen types (including both α1 and α2 chains for collagen type 1) as detected in the solubilised stromal matrix of the thyroid gland by LC-MS/MS SRM analysis (protocol 1= single experiment, as A; protocols 2 and 3= two separate experiments, as A and B). A different distribution of collagen types was apparent, in dependence on the de-cellularization protocol. Peaks of collagen type II were undetectable in both protocols 1 and 2, the former also showing absence of peaks for collagen type III. However, a good consistency ensued between retention times of each specific collagen type present in each de-cellularization protocol and the corresponding collagen standard, thus allowing for proportional comparison of ionic intensities, to deduce a specific amount for each collagen type in the sample of stromal matrix.

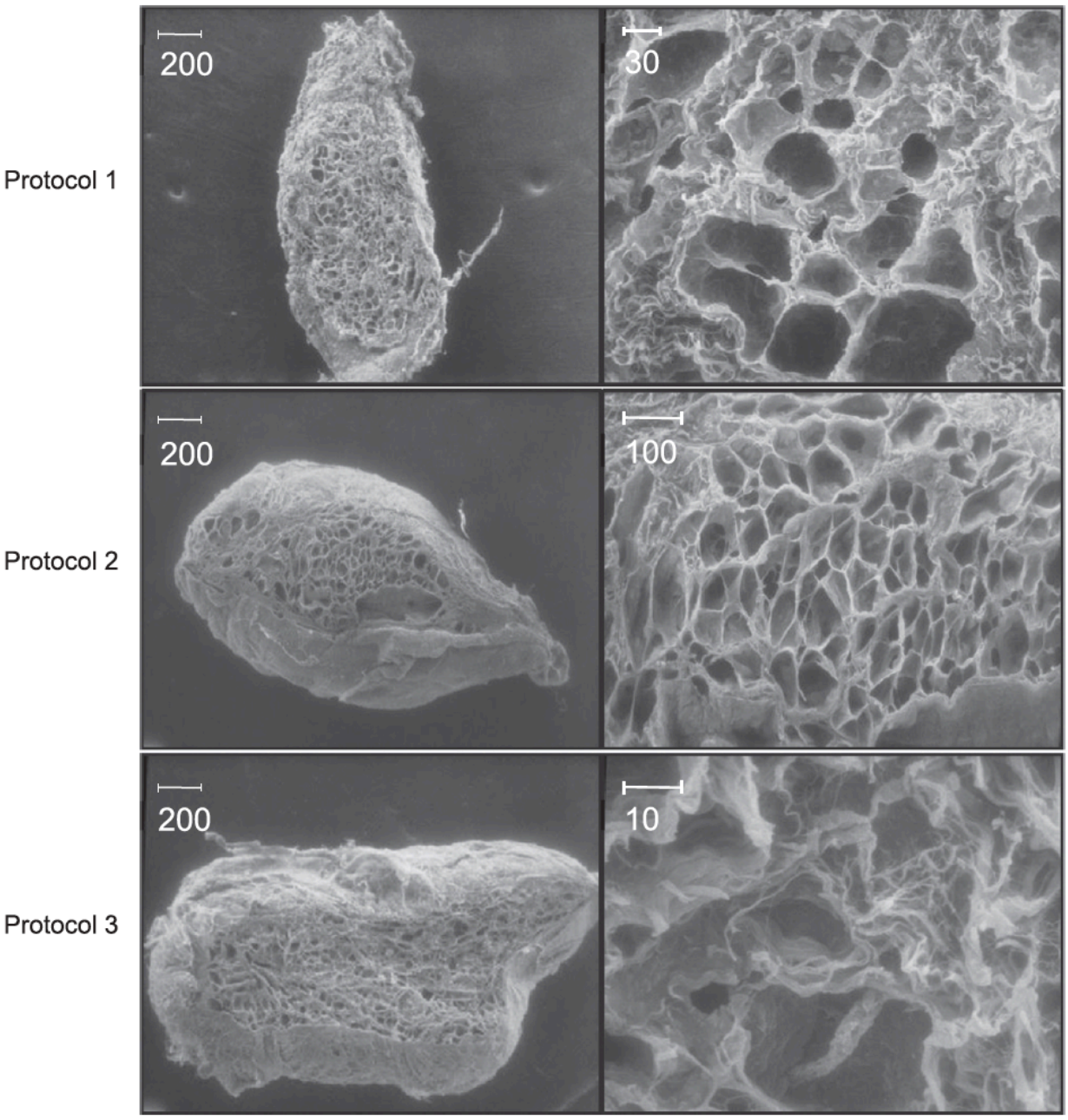

Fig. 2. Section of decellularized rat thyroid lobe and its follicles, divided for each decellularization protocol (SEM analysis).

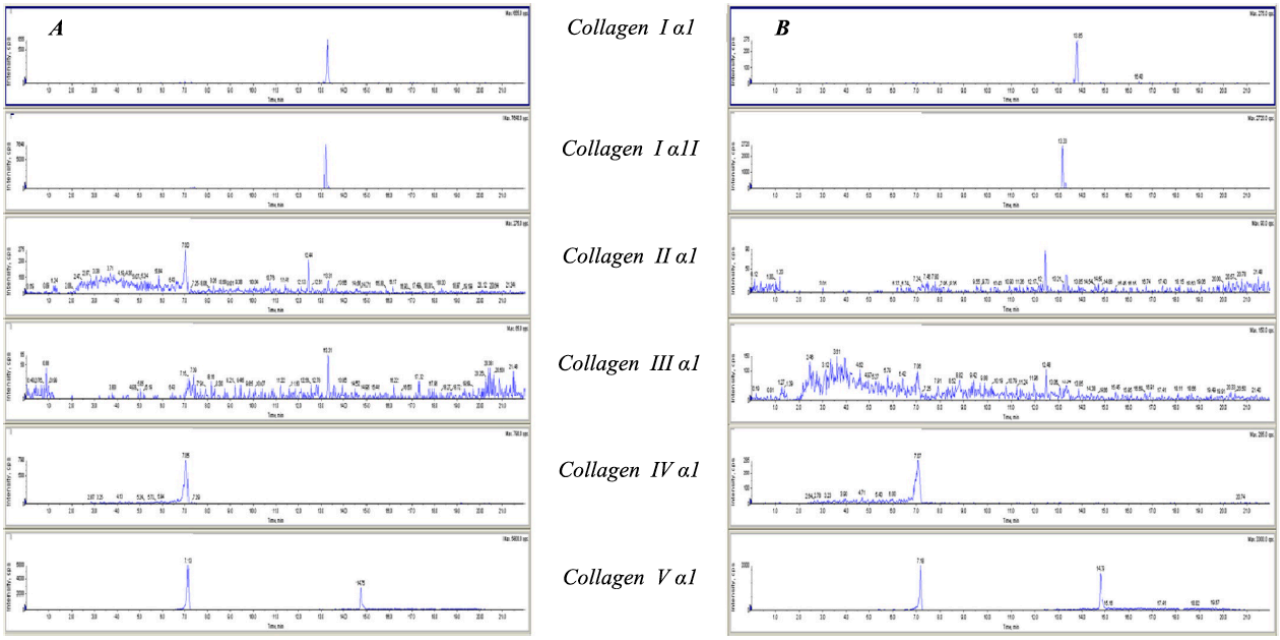

Fig. 3. LC-MS/MS SRM chromatograms of collagens type I-V (including alpha1 and alpha2 chains of collagen type I) obtained from the thyroid stromal matrix prepared with (A) the decellularization protocol n.2 and (B) the protocol n.3.

Table 3 shows the amounts of each collagen type in the stromal matrix of the thyroid in dependence on the decellularization protocol (protocol 1= single experiment; protocols 2 and 3= two separate experiments). As expected by the values of ionic intensity obtained by LC-MS/MS SRM analysis, protocol 1 resulted the most aggressive one as compared to protocols 2 and 3, yielding a reduction in collagen types I, IV and V ranging from 25% to 36% of the latter two, whereas complete disappearance occurred for collagens type II and III. Collectively, protoco 1 reduced the amount of the collagens studied in the thyroid stromal matrix of about 38% as compared to protocols 2 and 3.

Protocol	coll Iα1 (µg)	coll Iα2 (µg)	coll IIα1 (µg)	coll IIIα1 (µg)	coll IVα1 (µg)	
1	4.585	0.566	a		0.130	
2	12.624±2681	1.634±0.425		0.825±0.168	0.256±0.077	
3	12.660±2.346	1.662±0.605	0.868±0.613	0.504±0.357	0.192±0.043	

Table 3. Quantitation of collagen types I-V in the decellularized stromal matrix of the male rat tyroid.

Finally, Fig. 4 displays the percentage oscillations of the various collagen types in the thyroid stromal matrix with respect to the total of collagens analyzed, in dependence of the de-cellularization protocol used. Although protocol 1 most aggressively destroy specific collagen forms (types II and III), however it only moderately reduces other collagen types (IV and V) while substantially preserving collagen type I.

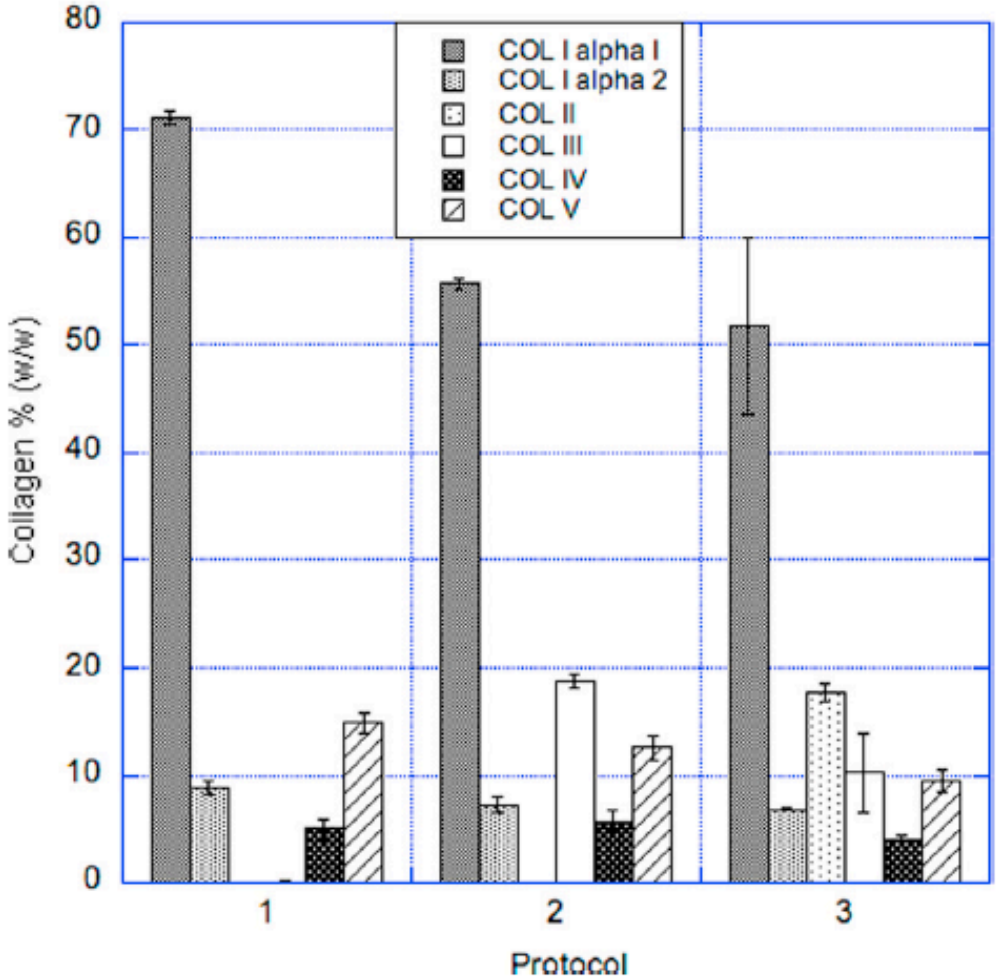

Fig. 4. Histogram showing the proportions of each collagen type (including alpha1 and alpha2 chains of collagen type I) in the decellularized matrix of the male rat thyroid with respect to the total amount of the collagen analyzed (% w/w), in dependance on the decellularization protocol used.

12.4 Discussion

12.4.1 Development and validation of the analytical procedure

Delineation of the protein composition of the thyroid stromal matrix may provide a guide for studying the capacity of its components to drive *in vitro* / *ex situ* the differentiation of colonizing stem cells / progenitors, as shown for a number of other organs [22,23].

To avoid false negative and positive results due to different procedures of preparation / digestion / solubilisation of the ECM, the same type of thyroid-specific 3D de-cellularized stromal matrix to be used for the *in vitro* / *ex situ* re-cellularization process should be available for the analytical evaluation of its components. The latter could profitably be obtained using a number of variably sensitive, specific, and accurate LC-MS/MS methods, recently shown to provide relative or absolute quantification of mammalian and human ECM proteins, including collagens of the thyroid gland [1–4]. On the other hand, although most recent LC-MS/MS techniques based on isotope labelling provide high analytical specificity and accuracy [5], some recent remarkable applications of this technology to human and rodent tissues have been based on an immediate extraction / fractionation of the stromal matrix, whose 3D architecture is gone lost since the beginning of the de-cellularization process [2,3]. In addition, it is well known that these procedures are associated to a high cost for targeting the proteins of interest, and require demanding analytical times [5].

In the attempt to overcome some of these limitations, we have envisaged an LC-MS/MS procedure reliable and flexible enough to quantitatively screen the protein composition of the stromal matrix of the de-cellularized thyroid gland, starting directly from the same type of 3D matrix preparations eventually used for re-cellularization protocols. We have choosen a combination of LC-LIT-Orbitrap XL and LCMS/MS SRM analyses to investigate the amounts of collagen types I-V in the adult, male rat thyroid stroma prepared with three different protocols of de-cellularization, specifically developed by our group to retain its native 3D architecture as a natural scaffold for engineering of bio-artificial thyroid organoids [9,15,17,20,21].

In a first step, solutions of collagen standards type I-V bearing a 100% aminoacidic homology with the corresponding rat collagens (see methods, Section 2.8), were individually characterized by LC-LIT-Orbitrap XL data-dependent analysis, to identify putative unique peptides for these specific collagen types. Several doubly and triply charged ions of the tryptic peptides were identified for all standards, allowing for a suitable degree of sequence coverage (range 35–68%). Taking into account the protein sequences reported in databases, it resulted that several fragments

were present for each collagen standard. Therefore, based on the software analysis, a single specific sequence (here coined as reference peptide) with a m/z value characteristic of each collagen standard was chosen.

In a second step, using the m/z value of the reference peptide identifying a selected collagen standard, an LC-MS/MS SRM approach was applied to provide its quantitation and, thus that of the original collagen type. A number of experimental adjustments were preliminary applied, to reach an optimal analytical condition for quantitation. Different working solutions, and fragmentation times of collagen standards by ultrasonic bath protocols (i.e. 3, 6, 12, 24 h) were tested, while the temperature was kept constant at 60 °C. In particular, using a Tris/HCl (0.2 M, pH 8.2) working solution and short times of sonication (3–6 h) chromatographic signature of all reference peptides exhibited a decrease in the signal-to-noise ratio independently from the number of repetitions (up to more than 3 injections), and was accompanied by an increase in column back-pressure. It is likely that this behavior depended on either incomplete peptide recovery during the subsequent enzymatic (trypsin) digestion and column purification, although an interference of these solvents (so called matrix-interference) affecting the ESI ionization efficiency could not be definitely ruled out. To improve sample handling and reduce potential matrix-interference, a Tris HCl 0.1M / NaCl 0.1M at pH 7.8 was used, and this increased the peptide signal intensity between 50% and 90% at 6 h. Using this working solution, the best recovery of the peptides was observed with a sonication at 60 °C for 24 h; these conditions led to an increase in the peak area of the six peptides monitored ranging from 20% to 120% in comparison to other sonication times, and it was selected as the procedure of choice.

All collagen standards were always digested using trypsin, under the assumption of specificity and constancy of the enzymatic breakdown and, thus of its repeatability also on the same collagen types harboured inside a 3D de-cellularized stromal matrix. In addition, the ESI ionization efficiency of each peptide was enhanced by testing different ESI sensitivities, and setting the lowest detection limit for each reference peptide at a femtomolar level. At the same time, the product-ion mass spectra of the reference peptides were acquired by optimizing the collision energy, in order to obtain selective fragment ions with high intensity. Finally, selectivity was obtained by keeping a very narrow mass window (± 0.5 Th) on the first quadrupole, thus reducing the number of ions transmitted to the collision cell in spite of method sensitivity. Based on these technical constraints, the single tryptic peptide with the highest peak of ionic intensity and specific retention time in the chromatograms of the collagen standards was identified as representative of the quantity of each collagen type under study.

Taking advantage of this result, of the evidence that collagen types I–V had been previously studied in rat tissues (skin, tail tendon, aorta) by LC MS/MS [1], and peptides generated by enzymatic digestion of the ECM can be studied by LC-MS/MS SRM [24], we decided to quantitate by LC-MS/MS SRM collagen types I-V also in the stromal matrix of the adult male rat thyroid.

12.4.2 Thyroid decellularization protocols

The matrix was intentionally prepared following decellularization procedures previously developed to keep intact its 3D architecture, as in the case of eventual recellularization with stem cells / progenitors [9,15,17,20,21]. The advantage of starting this analysis from an intact 3D architecture of the stromal matrix lies in the fact that different decellularization protocols differently affects the amount of ECM proteins [23], whose morphoregulatory activity in the recellularization processes changes in relation to their quantity in the same 3D environment, as in the case of collagens [14]. Similar, we have provided clues that this phenomenon could influence the ex situ self-assembly of thyroid follicles [9].

Although the different combinations of detergents and enzymes used for de-cellularization were known to maintain a 3D matrix architecture adequate for thyroid re-cellularization [20,21,25], only protocol 1 removed all DNA residues from the lobar matrix; in contrast, protocols 2 and 3 retained DNA contamination above the threshold limit of 50 ng mL^{-1}. This DNA content is considered not ideal for a matrix re-cellularization, due to immunereactive material (the nuclear debris) possibly interfering with the colonizing cells [26].

12.4.3 LC-MS/MS SRM application

However, HPLC-MS/MS SRM showed that protocol 1 removed from the rat thyroid matrix more than a third of all collagens studied and, in particular destroyed types II and III as opposed to protocol 3 and, to the less efficient protocol 2 where collagen type II was equally lost.

Collagens type II and III are the two most abundant fibrillar proteins of the vertebrate tissues beyond collagen type I, that forms the main core of the stromal matrix [27,28]. Type II collagen is one of the major component of the cartilage, where contributes to its mechanic-elastic structure and, similarly to type I self-associates into a D-periodic fibril structure with 67 nm axial D periodicity [29]. The same D periodicity is maintained in type III collagen, that is an interstitial collagen often colocalized with collagen type I in the same fibrils, and is particularly present in the skin and blood vessels [30,31]. Therefore, lack of these interstitial collagens is expected to reduce the elasticity of the de-cellularized thyroid matrix, negatively influencing the *in vitro / ex situ* differentiation procedure of eventually colonizing stem cells / progenitors [32–35].

Protocol 1 also hampered more aggressively than protocols 2 and 3 the amount of collagens type IV and V. Since collagen type IV is one of the major component of the basement membrane (BM,) forming a reticular network to promote cell attachment and stability of other proteins inside the

BM [36,37], while collagen type V regulates the assembly of collagen type I to ensure stiffness to the thyroid stroma [38,39], their reduction is expected to inhibit adhesion of the colonizing cells to the de-cellularized matrix and, possibly to lower the resistance of the thyroid ECM to mechanical insult.

The quantitative data on the matrix collagens obtained through our LC-MS/MS SRM procedure derived from a solubilisation protocol common to collagen standards and tissue samples, and based on the same solvents, fragmentation, and enzymatic digestions. As such, possible matrix-interference effects were reasonably minimal. In addition, since it was based on knowledge of ionic mass characteristics of the reference tryptic peptides, and this information could eventually be deductible also through *in-silico* analysis, our approach might be extended to the screening of other proteins of the thyroid ECM specifically prepared for re-cellularization. Finally, sensitivity of detection, reproducibility of results, cost-effectiveness ratio, and requirement of analytical time resulted consistent with expectations for preparation of de-cellularized 3D matrices of the rat thyroid gland.

In conclusion, since the LC-MS/MS SRM procedure here presented has features of reliability and flexibility of application in the tissue engineering setting, we believe it could also be suitable for quantitation of collagen types in 3D stromal matrices of organs like the liver, pancreas, and lungs whose developmental features are consistent with those of the thyroid gland.

12.5 Acknowledgments

This work has been done under the tenure of a 2016–2018 PhD Fellowship / 2018 International Mobility Fellowship of the Ph.D. program in Molecular Medicine at the University of Parma (M.A.), and supported by research grants FIR RBAP10 MLK7_004, University of Parma FIL 2017 – 558/32063, and Horizon 2020, 825745 – SCREENED (R.T.).

12.6 References

[1] S. Pataridis, A. Eckhardt, K. Mikulìkovà, P. Sedlàkovà, I. Mikšìk, Identification of collagen types in tissues using HPLC-MS/MS, J. Sep. Sci. 31 (2008) 3483–3488.

[2] T.D. Johnson, R.C. Hill, M. Dzieciatkowska, V. Nigam, A. Behfar, K.L. Christman, K.C. Hansen, Quantification of decellularized human myocardial matrix: a comparison of six patients, Proteom. Clin. Appl. 10 (2016) 75–83.

[3] E.T. Goddard, R.C. Hill, A. Barrett, C. Betts, Q. Guo, O. Maller, V.F. Borges, K.C. Hansen, P. Schedin, Quantitative extracellular matrix proteomics to study mammary and liver tissue microenvironments, Int. J. Biochem. Cell Biol. 81 (2016) 223–232.
[4] X. Liu, Z. Guo, H. Sun, W. Li, W. Sun, Comprehensive map and functional annotation of human pituitary and thyroid proteome, J. Proteome Res. 16 (2017) 2680–2691.
[5] O. Chahrour, D. Cobice, J. Malone, Stable isotope labelling methods in mass spectrometry-based quantitative proteomics, J. Pharm. Biomed. Anal. 113 (2015) 2–20.
[6] J.K. Frantz, K.M. Stewart, V.M. Weaver, The extracellular matrix at a glance, J. Cell Sci. 123 (2010) 4195–4200.
[7] K.M. Park, H.M. Woo, Systemic decellularization for multi-organ scaffolds in rats, Transplant. Proc. 44 (2012) 1151–1154.
[8] R. Toni, A. Tampieri, N. Zini, V. Strusi, M. Sandri, D. Dallatana, G. Spaletta, E. Bassoli, A. Gatto, A. Ferrari, I. Martin, Ex situ bioengineering of bioartificial endocrine glands: a new frontier in regenerative medicine of soft tissue organs, Ann. Anat. 193 (2011) 381–394.
[9] R. Toni, E. Bassi, F. Barbaro, N. Zini, A. Zamparelli, M. Alfieri, D. Dallatana, S. Mosca, C. Della Casa, C. Gnocchi, G. Lippi, G. Spaletta, E. Bassoli, L. Denti, A. Gatto, F. Ricci, P.L. Tazzari, A. Parrilli, M. Fini, M. Sandri, M. Sprio, A. Tampieri, Bioartificial endocrine glands: at the cutting edge of translational research in endocrinology, in: S. Sprio, A. Tampieri (Eds.), Bio-Inspired Regenerative Medicine: Material, Processes, and Clinical Applications, 15 Pan Standford Publishing, Singapore, 2016, pp. 357–387.
[10] D.L. Stocum, Regenerative biology and engineering: strategies for tissue restoration, Wound Repair Regen. 6 (1998) 276–290.
[11] H.A. McCauley, J.M. Wells, Pluripotent stem cell-derived organoids: using principles of developmental biology to grow human tissues in a dish, Development 144 (2017) 958–962.
[12] S.N. Bhatia, D.E. Ingber, Microfluidic organs-on-chip, Nat. Biotechnol. 32 (2014) 760–772.
[13] I. Martin, T. Smith, D. Wendt, Bioreactor-based roadmap for the translation of tissue engineering strategies into clinical products, Trends Biotechnol. 27 (2009) 495–502.
[14] K. Jakab, A. Neagu, V. Mironov, R.R. Markwald, G. Forgacs, Engineering biological structures of prescribed shape using self-assembling multicellular systems, Proc. Natl. Acad. Sci. USA 101 (2004) 2864–2869.
[15] R. Toni, C.D. Casa, G. Spaletta, G. Marchetti, P. Mazzoni, M. Bodria, S. Ravera, D. Dallatana, S. Castorina, V. Riccioli, E.G. Castorina, S. Antoci, E. Campanile, G. Raise, R. Rossi, G. Ugolotti, A. Martorella, E. Roti, F. Sgallari, A. Pinchera, The bioartificial thyroid: a

biotechnological perspective in endocrine organ engineering for transplantation replacement, Acta Biomed. 78 (2007) 129–155.
[16] M. Alfieri, An Experimental Model of the Rat Thyroid Gland Stromal Scaffold: Implications for Bioengineering of a Bioartificial Thyroid Gland (Thesis), University of Parma School of Biotechnologies, Re.Mo.BIO.S. lab, 2015, pp. 1–104. ⟨www.anfamedmuseo.unipr.it⟩.
[17] S. Sprio, M. Sandri, M. Iafisco, I. Panseri, C. Cunha, A. Ruffini, N. Zini, R. Toni, A. Tampieri, Biomimetic biomaterials in regenerative medicine, in: A.J. Ruys (Ed.), Biomimetic Biomaterials, Structure and Applications, Ch.1, Whoodhead Publishing, Cambridge, U.K., 2013, pp. 3–45.
[18] E. Bassoli, L. Denti, A. Gatto, G. Spaletta, A. Paderno, N. Zini, A. Parrilli, R. Giardino, V. Strusi, D. Dallatana, S. Mastrogiacomo, A. Zamparelli, M. Iafisco, R. Toni, A combined additive layer manufacturing / indirect replication method to prototype 3D vascular-like structures of soft tissue and endocrine organs, Virtual Phys. Prototyp. 7 (2012) 3–11.
[19] E. Bassoli, L. Denti, A. Gatto, G. Spaletta, M. Sofroniou, A. Parrilli, M. Fini, R. Giardino, A. Zamparelli, N. Zini, F. Barbaro, E. Bassi, S. Mosca, D. Dallatana, R. Toni, A planar fractal analysis of the arterial tree of the human thyroid gland: implications for additive manufacturing of 3D ramified scaffolds, in: P.S. Bartolo, et al. (Ed.), High Value Manufacturing: Advanced Research in Virtual and Rapid Prototyping, CRC Press, Taylor & Francis group, London, 2014, pp. 423–429.
[20] V. Strusi, N. Zini, D. Dallatana, A. Parrilli, R. Giardino, G. Lippi, G. Spaletta, E. Bassoli, A. Gatto, M. Iafisco, M. Sandri, A. Tampieri, R. Toni, Ex situ bioengineering of the rat thyroid using as a scaffold the three dimensional (3D) decellularized matrix of the glandular lobe: clues to the organomorphic principle, It. J.Anat. Embryol. 116 (Suppl 1) (2011) S180 (Abstract).
[21] R. Toni, V. Strusi, N. Zini, D. Dallatana, S. Mastrogiacomo, A. Parrilli, R. Giardino, G. Lippi, G. Spaletta, E. Bassoli, A. Gatto, M. Iafisco, M. Sandri, A. Tampieri, Bioengineering of the thyroid lobe: use of its stromal/vascular matrix as a scaffold for ex situ reconstruction, in: Proceedings of the Endocrine Society's 94th Annual Meeting and Expo, Houston, OR26-3, 2012 (Abstract).
[22] A. Atala, Engineering organs, Curr. Opin. Biotechnol. 20 (2009) 575–592.
[23] S.F. Badylak, The extracellular matrix as a scaffold for tissue reconstruction, Semin. Cell Dev. Biol. 13 (2002) 377–383.
[24] M. Bantscheff, M. Schirle, G. Sweetman, J. Rick, B. Kuster, Quantitative mass spectrometry in proteomics: a critical review, Anal. Bioanal. Chem. 389 (2007) 1017–1031.

[25] V. Strusi, N. Zini, D. Dallatana, S. Mastrogiacomo, A. Parrilli, R. Giardino, G. Lippi, G. Spaletta, E. Bassoli, A. Gatto, M. Iafisco, M. Sandri, A. Tampieri, R. Toni, Endocrine bioengineering: reconstruction of a bioartificial thyroid lobe using its three-dimensional (3D) stromal / vascular matrix as a scaffold, Endocr. Abstr. 29 (2012) 1586 (Abstract).
[26] P.M. Crapo, T.W. Gilbert, S.F. Badylak, An overview of tissue and whole organ decellularization processes, Biomaterials 32 (2012) 3233–3243.
[27] C.A. Miles, T.J. Sims, N.P. Camacho, A.J. Bailey, The role of the α2 chain in the stabilization of the collagen type I heterotrimer: a study of the type I homotrimer in oim mouse tissues, J. Mol. Biol. 321 (2002) 797–805.
[28] M.L. Tiku, B. Madhan, Preserving the longevity of long-lived type II collagen and its implication for cartilage therapeutics, Ageing Res. Rev. 28 (2016) 62–71.
[29] K. Blumbach, Y.M. Bastiaansen-Jenniskens, J. DeGroot, M. Paulsson, G.J.V.M. Van Osch, F. Zaucke, Combined role of type IX collagen and cartilage oligomeric matrix protein in cartilage matrix assembly: cartilage oligomeric matrix protein counteracts type IX collagen-induced limitation of cartilage collagen fibril growth in mouse chondrocyte cultures, Arthritis Rheum. 60 (2009) 3676–3685.
[30] R. Fleischmajer, J.S. Perlish, R.E. Burgeson, F. Shaikh-Bahai, R. Timpl, Type I and type III collagen interactions during fibrillogenesis, Ann. N. Y. Acad. Sci. 580 (1990) 161–175.
[31] X. Liu, H. Wu, M. Byrne, S. Krane, R. Jaenisch, Type III collagen is crucial for collagen I fibrillogenesis and for normal cardiovascular development, Proc. Natl. Acad. Sci. USA 94 (1997) 1852–1856.
[32] V. Strusi, N. Zini, S. Mastrogiacomo, A. Zamparelli, F. Barbaro, D. Dallatana, A. Parrilli, R. Giardino, R. Toni, Identification of putative adult stem cells in the rat thyroid and their use in ex situ bioengineering, It. J. Anat. Embryol. 117 (2012) 184.
[33] F. Barbaro, A. Zamparelli, N. Zini, D. Dallatana, E. Bassi, S. Mosca, A. Parrilli, M. Fini, R. Giardino, R. Toni, Adult stem / progenitor cells of the rat thyroid: side population distribution, intermediate filament expression, and long-term *in vitro* expansion, It. J. Anat. Embryol. 118 (2013) 19.
[34] E. Bassi, F. Barbaro, A. Zamparelli, N. Zini, L. Cattini, D. Dallatana, C. Gnocchi, G. Lippi, S. Mosca, A. Parrilli, M. Fini, R. Giardino, R. Toni, Thyrogenic adipogenic, and osteogenic differentiation of adult rat, thyroid stem cells enriched by long-term adherent subculture, It. J. Anat. Embryol. 119 (2014) 15.
[35] E. Bassi, F. Barbaro, A. Zamparelli, N. Zini, G. Spaletta, F. Ricci, C. Velati, D. Dallatana, C. Gnocchi, G. Lippi, M. Alfieri, S. Mosca, C. Della Casa, P. Crafa, A. Parrilli, M. Fini, R. Toni,

Multipotent adult rat, thyroid stem cells can be differentiated to follicular thyrocytes, and hepatocyte-like cells in 2D and 3D culture systems, It. J. Anat. Embryol. 120 (2015) 87.
[36] K. Kühn, Basement membrane (type IV) collagen, Matrix Biol. 14 (1994) 439–445.
[37] S. Söder, E. Pöschl, The NC1 domain of human collagen IV is necessary to initiate triple helix formation, Biochem. Biophys. Res. Commun. 325 (2004) 276–280.
[38] L.D. Muiznieks, F.W. Keeley, Molecular assembly and mechanical properties of the extracellular matrix: a fibrous protein perspective, Biochim. Biophys. Acta 2013 (1832) 866–875.
[39] D.E. Birk, Type V collagen: heterotypic type I/V collagen interactions in the regulation of fibril assembly, Micron 32 (2001) 223–237.

13 Chapter 10: "3D printed chitosan scaffolds: A new TiO_2 support for the photocatalytic degradation of amoxicillin in water"

Laura Bergamonti [a], Carlo Bergonzi [b], Claudia Graiff [a], *, Pier Paolo Lottici [c], Ruggero Bettini [b], Lisa Elviri [b]

[a] Department of Chemistry, Life Science and Environmental Sustainability, University of Parma, Parco Area delle Scienze 17/A, Parma, Italy
[b] Food and Drug Department, University of Parma, Parco Area delle Scienze 27/A, I-43124, Parma, Italy
[c] Department of Mathematical, Physical and Computer Sciences, University of Parma, Parco Area delle Scienze 7/A, Parma, Italy

Published on 15 October 2019, Water Res. Vol 163:114841. doi: 10.1016/j.watres.2019.07.008. Epub 2019 Jul 6.

IF 7.913

Personal contribution

CB performed the experimental work related to material development, 3D development, analytical characterization, drug photodegradation studies and contributed to the preparation of the manuscript.

Abstract

TiO_2-supported chitosan scaffolds (TiO_2/CS) are here proposed as promising material for wastewater treatment, in particular for the removal of pharmaceutical compounds. TiO_2/CS are tested for the amoxicillin photodegradation under UV/Vis irradiation. Amoxicillin (AMX) is an antibiotic of the beta-lactam family. Due to the release of antibiotics in wastewater and their persistence in the environment, harmful effects can develop on the aquatic and terrestrial organisms.

TiO_2 chitosan scaffolds with photocatalytic activity for wastewater remediation have been prepared by 3D printing using commercial P25-TiO_2. The formulation for the 3D printer was prepared by dispersion of chitosan and TiO_2 in powder form at the concentration 6% w/v and 1% w/v, respectively. The TiO_2 particles (crystalline anatase and rutile phases) embedded in the chitosan have a size of about 20 nm, like in the starting material, as verified by X-ray diffraction and Raman spectroscopy and are homogeneously distributed in the scaffold, also after repeated photocatalytic tests, as revealed by SEM-EDS.

The mechanical properties of the 3D structures are suitable for the targeted application as they can be easily handled without breakage.

The AMX photodegradation efficiency under light irradiation by TiO_2/CS made with scaffolds of different thicknesses (3, 5, 15 layers), was assessed in water by means of UV/Vis absorption and HPLC/UV measurements, at two different AMX:TiO_2 molar ratios: 1/100 and 1/10. The 3D printed TiO_2/CS system, even after repeated cycles, shows a high photodegradation efficiency, compared to the direct AMX photolysis. A zero-order kinetics for TiO_2 supported photodegradation was found, whereas a pseudo-first order was observed for water dispersed TiO_2. Mass spectrometry analysis revealed the presence of AMX degradates such as penilloic and penicilloic acids and diketopiperazine.

The proposed 3D printed chitosan scaffolds may be used as reusable substrate for the TiO_2 photocatalytic degradation of antibiotic pollutants in wastewater.

Keywords: 3D-printing, Supported TiO_2, Chitosan scaffolds, Wastewater remediation, Amoxicillin photodegradation

13.1 Introduction

The increasing pollution, due to a wide range of micropollutants, particularly in the aquatic ecosystem, has become a serious issue for the harmful effects on the environment and human health (Tousova *et al*., 2017; Petrie *et al*., 2015). Emerging contaminants, such as pharmaceuticals, personal care products, pesticides, heavy metals, have been found in sewage discharge, in surface and ground water and in drinking water, at concentrations from few ng L^{-1} to several mg L^{-1} (Schulze *et al*., 2019; Sousa *et al*., 2018; Taheran *et al*., 2018; Gogoi *et al*., 2018; Deblonde *et al*., 2011; Santos *et al*., 2010). The pharmaceutical compounds and in particular the antibiotics play a relevant role due to their large use in both human and veterinary medicine (Yi *et al*., 2019; Li, 2014; Osorio *et al*., 2012, Watkinson *et al*., 2009; Stackelberg *et al*., 2004).

As reported by several studies, up to 95% of antibiotics can be excreted and discharged into the sewers in unaltered state (Homem and Santos, 2011; Gros *et al*., 2010) and with conventional wastewater treatment only incomplete removal can be achieved (Manaia *et al*., 2018). One of the most known effects on the environment is the development of resistant pathogenic bacteria (Proia *et al*., 2018; Figueira *et al*., 2011).

Amoxicillin (AMX), one the most common b-lactam antibiotics, is characterized by chemical stability, low rate of biodegradation and high level of toxicity. AMX is used to treat several diseases in human medicine and in veterinary practice. AMX metabolism is slow: the excretion by human is from 80% to 90%. AMX is found in surface water, secondary sewage treated and drinking water at a concentration of mg L^{-1} but in pharmaceutical industry effluents at a concentration of mg L^{-1} (Githinji *et al*., 2011; Garcia-Reiriz *et al*., 2007; Andreozzi *et al*., 2004). By conventional filtration methods it is very difficult to eliminate the AMX residue (Dimitrakopoulou *et al*., 2012; Abazari and Mahjoub, 2018). For the above reasons, AMX was selected as a model contaminant.

Advanced oxidation processes (AOPs), based on the *in situ* generation of highly reactive species, (H_2O_2, •OH, $O_2^{\bullet-}$ and O_3) are a promising route for the nonselective oxidative degradation of a wide variety of organic and inorganic water pollutants into harmless end-products (Kanakaraju *et al*., 2018; Andreozzi *et al*., 2005). AOPs technologies involve a wide range of methods (ozone-based, UV-based, catalytic, physical and electrochemical) for the generation of the oxidant species (Miklos *et al*., 2018; De Witte *et al*., 2011; Elmolla and Chaudhuri, 2010b).

AMX degradation by different techniques has been reported by several authors (Verma and Haritash, 2019; Abazari and Mahjoub, 2018; Kanakaraju *et al*., 2018; Ganiyu *et al*., 2016; Moreira *et al*., 2015; Palmisano *et al*., 2015; Li *et al*., 2012; Trovò *et al*., 2008).

Heterogeneous photocatalysis, a photoinduced reaction, is an effective and environmentally friendly AOP that uses semiconductors such as oxides (TiO_2, ZnO, CeO_2, ZrO_2, WO_3, V_2O_5) and sulfides (CdS, ZnS) to increase the production of reactive species (Arcanjo *et al*., 2018), without the use of potentially hazardous oxidants (e.g. ozone, chlorine), to decompose and completely mineralize organic pollutants (Elhahil *et al*. 2017; McCullagh *et al*., 2010; Mozia, 2010; Rizzo *et al*., 2009).

TiO_2 mediated photocatalysis is one the most used AOPs to degrade a wide range of water recalcitrant contaminants (Favier *et al*., 2016; Li *et al*., 2015; Ounnar *et al*., 2016; Tong *et al*., 2012; Chong *et al*., 2010). Due to its photo and chemical stability, non-toxicity and high photoactivity, nanocrystalline TiO_2 has been employed for many significant applications as the self-cleaning coatings for buildings materials (Colangiuli *et al*., 2019; Luna *et al*., 2018; Bergamonti *et al*., 2017; Pinho *et al*., 2015), glasses and tiles (De Niederh~ausern *et al*., 2013; Murugan *et al*., 2013), self-sterilizing solid surfaces (Sciancalepore *et al*., 2014; Leong *et al*., 2014; Evans and Sheel, 2007), bone-implant fixation (Bjursten *et al*., 2010; Sykaras *et al*., 2000), purification of water (Zangeneh *et al*., 2015) and air (Shayegan *et al*., 2018; Mo *et al*., 2009; Fujishima *et al*., 2008), dye-sensitized solar cells (Gong *et al*., 2012; O'Regan and Grätzel, 1991).

AMX degradation by TiO_2 photocatalytic based systems has been reported by several authors (Li *et al*., 2015, 2019; Awfa *et al*., 2018; Olama *et al*., 2018; Arce-Sarria *et al*., 2018; Radosavljević *et al*., 2017; Moreira *et al*., 2015; Dimitrakopoulou *et al*., 2012; Kanakaraju *et al*., 2015; Tong *et al*., 2012; Klauson *et al*., 2010; Elmolla and Chaudhuri, 2010a).

In a photocatalytic system, the photoinduced reactions take place at the surface of the catalyst. When irradiated by light with energy equal to or greater than its bandgap energy (Eg), the semiconductor absorbs photons leading to the formation of electron (e^-) - hole (h^+) pairs: the e^- is promoted in the conduction band leaving h^+ in the valence band. The photogenerated electron-hole pair can migrate at the surface of the catalyst and react with the adsorbed species such as H_2O, -OH, O_2, to form hydroxyl radicals, superoxide radical anions and hydroperoxyl radicals, able to destroy the organic compounds (Schneider *et al*., 2014; Fujishima *et al*., 2008; Hashimoto *et al*., 2005; Herrmann, 1999; Linsebigler *et al*., 1995).

Titanium dioxide is found in nature in three crystalline polymorphs: brookite (orthorhombic), anatase and rutile (both crystallizing in the tetragonal system). Rutile is the thermodynamically

stable phase, anatase and brookite phases are transformed to rutile at high temperatures. All crystalline forms are photoactive: anatase is usually considered to be the most active even if good results are also obtained for TiO_2 in brookite or rutile forms (Di Paola *et al.*, 2013; Pigeot-Rèmy *et al*., 2019), and for mixed phases (Ohno *et al*., 2001).

Particle size and surface area are the key factors in heterogeneous catalysis: large surface area, thanks to the increase of the active surface sites, leads to high photocatalytic efficiency (Leong *et al*., 2014). The main drawback of the TiO_2 nanoparticles, limiting the widespread technical application of heterogeneous photocatalysis in water treatment, is the difficulty of the photocatalyst separation from water and its regeneration after use. To solve this problem, researchers attempt to immobilize TiO_2 nanoparticles on some active support such as activated carbon, glass, zeolites, polymer films or natural biopolymers (Siripatrawan and Kaewklin, 2018; Karthikeyan *et al*., 2017; Kanakaraju *et al*., 2015; Cendrowski *et al*., 2011; Nawi *et al*., 2009; Suwanchawalit *et al*., 2009).

In this work, a new method for immobilizing TiO_2 nanoparticles is proposed, exploiting an emerging easily scalable technology such as fused modelling 3D deposition, to process an environmentally friendly material (Do *et al*., 2015). Moreover, 3D printing allows obtaining identical objects, defined in terms of designed geometries rather than dimensions that can be arbitrarily set during the design phase (Wang *et al*., 2018; Elviri *et al*., 2017). Chitosan, chosen as embedding material for TiO_2 nanoparticles, is a naturally derived polymer, extracted mostly from crabs and other crustaceans. It is non-toxic for the environment, biocompatible with human body and demonstrated to provide bacteriostatic effects (Elviri *et al*., 2014; Elviri *et al*., 2016; Galli *et al*., 2016; Goy R.C. *et Al*., 2009). 3D printed chitosan scaffolds, constituted by many layers of an orthogonal grid, are here investigated in the form of stable hydrogels as supports for photocatalytic TiO_2. For the realization of the functionalized chitosan scaffolds (TiO_2/CS), commercial P25-TiO_2 was used: it is known for high photocatalytic activity and often taken as reference sample for photocatalytic tests (Ohno *et al*., 2001; Klauson *et al*., 2010). TiO_2-P25 powder contains anatase and rutile phases in about 80/20 ratio: the mixed-phase system improves the photocatalytic performances through charge transfer mechanisms affecting the electron-hole recombination times (Hurum *et al*., 2003).

13.2 Materials and methods

13.2.1 Chemicals

Aeroxide@ P25-TiO_2 (Evonik Degussa, D) and amoxicillin (>97%) obtained from Sigma-Aldrich (USA), were used as received.
Chitosan Chitoclear™ (CAS 9012-76-4, degree of deacetylation 95%; molecular weight by gel permeation chromatography 150-200 kDa; allergen free, water insoluble, soluble in acid media) was from PRIMEX Ehf (Siglufjordur, Iceland). Ultrapure water (Flex ultra-pure water, Elga Veolia, Italy) was used for all experiments.

13.2.2 Chitosan-TiO_2 formulation

Chitosan Chitoclear™ and Aeroxide@ P25-TiO_2 powders were accurately weighted to obtain a final concentration in the formulation of 6% w/v and 1% w/v, respectively (i.e. g of solute/100mL of solution). Powders were then mixed together in a beaker and suspended in de-ionized (DI) water. The mixture was put under magnetic stirring till the two materials were homogeneously dispersed, then glacial acetic acid to obtain a final concentration of 2% v/v was added to let the polymer dissolve, embedding TiO_2 nanoparticles. The formulation was maintained under magnetic stirring for 24 h: the blended material to be printed was then ready to use.

13.2.3 3D scaffold design

Scaffolds were designed using the software Solidworks™ (Dassault Systems, USA) allowing the creation of 3D models in.stl electronic format (Stereo Lithography interface). These models are elaborated by a slicing program, Slic3r™(RepRap), which generates a machine code (.gCode) for the 3D printer. The 3D printer employed in this work was in-house-built. The hardware used consisted of an Arduino Mega2560 coupled with a RAMPS 1.4. and the software used was Marlin™.
The 3D printer is equipped with a printing surface constituted by aluminum plates cooled by Peltier's cells, able to freeze the material instantaneously after its deposition. The extrusion apparatus, a pump acting on a 5 ml syringe mounting a 26 G (inner diameter 192 μm) and charged with the polymeric formulation, moves along *x*,*y*,*z* axes during the process. The scaffolds were made by an orthogonal grid, characterized by an inter-filament distance of 200 μm and a number

of layers arbitrarily chosen. Once the three-dimensional object was made, the plate was detached from Peltier's cells: the scaffold on top completely frozen was then placed in a gelling environment to maintain the three dimensional structure (Elviri *et al*., 2017).

13.2.3.1 Gelation process

The structure formed by the 3D printer can be maintained by gelling chitosan which can undergo the sol-gel transition when exposed to alkaline environment. The frozen TiO_2-Chitosan scaffolds (TiO_2/CS) were transferred into a chamber saturated with ammonia vapors (ammonia solution 28%). In this process, the positive charges of acetic acid used to dissolve the polymer during the preparation are neutralized and an ionotropic gelation takes place permitting a stable network formation among the polymeric chains (Bergonzi *et al*., 2019).

13.2.4 Characterization of immobilized TiO_2 material

Brunauer-Emmett-Teller (BET) model was applied to determine the specific surface area of TiO_2 P25 nanoparticles by means of a Micromeritics Pulse Chemisorb 2705 analyzer using nitrogen at 77 K (single point method). Prior to measuring, the samples (150 mg) were outgassed under helium flow at 473 K for 2 h. The crystal structure of the TiO_2 nanoparticles embedded in the 3D chitosan scaffold was determined by Thermo ARL X'TRA X-ray diffractometer with Si-Li detector, using CuKα radiation (λ 1.5406 Å) at 40 kV and 40 mA. Room-temperature X-ray powder diffraction patterns were collected in the range 10°-60°, at 0.2° scan rate (in 2θ) by dispersing powders on a glass sample holder. The XRD patterns were compared with standard anatase and rutile diffractograms (JCPDS card #21-1272 and JCPDS card #76-1940, respectively). The average diameter of the crystallites was estimated by the Scherrer equation from the line broadening of the main diffraction peaks.

A Jobin Yvon LabRAM microspectrometer (300mm focal length spectrograph) equipped with an integrated Olympus BX40 microscope was employed for non-polarized Raman scattering measurements in nearly backscattered geometry. The samples were excited with the 473.1 nm blue light of a doubled Nd:YAG laser. The spectral resolution was about 1.5-2 cm^{-1}.

The microstructure of the scaffolds surfaces and the distribution of the TiO_2 nanoparticles before and after the photodegradation tests was examined by a Scanning Electron Microscope Jeol JSM 6400 equipped with an Oxford Instruments Link Analytical Si (Li) Energy Dispersive System detector (SEM-EDS). The data analysis was performed by INCA built-in software.

13.2.5 Mechanical characterization

Mechanical resistance under traction as well as elasticity are crucial features for manipulating scaffold designed for industrial applications. A traction dynamometer (Acquati, Italy) has been used to evaluate the mechanical strength of the 3D printed scaffolds, calculated both as Young's elastic modulus (E) and mechanical stress at break. Scaffold sizes were 5 layers (15mm15mm x 1 mm). The traction tests were performed by setting the following parameters: pre-fixed distance between clips, ±25 mm; traction speed, 25mm min^{-1}, 5 daN top head. Force and movement were digitalized by PowerLab 4/35 and registered by LabChart® Pro software. Force and elongation were continuously registered till break. Before the traction test, the thickness of the samples was measured by a caliper and a digital thickener (Mitutoyo Corporation). The obtained data were compared to those on pure chitosan scaffolds. Measurements were done in triplicate.

13.2.6 Photodegradation experiments

To evaluate the adsorption capacity and photocatalytic activity of the TiO_2 immobilized on chitosan scaffold (TiO_2/CS), experiments in dark (i) and under UV/Vis irradiation (ii) were performed. As control, experiments were also carried out with the scaffold made of chitosan alone (CS) and with the Aeroxide@ P25-TiO_2:

(i) to ensure the achievement of the adsorption/desorption equilibrium, 40 ml of AMX aqueous solution (pH = 6.7) was placed in a reactor (see Fig. 1a) with CS, TiO_2 or TiO_2/CS and stirred in the dark until constant concentration, measured by UV/Vis spectrophotometer. The AMX:TiO_2 molar ratios tested were 1/100 and 1/10.
(ii) The photodegradation of AMX aqueous solutions was investigated under external UV/Vis irradiation using a 125W Helios-Italquartz medium pressure mercury-vapor, waterjacketed lamp, with emission range 300-800 nm. The irradiation power at the water surface was 3.5 mW/cm^2, measured by a digital meter PCE-UV34. The absorption spectrum of AMX and the emission spectrum of the lamp are show in Fig. 1b and c, respectively.

The photolysis of the AMX under irradiation (without any catalyst), in the same condition of the photodegradation experiments, was also verified.
The UV absorbance at equilibrium (A0), measured at the end of the dark experiment, was taken as reference for the initial concentration (C0), then the solution was irradiated with UV lamp

under continuous stirring. Aliquots (2 ml) were taken at defined time intervals and filtrated by 0.45 μm Cronus 13mm nylon syringe filters, to remove suspended particles before the analysis. The concentration of AMX molecules at time t, Ct, was measured with both a Lambda-Bio 20 UV/Vis Spectrometer (PerkinElmer, USA) and with HPLC/UV LC Agilent 1200 binary pump equipped with a 100-vial position autosampler (Agilent Technologies, UK), by monitoring the absorbance at 230 nm (UV_{230}) and 272 nm ($HPLC/UV_{272}$), respectively. The normalized absorbance At/A0 of AMX solution was taken as the measure of concentration ratio C_t/C_0 at time t. All the experiments were done in triplicate.

HPLC analysis was performed to check the results obtained with UV/VIS spectrophotometry, a technique more easily accessible in the laboratories.

To investigate the optimal photodegradation condition, the reaction was carried out with three types of chitosan scaffolds: a scaffold made by 3 layers, CS3 (15 mm x 25mm x 0.6 mm), a 5 layers scaffold CS5 (15mm x 15mm x 1 mm) and a 15 layers scaffold CS15 (8.7mm x 8.7mm x 3 mm) with the same amounts of chitosan and TiO_2.

Chromatographic separation was achieved on a C18 Gemini (100 x 4.6 mm, 5 μm) column (Phenomenex, USA). The mobile phase consisted of a mixture of ultrapure water/acetonitrile (ratio 90/10) with 0.2% of formic acid; the flow rate was maintained at 0.6 mL/min and the detector wavelength at 272 nm. Column temperature was not controlled (room temperature: 24 °C). Injection volume was 20 mL. Elution was carried out in isocratic mode at the flow rate of 0.6 mL/min. The stationary phase consisted of a C18 Phenomenex Gemini 5 μm 110A (100 x 4.60 mm).

The amount of AMX was measured by performing calibration using AMX standards from 1 to 100 mg/mL prepared in UP water.

13.2.7 High resolution mass spectrometer analysis of AMX degradation products

Amoxicillin sample solutions were characterized by direct infusion analysis at a flow-rate of 10 μL min^{-1} into an LTQ linear ion trap-Orbitrap XL mass spectrometer (ThermoScientific Corporation, San Josè, CA, USA) equipped with ESI interface and controlled by Xcalibur software.

Optimized conditions of the interface were as follows: ESI voltage 3.5 kV, capillary voltage 13 V, capillary temperature 275 °C, tube lens voltage 85 V. High resolution mass spectra were acquired in positive ion full scan mode in the m/z window 100-1800 with a resolution of 60.000 and in MS/MS product ion mode. For the analysis of degradation, intermediate samples were

collected from the reaction media after 30 and 180 min of reaction and the results compared with those of pure AMX.

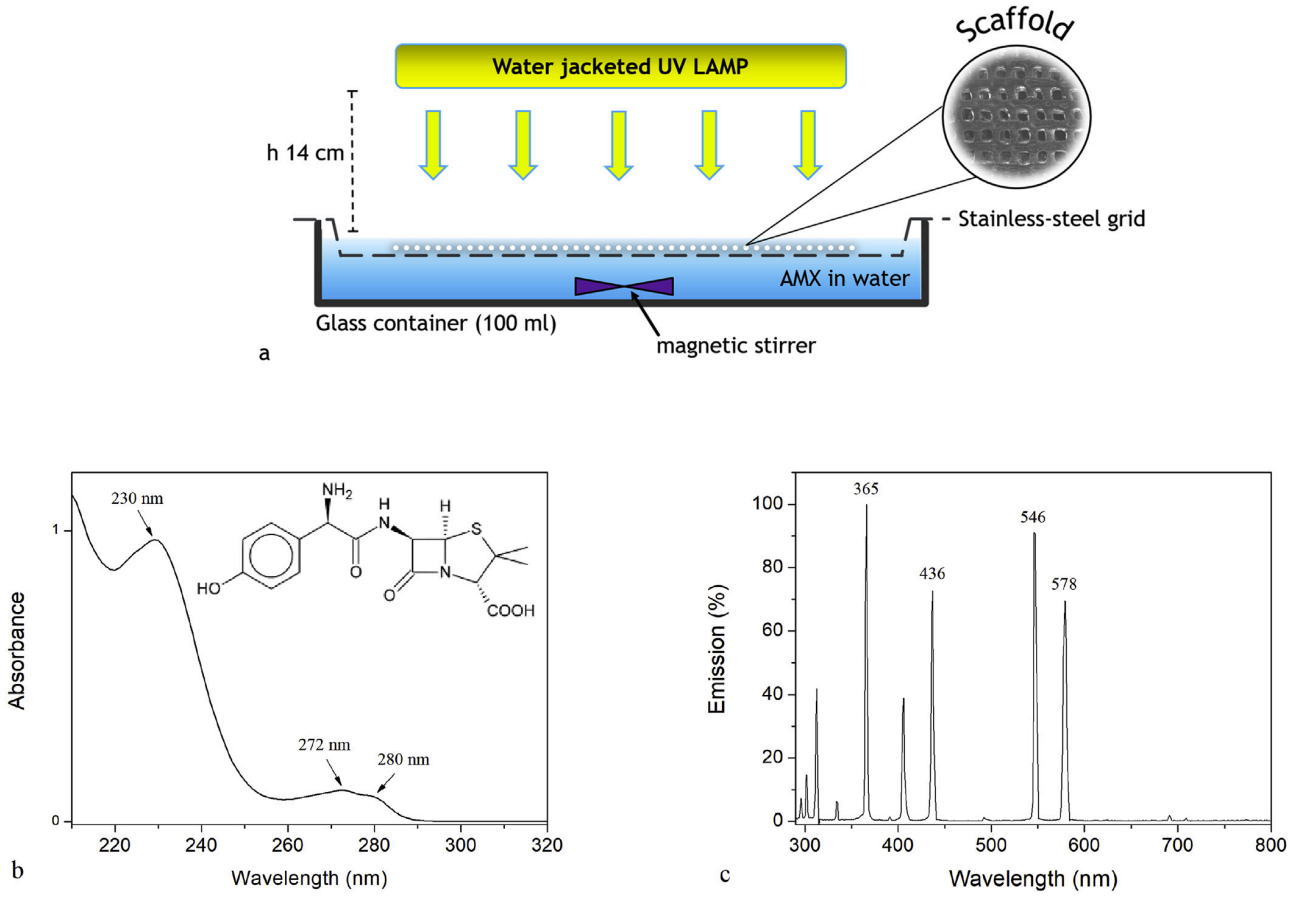

Fig. 1. a) Scheme of the small scale reactor used for the photocatalysis tests; b) UV absorption spectrum of amoxicillin; c) emission spectrum of the 125W Helios-Italquartz irradiation lamp in the 300-800 nm range.

13.3 Results and discussion

13.3.1 Scaffold characterization

The X-ray diffraction patterns of TiO_2/CS 3D scaffold compared to those of pure TiO_2 powder and of chitosan (CS) are shown in Fig. 2. The 2θ peaks at 25.3°, 38.0°, 48.1°, 53.9°, 55.2° correspond to the anatase crystalline phase and are due to the reflection planes (101), (004), (200), (105) and (211), respectively, while the peaks at 27.6°, 36.2°, 41.3°, 44.5°, 54.4° correspond to the rutile crystalline phase and are due to the reflection planes (110), (101), (111), (210) and (211), respectively. The rutile and anatase features are seen in the TiO_2/CS diffraction pattern together

with the contribution of chitosan, showing a broad peak at 2θ ~20.2°, characteristic of an amorphous structure (Bergamonti *et al.*, 2015).

The rutile weight fraction in the TiO_2 powder was estimated by Zhang and Banfield (2000) method to be ~0.21. The size of the TiO_2 nanocrystals, as expected, is not influenced by the immobilization into the 3D scaffold: the full width at half maximum (FWHM) of the main anatase and rutile peaks in the TiO_2/CS doesn't change. The TiO_2 nanoparticle size, both pure or embedded in the scaffold, determined by Scherrer equation, is ~20 nm for anatase and ~25 nm for rutile phase. These values agree with Aeroxide@ P25 nanoparticles average sizes reported in literature (Ohno *et al.*, 2001). The specific surface area of the P25 powder, as determined by BET isotherm, was 51 m^2g^{-1}, in accordance with values reported in literature (Ohno *et al.*, 2001).

The Raman spectrum of TiO_2/CS is reported in Fig. 3 compared with that of pure P25-TiO_2: anatase (144, 197, 396, 517, 639 cm^{-1}) and rutile (448, 612 cm^{-1}) features are present in both spectra. The width (FWHM) of the main anatase peak, both in TiO_2/CS and in TiO_2 powder, is about 15 cm^{-1}, compatible with a nanocrystalline size of ~20 nm (Bersani *et al.*, 1998). This result agrees with the XRD analysis. Chitosan features at 899, 1110 and 1378 cm^{-1} are observed in the TiO_2/CS spectrum (Nishad *et al.*, 2014).

Highly-ordered 3D chitosan structure was easily achieved by 3D printing. In Fig. 4 is reported the SEM image of chitosan scaffold CS_5 before photodegradation tests. The scaffold shape is characterized by a well-defined 3D structure composed by crossing filaments with size of about 100 μm forming a uniform grid. The resulting channels have nearly square section with a side of 150-200 μm. The surface of filaments is compact with a wrinkled homogenous distribution of not interconnected pores (size distribution: 10-20 μm). This ordered morphology does not change after UV irradiation.

The TiO_2 addition does not influence the structure of the scaffold as evident in Fig. 5a. The shape and size of the interconnected channels is not modified, even after UV irradiation (Fig. 5b). Moreover it can be seen by the EDS Ti map that TiO_2 is uniformly dispersed into the chitosan matrix, with micrometer sized agglomerates (Fig. 5c).

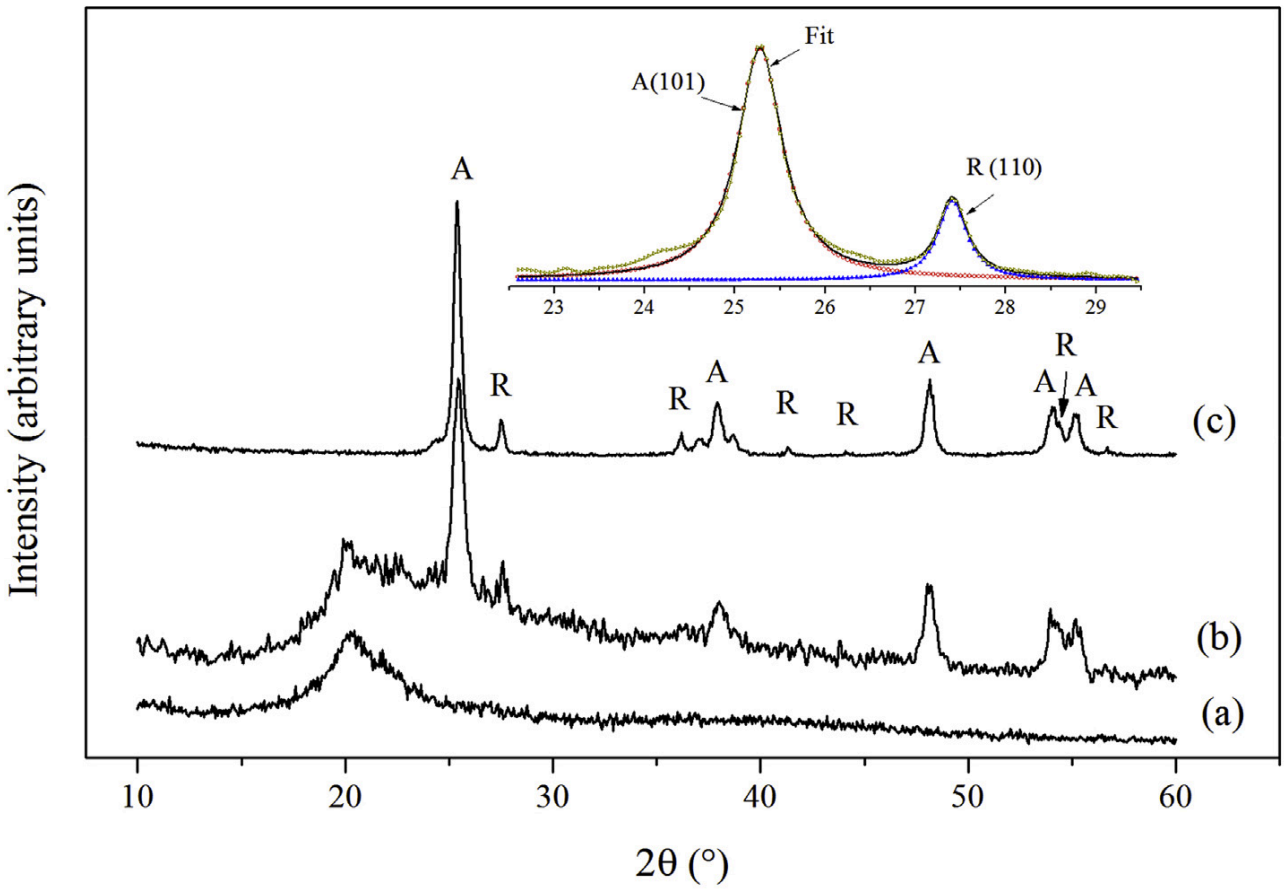

Fig. 2. X-ray diffraction patterns of (a) Chitosan, (b) P25-TiO_2 embedded in chitosan scaffold, (c) Pure P25-TiO_2. A and R indicate anatase and rutile phases, respectively. In the insert: fit of the main anatase and rutile diffraction peaks to determine the rutile content.

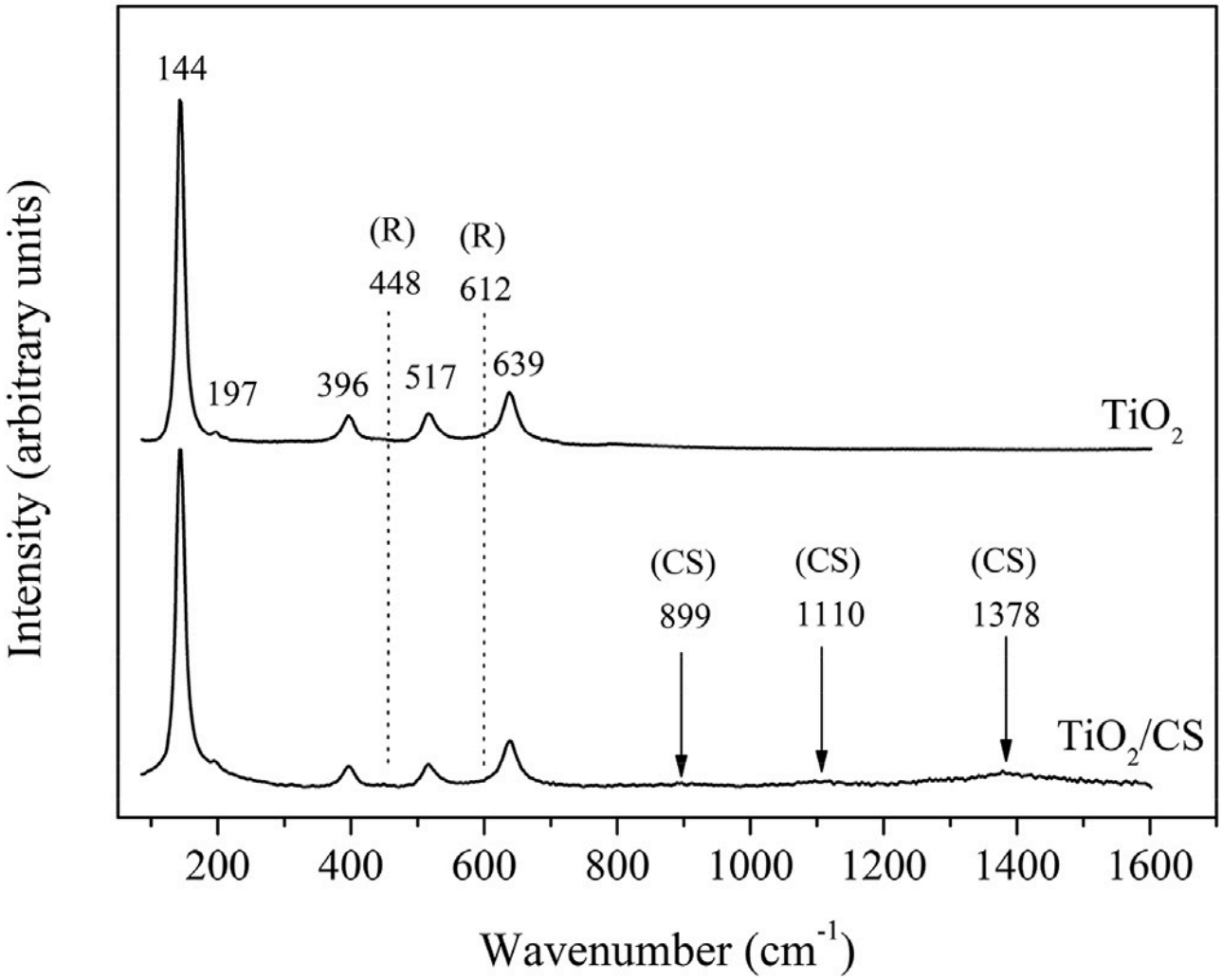

Fig. 3. Raman spectra of nanocrystalline P25-TiO_2 powder and of TiO_2-chitosan scaffold (TiO_2/CS).

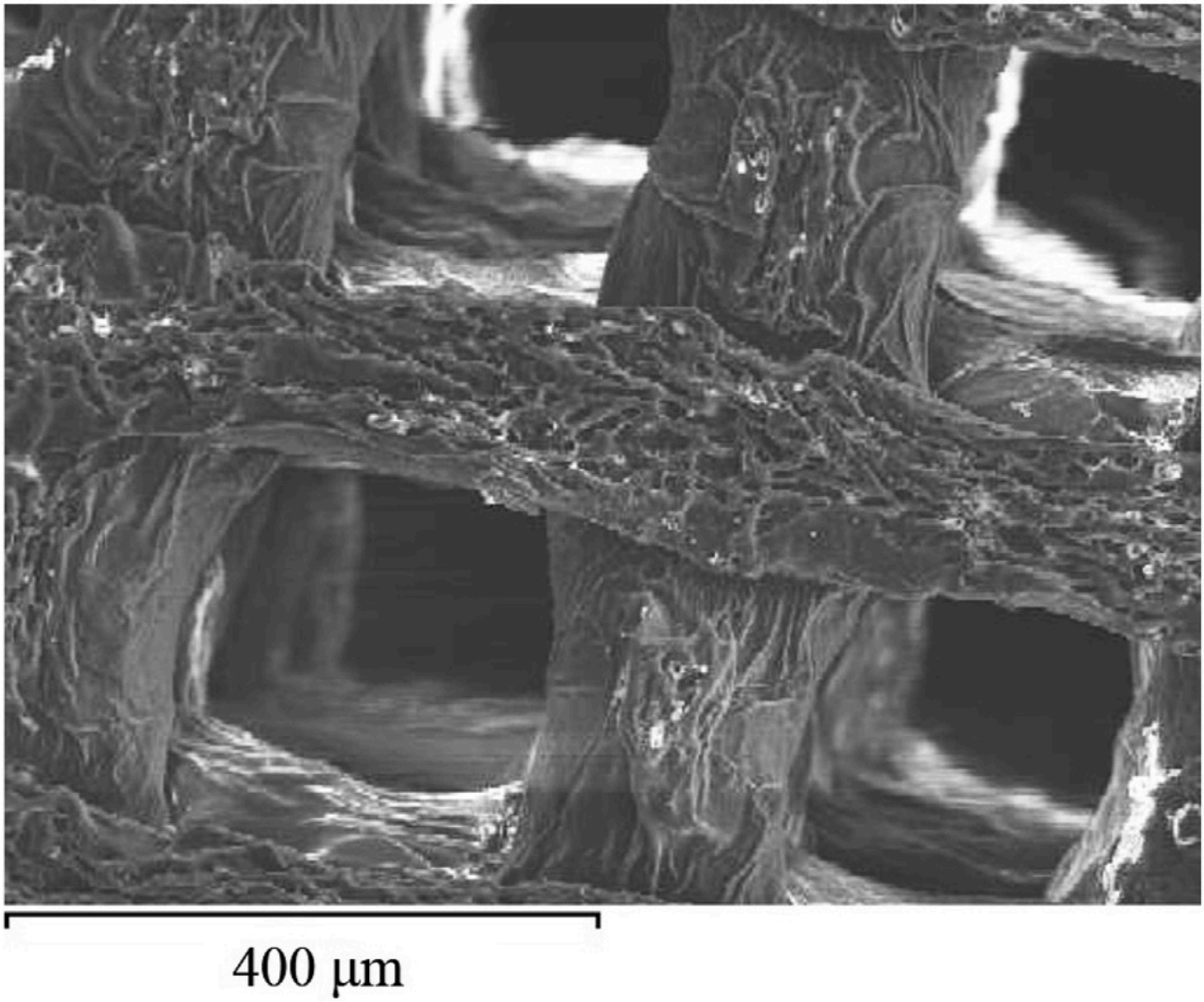

Fig. 4. SEM image (magnification 150X) of chitosan 5-layers scaffold CS_5 (filament surface).

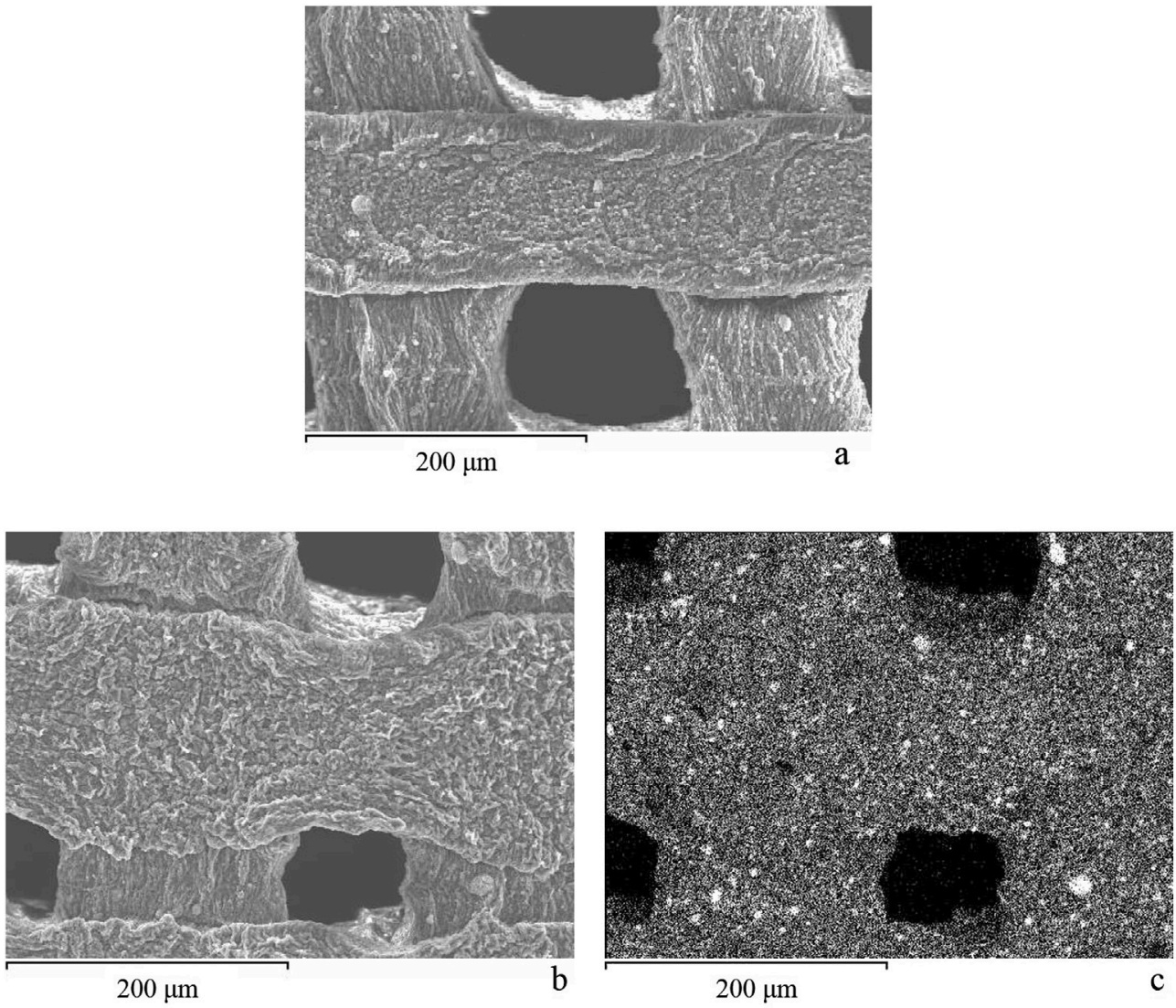

Fig. 5. SEM images (magnification 300x) of TiO_2/CS_5 before (a) and after (b) the photocatalytic tests; (c) EDS Ti map of (b).

13.3.2 Mechanical characterization

The value of Young's modulus was slightly higher in TiO_2/CS_5 (0.49 ± 0.10 MPa) than in CS_5 (0.36 ± 0.05 MPa): the deposition of the TiO_2 nanoparticles among the polymeric chains of the hydrogel causes loosening of the structure and lowering of the elasticity.
Despite this fact, the breaking force (0.047 ± 0.010 kgf) is high enough to allow the application of TiO_2/CS in photocatalytic reactors.

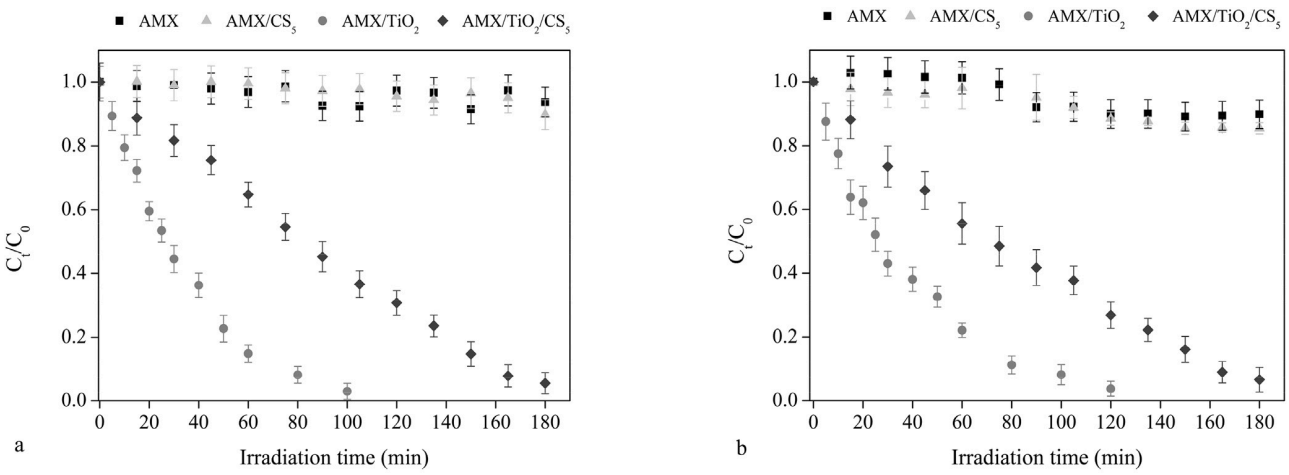

Fig. 6. Photolysis and photocatalysis of AMX versus time. Molar ratio AMX:TiO_2 =1/100; 5 layers scaffold. The degradation profile was monitored by a) UV_{230}; b) HPLC/UV_{272} measurements.

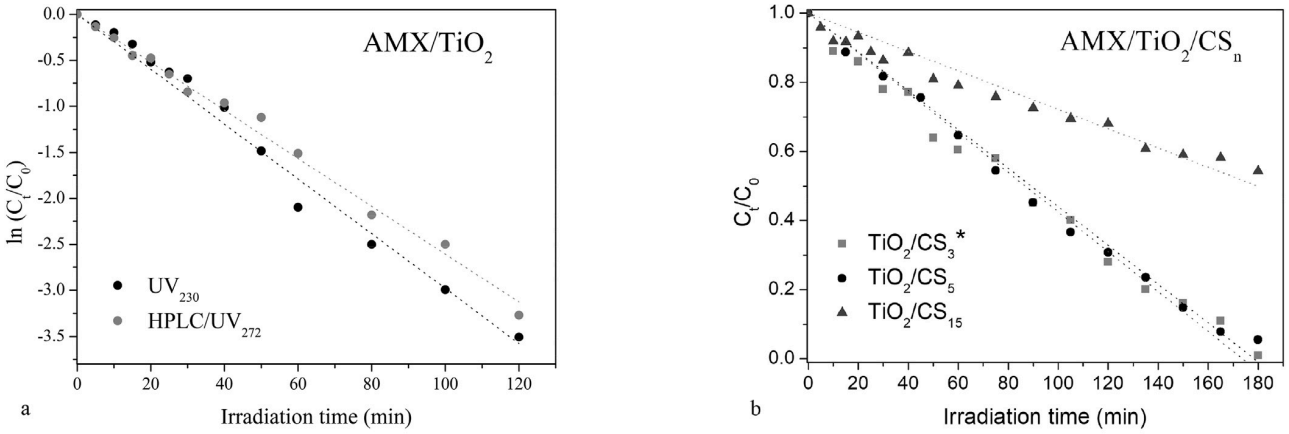

Fig. 7. a) Linear fits to $\ln(C_t/C_0)$ for AMX degradation with pure TiO_2 as measured by UV_{230} and HPLC/UV_{272} (first-order kinetics) for AMX:TiO_2 =1/100. b) Linear fit to (C_t/C_0) for AMX degradation with $TiO_2/CS_{3\text{-}5\text{-}15}$ measured by UV_{230} (zero-th order kinetics). The asterisk to recall that AMX:TiO_2 = 1/10 only for CS[3].

Sample	AMX:TiO_2	UV230 k x 10^{-2} (min^{-1})	UV230 $t_{1/2}$ (min)	UV230 r^2	HPLC/UV_{272} k x 10^{-2} (min^{-1})	HPLC/UV_{272} $t_{1/2}$ (min)	HPLC/UV_{272} r^2
TiO_2	1/100	2.98[a] (0.07)	23[a] (1)	0.99 [a]	2.61 [a] (0.04)	26.5 [a] (0.5)	0.99 [a]
TiO_2/CS_5	1/100	0.57 (0.05)	88 (8)	0.99	0.58 (0.02)	86 (3)	0.95
TiO_2/CS_{15}	1/100	0.28 (0.01)	179 (6)	0.89	0.31 (0.02)	161 (10)	0.91
TiO_2	1/10	1.65 [a] (0.07)	42 [a] (2)	0.96 [a]			
TiO_2/CS_3	1/10	0.56 (0.01)	89 (2)	0.99			

Table 1. Parameters for the photodegradation kinetics (zero or first order) for UV_{230} and HPLC/UV_{272} measurements. Standard errors are given in parentheses; r^2 is the coefficient of determination. [a] First Order.

13.3.3 Photodegradation tests

The removal of AMX in aqueous solution (0.1 mM) was investigated by both UV-Vis absorbance and HPLC/UV measurements. To assess the AMX adsorption, dark tests were done with TiO_2, CS and TiO^2/CS: the reduction in the AMX concentration after 18 h was about 7%, 15% and 15%, respectively. The adsorption of organic molecules on the TiO_2 catalyst surface is due to its affinity for polar or ionizable groups, as those found in AMX (Thomas and Syres, 2012). In the case of chitosan, the NH_2 amino groups are responsible for its capacity to adsorb drugs through interactions of the polar groups of both molecules (Semwal *et al*., 2013; Rinaudo, 2006).

Fig. 6a and b show the normalized AMX concentrations (C_t/C_0), for direct photolysis (AMX, AMX/CS) and photocatalysis (AMX/TiO_2 and AMX/TiO_2/CS) tests, obtained monitoring the absorbance peaks at 230 nm and at 272 nm by the UV-Vis (UV_{230}) and HPLC/UV ($HPLC/UV_{272}$) measurements, respectively.

The contribution of the direct photolysis on the AMX degradation, in the experimental conditions adopted, is quite low: almost 15% of AMX is degradated after 180 min exposure to irradiation. As reported by several authors (see for example Moreira *et al*., 2015; Kanakaraju *et al*., 2015) AMX is very stable to photolysis for irradiation wavelengths above 300 nm. The photolytic degradation here observed can be attributed to the AMX hydrolysis, that proceeds via attack by H_2O, acting as nucleophile, to the b-lactam ring, followed by ring opening (Elmolla and Chaudhuri, 2010a; Andreozzi *et al*., 2005). No significant changes are observed for the AMX photolysis adsorbed on chitosan scaffold (CS_5), confirming the photo-inactivity of the chitosan support.

A considerable enhancement of the photodegradation rate can be observed in presence of the TiO_2 catalyst, both pure and CS_5-immobilized. For a 1:100 AMX:TiO_2 molar ratio the complete removal of AMX adsorbed on P25 catalyst (AMX/TiO_2) is reached in 2 h, in agreement with similar investigations (see, for example, Radosavljević *et al*., 2017). The complete AMX degradation for TiO_2/CS_5 is slightly slower and requires about 3 h of irradiation, despite the use of the same loading of TiO_2 in the scaffold.

It is known that the redox photochemical reaction takes place on the TiO_2 surface when irradiated with UV-light. In the case of the immobilized-TiO_2, only the nanoparticles easily reached by the light can participate to the photocatalytic processes. The decrease in the photodegradation rate of the CS-supported TiO_2 with respect the pure TiO_2 in the slurry experiment is due to the less

amount of available TiO_2 nanoparticles in the scaffold for the photocatalysis (Kanakaraju *et al.*, 2015).

AMX photodegradation experiments done using scaffolds with 15 layers (TiO_2/CS_{15}) show low photocatalytic efficiency, with irradiation time as for TiO_2/CS_5, confirming the above results: the TiO_2 nanoparticles are mainly embedded in the matrix and cannot be reached by UV irradiation. The AMX photodegradation, after 3 h of irradiation, was about 50% (see Fig. 7).

AMX photodegradation tests performed using a 3 layers chitosan scaffold (TiO_2/CS_3), made with the same formulation used for TiO_2/CS_5, show a faster photodegradation rate, even at larger AMX concentrations (AMX:TiO_2 = 1/10): the complete photodegradation is reached in less than 3 h.

The photocatalytic degradation kinetics using pure P25 for both measurement techniques follows a (pseudo) first-order kinetics (Fig. 7a), according to the most referred models for heterogeneous catalysis (Langmuir-Hinshelwood mechanism) with a half-life of ~23 min for AMX:TiO_2 molar ratio 1/100 and ~42 min for 1/10 (Favier *et al*., 2016; Ounnar *et al*., 2016; Herrmann, 1999).

The results for AMX degradation with TiO_2/CS are better described by a zero-order reaction kinetics $C_t/C_0 = 1\text{-}kt$, with k a zero-th order rate constant (Fig. 7b). The half-life for AMX:TiO_2 molar ratio 1/100 for TiO_2/CS_5 is ~90 min and ~180 min for TiO_2/CS_{15}. It is interesting to notice that for AMX:-TiO_2 =1/10 the geometry of TiO_2/CS_3 scaffold influences the photocatalysis allowing high photodegradation efficiency, comparable to that of TiO_2/CS_5 with a photocatalyst amount 10 times higher.

Table 1 summarizes the results for the rate constants and the half-lives obtained for the different measurement conditions.

To verify the reusability of the TiO_2/scaffolds, three cycles of photocatalysis were performed after repeated washes in distilled water. The test was carried out on CS_3 and CS_5, which showed the highest photocatalytic activity, for 180 min of UV irradiation, even if for two different AMX:TiO_2 molar ratios (Fig. 8). For CS_5, also after the last cycle, a good photocatalytic efficiency is maintained and about 80% of AMX is photodegradated. In the case of 3 layer scaffold, already from the second cycle, the efficiency decreases: only 60% of AMX is degraded after a third cycle.

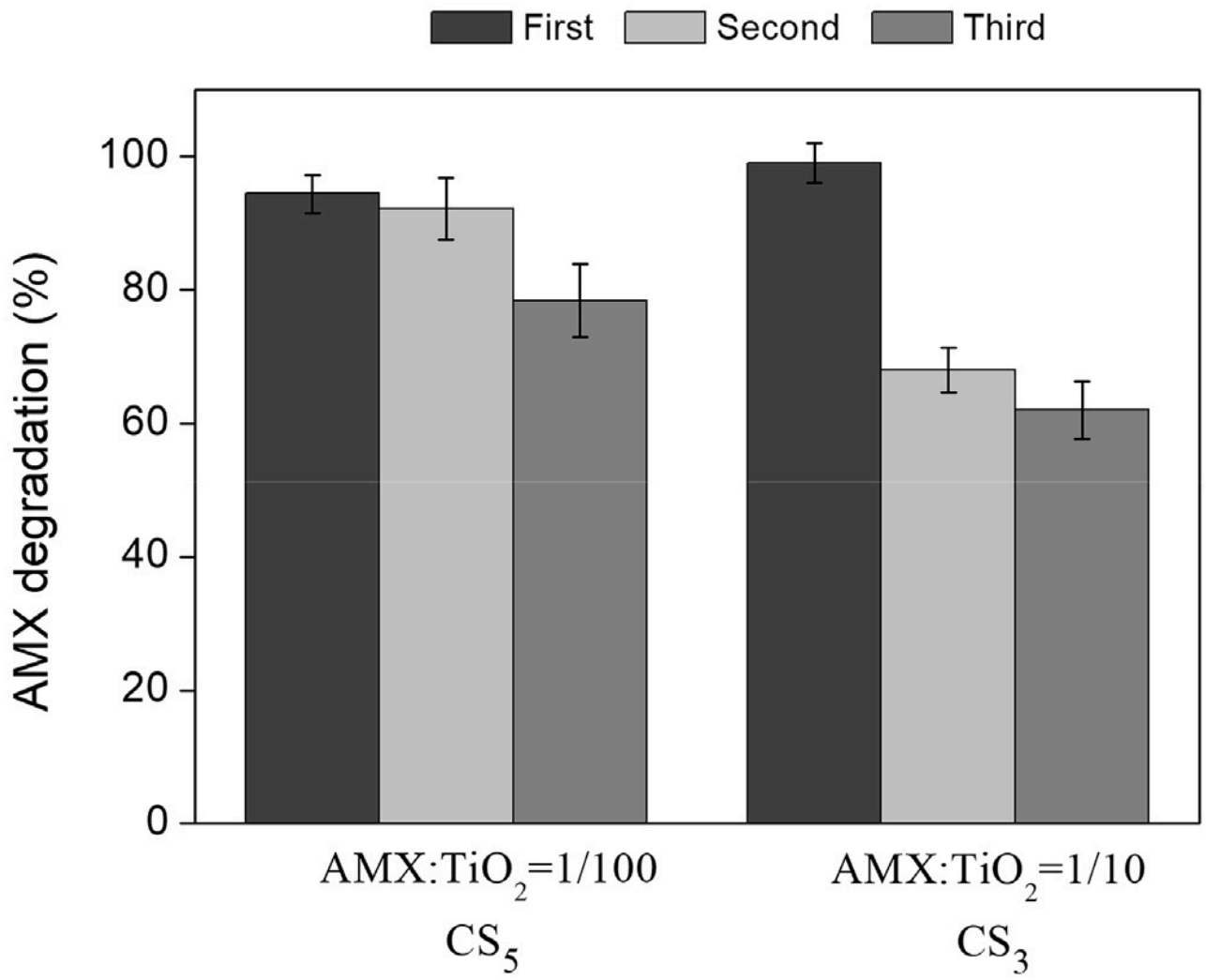

Fig. 8. AMX degradation percentage after three photodegradation cycles with CS_5 and CS_3.

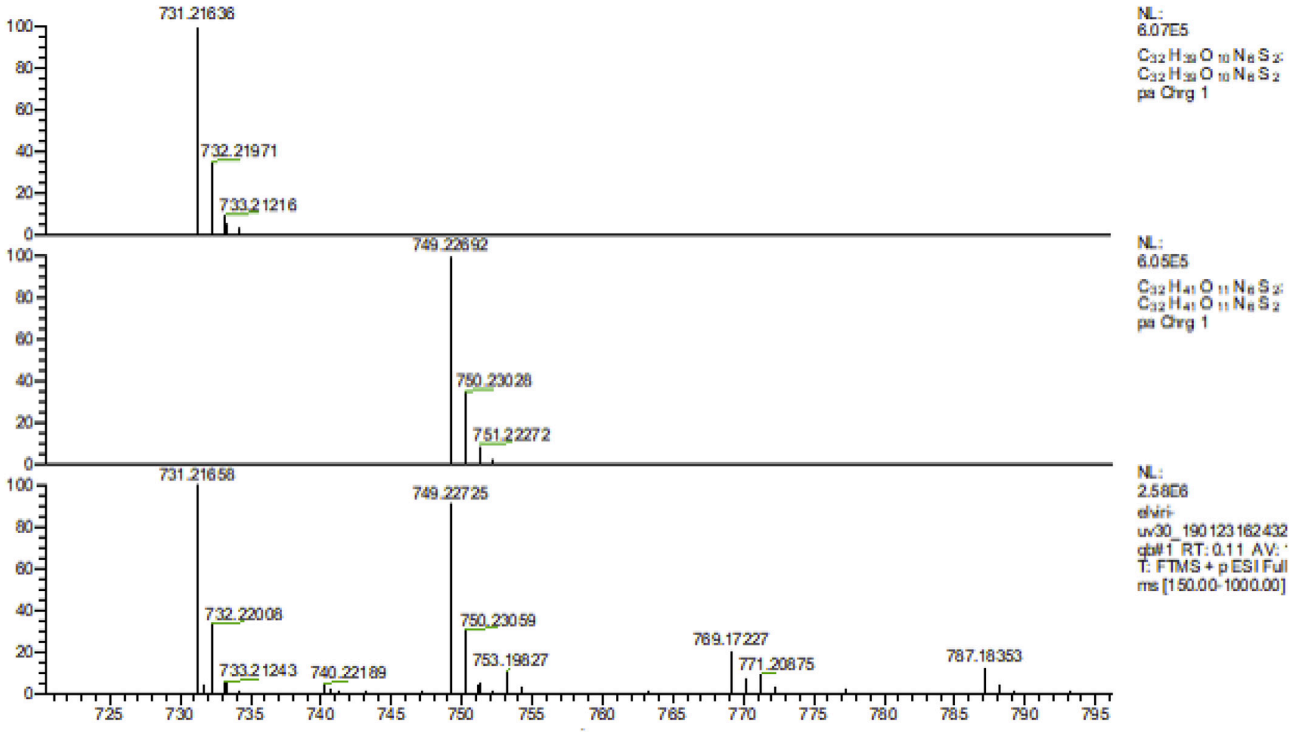

Fig. 9. MS full-scan spectrum showing amoxicillin dimers after 30 min of irradiation.

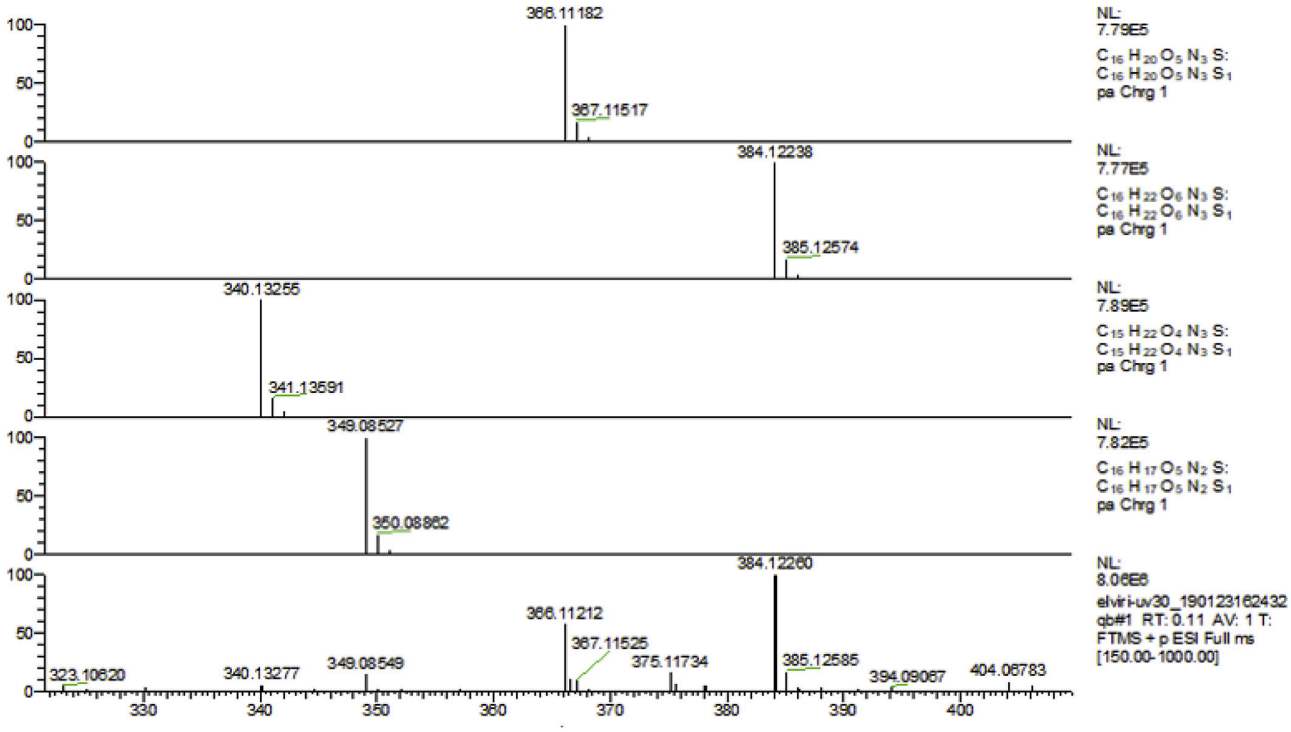

Fig. 10. MS full-scan spectra showing two AMX degradates in the sample at 180 min.

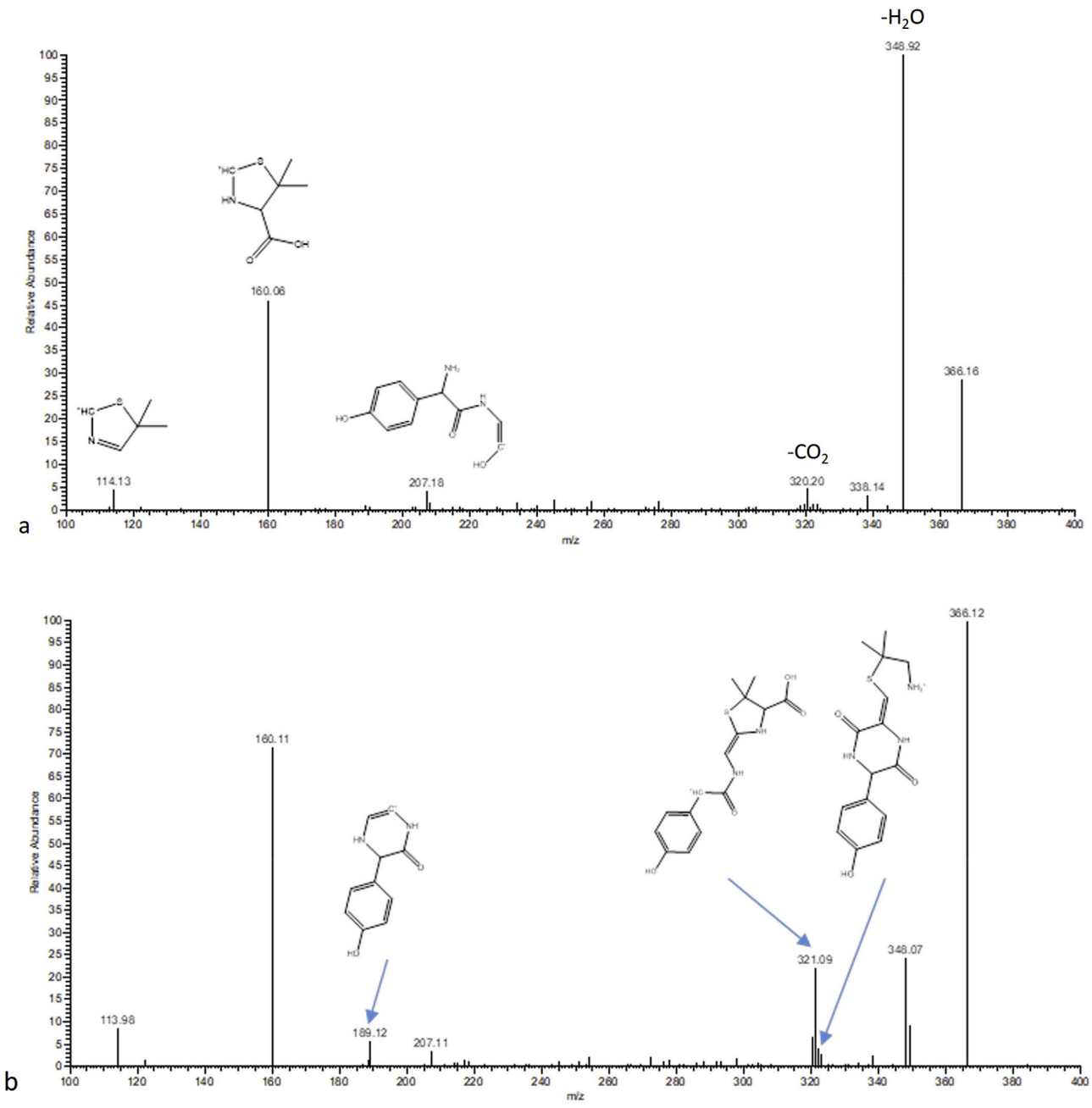

Fig. 11. MS/MS product-ion mass spectra of a standard solution (conc. 1 µg/ml) of AMX (a) and AMX with TiO_2/CS_5 scaffold (b) irradiated for 180 min showing the presence of diketopiperazine.

13.3.4 High resolution mass spectrometer analysis of AMX degradation products

High resolution mass spectrometry allowed to check the presence of amoxicillin and its degradation products. AMX/TiO_2/CS_5 analysed after 30 min of irradiation revealed the presence of amoxicillin dimers, both hydrated and not by a water molecule, at m/z values 749 and 731, respectively (Fig. 9). Amoxicillin penilloic acid (m/z 340) was also found, suggesting the beginning of a degradation pattern. After 180 min, dimers are no more present whereas three

types of degradation products were found: penilloic acid (m/z 340), penicilloic acid (m/z 384) and a product at m/z 366 that could correspond to the protonated molecular ion of AMX and/or its degradation product diketopiperazine (Fig. 10). The comparison made between the product-ion MS/MS mass spectrum of a standard solution of AMX and AMX/TiO_2/CS_5 irradiated for 180 min revealed the presence of the diketopiperazine degradate (Fig.11). In Fig. 11a the typical AMX fragmentation pattern is observed with m/z ions corresponding to the loss of a water molecule (m/z 348) and -CO_2 (m/z 320) and characteristic fragments at m/z 207, 160 and 114, respectively. The presence in Fig. 11b of the ion at m/z 189, attributable to phenol hydroxypyrazine, and the different relative intensity among ions strongly indicates the presence of the AMX degradation compound diketopiperazine (Gozlan *et al*., 2013; Lamm *et al*., 2009; Andreozzi *et al*., 2005).

13.4 Conclusions

Here the preparation and use of 3D printed chitosan-based scaffolds as support for the photocatalytic activity of TiO_2 in environmental wastewater treatment applications were investigated for the first time. The advantage of 3D printed scaffolds embedding TiO_2 is represented by the possibility of modulating their shape and size, thus offering a very high area/volume ratio, crucial parameter for amoxicillin photocatalysis. The availability of catalytic TiO_2 on scaffold surfaces allows to degrade large quantities of amoxicillin residues from wastewaters.

Moreover, three dimensional scaffolds can serve as fixing substrates for titanium dioxide, since their mechanical properties are suitable for handling, manipulation in the industrial environments and they might constitute a prototype of filters for cleaning water discharges. Degradation kinetics of AMX achieved using TiO_2/CS scaffolds is almost as fast as that obtained with pure TiO_2 powder, making them innovative tools, easy to produce in series and reusable for water purification from pollutants such as amoxicillin, having a positive impact on the environment rather than for drinking-water.

TiO_2 immobilized on 3D chitosan scaffold, characterized by good mechanical strength and elasticity, can be conveniently used for repeated photocatalytic applications making these objects suitable for green wastewaters cleaning systems improvement.

13.5 References

De Niederhãusern, S., Bondi, M., Bondioli, F., 2013. Self-cleaning and antibacteric ceramic tile surface. Int. J. Appl. Ceram. Technol. 10, 949e956. https://doi.org/10.1111/j.1744-7402.2012.02801.x.

Abazari, R., Mahjoub, A.R., 2018. Amine-functionalized Al-MOF#@yxSm2O3eZnO: a visible light-driven nanocomposite with excellent photocatalytic activity for the photo-degradation of amoxicillin. Inorg. Chem. 57, 2529-2545. https://doi.org/10.1021/acs.inorgchem.7b02880.

Andreozzi, R., Caprio, V., Ciniglia, C., De Champdore, M., Lo Giudice, R., Marotta, R., Zuccato, E., 2004. Antibiotics in the environment: occurrence in Italian STPs, fate, and preliminary assessment on algal toxicity of amoxicillin. Environ. Sci. Technol. 38, 6832-6838. https://doi.org/10.1021/es049509a.

Andreozzi, R., Canterino, M., Marotta, R., Paxeus, N., 2005. Antibiotic removal from wastewaters: the ozonation of amoxicillin. J. Hazard Mater. 122, 243-250. https://doi.org/10.1016/j.jhazmat.2005.03.004.

Arcanjo, G.S., Mounteer, A.H., Bellato, C.R., da Silva, L.M.M., Dias, S.H.B., da Silva, P.R., 2018. Heterogeneous photocatalysis using TiO_2 modified with hydrotalcite and iron oxide under UV-visible irradiation for color and toxicity reduction in secondary textile mill effluent. J. Environ. Manag. 211, 154-163. https://doi.org/ 10.1016/j.jenvman.2018.01.033.

Arce-Sarria, A., Machuca-Martínez, F., Bustillo-Lecompte, C., Hernandez-Ramírez, A., Colina-Márquez, J., 2018. Degradation and loss of antibacterial activity of commercial amoxicillin with TiO_2/WO_3-assisted solar photocatalysis. Catalysts 8, 222. https://doi.org/10.3390/catal8060222.

Awfa, D., Ateia, M., Fujii, M., Johnson, M.S., Yoshimura, C., 2018. Photodegradation of pharmaceuticals and personal care products in water treatment using carbonaceous-TiO_2 composites: a critical review of recent literature. Water Res. 142, 26-45. https://doi.org/10.1016/j.watres.2018.05.036.

Bergamonti, L., Alfieri, I., Lorenzi, A., Montenero, A., Predieri, G., Di Maggio, R., Girardi, F., Lazzarini, L., Lottici, P.P., 2015. Characterization and photocatalytic activity of TiO_2 by sol-gel in acid and basic environments. J. Sol. Gel Sci. Technol. 73, 91-102. https://doi.org/10.1007/s10971-014-3498-y.

Bergamonti, L., Predieri, G., Paz, Y., Fornasini, L., Lottici, P.P., Bondioli, F., 2017. Enhanced self-cleaning properties of N-doped TiO_2 coating for Cultural Heritage. Microchem. J. 133, 1-12. https://doi.org/10.1016/j.microc.2017.03.003.

Bergonzi, C., Di Natale, A., Zimetti, F., Marchi, C., Bianchera, A., Bernini, F., Silvestri, M., Bettini, R., Elviri, E., 2019. Study of 3D-printed chitosan scaffold features after different post-printing gelation processes. Sci. Rep.-UK. 23, 362-373. https://doi.org/10.1038/s41598-018-36613-8.

Bersani, D., Lottici, P.P., Ding, X.Z., 1998. Phonon confinement effects in the Raman scattering by TiO_2 nanocrystals. Appl. Phys. Lett. 72, 73-75. https://doi.org/10. 1063/1.120648.

Bjursten, L.M., Rasmusson, L., Oh, S., Smith, G.C., Brammer, K.S., Jin, S., 2010. Titanium dioxide nanotubes enhance bone bonding *in vivo*. J. Biomed. Mater. Res. A. 92A, 1218-1224. https://doi.org/10.1002/jbm.a.32463.

Cendrowski, K., Chen, X., Zielinska, B., Kalenczuk, R.J., Rümmeli, M.H., Büchner, B., Klingeler, R., Borowiak-Palen, E., 2011. Synthesis, characterization, and photocatalytic properties of core/shell mesoporous silica nanospheres supporting nanocrystalline titania. J. Nanopart. Res. 13, 5899-5908. https://doi.org/10. 1007/s11051-011-0307-1.

Chong, M.N., Jin, B., Chow, C.W.K., Saint, Chris, 2010. Recent developments in photocatalytic water treatment technology: a review. Water Res. 44, 2997-3027. https://doi.org/10.1016/j.watres.2010.02.039.

Colangiuli, D., Lettieri, M., Masieri, M., Calia, A., 2019. Field study in an urban environment of simultaneous self-cleaning and hydrophobic nanosized TiO_2-based coatings on stone for the protection of building surface. Sci. Total Environ. 650, 2919-2930. https://doi.org/10.1016/j.scitotenv.2018.10.044.

De Witte, B., van Langenhove, H., Demeestere, K., Dewulf, J., 2011. Advanced oxidation of pharmaceuticals: chemical analysis and biological assessment of degradation products. Crit. Rev. Environ. Sci. Technol. 41, 215-242. https://doi. org/10.1080/10643380902728698.

Deblonde, T., Cossu-Leguille, C., Hartemann, P., 2011. Emerging pollutants in wastewater: a review of the literature. Int. J. Hyg Environ. Health 214, 442-448. https://doi.org/10.1016/j.ijheh.2011.08.002.

Di Paola, A., Bellardita, M., Palmisano, L., 2013. Brookite, the least known TiO2 photocatalyst. Catalysts 3, 36-73. https://doi.org/10.3390/catal3010036.

Dimitrakopoulou, D., Rethemiotaki, I., Frontistis, Z., Xekoukoulotakis, N.P., Venieri, D., Mantzavinos, D., 2012. Degradation, mineralization and antibiotic inactivation of amoxicillin by UV-A/TiO2 photocatalysis. J. Environ. Manag. 98, 168-174. https://doi.org/10.1016/j.jenvman.2012.01.010.

Do, A.-V., Khorsand, B., Geary, S.M., Salem, A.K., 2015. 3D printing of scaffolds for tissue regeneration applications. Adv. Healthc. Mater. 4, 1742-1762. https://doi. org/10.1002/adhm.201500168.

Elhahil, A., Elmoubarki, R., Sadiq, M., Abdennouri, M., Kadmi, Y., Favier, L., Qourzal, S., Barka, N., 2017. Enhanced photocatalytic degradation of caffeine as a model pharmaceutical pollutant by Ag-ZnO-Al_2O_3 nanocomposite. Desalin. Water. Treat. 94, 254-262. https://doi.org/10.5004/dwt.2017.21587.

Elmolla, E.S., Chaudhuri, M., 2010. Photocatalytic degradation of amoxicillin, ampicillin and cloxacillin antibiotics in aqueous solution using UV/TiO_2 and UV/H_2O_2/TiO_2 photocatalysis. Desalination 252, 46-52. https://doi.org/10.1016/j. desal.2009.11.003.

Elmolla, E.S., Chaudhuri, M., 2010. Comparison of different advanced oxidation processes for treatment of antibiotic aqueous solution. Desalination 256, 43-47. https://doi.org/10.1016/j.desal.2010.02.019.

Elviri, L., Asadzadeh, M., Cucinelli, R., Bianchera, A., Bettini, R., 2014. Macroporous chitosan hydrogels: effect of sulfur on the loading and release behaviour of amino-acid based compounds. Carbohyd. Polym 132, 50-58. https://doi.org/10. 1016/j.carbpol.2015.06.048.

Elviri, L., Bianchera, A., Bergonzi, C., Bettini, R., 2016. Controlled local drug delivery strategies from chitosan hydrogels for wound healing Expert Opin. Drug Deliv. 14, 897-908. https://doi.org/10.1080/17425247.2017.1247803.

Elviri, L., Foresti, R., Bergonzi, C., Zimetti, F., Marchi, C., Bianchera, A.a, Bernini, F., Silvestri, M., Bettini, R., 2017. Highly defined 3D printed chitosan scaffolds featuring improved cell growth. Biomed. Mater. 12, 045009. https://doi.org/10. 1088/1748-605X/aa7692.

Evans, P., Sheel, D.W., 2007. Photoactive and antibacterial TiO_2 thin films on stainless steel. Surf. Coating. Technol. 201, 9319-9324. https://doi.org/10.1016/j. surfcoat.2007.04.013.

Favier, L., Simion, A.I., Matei, E., Grigoras, C.-G., Kadmi, I., Bouzaza, A., 2016. Photocatalytic oxidation of a hazardous phenolic compound over TiO_2 in a batch system. Environ. Eng. Manag. J. 15, 1059-1067. https://doi.org/10.30638/eemj. 2016.117.

Figueira, V., Vaz-Moreira, I., Silva, M., Manaia, C.M., 2011. Diversity and antibiotic resistance of Aeromonas spp. in drinking and waste water treatment plants. Water Res. 45, 5599-5611. https://doi.org/10.1016/j.watres.2011.08.021.

Fujishima, A., Zhang, X., Tryk, D.A., 2008. TiO_2 photocatalysis and related surface phenomena. Surf. Sci. Rep. 63, 515-582. https://doi.org/10.1016/j.surfrep.2008. 10.001.

Galli, C., Parisi, L., Elviri, L., Bianchera, A., Smerieri, A., Lagonegro, P., Lumetti, S., Manfredi, E., Bettini, R., Macaluso, G.M., 2016. Chitosan scaffold modified with D-(þ) raffinose and

enriched with thiol-modified gelatin for improved osteoblast adhesion. Biomed. Mater. 11, 015004. https://doi.org/10.1088/1748-6041/11/ 1/015004.

Ganiyu, S.O., Oturan, N., Raffy, S., Cretin, M., Esmilaire, R., van Hullebusch, E., Esposito, G., Oturan, M.A., 2016. Sub-stoichiometric titanium oxide (Ti_4O_7) as a suitable ceramic anode for electrooxidation of organic pollutants: a case study of kinetics, mineralization and toxicity assessment of amoxicillin. Water Res. 106, 171-182. https://doi.org/10.1016/j.watres.2016.09.056.

Garcia-Reiriz, A., Damiani, P.C., Olivieri, A.C., 2007. Different strategies for the direct determination of amoxicillin in human urine by second-order multivariate analysis of kinetic-spectrophotometric data. Talanta 71, 806-815. https://doi. org/10.1016/j.talanta.2006.05.050.

Githinji, L.J.M., Musey, M.K., Ankumah, R.O., 2011. Evaluation of the fate of ciprofloxacin and amoxicillin in domestic wastewater. Water. Air. Soil. Pollut. 219, 191-201. https://doi.org/10.1007/s11270-010-0697-1.

Gogoi, A., Mazumder, P., Tyagi, V.K., Chaminda, G.G.T., An, A.K., Kumar, M., 2018. Occurrence and fate of emerging contaminants in water environment: a review.

Groundw. Sustain. Dev. 6, 169-180. https://doi.org/10.1016/j.gsd.2017.12.009. Gong, J., Liang, J., Sumathy, K., 2012. Review on dye-sensitized solar cells (DSSCs): fundamental concepts and novel materials. Renew. Sustain. Energy Rev. 16, 5848-5860. https://doi.org/10.1016/j.rser.2012.04.044.

Goy, R.C., de Britto, D., Assis, O.B.G., 2009. A review of the antimicrobial activity of chitosan. Polímeros 19, 241e247. https://doi.org/10.1590/S0104-14282009000300013.

Gozlan, I., Rotstein, A., Avisar, D., 2013. Amoxicillin-degradation products formed under controlled environmental conditions: identification and determination in the aquatic environment. Chemosphere 91, 985e992. https://doi.org/10.1016/j. chemosphere.2013.01.095.

Gros, M., Petrović, M., Ginebreda, A., Barcelò, D., 2010. Removal of pharmaceuticals during wastewater treatment and environmental risk assessment using hazard indices. Environ. Int. 36, 15-26. https://doi.org/10.1016/j.envint.2009.09.002.

Hashimoto, K., Irie, H., Fujishima, A., 2005. TiO_2 photocatalysis: a historical overview and future prospects. Jpn. J. Appl. Phys. 44, 8269-8285. https://doi.org/10.1143/JJAP.44.8269.

Herrmann, J.-M., 1999. Heterogeneous photocatalysis: fundamentals and applications to the removal of various types of aqueous pollutants. Catal. Today 53, 115-129. https://doi.org/10.1016/S0920-5861(99)00107-8.

Homem, V., Santos, L., 2011. Degradation and removal methods of antibiotics from aqueous matrices e A review. J. Environ. Manag. 92, 2304-2347. https://doi.org/10.1016/j.jenvman.2011.05.023.

Hurum, D.C., Agrios, A.G., Gray, K.A., Rajh, T., Thurnauer, M.C., 2003. Explaining the enhanced photocatalytic activity of Degussa P25 mixed-phase TiO_2 using EPR. J. Phys. Chem. B 107, 4545-4549. https://doi.org/10.1021/jp0273934.

Kanakaraju, D., Kockler, J., Motti, C.A., Glass, B.D., Oelgemöller, M., 2015. Titanium dioxide/zeolite integrated photocatalytic adsorbents for the degradation of amoxicillin. Appl. Catal. B Environ. 166-167, 45e55. https://doi.org/10.1016/j.apcatb.2014.11.001.

Kanakaraju, D., Glass, B.D., Oelgemöller, M., 2018. Advanced oxidation process mediated removal of pharmaceuticals from water: a review. J. Environ. Manag. 219, 189-207. https://doi.org/10.1016/j.jenvman.2018.04.103.

Karthikeyan, K.T., Nithya, A., Jothivenkatachalam, K., 2017. Photocatalytic and antimicrobial activities of chitosan-TiO_2 nanocomposite. Int. J. Biol. Macromol. 104, 1762-1773. https://doi.org/10.1016/j.ijbiomac.2017.03.121.

Klauson, D., Babkina, J., Stepanova, K., Krichevskaya, M., Preis, S., 2010. Aqueous photocatalytic oxidation of amoxicillin. Catal. Today 151, 39-45. https://doi.org/10.1016/j.cattod.2010.01.015.

Lamm, A., Gozlan, I., Rotstein, A., Avisar, D., 2009. Detection of amoxicillin-diketopiperazine-2', 5' in wastewater samples. J. Environ. Sci. Health A 44, 1512-1517. https://doi.org/10.1080/10934520903263306.

Leong, S., Razmjou, A., Wang, K., Hapgood, K., Zhang, X., Wang, H., 2014. TiO_2 based photocatalytic membranes: a review. J. Membr. Sci. 472, 167-184. https://doi.org/10.1016/j.memsci.2014.08.016.

Li, W.C., 2014. Occurrence, sources, and fate of pharmaceuticals in aquatic environment and soil. Environ. Pollut. 187, 193-201. https://doi.org/10.1016/j.envpol.2014.01.015.

Li, X., Shen, T., Huang, D., Yue, X., Liu, X., Yang, Q., Cao, J., Zheng, W., Zeng, G., 2012. Photodegradation of amoxicillin by catalyzed Fe^{3+}/H_2O_2 process. J. Environ. Sci. 24, 269-275. https://doi.org/10.1016/S1001-0742(11)60765-1.

Li, D., Zhua, Q., Hana, C., Yanga, Y., Jiang, W., Zhanga, Z., 2015. Photocatalytic degradation of recalcitrant organic pollutants in water using a novel cylindrical multi-column photoreactor packed with TiO_2-coated silica gel beads. J. Hazard Mater. 285, 398-408. https://doi.org/10.1016/j.jhazmat.2014.12.024.

Li, Q., Jia, R., Shao, J., He, Y., 2019. Photocatalytic degradation of amoxicillin via TiO_2 nanoparticle coupling with a novel submerged porous ceramic membrane reactor. J. Clean. Prod. 209, 755-761. https://doi.org/10.1016/j.jclepro.2018.10.183.

Linsebigler, A.L., Lu, G., Yates Jr., J.T., 1995. Photocatalysis on TiO_2 surfaces: principles, mechanisms, and selected results. Chem. Rev. 95, 735-758. https://doi.org/10.1021/cr00035a013.

Luna, M., Delgado, J.J., Gil, M.L.A., Mosquera, M.J., 2018. TiO_2-SiO_2 coatings with a low content of AuNPs for producing self-cleaning building materials. Nanomaterials 8, 177-203. https://doi.org/10.3390/nano8030177.

Manaia, C., Rocha, J., Scaccia, N., Marano, R., Radud, E., Biancullo, B., Cerqueira, Fortunato, G., Iakovides, I.C., Zammit, I., Kampourius, I., Vaz-Moreira, I., Nunes, O.C., 2018. Antibiotic resistance in wastewater treatment plants: tackling the black box. Environ. Int. 115, 312-324. https://doi.org/10.1016/j.envint.2018.03.044.

McCullagh, C., Robertson, P.K.J., Adams, M., Pollard, P.M., Mohammed, A., 2010. Development of a slurry continuous flow reactor for photocatalytic treatment of industrial waste water. J. Photochem. Photobiol., A 211, 42-46. https://doi.org/10.1016/j.jphotochem.2010.01.020.

Miklos, D.B., Remy, C., Jekel, M., Linden, K.G., Drewes, J.E., Hübner, U., 2018. Evaluation of advanced oxidation processes for water and wastewater treatment – A critical review. Water Res. 139, 118-131. https://doi.org/10.1016/j.watres.2018.03.042.

Mo, J., Zhang, Y., Xu, Qiujian, Lamson, J.J., Zhao, R., 2009. Photocatalytic purification of volatile organic compounds in indoor air: a literature review. Atmos. Environ. 43, 2229-2246. https://doi.org/10.1016/j.atmosenv.2009.01.034.

Moreira, N.F.F., Orge, C.A., Ribeiro, A.R., Faria, J.L., Nunes, Olga, C., Pereira, M.F.R., Silva, A.M.T., 2015. Fast mineralization and detoxification of amoxicillin and diclofenac by photocatalytic ozonation and application to an urban wastewater. Water Res. 87, 87-96. https://doi.org/10.1016/j.watres.2015.08.059.

Mozia, S., 2010. Photocatalytic membrane reactors (PMRs) in water and wastewater treatment. A review. Sep. Purif. Technol. 73, 71-91. https://doi.org/10.1016/j.seppur.2010.03.021.

Murugan, K., Subasri, R., Rao, T.N., Gandhi, A.S., Murty, B.S., 2013. Synthesis, characterization and demonstration of self-cleaning TiO_2 coatings on glass and glazed ceramic tiles. Prog. Org. Coating 76, 1756-1760. https://doi.org/10.1016/j.porgcoat.2013.05.012.

Nawi, M.A., Sabar, S., Jawad, A.H., Sheilatina, Wan Ngah, W.S., 2009. Adsorption of Reactive Red 4 by immobilized chitosan on glass plates: towards the design of immobilized TiO_2-chitosan synergistic photocatalyst-adsorption bilayer system.

Biochem. Eng. J. 49, 317-325. https://doi.org/10.1016/j.bej.2010.01.006. Nishad, P.A., Bhaskarapillai, A., Velmurugan, S., 2014. Nano-titania-crosslinked chitosan composite as a superior sorbent for antimony (III) and (V). Carbohydr. Polym. 108, 169-175. https://doi.org/10.1016/j.carbpol.2014.02.091.

O'Regan, B., Grätzel, M., 1991. A low-cost, high-efficiency solar cell based on dyesensitized colloidal TiO_2 films. Nature 353, 737-740. https://doi.org/10.1038/353737a0.

Ohno, T., Sarukawa, K., Tokieda, K., Matsumura, M., 2001. Morphology of a TiO_2 photocatalyst (Degussa, P-25) consisting of anatase and rutile crystalline phases. J. Catal. 203, 82-86. https://doi.org/10.1006/jcat.2001.3316.

Olama, N., Dehghani, M., Malakootlan, M., 2018. The removal of amoxicillin from aquatic solutions using the TiO_2/UV-C nanophotocatalytic method doped with trivalent iron. Appl. Water Sci. 8, 97. https://doi.org/10.1007/s13201-018-0733-7.

Osorio, V., Marcè, R., Pèrez, S., Ginebreda, A., Cortina, J.L., Barcelò, D., 2012. Occurrence and modeling of pharmaceuticals on a sewage-impacted Mediterranean river and their dynamics under different hydrological conditions. Sci. Total Environ. 440, 3-13. https://doi.org/10.1016/j.scitotenv.2012.08.040.

Ounnar, A., Favier, L., Bouzaza, A., Bentahar, F., Trari, M., 2016. Kinetic study of spiramycin removal from aqueous solution using heterogeneous photocatalysis. Kinet. Catal. 57, 200-206. https://doi.org/10.1134/S0023158416020087.

Palmisano, R., Campanella, L., Ambrosetti, B., 2015. Photo-degradation of amoxicillin, streptomycin, erythromycin and ciprofloxacin by UV and UV/TiO_2 processes. Evaluation of toxicity changes using a respirometric biosensor.

J. Environ. Anal. Chem. 2, 10000143. https://doi.org/10.4172/jreac.1000143. Petrie, P., Barden, R., Kasprzyk-Hordern, B., 2015. A review on emerging contaminants in wastewaters and the environment: current knowledge, understudied areas and recommendations for future monitoring.Water Res. 72, 3-27. https://doi.org/10.1016/j.watres.2014.08.053.

Pigeot-Rèmy, S., Gregori, D., Hazime, R., Hèrissan, A., Guillard, C., Ferronato, C., Cassaignon, S., Colbeau-Justin, C., Durupthy, O., 2019. Size and shape effect on the photocatalytic efficiency of TiO2 brookite. J. Mater. Sci. 54, 1213. https://doi.org/10.1007/s10853-018-2924-x.

Pinho, L., Rojas, M., Mosquera, M.J., 2015. AgeSiO2-TiO2 nanocomposite coatings with enhanced photoactivity for self-cleaning application on building materials. Appl. Catal. B Environ. 178, 144-154. https://doi.org/10.1016/j.apcatb.2014.10.002.

Proia, L., Anzil, A., Subirats, J., Borrego, C., Farrè, M., Llorca, M., Balcazar, J.L., Servais, P., 2018. Antibiotic resistance in urban and hospital wastewaters and their impact on a receiving

freshwater ecosystem. Chemosphere 206, 70-82.https://doi.org/10.1016/j.chemosphere.2018.04.163.

Radosavljević, K.D., Golubović, A.V., Radišić, M.M., Mladenović, A.R., Mijin, D.Z., Petrovic, S.D., 2017. Amoxicillin photodegradation by nanocrystalline TiO_2. Chem. Ind. Chem. Eng. Q. 23, 187-195. https://doi.org/10.2298/CICEQ160122030R.

Rinaudo, M., 2006. Chitin and chitosan: properties and applications. Prog. Polym. Sci. 31, 603-632. https://doi.org/10.1016/j.progpolymsci.2006.06.001.

Rizzo, L., Merica, S., Guida, M., Kassinos, D., Belgiorno, V., 2009. Heterogenous photocatalytic degradation kinetics and detoxification of an urban wastewater treatment plant effluent contaminated with pharmaceuticals. Water Res. 43, 4070-4078. https://doi.org/10.1016/j.watres.2009.06.046.

Santos, L.H.M.L.M., Araújo, A.N., Fachini, A., Pena, A., Delerue-Matos, C., Montenegro, M.C.B.S.M., 2010. Ecotoxicological aspects related to the presence of pharmaceuticals in the aquatic environment. J. Hazard Mater. 175, 4595.

https://doi.org/10.1016/j.jhazmat.2009.10.100. Schneider, J., Matsuoka, M., Takeuchi, M., Zhang, J., Horiuchi, Y., Anpo, M., Bahnemann, D.W., 2014. Understanding TiO_2 photocatalysis: mechanisms and materials. Chem. Rev. 114, 9919-9986. https://doi.org/10.1021/cr5001892.

Schulze, S., Zahn, D., Montes, R., Rodil, R., Quintana, J.B., Knepper, T.P., Reemtsma, T., Berger, U., 2019. Occurrence of emerging persistent and mobile organic contaminants in european water samples. Water Res. 153, 80-90. https://doi.org/10.1016/j.watres.2019.01.008.

Sciancalepore, C., Manfredini, T., Bondioli, F., 2014. Antibacterial and self-cleaning coatings for silicate ceramics: a review. Adv. Sci. Technol. 92, 90-99. https://doi.org/10.4028/www.scientific.net/AST.92.90.

Semwal, A., Singh, R., Dutta, P.K., 2013. Chitosan: a promising substrate for pharmaceuticals. J. Chitin and Chitosan Science 1, 87-102. https://doi.org/10.1166/jcc.2013.1012.

Shayegan, Z., Lee, C.-S., Haghighat, F., 2018. TiO_2 photocatalyst for removal of volatile organic compounds in gas phase e a review. 2018. Chem. Eng. J. 334, 2408-2439. https://doi.org/10.1016/j.cej.2017.09.153.

Siripatrawan, U., Kaewklin, P., 2018. Fabrication and characterization of chitosan-titanium dioxide nanocomposite film as ethylene scavenging and antimicrobial active food packaging. Food Hydrocolloids 84, 125-134. https://doi.org/10.1016/j.foodhyd.2018.04.049.

Sousa, J.C.G., Ribeiro, A.R., Barbosa, M.O., Fernando, M., Pereira, R., Silva, A.M.T., 2018. A review on environmental monitoring of water organic pollutants identified by EU guidelines. J. Hazard Mater. 344, 146-162. https://doi.org/10. 1016/j.jhazmat.2017.09.058.

Stackelberg, P.E., Furlong, E.T., Meyer, M.T., Zaugg, S.D., Henderson, A.K., Reissman, D.B., 2004. Persistence of pharmaceutical compounds and other organic wastewater contaminants in a conventional drinking-water treatment plant. Sci. Total Environ. 329, 99-113. https://doi.org/10.1016/j.scitotenv.2004.03.015.

Suwanchawalit, C., Patil, A.J., Kumar, R.K.,Wongnawa, S., Mann, S., 2009. Fabrication of ice-templated macroporous TiO_2echitosan scaffolds for photocatalytic applications. J. Mater. Chem. 19, 8478-8483. https://doi.org/10.1039/B912698H.

Sykaras, N., Iacopino, A.M., Marker, V.A., Triplett, R.G., Woody, R.D., 2000. Implant materials, designs, and surface topographies: their effect on osseointegration. A literature review. Int. J. Oral Maxillofac. Implant. 15, 675-690.

Taheran, M., Naghdi, M., Brar, S.K., Verma, M., Surampalli, R.Y., 2018. Emerging contaminants: here today, there tomorrow! Environ. Nanotechnol. Monit. Manag. 10, 122-126. https://doi.org/10.1016/j.enmm.2018.05.010.

Thomas, A.G., Syres, K.L., 2012. Adsorption of organic molecules on rutile TiO_2 and anatase TiO_2 single crystal surfaces. Chem. Soc. Rev. 41, 4207-4217. https://doi.org/10.1039/C2CS35057B.

Tong, A.Y.C., Braund, R., Warren, D.S., Peake, B.M., 2012. TiO_2-assisted photodegradation of pharmaceuticals e a review. Cent. Eur. J. Chem. 10, 989-1027. https://doi.org/10.2478/s11532-012-0049-7.

Tousova, Z., Oswald, P., Slobodnik, J., Blaha, L., Muz, M., Hu, M., Brack,W., Krauss, M., Di Paolo, C., Tarcai, Z., Seiler, T.B., Hollert, H., Koprivica, S., Ahel, M., Schollee, J.E., Hollender, J., Suter, M.J., Hidasi, A.O., Schirmer, K., Sonavane, M., Ait-Aissa, S., Creusot, N., Brion, F., Froment, J., Almeida, A.C., Thomas, K., Tollefsen, K.E., Tufi, S., Ouyang, X., Leonards, P., Lamoree, M., Torrens, V.O., Kolkman, A., Schriks, M., Spirhanzlova, P., Tindall, A., Schulze, T., 2017. European demonstration program on the effect-based and chemical identification and monitoring of organic pollutants in European surface waters. Sci. Total Environ. 601, 1849-1868. https://doi.org/10.1016/j.scitotenv.2017.06.032.

Trovó, A.G., Melo, S.A.S., Nogueira, R.F.P., 2008. Photodegradation of the pharmaceuticals amoxicillin, bezafibrate and paracetamol by the photo-Fenton processed-application to sewage treatment plant effluent. J. Photochem. Photobiol., A 198, 215-220. https://doi.org/10.1016/j.jphotochem.2008.03.011.

Verma, M., Haritash, A.K., 2019. Degradation of amoxicillin by Fenton and Fenton-integrated hybrid oxidation processes. J. Environ. Chem. Eng. 7, 102886. https://doi.org/10.1016/j.jece.2019.102886.

Wang, X., Wei, C., Cao, B., Jiang, L., Hou, Y., Chang, J., 2018. Fabrication of multiple layered hydrogel scaffolds with elaborate structure and good mechanical properties via 3D printing and ionic reinforcement. Appl. Mater. Interfaces 10, 18338-18350. https://doi.org/10.1021/acsami.8b04116.

Watkinson, A.J., Murby, E.J., Kolpin, D.W., Costanzo, S.D., 2009. The occurrence of antibiotics in an urban watershed: from wastewater to drinking water. Sci. Total Environ. 407, 2711-2723. https://doi.org/10.1016/j.scitotenv.2008.11.059.

Yi, X., Lin, C., Ong, E.J.L., Wang, M., Zhou, Z., 2019. Occurrence and distribution of trace levels of antibiotics in surface waters and soils driven by non-point source pollution and anthropogenic pressure. Chemosphere 216, 213-223. https://doi.org/10.1016/j.chemosphere.2018.10.087.

Zangeneh, H., Zinatizadeh, A.A.L., Habibi, M., Akia, M., Hasnain Isa, M., 2015. Photocatalytic oxidation of organic dyes and pollutants in wastewater using different modified titanium dioxides: a comparative review. J. Ind. Eng. Chem. 26, 1-362. https://doi.org/10.1016/j.jiec.2014.10.043.

Zhang, H., Banfield, J.F., 2000. Understanding polymorphic phase transformation behavior during growth of nanocrystalline aggregates: insights from TiO_2. J. Phys. Chem. B 104, 3481-3487. https://doi.org/10.1021/jp000499j.

14 Gamma rays hydrogel sterilization

As mentioned in the section 3.5, hydrogel scaffolds sterilization through gamma rays (ϒ rays) was investigated as potential industrial procedure.
In particular chitosan-based hydrogel scaffolds were chosen as a model; relevant literature concerning the topic reported the treatment of hydrogel chitosan membranes intended as wound dressings[1].
The conditions tested were:

- Not-treated scaffolds: Stored in De Ionized (DI) water after washing at 4 °C.
- Scaffold sterilized under UV gamma rays at 2 KGy.

The features of chitosan scaffolds before and after sterilization that were investigated were:

- Micro-porosity (SEM analysis and respective computational image analysis through ImageJ software (NIH, Bethesda, MD,USA)) in terms of interconnectivity and pore size distribution at the surface and in the cross section.
- Water content (gravimetric analysis)
- Mechanical properties (force applied at break and Young's modulus)
- ATR FT-IR spectra comparison: raw material (Chitosan ChitoClearTM (CAS 9012-76-4, degree of deacetylation 95%; molecular weight by gel permeation chromatography 150–200 kDa; allergen free, water insoluble, soluble in acid media; PRIMEX Ehf Siglufjordur, Iceland) versus chitosan NOT-treated scaffold versus those "sterilized" by means of ethanol and gamma rays.
- Total bacterial load

14.1 Experimental and results

14.1.1 SEM/imageJ analysis

Samples consisted of 20 layers chitosan hydrogel scaffolds, with 200 μm thick filaments and macro-pores of the same dimension (see chapter 1). Dehydration procedure was carried out by freeze-drying with a Alpha 2–4 LCS Plus lyophylizer (Martin Christ, Osterode am Harz, Germany) over 24 h. Dried samples were mounted on aluminium stubs and metallized (Balzers) to cover scaffolds with a 60 nm gold film. Samples were then observed with a Philips SEM501.

The only scaffold types compared in this analysis were chitosan NOT-treated scaffolds and those irradiated, since scaffolds disinfected with ethanol were studied in these terms in previous works (chapter 1, 3)

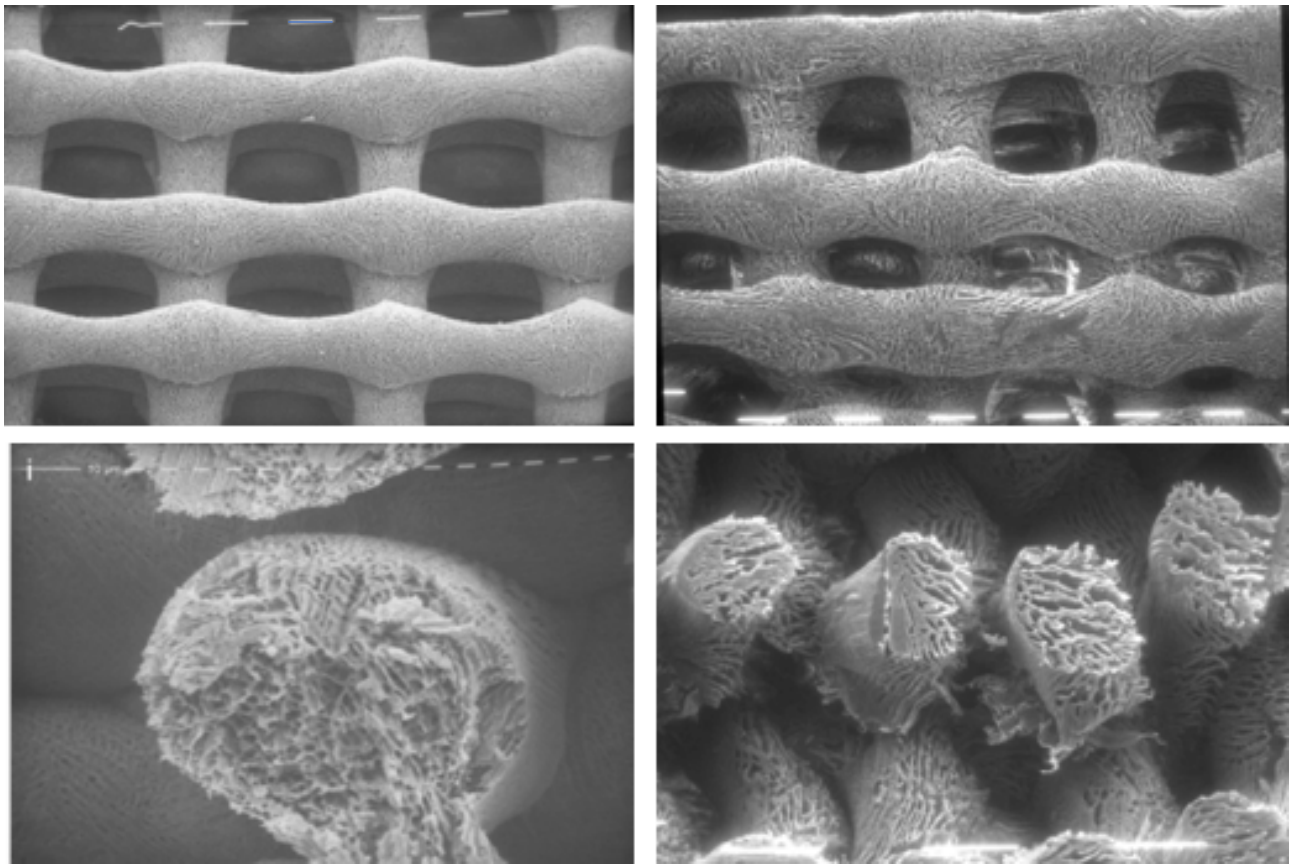

Fig. 1. Images on the left side: (Scale bar: 100 and 10 µm, respectively) Not irradiated scaffolds; Images on the right side: (Scale bar: 100 µm) irradiated scaffolds

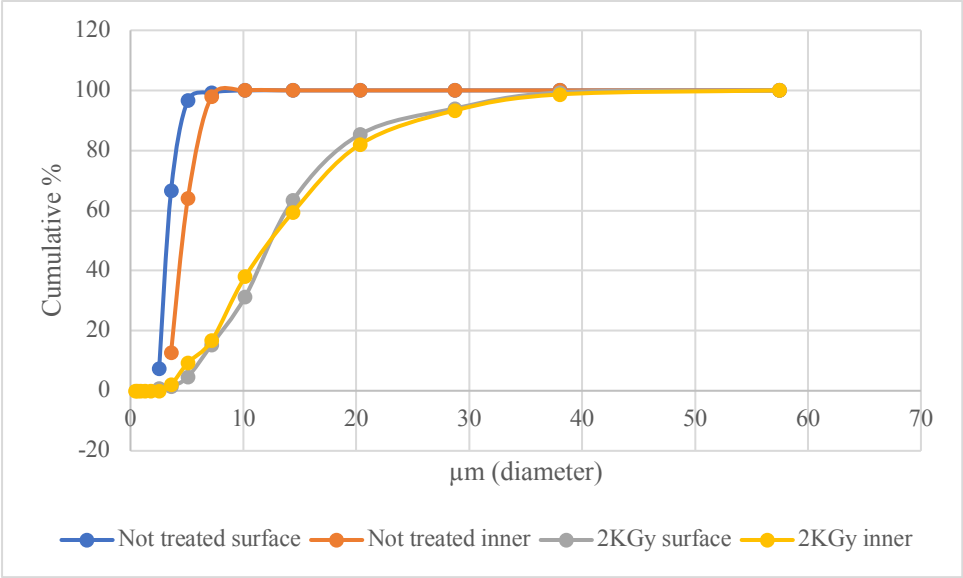

Fig. 2. Cumulative graph representing pore size distributions

SEM images, as appreciable from figure 1 and figure 2, show that average pore size of irradiated scaffold is significantly bigger both in the cross section and in the surface area.
On the contrary, the overall macro-morphology of the compared scaffolds remained unchanged, further investigations will be addressed *in vitro* to evaluate human fibroblast/keratinocytes biological behavior.

14.1.2 Water content determination

Percent water content was measure through the following formula: 100-(100 x Dw)/Ww; where "Dw" stands for "dry weight" and "Ww" for "wet weight".
NOT treated samples, as measured in previous works (chapter 1, 2, 3), had a value of 92,77 ± 1,17, irradiated ones had a value of 93,18 ± 0,56, indicating that water content did not significantly change and that the value is independent from porosity characteristics.

14.1.3 Mechanical properties

A tractional dynamometer (Acquati, Italy) has been used to evaluate the mechanical strength of the 3D printed scaffolds, calculated as Young's elastic modulus (E). Scaffold sizes were 20 layers×5 cm×1.5 cm. The traction tests were performed by setting the following parameters: pre-fixed distance between clips ± 25 mm, traction speed 25mmmin^{-1}, 5 DaN top head.
In figure 3 the comparison between NOT treated and irradiated scaffolds is shown

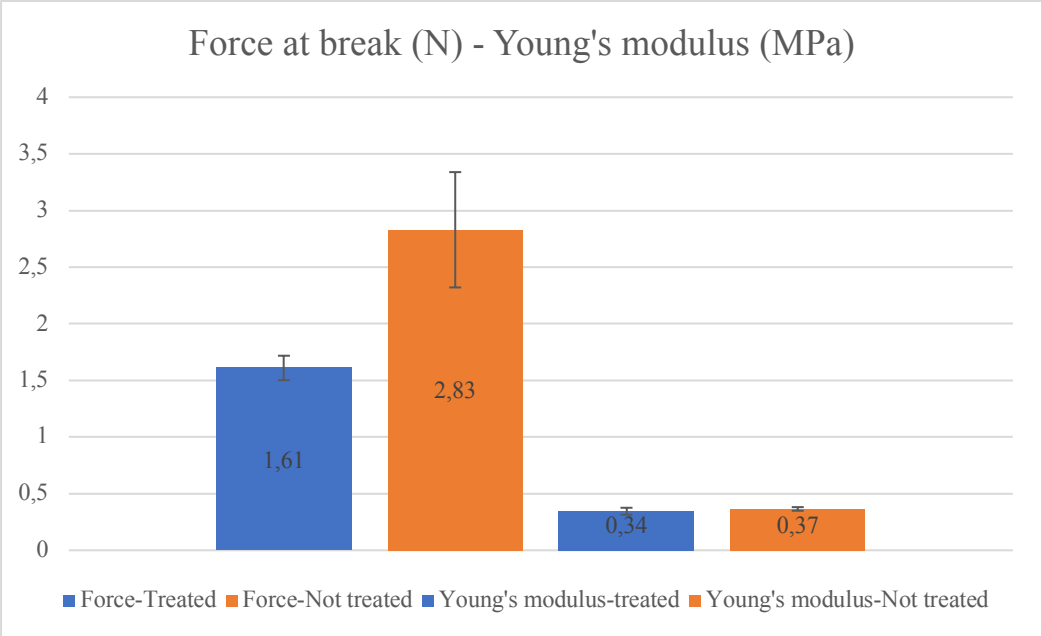

Fig. 3. Comparison between NOT-treated and irradiated scaffolds

As deducible from the histograms, Young's modulus is totally comparable since the values do not differ from each other, that means elasticity is not compromised at all.
On the other hand, force at break is significantly different, indicating that the mechanical tensile resistance of irradiated scaffolds is reduced by ~ 43 %.

14.1.4 ATR FT-IR spectra comparison

IR analysis were performed by a Nicolet 5700 (Thermo Scientific, USA) in the range 400–4000 wavenumbers (cm^{-1}) with a resolution of 30 scan per second. Scaffolds were beforehand dehydrated in oven at 40 °C till constant weight was attained.

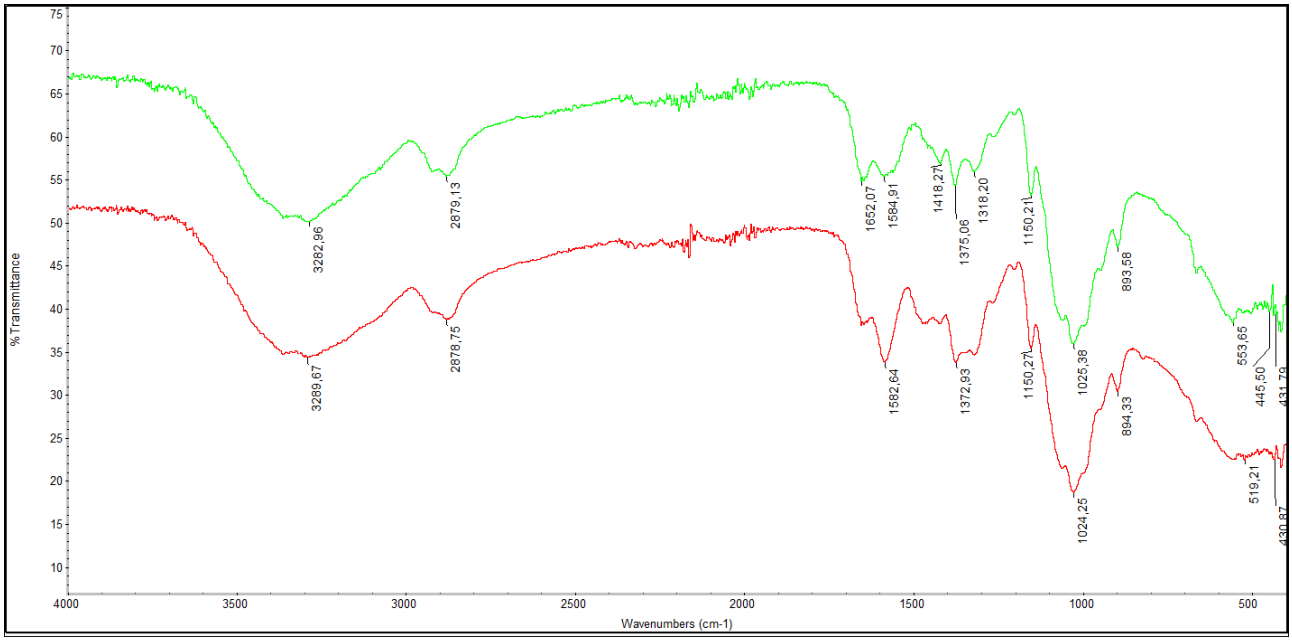

Fig. 4. Yellow spectrum: NOT treated scaffold; red spectrum: Irradiated scaffold

The spectra resulted superimposable, no significant shifts were recorded, giving a clear sign that the material did not degrade and was not affected by irradiation

14.1.5 Total bacterial load

Scaffolds disinfected by immersion in 70 % v/v ethanol were poured into 3 mL of sterile Tryptone soya broth (pH 7.3), previously prepared, as control. The same procedure was adopted for irradiated scaffolds, then the containers (Falcon®,VWR), were incubated for 14 days h at 37 °C, as suggested by the method reported in the "Farmacopea XII"[2] . Preliminary, Falcon tubes were empirically observed, no turbidity was detected, suggesting no bacterial growth. A further confirmation was given by inoculating 100 µL of broth on Tryptic Soy Agar (TSA), incubating it for 5 days at 37 °C. No bacterial growth was observed at all, sterilization by gamma rays irradiation was achieved.

14.2 Concluding considerations

Chemico-physical features of irradiated scaffolds mostly varied in terms of mechanical parameters and pore size distribution at the micrometric level. These two information can be in accordance, since it seems quite logical that a more porous structure presents lower tensile strength, whereas hydrogel function of holding water in its polymeric network did not change.

Sterility was achieved, thus, the method could potentially be employed for hydrogel chitosan scaffold sterilization, providing that the actual properties do not negatively affect their behavior in terms of cell growth supporting capacity.

Referring to chapter 2, in which is reported the study of different preparation mechanisms and their influence on chemico-physical parameters, chitosan hydrogel can vary significantly as well; nevertheless, in that study *in vitro* biocompatibility was assayed demonstrating all of them could host cells growth, suggesting that chitosan hydrogel scaffolds featuring different properties, such as those irradiated, could anyway reveal themselves valid for tissue engineering purposes.

To find out these aspect and firmly confirm these hypothesis, more addressed investigations, such as cell cultures and molecular weight distribution comparison between irradiated and NOT treated scaffolds have been scheduled.

1. Marreco P. R., da Luz Moreira P., Candelária Genari S., Moraes A. M. Effects of Different Sterilization Methods on the Morphology, Mechanical Properties, and Cytotoxicity of Chitosan Membranes Used as Wound Dressings. Journal of Biomedical Materials Research Part B. Vol 71B, Issue 2, 2004, pp. 268-277.
2. Pharmacopoeia Italica Ufficiale della Repubblica Italiana (XII Edizione), 2008, pp. 193-194.

15 Conclusions

Several manufacturing techniques are more and more studied for the development of effective medications for the cure of chronic wounds and other damaged tissues.

Scaffolding approach implies the use of biocompatible materials, processed in order to mimic the extra cellular matrix of a tissue in terms of geometries and composition.

In particular, three-dimensionality of scaffolds started to be investigated since a couple of decades, to better mimic the cytoskeleton structure that is often impaired or lacking in difficult-to-heal tissues impeding correct regeneration.

The very vast spectrum of material forms employed in tissue engineering led us to mainly focus on hydrogels that, properly processed, possess adequate chemico-physical properties for scaffolding purposes, that means providing a biocompatible matrix supporting and guiding cells growth towards tissue reconstruction.

Naturally derived materials formulations were thus *ad hoc* designed, developed and successfully applied to an innovative in-house developed freezing deposition additive manufacturing technique, ideated for the easy manipulation of liquid viscous materials in controlled three-dimensional shapes.

The fabrication procedure, after proper adjustments, resulted highly reproducible and capable of obtaining 3D hydrogels with controlled parameters such as porosity, water content, mechanical behaviors, all of primary relevance for reproduction of biomimetic environments and their applicability.

Native human cells profitably grew on several types of prepared hydrogels, processed or not by 3D printing, but making emerge significant differences in terms of viabilities, proliferation and three-dimensional spread between 2D and 3D prototypes. The latter resulted particularly advantageous; in specific, chitosan-based 3D scaffolds dedicated to wound healing showed to support fibroblast/keratinocytes colonization, for this reason an *in vivo* evaluation of their effectiveness was worth. Diabetic ulcerated rats, independently from the treatment, healed completely, anyway, histological analysis showed faster and better hierarchically organized repair in tissues treated with chitosan 3D scaffolds.

Several advanced wound dressings available on the market, rather than still studied at the laboratory stage, are loaded with active compounds that should ameliorate the physio-pathological condition targeted. Models of silver sulfadiazine release chitosan-alginate combined dressings were successfully designed and created, being characterized for different partially

tunable release patterns as a function of the assembling and exerting anti-microbial activity on wounds characteristic pathogenic bacteria, showing 100 % growth inhibition.

As mentioned, functionalization of biomedical materials for tissue engineering purposes different from wound healing and dedicated to applications in dentistry for implants was investigated. Chitosan hydrogel films were optimally decorated on their surface with fibronectin through the employment of an engineered aptamer; HDX-MS confirmed the hypothesis that the aptamer bound selectively chitosan and the protein. This, with high probability allowed the protein to maintain its tertiary structure, explaining the significant major growth of osteoblasts and epithelial cells seeded on the hand-woven substrates, exerting biological functions such as the activation of the integrin-mediated pathway in a directly proportional trend to the amount of aptamer inoculated in terms of cell morphology control.

Moreover, 3D chitosan scaffolds studied, were functionalized by coating with collagen type IV, improving drastically epithelial cells compatibility.

Drug development efforts involving therapeutic peptides or proteins can lead to optimization of drug delivery, drug stability, solubility and functionality. The use of biocompatible polymers as potential drug delivery molecules able to interact via non-covalent bonds with an active principle through multiple functional groups was investigated. HDX-MS was then employed to localize insulin dynamics induced by interactions with natural polysaccharides such ad chitosan, sodium alginate and chondroitin sulfate.

HDX-MS method demonstrated the capabilities of the technique to obtain useful information toward the flexibility and the behavior of native insulin and could provide insights to study the behavior of pharmaceutical formulations in the presence of natural polysaccharides.

Mass spectrometry was utilized also for the determination and quantitation at the femtomolar level of collagen types I-V constituting the stromal thyroid gland matrix in a reproducible way, giving the possibility of better studying decellularized organs as natural occurring scaffolds rather than evaluation of which decellularization protocol among the tested ones works best.

The application of 3D printing in environmental sciences showed to be quite effective in the obtainment of prototypes of wastewaters filtering systems. TiO_2, was perfectly embedded in the chitosan formulation as well as in the resulting hydrogel after process, as demonstrated by characterizations. TiO_2 served as drug photocatalytic compound, showing good degradation properties versus amoxicillin under UV irradiation. Moreover, reusability of TiO_2 scaffolds was assessed, finding out catalytic efficiency could be considered relevant till third use.

Currently, several aspects are investigated; a particular focus points towards the development of novel printable blends and their use in hydrogel scaffolds creation for the performance improvement as medication prototypes.

3D alginate/nanocrystalline cellulose dressings loaded with in-house produced silver nanoparticles were successfully produced, characterized and tested *in vitro* as antimicrobics delivery systems (figure 1).

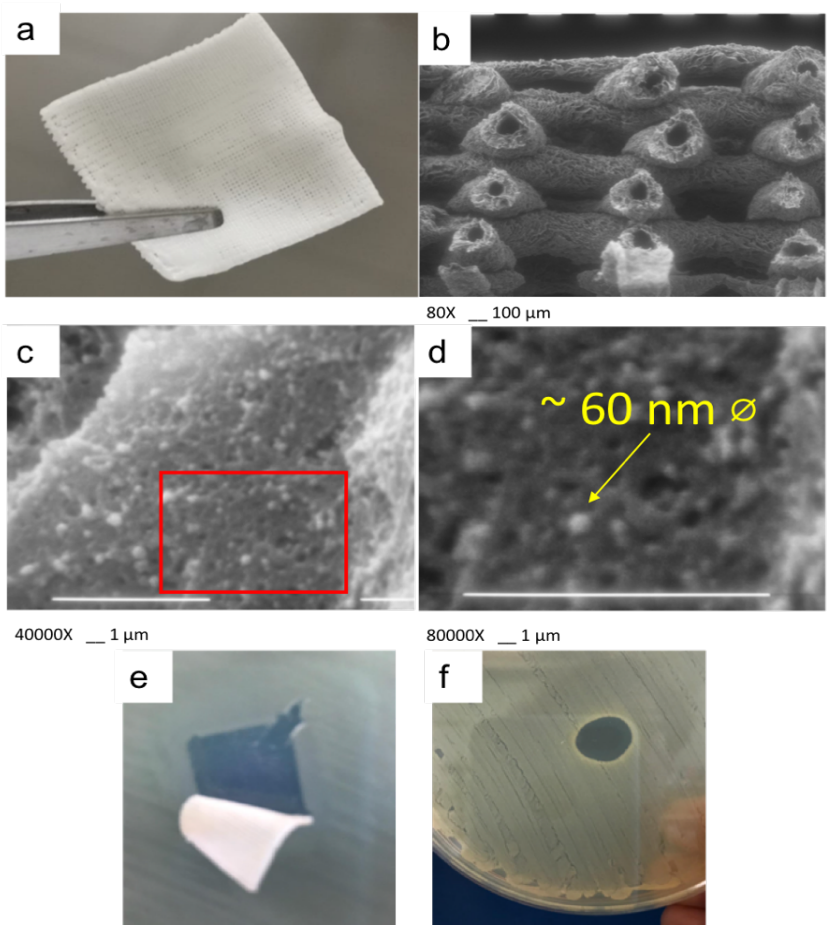

Figure 1. a) Prototype of calcium alginate/nanocrystalline cellulose 3D printed dressing; b) SEM photograph of cross section; c) & d) SEM photographs focus on silver nanoparticles; e) & f) Kirby-Bauer assay on *P. aeruginosa* and *S. aureus* demonstration of antimicrobial activity.

These prototypes are as well running experimentations as HepG2 cells, exploiting silver nanoparticles cytotoxicity against these tumor cells and suggesting in a preliminary way a further application.

Moreover, organ decellularization protocols are investigated in order to obtain naturally occurring matrix compounds to be included in novel polymer printable inks.

Cell biological response is crucial for the development of materials intended to be finely tailored for tissue engineering. Mass spectrometry proteomic methods are under development to better understand at molecular level which mechanisms are involved under specific stimuli, already giving a positive scenario of the materials that seem more promising (e.g. figure below represents a comparison between the relevant biological responses of equine chondrocytes cultured in different conditions: isolated cells; standard Petri dishes, on chitosan-based 3D scaffolds and on chitosan/hyaluronic acid 3D scaffolds).

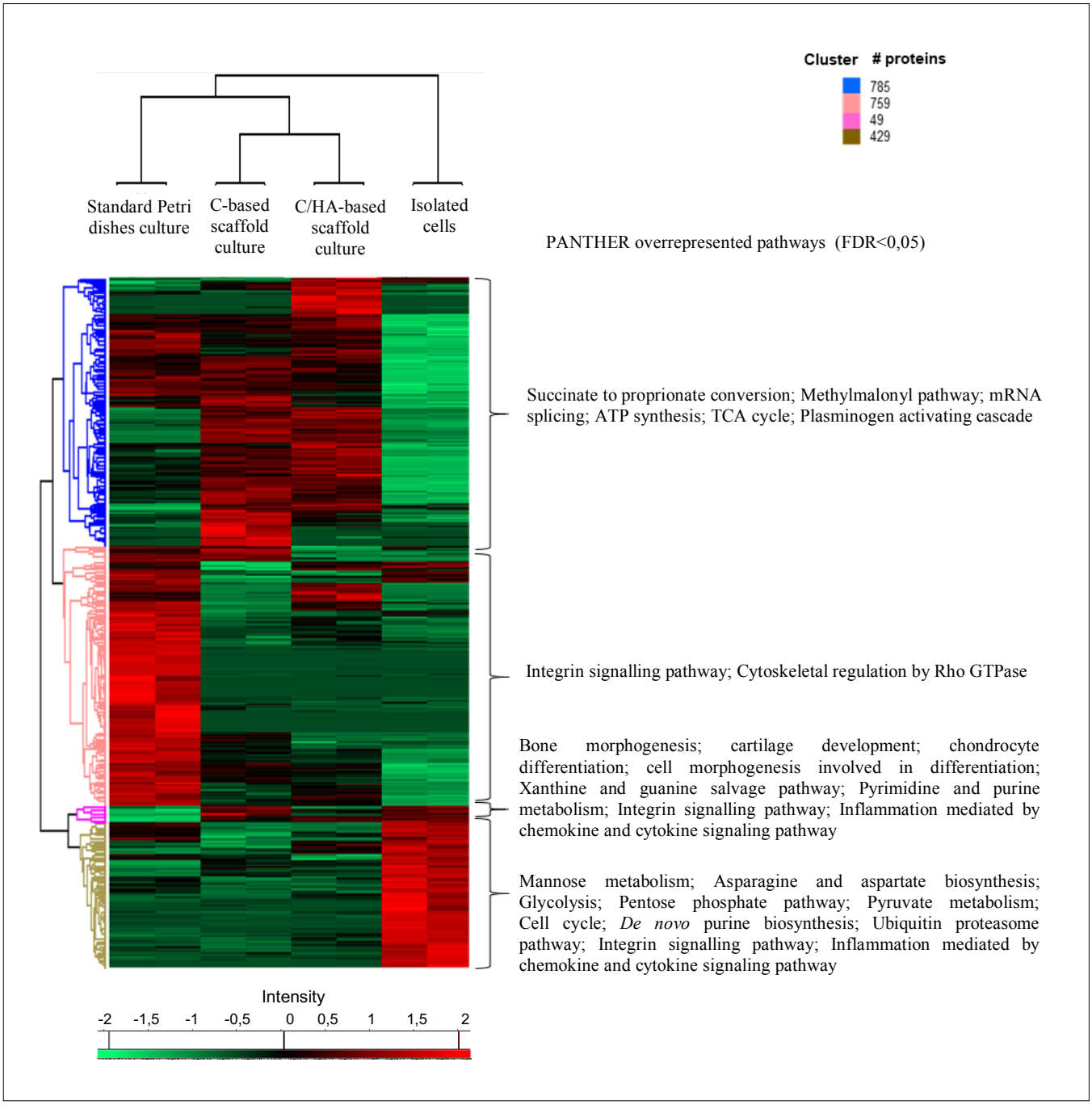

Acknowledgements

I want to spend a few words for all the people who supported me from the beginning to the end of this incredible experience and school of life.

My gratitude goes primarily to Prof. Lisa Elviri, who followed me up from the first days of internship until now from both the technical and behavioral point of view, always triggering my research interests positively as well as teaching me the job step by step.

The second person I really thank is Prof. Ruggero Bettini, who gave me the opportunity, in conjunction with Lisa, to work with him in the laboratories that they manage, letting me understand how order and attention to details are crucial in terms of results achievable.

I would like to be grateful to the colleague Annalisa Bianchera, who also accompanied me, especially during my first lab experiences, teaching me how to move in the lab as well as preparing experiments.

Diana Carolina Angèl is for sure among the persons who I was more in contact with, and provided that playfully verbal fights were not rare, we tightened a deep friendship.

I sincerely thank all the people that I met along this way: Dr. Davide Frascio, Dr. Giuseppe Marseglia, Dr. Cinzia Marchi, Dr. Enrica Scalera, Dr. Greta Adorni, Dr. Adriana Rocha Clementìno, Dr. Miriam Corrado, Dr. Miriam Girardini, Dr. Luca Palese, Dr. Francesco Candela, Dr. Ayca Altay, Dr. Marta Cito, Dr. Francesco Marchesani, Davide Dallatana, Dr. Fulvio Barbaro, Dr. Elia Consolini.

In particular, I want also to express my special thankfulness to one of my best friends, Dr. Marco Alfieri, for his human support and for its willingness as scientific collaborator.

I also specially thank for the precious collaboration Dr. Silvia Marando, Dr. Ludovica Parisi, Prof. Carlo Galli, Prof. Borghetti, Prof. Maria Cristina Ossiprandi, Dr. Cinzia Reverberi, Dr. Elena De Angelis, Dr. Laura Bergamonti, Prof. Claudia Graiff, Prof. Lottici, Dr. Fabio Corradini, Dr. Ruben Foresti, Prof. Marco Silvestri, Dr. Claudio Intini, Dr. Daniele Andreani, Manuel Baldinu, Dr. Marco Ricci, Dr. Manola Fioravanti.

Nevertheless, my parents, Erminia and Maurizio, for their love and never-ending support, my sister Martina and her partner Alexander Ehm as well as my friends.

Concluding, I would like to dedicate the work made for the preparation of this thesis to my grandmother Maria Luisa Barbarini, who recently passed away, leaving a big sense of emptiness in me but making me feel proud to succeed in this challenge as she desired.